



MONASH University

Development of Quasi-active Thermography on Large Scale Geomembrane Structures

Yue Ma

A thesis submitted for the degree of *Doctor of Philosophy* at
Monash University in 2021

Department of Mechanical and Aerospace Engineering

Copyright notice

Notice 1

© Yue Ma (2021).

Under the Copyright Act 1968, this thesis must be used only under the normal conditions of scholarly fair dealing. In particular, no results or conclusions should be extracted from it, nor should it be copied or closely paraphrased in whole or in part without the written consent of the author. Properly written acknowledgement should be made for any assistance obtained from this thesis.

Notice 2

© Yue Ma (2021).

I certify that I have made all reasonable efforts to secure copyright permissions for third-party content included in this thesis and have not knowingly added copyright content to my work without the owner's permission.

Abstract

Thermal imaging monitoring technique has been extensively used in the field of non-destructive structural health monitoring. Although traditional thermal imaging is useful in inspecting small scales of structures, it is difficult to monitor large-scale on-site structures such as geomembranes located over a large area. Traditional on-site thermography techniques are limited by the environmental conditions and the monitoring time. This research aims to develop a novel thermography method that can be used to perform structural health monitoring tasks over large scale of membrane structures. The developed strategy uses ambient weather information such as solar intensity and ambient temperature to analyse the long-term transient temperature evolutions of geomembranes and enhance the monitor results. A series of lab-scale experiments were conducted to verify the developed technique's reliability and practicality.

In this thesis, a preliminary experiment was first set up to test the temperature response of the high-density polyethylene (HDPE) geomembrane under the variation of the solar intensity. It was found that short terms of solar intensity fluctuations can result in short terms of transient temperature variations on the surface of the HDPE geomembrane, and the daily solar intensity cycles can also lead to a cycled transient temperature variation of the HDPE geomembrane. The transient temperature variation events were at first used to monitor the soil accumulations under the geomembrane. It was found that the development of the soil under the opaque geomembrane can be monitored with long-term monitoring.

The developed quasi-active thermography technique was then used to detect the defects under the geomembrane. Short terms of cloud shades in the experiments were used to stimulate the transient events on the geomembrane. It was found that non-penetrating defects can be found with these events, and the penetrating and non-penetrating defects can be detected with the frame subtraction based thermal imaging analysis method.

To further enhance the reliability and efficiency of the quasi-active thermography, the desired monitoring period was investigated. The improved quasi-active thermography technique can identify the subsurface objects with four frames of thermal images. In addition, multi-interfaces under the geomembrane can be classified with the integration of quasi-active thermography and clustering-based image segmentation algorithms.

The non-penetrating defects under the geomembrane were then made to contact different states of objects (gases, liquids, solids) such as water and soil. The experiment set-up simulates the complex condition under the floating covers. The developed thermography technique can distinguish two different interfaces under the geomembrane, and the defects on different regions were also detected.

To further understand the heat transfer process on the geomembrane and the transfer process of the scums, a series of finite element analyses were conducted to simulate the evolution of the geomembrane during the transition of scums. The computational analysis results show agreed temperature profiles with the profiles from experiment results.

An on-site thermal imaging study was conducted to verify the above laboratory experiments and models. The inspections at the geomembrane floating covers at the Western Treatment Plant (WTP) successfully detected the structural differences, including scums, sewages and biogas with the aid of local solar radiation and ambient temperature cycles.

The development quasi-active thermography technique uses the ambient weather information to conduct robust and efficient structural health monitoring on large-area structures. This technique can contribute to the future maintenance process for the geomembrane structures, significantly extends the expected service life of the structures, and ensures the safe and efficient operation of renewable energy collection.

Declaration

I, Yue Ma, declare that this thesis titled “Quasi-active Thermography Based Non-destructive Structural Health Monitoring of Large Floating Cover” and work presented in it are my own. This thesis is an original work of my research and contains no material which has been accepted for the award of any other degree or diploma at any university or equivalent institution and that, to the best of my knowledge and belief, this thesis contains no material previously published or written by another person, except where due reference is made in the text of the thesis.

Print Name:Yue Ma.....

Date:2021-10-26.....

Publications during enrolment

Peer-reviewed journal papers

Ma, Y., Wong, L., Vien, B. S., Kuen, T., Kodikara, J., & Chiu, W. K. (2020). Quasi-Active Thermal Imaging of Large Floating Covers Using Ambient Solar Energy. *Remote Sensing*, 12(20), 3455.

Ma, Y., Rose, F., Wong, L., Vien, B. S., Kuen, T., Rajic, N., Kodikara, J., & Chiu, W. K. (2020). Detection of defects in geomembranes using quasi-active infrared thermography. *Sensors*. 21, 5365.

Conferences

Ma, Y., Wong, L., Vien, B. S., Kuen, T., Rajic, N., Rose, F., Kodikara, J., & Chiu, W. K. (2021). Quasi-Active Thermography for Structural Health Assessment of Large Geomembranes. Structural Health Monitoring: 8APWSHM, 18, 79.

Acknowledgements

At first, I hope to express my sincere gratitude to my primary supervisor, Professor Wing Kong Chiu, for his unreserved support and meticulous guidance throughout my PhD study. I always feel so lucky to study under the supervision of Prof. Chiu. With his endless support and valuable suggestions, I enjoyed my project and found it exciting and satisfying to do research jobs. I am also so grateful that Prof. Chiu always gives me reliable advice when I meet challenges. He is so kind, helpful, wise, and responsible. It is my great honour to have Prof Chiu to be my supervisor.

Secondly, I would like to express my appreciation to Dr. L. R. Francis Rose and Dr. Nik Rajic from DSTG, and Mr. Thomas. Kuen from Melbourne Water Corporation. Dr. L. R. Francis Rose and Dr. Nik Rajic provided many suggestions in my study. They let me know how to be a professional academic researcher. I got many useful experiences such as critical thinking and a cautious attitude from their kindly guidance. Mr. Thomas. Kuen helped me combine the research and applied engineering, and I also got many useful suggestions and helped from him when I conducted the field trials for my project.

I would also like to show my appreciation to Dr. Leslie Wong, and Dr. Ben vien for their generous support in my works. I am grateful that I can work in the acoustic lab team and always get a lot of support and suggestions from you.

I am also grateful to my parents Xiaodong Ma, Xiaoyan Li, who gave me endless support throughout my PhD study. Although they are not in Australia, they are always concerned about my life and my studies in Australia. Thank you for every phone call, video call and unreserved support.

The Support from the Monash University Graduate Research Completion award is acknowledged.

Contents

1	Introduction	14
1.1	Introduction	14
1.2	Motivation for the research	16
1.3	Research aims	19
1.4	Thesis outline	19
2	Literature review	23
2.1	Properties and applications of high-density polyethylene geomembrane	23
2.1.1	Introduction	23
2.1.2	Temperature monitoring for geomembranes	24
2.1.3	Scums in the sewage water treatment plant	25
2.2	Structural health monitoring techniques	26
2.2.1	Non-contact structural health monitoring techniques	26
2.2.2	On-site wide coverage remote sensing structural health monitoring	27
2.3	Infrared thermography monitoring	33
2.3.1	Introduction	33
2.3.2	Thermal imaging methods	34
2.3.3	Application of thermal infrared thermography	36
2.3.4	Infrared thermal imaging on HDPE	38
2.4	Infrared thermal imaging on large on-site structures	41
2.5	Environmental effects on thermal imaging of on-site structures	46
2.6	Infrared thermal imaging theory	49
2.6.1	Fundamental concepts	49
2.6.2	Heat transfer of geomembrane under the solar radiation loading	51
2.6.3	Theories of thermal imaging monitoring on structures	53
2.7	Clustering-based image segmentation method	56
2.7.1	Algorithms for thermal imaging	56
2.8	Conclusions	61
3	Methodology & equipment	63
3.1	Introduction	63
3.2	Experiment Set up of the thermal monitoring system for the quasi-active thermography	63
3.3	Finite element analysis set up and preliminary computational analysis	66
3.4	Analysis of thermal image sequences	70
3.4.1.1	Newton's cooling law method	71
3.4.1.2	Logarithmic peak second-order derivative (LPSD) method	72
3.4.1.3	Frame subtraction method	73
3.5	Image procession methodology	74
4	Development of Quasi-active Thermal Imaging to Identify Features under the Geomembrane Covers Using Ambient Solar Energy	77
4.1	Introduction	77

4.2	Development of Long Periods Quasi-Active Thermal Imaging to Monitor the Accumulation of Scums under the Geomembrane Covers	78
4.2.1	Introduction	78
4.2.2	Quasi-Active thermographic method	80
4.2.2.2	Newton's cooling law for quasi-active thermography.....	82
4.2.3	Proof of concept (quasi-active thermography).....	82
4.2.3.1	Experiment setup	82
4.2.3.2	Cooling constant estimation using Newton's law of cooling	85
4.2.3.3	Verification of the consistency of the quasi-active thermography	89
4.2.4	Monitoring of accumulation of soil build-up under the geomembrane	95
4.3	Clustering-based Thermal Imaging Monitoring on Large Floating Covers using Ambient Weather Information	98
4.3.1	Introduction.....	98
4.3.2	Thermal imaging method	98
4.3.2.1	Thermography monitoring on large structures.....	98
4.3.2.2	Newton's cooling law for comparison of cooling rate	98
4.3.3	Thermal imaging monitoring on the HDPE geomembrane.....	99
4.3.3.1	Investigation of the suitable thermal imaging monitoring period with ambient weather information.....	99
4.3.3.2	Classification of different interfaces under the HDPE geomembrane	106
4.4	Conclusions.....	113
5	Detection of the defects in geomembranes with different interfaces using the quasi-active thermography.....	115
5.1	Introduction.....	115
5.2	Development of Short Periods of Quasi-active Thermography to Detect the Defects in Geomembranes.....	116
5.2.1	Introduction.....	116
5.2.2	Identification of transient event due to cloud movement.....	117
5.2.3	Procession of thermal image	118
5.2.4	Detection of part-penetrating damages on air	119
5.2.5	Detection of part-penetrating damages with different interfaces	122
5.2.6	Detection of surface penetrating defects	125
5.3	Detection of Defects in Geomembranes on Different features	127
5.3.1	Introduction.....	127
5.3.1.1	Experiment set up.....	128
5.3.1.2	Defects in the HDPE geomembrane with substrates.....	129
5.3.2	Results and discussion	132
5.3.2.1	Case 1: Inspection of defects on water and air substrates	132
5.3.2.2	Case 2: Inspection of defects on soil and air substrates.....	136
5.3.2.3	Investigation and Monitoring period and frame rate.....	139
5.3.3	Conclusions.....	141

6	Assessing the state of scum-berg transition process under the floating covers using thermal means.....	143
6.1	Introduction.....	143
6.2	Methodology	145
6.2.1	Experiment set up	145
6.2.2	Finite element model.....	147
6.2.3	Newton’s cooling law and temperature validation	148
6.3	Results and discussions	149
6.4	Monitoring scum transition.....	150
6.5	Conclusion	157
7	Structural health monitoring on large scale geomembranes floating covers using thermography 158	
7.1	Introduction.....	158
7.2	On-site quasi-thermography methodology	159
7.2.1	Regions for the thermography inspection	160
7.2.2	Experiment set up	161
7.3	Result and discussion.....	162
7.3.1	Trial 1	162
7.3.2	Trial 2	168
7.4	Conclusion	171
8	Conclusions and future works	173
8.1	Conclusions.....	173
8.2	Future works.....	174
9	References	176

List of Figures

Figure 1.1 Satellite view of floating HDPE geomembrane covers in covered anaerobic lagoons(CAL) at the Western Treatment Plant(WTP)	15
Figure 1.2 High-density polyethylene geomembrane floating covers at the WTP.....	16
Figure 1.3 Illustration of the degradation process at the CAL. (a)condition of the lagoon when sewage water flows from the lagoon's inlet (b) condition after degradation of the sewage water.	18
Figure 2.1 Temperature measurement arrays along with the geomembrane cover [63]	24
Figure 2.2 Experiment set up for the inspection of an aluminium beam with a pair of cameras [99]	28
Figure 2.3 Digital elevation model of six surveys with UAV scans over four seasons at a geomembrane floating cover [25].....	31
Figure 2.4 Experiment set up of lock-in thermography	35
Figure 2.5 Optimal inspection frame time for different areas of the rudder surface (green area in the images, time refers to the temperature where the first area reaches 5 °C [139]	37
Figure 2.6 Thermal map of thickness showing the delamination of the HDPE joints{Omar, 2006 #9}.....	39
Figure 2.7 GUI of the inspection algorithm for the polyethylene pipe.....	40
Figure 2.8 (a) Stitched thermal image for a building. (b) overlapped fused image for the building. (c) Point mesh of a building from a surface dense modelling algorithm. (d) 3D thermographic model [161]	42
Figure 2.9 Time lapsed thermal images of a building. (120 min image interval, every 4 images)[162].....	42
Figure 2.10 (a) Daytime thermal imaging result. (b) night-time thermal imaging result [169].....	44
Figure 2.11 Temperature profile and heat flow of a concrete structure with delamination [181].....	47
Figure 2.12 Concrete block temperature profiles with the (a) ambient temperature. (b)solar intensity. (c) wind speed.	48
Figure 2.13 Wavelength of radiometry spectrum[184].....	50
Figure 2.14 Emissivity spectrum of the HDPE geomembrane material [127]	50
Figure 2.15 General procedures of analysing the thermography.....	57
Figure 2.16 Illustration of superpixel segmentation. The left two images are the images after the proposed clustering stage, right two images are the final results after the merging stage.....	59
Figure 3.1 Emissivity spectrum of the HDPE membrane from Fourier-transform infrared (FTIR) spectroscopy.	64
Figure 3.2 Illustration of the IR thermography experiment set up	64
Figure 3.3 Experiment equipment of outdoor thermal imaging monitoring system.....	65
Figure 3.4 Cross-sectional boundary conditions for heat transfer in the FEA.....	67
Figure 3.5 Illustration of FEA results (no external heat flux, ambient temperature is constant)	69
Figure 3.6 Illustration of FEA results (external heat flux was applied for 500s and then stopped, ambient temperature is constant)	70
Figure 3.7 Flow chart of image procession.....	74
Figure 4.1 A high-density polyethylene (HDPE) geomembrane specimen was clamped on the aluminium container	83
Figure 4.2 A clayey soil block in a 0.1 m deep rectangular aluminium container was used to simulate the scum at WTP.	84
Figure 4.3 (a) FLIR A615 thermal camera and (b) Apogee SP-110 pyranometer.	84
Figure 4.4 Schematic drawing of the experimental set-up.	84
Figure 4.5 Temperature profile of geomembrane and solar intensity history.....	86
Figure 4.6 (a) curve fitting of the temperature decay curve of the no-soil region on the geomembrane and (b) curve fitting of the temperature decay curve of the soil region on the geomembrane.	87
Figure 4.7 Comparison of profiles of soil under HDPE geomembrane: (a) optical photography. (b) raw thermal image was taken during the experiment. (c) map of cooling constant derived from Newton's cooling law.	89
Figure 4.8 Geomembrane temperature and solar intensity history.	91
Figure 4.9 Curve fittings of pixels over two days. (a) pixel example on the no-soil region on day 1. (b) pixel example on the soil region in day 1. (c) pixel example on the no-soil region on day 2. (d) pixel example on the soil region on day 2.	92
Figure 4.10 Processed cooling constant maps over two days. (a) cooling constant map on day 1. (b) cooling constant map on day 2.....	93

Figure 4.11 Cooling constant distribution in cooling constant maps of the two days experiment. (a) day 1. (b) day 2.....	94
Figure 4.12 Normalized cooling constant maps of two days experiment. (a) cooling constant map on day 1. (b) cooling constant map on day 2.	94
Figure 4.13 Soil profile measurement difference in two days monitoring.....	95
Figure 4.14 HDPE geomembrane temperature profile and solar intensity history in three-day quasi-active thermography experiment.....	97
Figure 4.15 Comparison of photography and processed thermal images. (a) soil composite profiles from photography. (b) zoomed soil composite profiles from processed thermal images.....	98
Figure 4.16 Recorded experiment data (solar intensity, ambient temperature and temperature profiles of a randomly selected point on soil region and a randomly selected point on the no-soil region on the geomembrane)	100
Figure 4.17 Illustration of cooling constants on soil region and no-soil region with solar intensity and ambient temperature change. (a) local ambient temperature history and cooling constant profiles. (b) local solar intensity history and cooling constant profiles	102
Figure 4.18 Generated cooling constant maps at different periods in the two days experiment. (a-e) the sum of cooling constants from thermal image sequences in Figure 4.17. (f-j) average of cooling constants from thermal image sequences in Figure 4.17. (a and f) period 1.(b and g) period 2. (c and h) period 3 (d and i) period 1, 2 and 3 (e and j) period 4.....	104
Figure 4.19 Comparison of cooling constant maps generated from different lengths of periods. (a) sum of period 2 thermal image sequences (b)sum of 60 mins thermal image sequences (6 frames) (c) sum of 40 mins thermal image sequences (4 frames) (d) single frame of cooling constant maps in 40 min	106
Figure 4.20 Test rig filled with soil, air and water at different regions under the HDPE geomembrane cover	107
Figure 4.21 Cooling constant maps with three regions (soil region, water region and air region) on the HDPE geomembrane	108
Figure 4.22 Comparison of results from K-means clustering method with different k values (a) Cooling constant map (b) k=3 (c) k=4 (d) k=5.....	109
Figure 4.23 (a) classification of regions with K-means clustering method (k=4) (b) data distribution of each cluster.....	109
Figure 4.24 Comparison of results from DBSCAN method .(a) cooling constant map (b) $\epsilon=0.000055$, $N_{min}=600$ (c) $\epsilon=0.0001$, $N_{min}=600$ (d) $\epsilon=0.000055$, $N_{min}=200$	110
Figure 4.25 (a) Classification of regions with DBSCAN method ($\epsilon=0.000055$, $N_{min}=600$) (b) data distribution of each cluster.....	111
Figure 4.26 Comparison of results from GMM method .(a) cooling constant map (b) components number=3 (c) components number=4 (d) components number=5	112
Figure 4.27 (a) Classification of regions with GMM method (components number=4) (b) data distribution of each cluster.....	112
Figure 5.1 Experiment set up (a) high-density polyethylene(HDPE) geomembrane was clamped on the test rig. (b) illustration of the data acquisition phase	118
Figure 5.2 Temperature profile on HDPE membrane and local solar intensity history	118
Figure 5.3 Distribution of part-penetrating defects on HDPE geo-membrane	120
Figure 5.4 Experiment set up of detecting part-penetrating defects on air	121
Figure 5.5 Geomembrane temperature profile and local solar intensity history. 2 transient events are highlighted	121
Figure 5.6 Temperature evolution and solar intensity history on the membrane in event 1 in Figure 5.5 ...	121
Figure 5.7 Temperature evolution and solar intensity history on the membrane in event 2	122
Figure 5.8 (a) Processed thermal image sequence with Equation 3.17. (b) Processed thermal image sequence with Equation 3.19	122
Figure 5.9 Experiment set up of detecting part-penetrating defects on air and water.....	124
Figure 5.10 Geomembrane temperature profile and local solar intensity history. 6 transient events are highlighted	124
Figure 5.11 (a) Raw infrared thermal image (b) processed thermal image sequence with Equation 3.17 (c) processed thermal image sequence with Equation 3.19.....	125
Figure 5.12 Geomembrane with 4 different lengths of cut-through defects.....	126
Figure 5.13 Temperature profile of the geomembrane and the local solar intensity history.....	126

Figure 5.14 Temperature profile of the geomembrane and the local solar intensity history in event 1 in Figure 5.13	127
Figure 5.15 (a) Processed thermal image sequence with Equation 3.17 (b) Processed thermal image sequence with Equation 3.19	127
Figure 5.16 Illustration of data acquisition phase in the quasi-active thermography experiment.....	129
Figure 5.17 Side profiles of the test rig. (a) HDPE geomembrane on air and water. (b) HDPE geomembrane on air and soil	130
Figure 5.18 Distribution of defects on the HDPE geomembrane. (a) defects in contact with soil and air. (b) defects in contact with water and air	131
Figure 5.19 Cross-sectional review of two HDPE geomembranes. (a) profiles of defect 1 and defect 5 on the first geomembrane. (b) profiles of defects 1, 2 and 3 on the second geomembrane.....	131
Figure 5.20 Temperature profile from a pixel on no-water region in the thermal image sequences and solar intensity history.....	134
Figure 5.21 Results of analysis of thermal image sequences with different methods: (a) a single frame of the raw thermal image, (b) cooling constant map based on Newton's cooling law analysis, (c) LPSD method, and (d) frame subtraction method.	135
Figure 5.22 Temperature profile from a pixel on the air region in thermal image sequences and solar intensity history.....	137
Figure 5.23 Results of analysis of thermal image sequences. (a) a single frame of the raw thermal image. (b) cooling constant map of Newton's cooling law analysis. (c) result of the LPSD method. (d) result of the frame subtraction method	138
Figure 5.24 Cooling constant maps from Newton's cooling law (a) monitoring period 20mins, frame rate 5mins/frame, (b) monitoring period 5 mins, frame rate 3 frame/second	140
Figure 5.25 Error bars with 2σ for cooling constants of defects on the air region and the soil region	141
Figure 6.1 Illustration of the procedure of using ambient solar intensity and temperature to estimate the temperature profile of HDPE geomembrane	144
Figure 6.2 HDPE geomembrane specimen on test apparatus	145
Figure 6.3 Illustration of the experiment set-up	146
Figure 6.4 Recorded solar intensity and ambient temperature profile	147
Figure 6.5 Temperature profiles of soil region and no-soil region points on the HDPE geomembrane	147
Figure 6.6 Finite element model (FEM) of geomembrane contacts with soil	148
Figure 6.7 Temperature contour of geomembrane.....	149
Figure 6.8 Predicted temperature profile of HDPE geomembrane from FE analysis	149
Figure 6.9 Comparison of FE results and experiment measurements	150
Figure 7.1 Scums at the WTP, they exist under the HDPE floating covers and float on the sewage	159
Figure 7.2 Digital elevation model with Unmanned aerial vehicle scan by Leslie et al. [25]	160
Figure 7.3 Illustration of structures on the monitored region of the floating covers	161
Figure 7.4 Illustration of the thermography set up at the floating covers.	162
Figure 7.5 Monitored regions of trial 1 in day 1 and day 2	163
Figure 7.6 Recorded experiment data for site 1 inspection	163
Figure 7.7 (a) optical photo of to illustrate the structures of site 1 (F-flotation line, B-ballast line, W-wrinkle or curvature on the covers). (b) single frame of raw thermal image for site 1. (c) LPSD map for site 1. (d) K-means image segmentation map for site 1.	166
Figure 7.8 Recorded experiment data for site 2 inspection	167
Figure 7.9 (a) optical photo of to illustrate the structures of site 2 (F-flotation line, B-ballast line, W-wrinkle or curvature on the covers). (b) single frame of raw thermal image for site 2. (c) LPSD map for site 2. (d) K-means image segmentation map for site 2.	168
Figure 7.10 Monitored region in trial 2.....	169
Figure 7.11 Recorded experiment data for site 3.....	169
Figure 7.12 (a) optical photo of to illustrate the structures of site 3 (F-flotation line, B-ballast line, W-wrinkle or curvature on the covers). (b) single frame of raw thermal image for site 3. (c) LPSD map for site 3. (d) K-means image segmentation map for site 3.	171

CHAPTER ONE

1 Introduction

1.1 Introduction

Geomembranes have been extensively used as covers in the mining industry[1, 2], liners in landfill plants[3-5], liners in water reservoirs[6, 7] and floating covers in sewage water treatment plants[8, 9]. They are deployed to control odour [10] and air pollution[11]; to trap sewage [8, 12, 13] and hazardous solid wastes[14, 15]; and to assist in the generation of renewable energy during the waste degradation process as floating covers[16-18]. Because of their stable material properties and high resistance to chemicals[19-21], high-density polyethylene (HDPE) geomembranes have been widely deployed in waste treatment plants. These membranes also have a very long expected service life of more than twenty years [5, 22]. However, the long-term performance of HDPE geomembranes can be significantly affected by high temperatures and high local stress concentration that can reduce their expected service life [23, 24].

Melbourne Water Corporation (MWC) in Victoria operates the Western Treatment Plant (WTP) at Werribee, Victoria, Australia, which treats more than half of the sewage from Melbourne. The sewage is degraded into renewable sources such as biogas and recycled water that can be used in electricity generation and agriculture, respectively [13]. As shown in Figure 1.1, WTP owns multiple anaerobic lagoons to treat more than half of the sewage water from Melbourne, where the first lagoons from the inlets are covered by large sheets made of HDPE geomembranes. Covered anaerobic lagoons (CAL) provide an anaerobic environment for the bacteria to degrade the wastes into biogas and sludge.

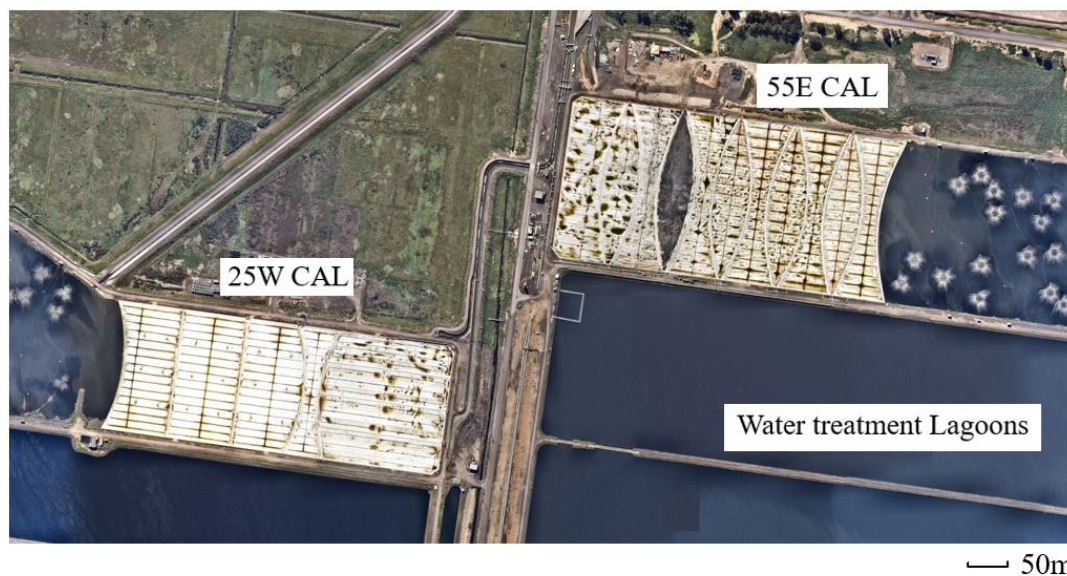


Figure 1.1 Satellite view of floating HDPE geomembrane covers in covered anaerobic lagoons (CAL) at the Western Treatment Plant (WTP)

At the WTP, the raw sewage (from household waste, high-strength organic waste and waste from meat and dairy food industries) will first pump directly to the first treatment lagoon (a 6 to 8 m deep pond) to remove solids. The flow of sewage slows down as it enters these large and deep lagoons, allowing most of the suspended solids in the sewage to sink to the bottom and form a layer of sludge. The whole sewage degradation and renewable source collection process take up to 40 days, and the waste water is recycled or discharged to the adjacent bay of Port Philip [25]. During the degradation process, the raw sewage flows into anaerobic lagoons[26], where it is digested into biogas (i.e., methane and hydrogen sulphide, H₂S) and residual sludge by bacteria in the anaerobic environment[27, 28]. At WTP, large scale HDPE geomembrane covers, each with an area of up to 10 hectares (approximately 500 m × 200 m)[25], are placed over the anaerobic lagoons, as shown in Figure 1.2. These floating membranes are manufactured by welding multiple sheets of HDPE geomembranes together.



Figure 1.2 High-density polyethylene geomembrane floating covers at the WTP

The geomembrane material is designed to float on the water with the edges of the membranes anchored around the perimeter, thus providing an airtight environment for the sewage [26, 29]. These geomembrane covers are also known as floating covers since they rise and fall with the level of sewage [30]. At the WTP, these floating covers are used (1) to harvest the biogas for generating energy and (2) to prevent the release of the environmentally damaging. The resource recovery programs at WTP turn the sewage into valuable products, including biogas for on-site electricity production and recycled water for agriculture customers. WTP utilizes the biogas captured from the CAL to generate renewable energy to supply all the electricity required to run the site and exports surplus electricity to the grid. Based on current data from Melbourne Water, each cover harnesses 65,000 m³ of biogas per day which is equivalent to generating 7 MW of renewable energy per day [31]. These floating covers are valuable assets for the utilities. Hence, it is important to monitor the structural integrity effectively and accurately so that the asset can work continuously and safely. The expected service life of the cover can be extended. The current monitoring approach is for inspectors to walk on the covers and conduct visual inspections, which is inaccurate and inefficient. Thus, an effective structural health monitoring method needs to be developed to evaluate the structural integrity of the large-scale floating covers.

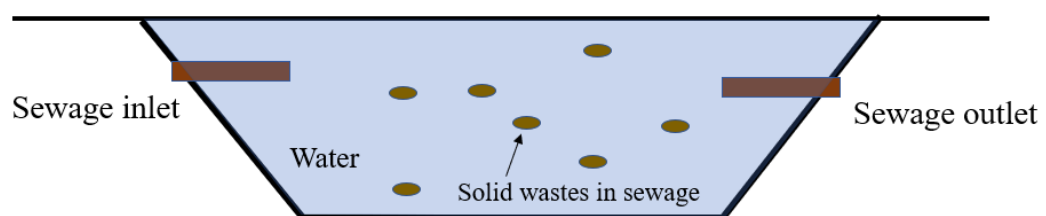
1.2 Motivation for the research

As already stated, despite the stable material properties, high corrosion resistance, and high tensile strength of the HDPE geomembrane, operation temperatures and the subsurface wastes can affect the structural integrity of the HDPE geomembrane materials. During the

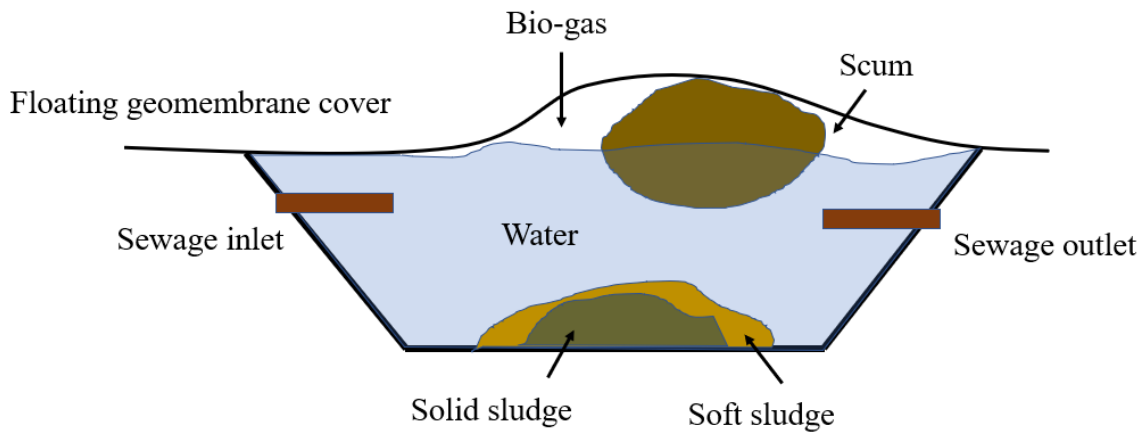
degradation process, some of the unscreened contents in the raw sewage, such as fats, oils, greases and fibrous materials, are separated from the sewage and become combined into solid objects named ‘scums’[32-35]. As shown in Figure 1.3, these scums can float on the water's surface and elevate the floating covers, resulting in local regions of stress concentration on the cover[36]. These scums can also accumulate over time and move under the covers. Given that these scums can adhere to the underside of the floating cover, they potentially cause local penetrating and non-penetrating defects on the surface of the geomembrane materials when it moves and stretches the cover[37]. These defects are hard to detect since they are in contact with sewage and scums. Therefore, a robust structural health monitoring technique needs to be developed to evaluate the structural health condition of the HDPE geomembranes. The challenges for the condition assessment of these membranes arise from:

- the fire-hazard (biogas) environment at the sewage treatment plant[38], where the utilities have set up a non-technology zone around these floating covers. The zone includes up to an altitude of 20 m above the floating membrane and 2 m around the perimeters of the covers.
- The large area of the covers where most of the traditional SHM methods cannot monitor such a large region at one time. Such monitoring tasks are very time-consuming and costly[39].
- Uncertainties about what substances are underneath the covers. Liquid sewage, gaseous biogas and solid scums are known to distribute unevenly under the cover. It is hard to predict the distribution of these materials under the opaque covers and to classify the different regions of the geomembranes which are in touch with the different substances

Floating geomembrane cover



(a) the CAL before degradation of the sewage



(b) the CAL after degradation of the sewage

Figure 1.3 Illustration of the degradation process at the CAL. (a) condition of the lagoon when sewage water flows from the lagoon's inlet (b) condition after degradation of the sewage water.

Currently, visual inspection is the method used for monitoring the structural health of the membranes. Inspectors have to walk on and around the membranes, and the usage of electrical measurement devices is prohibited. The experienced inspectors estimate the hardness of the scums under the floating covers and check visually for any damage or distress zones on the membranes. In addition, they need to measure the depth of the accumulated scum-bergs underneath the covers by putting their gloved hands into the sewage. Still, they are unable to measure large areas accurately and safely. The physical visual inspection is time-consuming and harmful to workers' health, and the inspectors might miss some damaged areas.

Thermography[40-42] has been used as a non-contact structural health monitoring method on many structures. It evaluates structural conditions by comparing the temperature distribution on the structures. A thermal camera can monitor a large structure by remote sensing and cover a large area with a long distance from the monitored objects [43]. However, traditional thermal imaging inspections mainly either requires external heat stimulation[44, 45] or monitor the self-heating objects[46-48]. The lack of external heat stimulation makes it difficult to stimulate the transient temperature changes on the surface of the geomembrane using active thermography. In addition, for passive thermography, traditional thermal imaging inspections on large on-site structures are based on the temperature contrast from a single frame of thermal image[49, 50], where the threshold was decided empirically, and the thermal contrast depends on the monitoring time of the frame[51]. As a result, the

monitoring result was affected by the ambient conditions and the threshold of the thermal image.

1.3 Research aims

The broad aim of this research is to develop an advanced thermography structural health monitoring technique to evaluate the structural health condition of the large-scale on-site structures. Such a technique will provide early warning of potential structural integrity problems and extend the expected service life of the structures by identifying structural differences efficiently and accurately. The specific aims of the research are to:

- develop a long-term (more than one day) infrared thermal imaging monitoring technology to identify the distribution, accumulation, and hardening progress of subsurface scums and present a detailed profile of the scums by the daily transient temperature changes surface of the HDPE geomembrane.
- Develop a short-term infrared thermal imaging technique to identify damages, such as penetrating defects, non-penetrating defects, and crack defects on geomembrane materials using the short-term transient temperature changes on the geomembrane surface.
- Use the developed thermography methods to identify the defects in different regions, such as the defects existing in the geomembrane-water interface and the defects at the geomembrane-soil interface.
- Improve the efficiency and the accuracy of the developed method to allow a large monitoring area through remote sensing. In addition, thermography is to be integrated with machine learning methods to classify the features under the geomembrane and identify each feature's area.
- Simulate the temperature evolution of the scums during the transition process of the scums with the ambient weather information such as ambient temperatures and solar radiation loadings.

1.4 Thesis outline

In Chapter 1, the background of this project is introduced. Anaerobic lagoons at the WTP and the anaerobic sewage degradation process in lagoons are introduced. The problems of

the structural integrity of the HDPE geomembrane resulting from the accumulation of scums will be described in detail. Building up a robust non-contact, wide coverage SHM technique for the large area of floating geomembrane covers is proposed as the motivation of the research. In addition, the research aim is to use a non-contact SHM technique to monitor the scums accumulation under the floating covers, to identify the location and the area of the scums, to distinguish the interfaces under the floating covers, hence ensure the efficient maintenance of the floating covers and extend the expected service life of this valuable asset in sewage water treatment plant.

Chapter 2 will present a literature review to cover the work done in this area of interest. Several kinds of geomembranes will be at first overviewed and compared with their material properties and applications in the waste treatment industry, temperature evolutions, and the expected service life over long-term usage. Scums problems in anaerobic lagoons, as well as their properties, will be reviewed and summarised. Existing non-contact SHM techniques in large structures will be summarised and discussed in detail. In addition, some previous on-site SHM on large scale structures were discussed, and the influence of some environmental factors was also discussed. The thermal imaging methods will be reviewed in detail with the classification of the techniques and the heat transfer theories, which raised the motivation to use thermal imaging to monitor the development of scums under the floating covers in the long term.

Chapter 3 introduced the methodologies of the quasi-active thermography, where the experiment set up for the inspection with the ambient weather information was illustrated. Some computational models to simulate the temperature evolution s and the scums transitions were verified with the FEA analysis, and the fundamental heat transfer theories were used to explain the results of the experiments and computational works.

Chapter 4 reports on developing a quasi-active thermography technique to monitor the temperature evolution of the HDPE geomembrane using ambient solar radiation. It experimentally demonstrates an investigation of measuring the surface temperature of the HDPE geomembranes floating covers using a thermal camera and solar intensity profiles using pyranometers to obtain the cooling process when solar intensity changes. In addition, Newton's cooling law is deployed to define the resultant cooling constants across the monitored cover. The results of laboratory-scale tests show the newly proposed quasi-active thermography capability to identify the presence and the extent of solid matters under the covers. The results also show that the daily transient temperature cycle can be used to show the growth in the extent of the soil under the cover. In the second topic section, quasi-active

thermography was improved and aimed to find out the regions of water, gas and scums under the floating cover, where thermal imaging deployed the ambient weather information to analyse the temperature responses of the HDPE floating covers. K-means clustering machine learning algorithms were developed to decide the area of each region under the cover. Laboratory experiments results show that thermography with the aid of the ambient temperature and the solar intensity can efficiently classify different interfaces by comparing the temperature changing rates. A contoured map was plotted to demonstrate areas of each region on the HDPE geomembrane. This technique will help predict the distributions of scums, sewages, and biogas under the cover without contacting measurements, hence assisting in the decision-making process of remove scums, maintain the effective operation of floating covers, and extending the service life of a membrane-like structure.

In Chapter 5, the developed quasi-active thermography technique is used to inspect the defects on HDPE geomembrane. HDPE geomembrane materials with artificially induced surface penetrating and non-surface penetrating sub-surface defects were used as the test samples. The test specimen was deployed outdoors on a flat roof top. An infrared thermal camera and a pyranometer were used to record the thermal response on the membrane material as a function of the solar intensity it is exposed to. The pyranometer was used to determine the periods of cloud cover, and this data was used to analyse the thermal transients. An algorithm was developed to compare frames of thermal images over the transient events resulting from the block of solar radiation from cloud covers. The temperature variation maps were used/ analysed to identify the defects on the cover. The results from this chapter provide insight into detecting defects in air and water using short-term thermography with the aid of weather information. In addition, in this chapter also the multi-interface defects were detected on a geomembrane. Defects will contact three kinds of objects under the cover (water, air and soil). The solar intensity data quantified the lengths of the transient temperature decay events, and these events were analysed by three algorithms to show the profiles of any defect. The proposed method was used to predict the multi-interface (gas, liquid and solid) defects on the geomembrane. It was found that the proposed method was able to identify different interface defects accurately. This new method that used the temperature fluctuation of solar radiation provided a non-contact method to inspect the structural defects on large-scale geomembranes.

In Chapter 6, a method using local weather information, such as ambient temperature and solar intensity, was used to determine the temperature cycles of geomembranes and simulate the geomembrane's regional temperature evolutions during the hardening process of under-

cover scums. Lab-scale measurements were conducted and followed by finite element analysis. A pyranometer and a thermal couple were deployed to record the local daily solar intensity and ambient temperature. The recorded data were imported into ABAQUS models to predict the temperature. The predicted temperature profiles were validated with the temperature measurements by the thermal camera. The results of this study reveal that local weather data can be used to estimate the temperature of geomembrane covers and predict the temperature profiles of the cover during the hardening process of under-cover scum. The findings in this chapter provide an insight into the daily thermal response of the geomembrane. This will assist the decision-making process of assets maintenance and provide guidance to correlate the experimental data from quasi-active thermography measurements in the future.

In Chapter 7, based on all experimental works and computational analysis, an on-site inspection study was conducted at the floating covers in the sewage treatment plant. Two regions on the floating covers were monitored based on previous Drone scans. Quasi-active thermography was set up along the side of the covers, and several long terms monitoring was carried out to figure out the features under the cover. The different materials, such as biogas pockets, sewage and scums, can be identified through the algorithms and image segmentation techniques. Previous studies were verified through this field study.

In Chapter 8, the main results and conclusions of the research are summarised, and recommendations are proposed for future research and in-site verifications.

CHAPTER TWO

2 Literature review

2.1 Properties and applications of high-density polyethylene geomembrane

2.1.1 Introduction

High-density polyethylene is one of the most widely used polymers worldwide. It has been extensively adopted in the waste treatment industry as the material for geomembranes and gas pipelines due to its good mechanical performance and outstanding chemical resistance to chemicals [52-54]. A wide range of corrosive chemicals such as concentrated acids, aromatic hydrocarbons, vegetable oils, and other municipal wastes only mildly attack HDPE. Hence, the HDPE is the most commonly used material in landfill liners and wastewater treatment liners.

Compared to other alternative polymers of geomembranes such as PVC, linear low-density polyethylene (LLDPE), HDPE is the least expensive material used in large land filler areas [55-57]. It is the most economical industrial geomembrane material and is adapted in 95% of geomembrane facilities [58]. Thicker sections of HDPE are recommended to accommodate welds and for applications requiring greater tensile strength. The lower cost of manufacturing HDPE per millimetre allows the industry to use thick HDPE geomembranes in the waste treatment plants. However, although the HDPE is more suitable and affordable in the waste treatment, it does have the following shortcomings:

- Although the cost of manufacturing HDPE is relatively low, the field welds on HDPE geomembranes would increase the installation cost and maintenance cost. The flexibility of the geomembrane gives rise to the formation of wrinkles and limits prefabrication. Due to the high stiffness of HDPE, factory welding cannot be applied before installation, HDPE will be delivered in a roll and welded on site.
- HDPE has a thermal expansion coefficient of 0.018%/0 C. The high thermal expansion coefficient of the HDPE leads to the formation of wrinkles on the surface of geomembranes. In the application of landfill liners or water storage which are exposed under the sun, the surface of geomembranes may be heated up by the radiation, especially for black coloured membrane, HDPE has a 60% higher thermal expansion coefficient than PVC, the increased temperature can cause the liner form waves, and this will push the weld line moves from the original position, which makes the working area around the weld point prone to fatigue.

Moreover, when the temperature decreases after sunset, the temperature of HDPE would decrease, and the surface contraction may result in a tensile force in the membrane.

- Stress cracking resistance (SCR) is identified as the most important material property for HDPE since it determines the mechanical durability of HDPE in the long term and the ability to prevent the geomembrane from being damaged during on-site welding and fabrication. It was reported that a minimum thickness of 1.5mm is required in most exposed HDPE applications due to the low SCR[58].

2.1.2 Temperature monitoring for geomembranes

Temperature evolutions and distributions are crucial for monitoring the scums development, the stress distribution, and the structural integrity for the cover[59-61]. Hanson [62] conducted long-term research to figure out the relation between the temperature variations and the depth of the wastes. They found that insulating materials would alleviate the temperature variations and determine the relationship between surface temperatures with different depth wastes. They also indicated that the regions with older wastes would result in a higher temperature at the cover due to sewage reaction. Also, Yesiller [63] did a long-term experiment to monitor the temperature evolutions of the cover as shown in Figure 2.1, some thermal couple arrays were deployed along with the geomembrane cover system. He stated that the temperature of landfill cover has phase lag with the seasonal trend and relate to the decrement of the waste depth amplitude. In addition, the thermal influence on the cover would lead to the shrinkage of the geomembrane and seam separation.

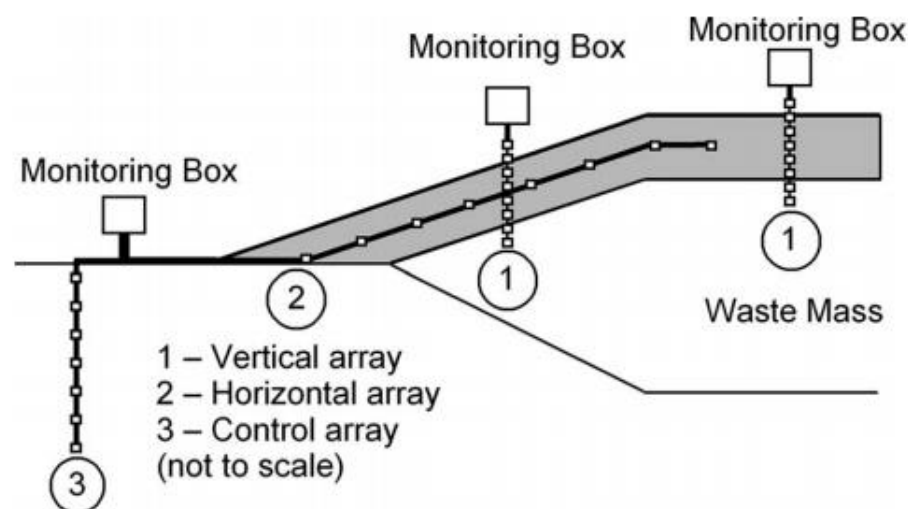


Figure 2.1 Temperature measurement arrays along with the geomembrane cover [63]

Needham [22] indicated that the temperature of landfill barriers would increase faster when the waste is under degradation. In 1993, Benson placed compacted clay together with thermocouples and fibreglass moisture probe at different depth into a PVC tube and covered with geomembrane on the top surface, the soil temperature and moisture content at different depth was monitored over two months in winter. They found that the depth of the frozen plane has good correlations with the average ambient air temperature. The hydraulic conductivity over different cross-sections along the pipe was also measured. They also predicted the temperature distribution of a larger 1m depth soil specimen. Yeşiller [64] applied thermocouples in the landfill cells to evaluate the influence of temperature fluctuations on the mechanical stress durability of geomembrane. Koerner [59] monitored the temperature evolutions of in situ geomembrane covers and liners at an anaerobic reactor and anaerobic reactor over 10.5 years with installed thermocouples.

Overall, almost all of the previous studies on temperature variation in landfill cells were based on installing thermocouples or temperature probes on the geomembrane. However, this method has some inevitable drawbacks, which means that monitoring a whole landfill cell needs to install many thermocouples and is at the mercy of durability of a thermocouple which would be affected by the corrosive wastes. Replacing thermocouples in the landfill cell is quite difficult and costly, and it will cause hazards to operators.

2.1.3 Scums in the sewage water treatment plant

The rapid increase in the production of daily wastes such as sewage and municipal wastes raised a greater concern of deploying an efficient wastes treatment method for the process of wastes collection, storage and treatment [65]. Compared to the traditional wastes treatment methods such as sanitary landfills[66, 67] or open burnings[68], anaerobic digestion has been used as a useful method for the digestion of municipal solid wastes (MSW) and sewage waters over decades[69]. Anaerobic digestion is used as a wastes degradation method to break the organic matters (such as food wastes, greases, manure, meats .etc) in the wastes into biogases (methane, sulphide, carbon dioxide and water vapour), sludges and other products with the absence of oxygen[70]. To reduce greenhouse emissions, anaerobic digestion systems can also produce fertilizer liquids and soil amendments as by-products[71, 72]. CAL [72] is one of the most common uses of anaerobic digestion systems, where geomembranes are installed on the top of lagoons to provide an anaerobic environment for the bacteria to degrade the sewage[73]. The floating covers are manufactured by welding multi-sheets of geomembranes together, and the perimeters of the covers are clamped around the lagoons to provide an airtight seal [30]. CAL has the advantages of (1) producing

renewable energy during the degradation. The produced biogas such as methane and sulphide can be recycled to generate electricity for industry usage or residents' usages[71, 74, 75]. (2) Reducing greenhouse gas emissions[76]. The CAL can assist recycle the greenhouse gases by harnessing these gases through the gas pipes under the floating covers. (3) Decreasing odours. CAL can prevent the emission of the harmful odours from emitting to the air and causing air pollution[77].

However, CAL is not able to digest all of the objects in the sewage. During the digestion, the raw sewage is unscreened and fed to the lagoon through the inlet end. Some untreated waste in the sewage, such as fats, matted hair, and fibrous material, can combine with sludges and transform into biomass named "scum"[33, 78-80]. This solid by-product is located on the surface of the lagoons and accumulates over time[81]. According to Halalshah et al.[82], the status of the scum is difficult to be quantified due to the heterogeneity of the scums. In addition, the scums can transform into a solid status throughout the anaerobic degradation process and develop into a larger body, known as "scumberg" [83]. Due to the various status of scums in a different period, the scum yield coefficients, scum composition and other material properties cannot be identified exactly[84]. Lettinga & Hulshoff pointed out that the accumulation of scums on the surface of the lagoon can block the pathway of the biogas and reduce the efficiency of energy collection. When attached to the subsurface of the floating covers, the scums can also lift the surface of the covers, resulting in a regional stress and strain concentration [30]. When the scums elevate the geomembrane, it will be laterally dragged by the wind force and result in tear damage. Furthermore, underside scums may also affect the expected service life of the floating covers by subsurface non-penetrating defects and an uneven regional distribution of temperatures. Hence, scums affect the operation of the anaerobic degradation systems in multiples ways. Therefore, the monitoring of the accumulation of scums, the evaluation of the influence of scums on the temperature evolutions of floating covers, and the investigation of the scums transformation process is critical for the operation of sewage treatment plants.

2.2 Structural health monitoring techniques

2.2.1 Non-contact structural health monitoring techniques

Ong (2017) stated that windy events could cause sewage movement attached under the cover laterally due to aerodynamic loading. This will change the stress and strain distribution on the cover significantly. Several non-destructive monitoring techniques are proposed to figure

out the accumulation and motion of the scum-berg. Ultrasonic test [85-87] is a classical NDT SHM technique, but in the environment where a high-level fire hazardous exists, the ultrasound sensors are hard to be installed on the membrane, and any electronic instrument or devices are restricted within the range of 20 m, this makes it impossible for using ultrasound technique. Vibration test is often utilized in the monitoring of solid structures, the vibration of a large-scale floating cover would need very strong activations, and the vibration on a membrane could not provide any information since the cover is floating at the same time. Other NDT methods such as magnetic test [88] and acoustic emission test [89, 90] are also not suitable for this kind of large floating membrane with restrictions of electronic devices.

Thermal imaging is a widely adopted technique in monitoring aerospace vehicle structures, civil structures and electrical components. This non-contact NDT inspection technique can monitor the large infrastructure remotely. The mechanism of thermal imaging is that when the structure has damage such as crack or breakage, the heat flow in that region would be stopped and cause uneven distribution of temperature on the surface of objects. Budiman [91] indicated that the mechanical and endurance performance of geomembrane depends on the temperature, and the impact of the temperature fluctuation during the anaerobic reaction on the geomembrane is quite significant. Especially when some of the sewages are attached to the underneath surface of the cover, the reaction procedure at the sewage will cause a regional temperature to rise and produce around one-meter lift on the sheet. Therefore, thermal imaging monitoring is proposed to be deployed for the inspection of HDPE floating covers.

2.2.2 On-site wide coverage remote sensing structural health monitoring

The large scale of infrastructures, such as bridges, historical buildings and industrial applications, experience varied loadings and deformations over the service life. A small scale of damage or deformation is hard to be observed due to the large area of the structures. When exposed to a strong external force such as vibration, wind loading or concentrated regional stress, a small scale of damage can lead to a catastrophic failure of the structures[92-94]. Therefore, an SHM technique is necessary for maintaining the large-scale structures and extending the expected service life of these valuable assets. Different from small structures, on-site SHM on a large area of structures eliminates the usage of contacting sensing method because the contact-based sensors such as the ultrasonic sensors, strain gauges or fibre optics cannot cover such a huge area, and the installation and maintenance costs are high [95, 96].

On-site SHM requires a remote sensing technology that can cover a large area and monitor the structure over a long time.

With the rapid development of remote sensing technology, many non-contact sensors were used on the structural assessment of on-site operating infrastructures. Camera-based vision sensing technology is one of the low-cost remote sensing methods[97], where digital image correlation (DIC) is a popular method that involves the phases of camera setup, image recording, measurements of movement and detection of damages. It works by comparing the recorded different frames of the structure at different deformation steps and generating a map that can present strains' distribution [98]. As shown in Figure 2.2, Helfrick et al.[99] used two cameras to identify the damages on an aluminium cantilever beam. They deployed a 3-D DIC method with damage inspection algorithms to predict the location of damages when the beam is under different modes of bending forces.

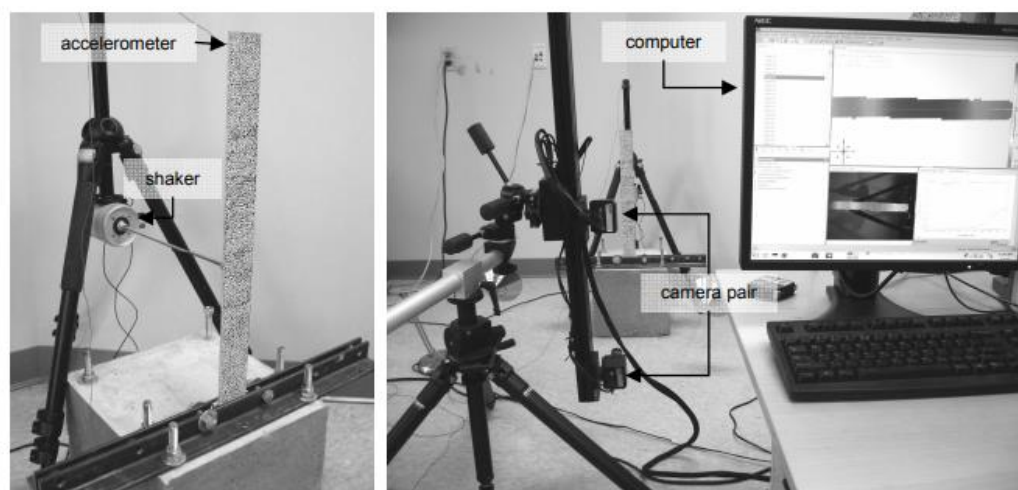


Figure 2.2 Experiment set up for the inspection of an aluminium beam with a pair of cameras [99]

Dworakowski et al. [100] deployed a consumer-grade camera to measure the in-plane strain of a cantilever. They used a line segment method and a voting method to generate the deflection curve of the cantilever. DIC is also widely used in the inspection experiments for bridges[101, 102]. Bell et al.[103] developed a technology that integrated the strain sensors and DIC to monitor the structural health condition of a bridge. The result can be used to do a risk assessment for the test project of the bridge. Xu et al. [104] also conducted a survey using 2D DIC with optic fibres to measure the displacement of the rail bridge under different set-up conditions. In addition, Radopoulou and Brilakis used two webcams to detect the defects on pavements. They identified the defects by processing the images with a supervised machine learning algorithm[105]. They also improved the method with a lower

frame rate, and the region of interest was identified by an inverse perspective mapping method[106]. DIC performs good in the measurement of structural deformation where the lateral or torsional displacements happens, but this technique highly relies on the number of cameras and the reflective points on the structures[107], it is difficult to monitor a structure that does not have a reflective point. In addition, DIC cannot monitor objects through an opaque surface, it can only identify the distribution of strains and displacement on the structures. Therefore, DIC can inspect the distribution of strains on the surface of the floating covers by monitoring the displacement, but the accumulation of scums and the distribution of different features cannot be detected with this technology.

Unmanned aerial vehicles (UAV) is another popular method for on-site wide coverage monitoring. It integrates a controllable flying system with remote sensing sensors, such as cameras or LiDARS to monitor the structures remotely. The ability to generate 3-D information is one of the advantages of UAV. Zhang and Elaksher [108] used the developed digital imaging method with UAV to assess the condition of the road and identified the internal defects using the developed 3-D models. Roca et al.[109] mounted a Kinect sensor on the UAV to acquire the 3-D geometric data for a building. They used the overlapped photos to generate a 3-D point cloud to present the profiles of the building. To identify the small scale of damages, the UAV can fly close to a structure for a detailed inspection. UAV can also be deployed to predict the strain distribution on a membrane-like structure through 3-D information. Leslie Wong et al. conducted a series of UAV scan surveys on a large scale of floating covers. They used the UAV assisted photography method to scan 475m*216m geomembrane floating covers at a sewage treatment plant[25, 31, 39]. As shown in Figure 2.3, A digital elevation model was created using the UAV RTK mapping method to measure the altitude of the surface of the geomembrane. The distribution of strains on the geomembrane surface was then identified by inputting the altitude data into finite element analysis software[30], and the in-plane stress for the geomembrane was also computed with the strain information.

Thermal imaging is a well-deployed structural health monitoring technique. It has been used in non-destructive monitoring studies for concert bridges [110-112], aerospace structures [113, 114], and composite structures [115-117]. Given that above -273°C emit infrared waves to the environment, a thermal camera detects anomaly regions of structures by receiving infrared waves from objects and transforming the signal into temperatures [118]. In addition, thermal imaging can also be used to detect fruits [119, 120] and medical

diagnoses [121, 122] through thermal contrast. According to the ways of inspection, thermal imaging is divided into active thermal imaging and passive thermal imaging, where active thermal imaging [123] requires an external heat source to apply the thermal wave into the deeper part of objects, and the defected region appears in the thermal image due to the block of the thermal energy [124]. On the other hand, passive thermal imaging [125] relies on the self-heating of the monitored objects, where the defected region can be detected with a different temperature from the surroundings. For the thermography on large scale infrastructures such as bridges and buildings, given that it is difficult to apply the external heat on the whole body uniformly, passive thermography was deployed to monitor the structures. T. Omar and ML, Nehdi mounted a thermal camera on the UAV to scan a concert bridge and rapidly assessed the condition of the structure by mapping the temperature distribution of the bridge[126], they also mounted the thermal camera on a moving platform to scan the temperature of another bridge, where maps of the temperature were stitched together to produce a complete condition map which can delineate different kinds of delamination. These studies provide an insight into integrating remote sensing technology with thermal imaging to allow the quick structural health assessment of large structures. However, due to the inspections were conducted with temperature scanning, the monitoring result may not be accurate. Given that there is a transient cycle for the ambient temperature and solar intensity, the temperature of the outside structures may rise from the morning with the absorption of the heat from the ambient and the solar radiation. In the evening, the temperature of the structure will fall with the emission of heat into the environment and the withdraw of the heat from the solar radiation. Therefore, the temperature contrast between the anomaly region and surroundings may depend on the occasion of the inspection, and the temperature thresholds were decided empirically. This will lead to the inaccuracy and unreliability of the inspection. A quasi-active thermography technique was proposed to increase the accuracy of thermal imaging on large structures[127], where the daily transient temperature cycles of the HDPE geomembrane were recorded by thermal imaging, and the temperature response of the geomembrane was correlated with the local solar intensity. The temperature changing rate of the geomembrane was obtained by curve fit the cooling curve of the geomembrane, and the anomaly region was identified by a different temperature cooling rate. This method is more accurate and reliable than a single shot of thermal imaging, but it requires the thermal camera to run over a whole day to get a condition map. So far, there is a lack of efficient, robust and repeatable thermal imaging techniques to evaluate the condition of a large structural

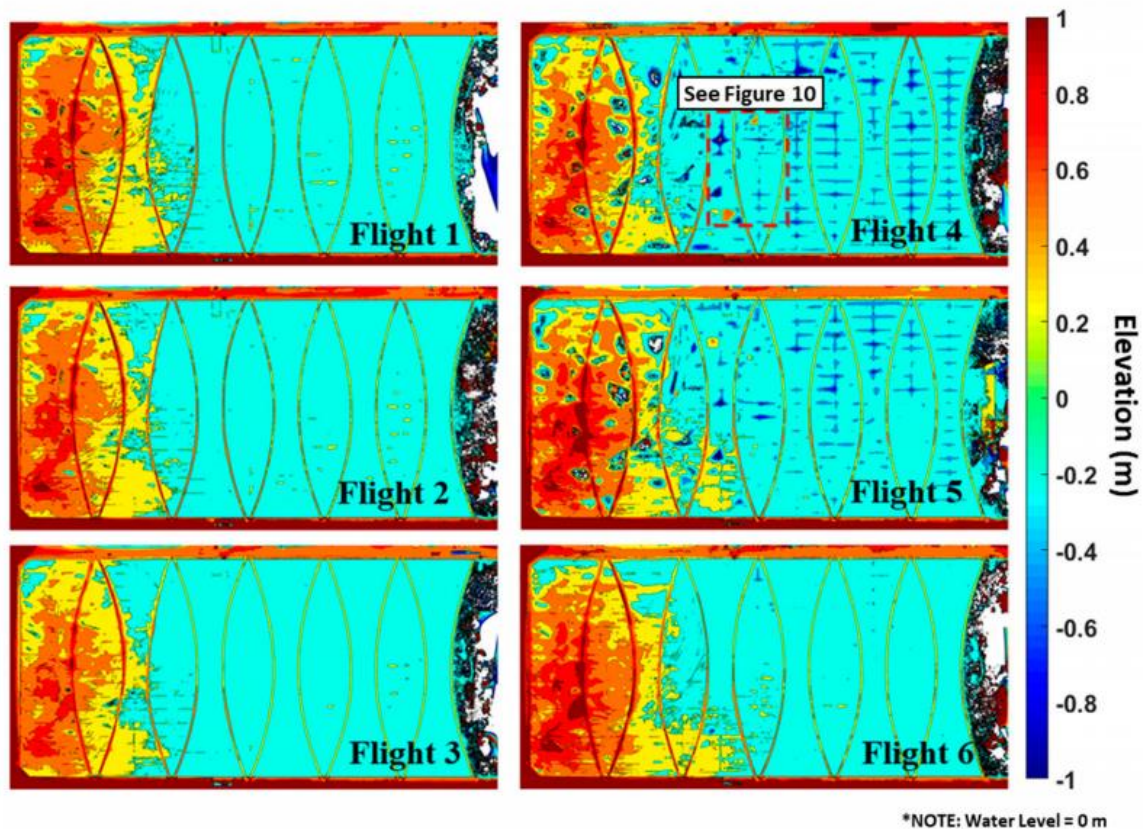


Figure 2.3 Digital elevation model of six surveys with UAV scans over four seasons at a geomembrane floating cover [25]

Hallermann N, Morgenthal G. performed UAV surveys on a 225m high concrete chimney, they scanned the structure in a circular mode, and the UAV scanned the whole structure at a constant distance[128]. It can be concluded that the remote sensing technology with UAV is useful for the monitoring of large structures, especially for inaccessible areas or for large area inspection. UAV scanning with the aid of visual algorithms can help establish 3-D models of structures and identify the surface damages such as cracks and surface cut defects on the structures, but similar with DIC technology, the scanning results of UAV depends on the reflection from the objects, and the UAV scanning is not able to detect the subsurface condition of the structures. In addition, the inherent drawbacks of the UAV, such as the instability and the limitation of battery, make long-term monitoring difficult.

Recently, with robotic technologies, visual sensors were also mounted on mobile systems such as moving vehicles or robots. Low-cost visual sensors can be used together with visual algorithms. Mobile remote sensing is widely adopted in bridge or road inspection, which allows the platform to move along the path and scan the structural health condition. Lorenc et al. [129] designed 4 degrees of freedom robot to perform on-site bridge maintenance tasks.

This robotic bridge maintenance system was used to scan the structure of the bridge and assist in painting and cleaning the bridge. Oh et al. [130] also developed 7 degrees of freedom mobile robotic systems to inspect the crack damages on the bridge. A car was used with a machine vision system and a control system to allow the automatic inspection of the bridge. In addition, Lim et al.[131] designed a path planning algorithm to ensure all parts of the bridges are scanned, a global crack map was also generated after a validation. Mobile sensor-based remote sensing technology can be for the inspection of a flat surface of structures. While this strategy needs to be assisted with a sophisticated control system and moving platform, which increased the cost and the complexity of the system.

This section reviewed some of the popular on-site remote sensing technologies for a series of structures. The application and findings for each method are summarised in Table 2.1. It can be concluded that with the advanced machine vision algorithms, remote sensing strategies such as DIC monitoring, UAV monitoring and Mobile sensor monitoring can provide a robust SHM for large scale civil structures. However, these technologies have inherent drawbacks. Images taken from these strategies cannot identify the internal defects and the distribution of subsurface objects through the opaque surface. An SHM that can find out the features under the up surface of the structures needs to be deployed for the covers at the geomembrane applications.

Table 2.1 Summarise of non-contact SHM methods

Remote sensing technology	Applications	Reference number	Comparisons
DIC	Bridges	[101-104]	<ul style="list-style-type: none"> Suitable for measuring displacements and strains on structures. Low cost with consumer-grade cameras.
	Aluminium beams	[99]	
	Pavements	[105, 106]	
	Buildings	[107]	<ul style="list-style-type: none"> Cannot detect internal strains and defects. Multiple cameras are required to improve the monitoring results. Needs reflection points on objects.

UAV	Roads	[50]	<ul style="list-style-type: none"> • Suitable for inaccessible area and large area monitoring, generating 3-D models with the DEM algorithms.
	Buildings	[109]	
	Geomembranes	[25, 31, 39]	
	Concrete structures	[128]	<ul style="list-style-type: none"> • Cannot detect internal strains and defects, cannot monitor objects under the up surface.
Mobile sensor	Bridges	[129-131]	<ul style="list-style-type: none"> • Suitable for the inspection of roads or bridges when moving along the path.
			<ul style="list-style-type: none"> • Need to work with complex control and robotic systems.

2.3 Infrared thermography monitoring

2.3.1 Introduction

Temperature distribution and infrared emissivity are common indexes to describe an object, it could also be utilized to evaluate the health condition of a structure. All objects whose temperatures are more than 0 K (-273⁰ C) would radiate infrared rays of the electromagnetic spectrum. The wavelength of the infrared rays varies from 0.75 to 1000 um. These are located in the region between the microwave and the visible part of the electromagnetic spectrum. Although the infrared rays are not visible, William Herschel first discovered the infrared ray, and his son created the first thermography image in 1800 [132]. Then the infrared thermography technology was gradually applied in the NDT through an infrared camera.

In the last several decades, infrared thermography technology has been developed as a quite popular non-destructive health monitoring method. It has been widely adopted to monitor the structural health of electrical devices, gas pipelines, aerospace composite materials and a wide range of civil infrastructures. Recently, infrared thermography (IRT) technology is also applied in the field of medical tests, facial recognition, nuclear reaction monitoring and the plastic industry. With the development of unmanned aerial vehicle (UAV) monitoring, IRT has gained even more popularity because the infrared camera could be installed on the UAV and the thermal image could be taken at a high amplitude, this would improve the efficiency of monitoring large infrastructure significantly since a larger area could be

monitored at the same time and the monitoring time would be reduced dramatically compared to traditional non-destructive monitoring technology.

2.3.2 Thermal imaging methods

The experimental methodology of thermography is divided into two categories: passive thermography and active thermography. A comparison of different thermography methods is summarised in Table 2.2. In passive thermography, it does not require any external heat energy, and the monitored objects themselves are regarded as the heat source with a different temperature from the ambient[133, 134], this method has been widely used in the condition where the temperature distribution on the surface of the objects is enough to illustrate the defects. It can be used in the application of a series of medical detections[135], sewer liners[136], and pipelines[137]. The transient heat flows within these objects are sufficient to present a contrast for detecting defects or features difference. While in active thermography, this thermal imaging method requires external heat sources. It could monitor a deeper part of the structure with the energy penetrating the deeper part of a structure and present a more clearly temperature contrast.

Based on the type of applied heat energy, active thermography could be classified into lock-in thermography, pulsed thermography, and step-heat thermography, respectively. Pulsed thermography applies a short period of heat pulse as stimulation, and the transient temperature change is detected during the cool-down process. The efficiency of the pulsed thermography depends on the thermal diffusivity. It was reported that thermal propagation time to a defect located at the 2mm subsurface of steel is about 40mm, while graphite-epoxy is around 30s [138]. Hence, pulsed thermography requires a higher thermal diffusion property for the material. Pulsed thermography includes flash heat and transient heat, where flash heat often exists for several milliseconds. The main advantage of flash thermography is the short measuring time and monitor thin plate or even membrane and the shallow defects. However, there is a limitation of monitored area and depth of the defects due to the power limits of lamps, also thermal loading on the monitored specimen is relatively large. As for transient thermography, the monitoring process lasts for seconds to minutes, and the monitored specimen is larger, and the thermal loading on the specimen is lower, but the thick specimen is not desirable to be monitored with transient thermography due to low thermal energy.

In lock-in thermography, sinusoidal or rectangular waveform heat energy is applied to the objects. As shown in Figure 2.4, the experiment set up for lock-in thermography is made up of a heat source, thermal camera and the analysis device. The temperature over the specimen

is captured by the thermal camera and transferred into the frequency domain. The temperature evolution of each pixel on the image is analysed through the Fourier-transform. The main advantages of the lock-in thermography are: (1) The phase image of lock-in thermography is not easy to be affected by the surrounding interference such as dust, sunlight and reflections. (2) Deeper defects could be detected due to the longer heating period. (3) The phase information would not be affected by the uniform applied heat energy. However, the lock-in thermography would take a significantly longer time during inspection, limiting its reliability on the high-speed scan monitoring. Furthermore, polymers monitoring is a challenge to thermography since its properties are orientation dependent.

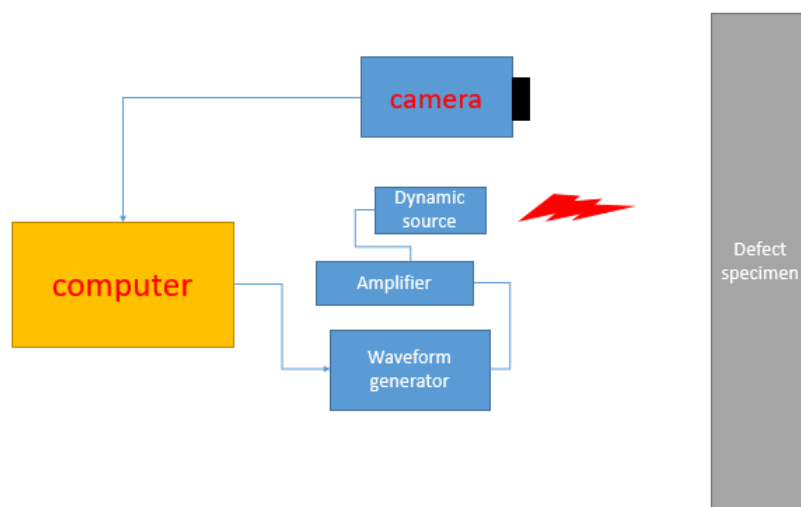


Figure 2.4 Experiment set up of lock-in thermography

Table 2.2. Comparison of active thermography and passive thermography

Thermography methods	Monitored objects	Equipment	Comparison	Reference
Active thermography	General objects	Halogen lamp, hot air gun, ultrasonic	Need external heat source	[138]
Passive thermography	Self-heating objects, objects temperature	N/A	Do not need an external heat source	[135]

higher than the
surrounding.

2.3.3 Application of thermal infrared thermography

The thermography test is one of the most widely used SHM methods in the aircraft industry due to the inconvenience of other monitoring technologies during the flight, IRT can monitor a large range of areas without taking apart the whole structure. In traditional inspections, IRT mainly monitors the metal parts or aircraft wings made of carbon-reinforced polymers and other composite structures. Common defects of composites including fibre pull out, fibre bridging, surface debonding and delamination. Active thermography is desirable for assessing since an external heat source must create a distinguishable thermal contrast between the defect spot and the surrounding area. Normally the heat source, for example, a halogen lamp, and the infrared camera is placed at one side for operation. As shown in Figure 2.5, E. Saarimaki & P. Ylinen [139] applied the IRT to locate the penetrated water in the composite structure on the aircraft, they froze the structure and then warmed the structure to the room temperature, the phase transition energy which was used to melt the ice into the water was monitored by thermography.

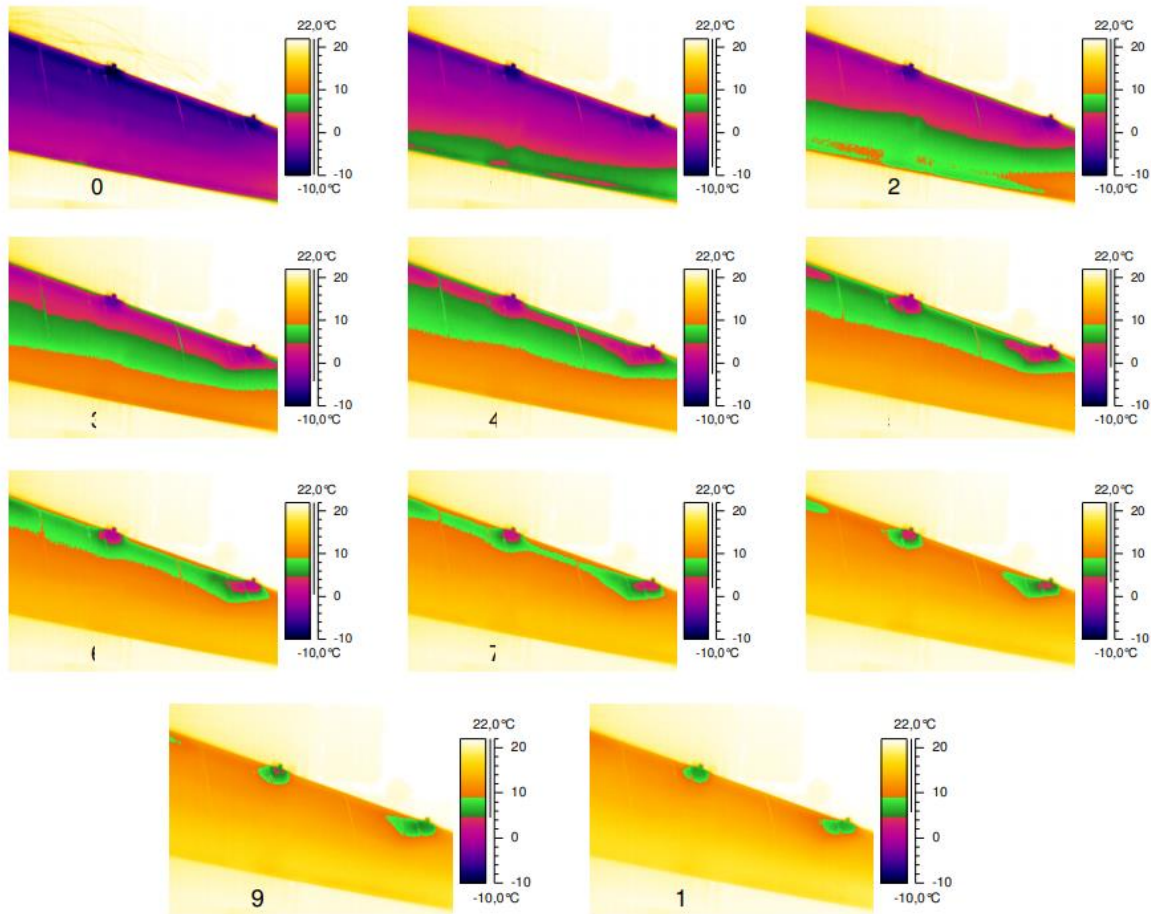


Figure 2.5 Optimal inspection frame time for different areas of the rudder surface (green area in the images, time refers to the temperature where the first area reaches 5 °C [139])

In addition, lightweight porous composite structures were monitored by a series of active thermography methods by Ibarra-Castaneda. et al. [140]. They stated that the quality of thermo-image depended not only on the heat flux applied to surfaces but also on the geometry of the surface, defects below 2.5 mm (the ratio of width to depth should be no less than 2) could be monitored by the pulsed phase thermography.

The large scale of civil infrastructure is suitable to be monitored by the IRT. Defects in the deck of the bridge, pit at the airstrip, crack at the inner part of the building, and large water and sewage storages and tear of the geomembrane can be monitored by IRT remotely, precisely, and efficiently in previous research. However, sometimes the monitoring result is not accurate due to the nonhomogeneous composition of the concrete, different grain sizes of the pebble may lead to a non-uniform transmission of thermal energy. Generally, the monitoring on civil structures utilizes passive thermography, which does not require an external heat source since it is impossible to heat a large structure. As a result, the quality of thermography on civil structures depends on the ambient temperature, and sufficient solar exposure is needed to get an image suitable for inspection. C. Maierhofer & M. Roellig [141]

did a series of experiments and verified that thermography could be used to monitor the interfaces between masonry and plasters, the mortar filling joints, and the subsurface moistures of the walls. Tavukcuoglu et al. [142] did a non-destructive monitoring study of an ancient building by IRT, they combined the IR thermography with levelling survey to evaluate the seasonal rising damp problems of a 13th-century caravanserai. The damped zones, including grounds, walls, pipelines and the underground drainage path are monitored by the thermography. They concluded that the source of the moisture was from the insufficient zone grading and reverse falls around the building.

The electrical devices and components would produce significant heat during the operation because of the transmission of electricity. Maintaining a suitable range of working temperatures is essential for most electrical devices. Monitoring the electrical device by IRT is quite suitable since it does not require the disassembly of the components. Corrosion of metal parts, defects on the joints, crack of the circuit board and wires, and IRT could efficiently detect the overload parts. J. Martinez & R. Lagioia [143] surveyed to classify the major sources of electrical problems of the distribution utilities from 1999 to 2005, and they found that most of the conductor connection faults happened because of the shortage of the materials or adjustments of the faults. Therefore, maintaining the operating temperature of the electrical device can help avoid a large portion of electrical faults.

2.3.4 Infrared thermal imaging on HDPE

Infrared thermal imaging has been successfully adopted to monitor a wide range of building materials, such as bricks, concrete in buildings [144, 145]. Favro [146] monitored the crack of composite on an aircraft structure through thermal imaging in 1995. Similarly, Varis [147] utilized thermography to identify cracks in unidirectional carbon fibre composites. Fatigue damages in graphite composites were monitored by Ahsan [148]. And the thermography inspection on defects of multi-layered composite materials in military applications was also conducted by Swiderski [149].

Recently, thermography was also used to detect the defects in polymers. Omar [150] applied thermography to evaluate the bond strength and adhesion integrity of the high-density polyethylene (HDPE) plastic joint. Boiling water was used as the heat source, and both transmission mode and reflection mode were used to assess the structural defects such as delamination, misalignment and uniformity adhesion. They successfully distinguished the defects in the joint specimens from undamaged specimens by comparing the thermal response of specimens to pulse stimulations. They also compared the thermal contrast of

specimens with different depths of delamination defects. Due to the air gaps between the 1cm thick joints, thermal energy diffusion was interrupted at the defect spots, the temperature-time plots were used to highlight the defect region. In addition, as shown in Figure 2.6, the thickness maps of the adhesion layer of the joints were analysed by thermal tomography. The generated map specified the drop of thickness at the defect area, and the results were verified with an ultrasound scan inspection.

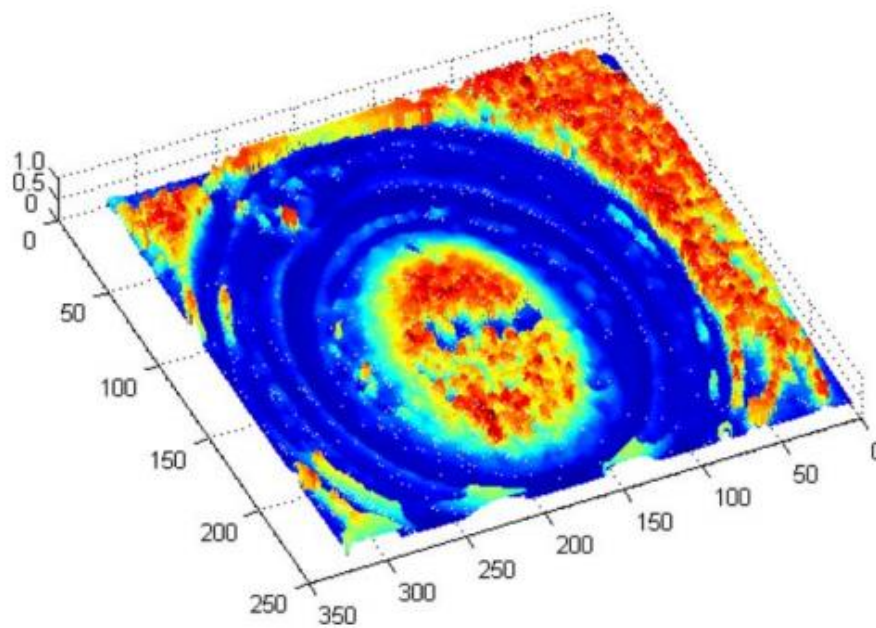


Figure 2.6 Thermal map of thickness showing the delamination of the HDPE joints[150]

Infrared thermal imaging was also applied to monitor the welding flaws at the polyethylene pipes by Kafieh [151]. Polyethylene pipes need to be welded to facilitate gas transfer. The ends of each pipe were melted and bonded during welding. Hafidh [151] detected the welding flaws through a sequence of cooling steps from infrared video. The monitoring procedure started immediately after the end of welding and sustained the whole cooling down process. As shown in Figure 2.7, they applied different clustering algorithms to distinguish different defects and classify them into different welding flaw groups. Three main flaws, including incorrect placement, unaligned pipe placement, and incomplete scrub, were identified through Infrared thermal imaging.

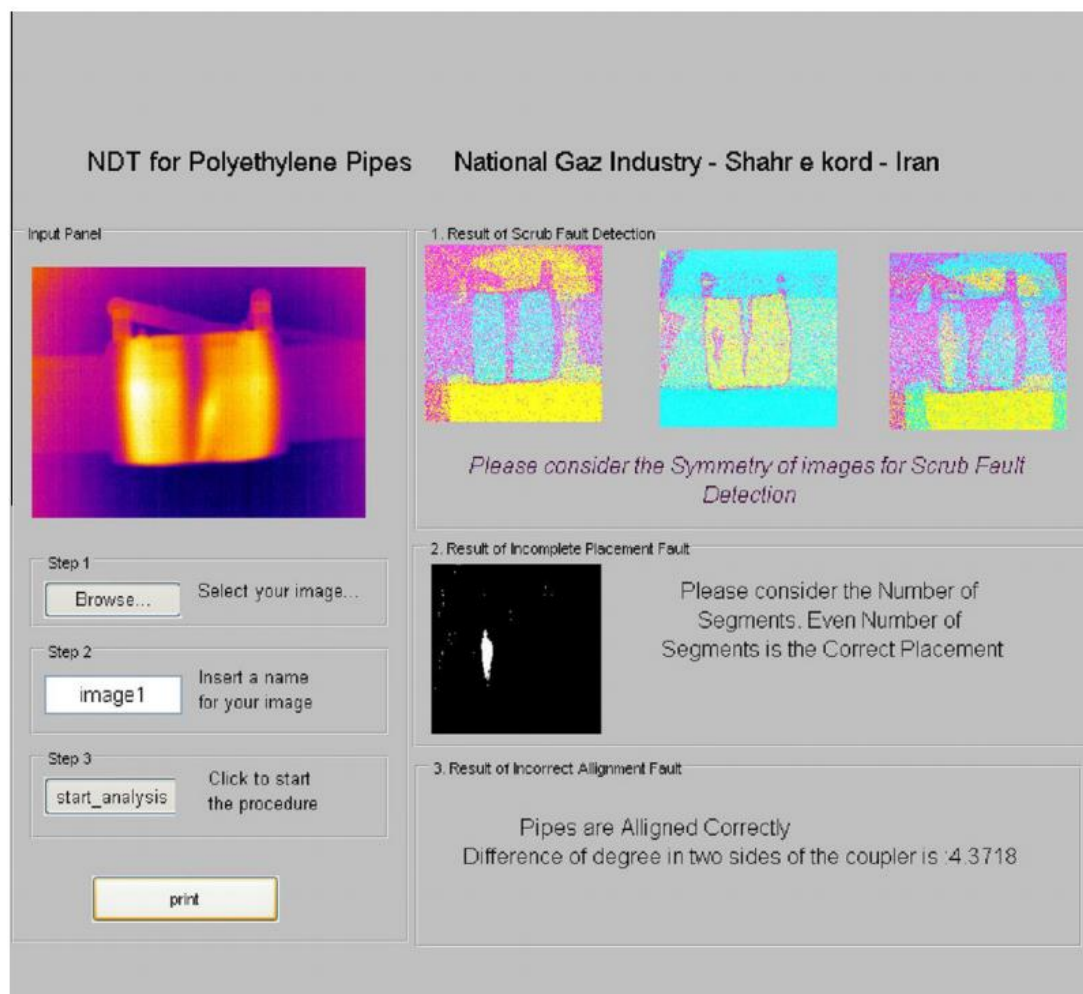


Figure 2.7 GUI of the inspection algorithm for the polyethylene pipe[151]

In 2008, J.M. Flores-Bolarin [152] conducted a series of thermography experiments to monitor the defects on High-density polyethylene (HDPE), polymethyl methacrylate (PMMA), polyvinyl chloride (PVC), and glass fibre reinforced polyester (GFRP). They indicated a proportionality relation between the diameter of the defect and the time of maximum thermal contrast, and the relation between the defect depth and time of maximum contrast was also proposed. In addition, it was stated that the slope of this relation is proportional to the thermal diffusivity of the plastics. Dassisti [153] applied thermography to detect the manufacturing process of HDPE membrane in the agricultural industry in Italy in 2016. Gheysari et al. investigated the influence of high-energy electron beams on the thermal properties of HDPE through a thermogram [154]. In 2005, Bendada et al.[155] used infrared thermal imaging to investigate the heat transfer mechanisms of HDPE during the cooling phase of manufacturing.

2.4 Infrared thermal imaging on large on-site structures

Infrared thermal imaging has been widely adopted on the SHM of large-scale structures. Given that thermal imaging has the advantages of wide coverage area, low cost and high compatibility with robotic systems and UAVs, it is used to evaluate the structural health condition of varied on-site infrastructures. Thermal imaging is mainly used to inspect the invisible internal defects, to evaluate the corrosion condition, and to detect the emission of harmful leakages such as gas or liquids for infrastructures.

Since thermal imaging measures the temperature by receiving the infrared waves ($0.9\text{--}14\mu\text{m}$) emitted by structures[156-158], and the infrared waves emitted by buildings are between $7\text{--}14\mu\text{m}$, thermal imaging is used to inspect varies of building structures. O’Grady [159] pointed out thermography performs well for the inspection of buildings and that thermal imaging is a non-destructive method to measure the building’s thermal performance and the external and internal structural difference through the temperature contrast. Grinzato et al. [160] used passive thermography to monitor the hidden structure in the wall, the moisture distributions, and the wall bonding status of a historical build, they also measured the thermal diffusivity of the bricks and plasters, allowing a detailed understanding of the status of the building. Lagüela et al.[161] generated a 3-D thermographic model through the image fusion and image matching methods. As shown in Figure 2.8, they fused the infrared mosaics and visible images and combined the geometric data with the thermal data to produce a thermographic model for the building.

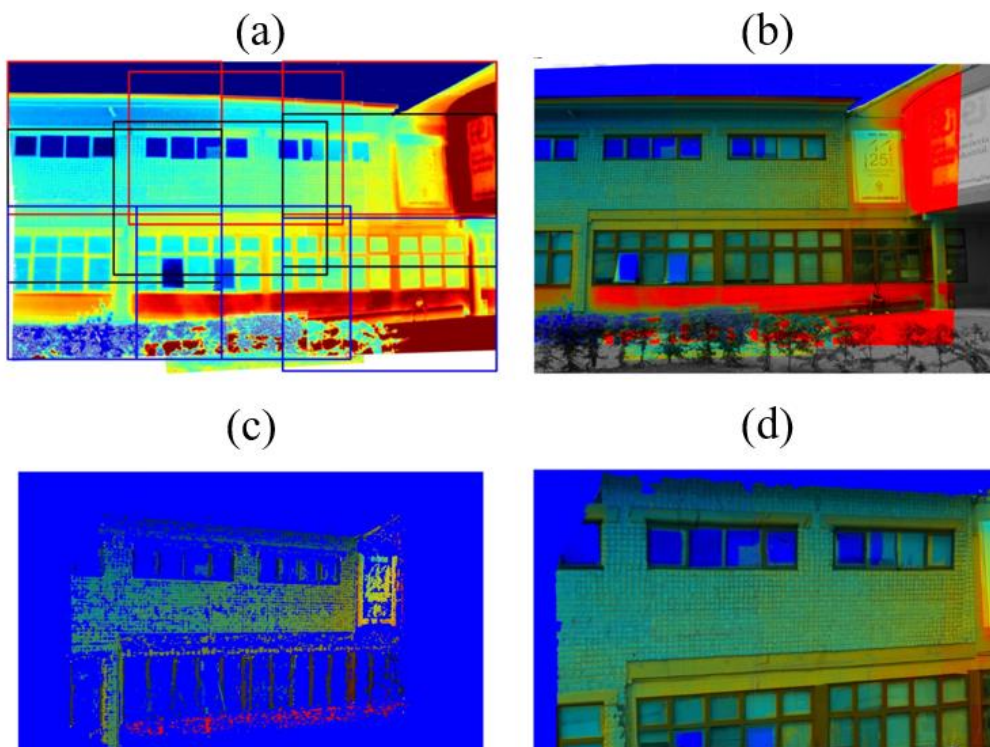


Figure 2.8 (a) Stitched thermal image for a building. (b) overlapped fused image for the building. (c) Point mesh of a building from a surface dense modelling algorithm. (d) 3D thermographic model [161]

The thermal imaging monitoring was conducted with an 80-90% overlapping surface for a high-quality model. The threshold of each image was set as the same in the image registration and the thermographic mosaic process. The generated 3-D thermographic model precisely integrated each part of the building and the corresponding thermal information. As the building was exposed outside, they could not reach a thermal equilibrium due to heat exchanges with the ambient. Fox et al. [162] conducted a time-lapse thermographic survey to monitor the building defects. They stated that the traditional on-site thermography capture objects at one moment in time, and the inspection result could be affected by a series of facts such as weather conditions[163], thermal camera resolutions [164] and the moistures on the material [156]. Therefore, they conducted two cases studies to investigate the time-lapse thermography on buildings. The camera was set up 20m away from the building. As shown in Figure 2.9, the first monitoring last for 15h and they found that the average temperature difference at a 30 min image interval is 0.1K, and the temperature of the structure dropped from 279K in the morning to 269K in the night.

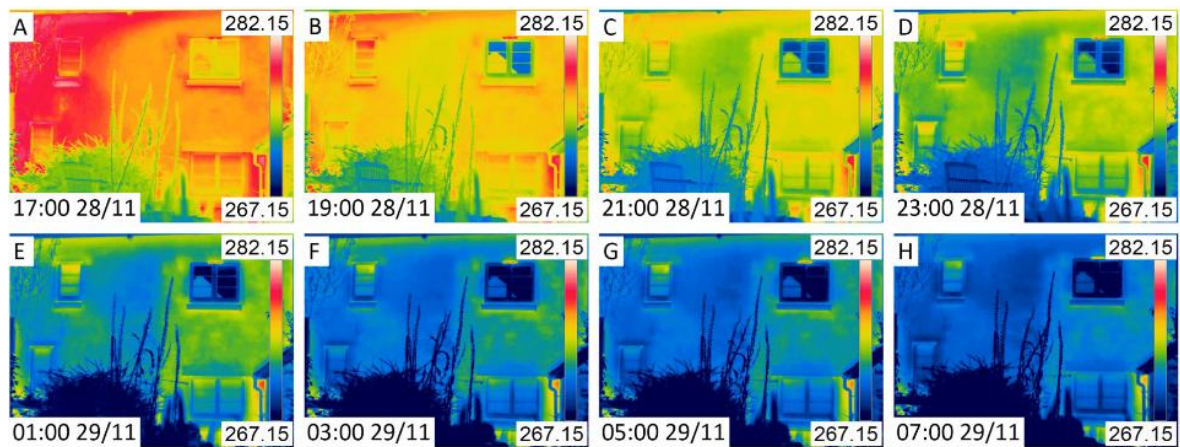


Figure 2.9 Time lapsed thermal images of a building. (120 min image interval, every 4 images)[162]

The second monitoring last for 63h and they found that the average temperature difference at a 60 min image interval is 0.5K, and the structure temperature drops 10K from the morning to the night. They concluded that the temperature of outside structures varied at different times in a day, and a single threshold of thermal images is not fit for all circumstances. For the active thermography, given that active thermography needs an external heat source, and it is impossible to apply heat on a whole building structure, only some parts within the

building were inspected by active thermography. Freitas et al. [165] used active thermography to monitor a region on the exterior wall of a building, and Cadelano et al. [166] used active thermography to inspect the marble, sandstones and bricks on the external part of the building.

For the monitoring of bridges, thermal cameras were mounted on a UAV or a moving platform to scan along the path of the bridges[167]. The captured thermal image sequences were stitched together to generate a complete temperature distribution map. S. Abu Dabous et al. [168] conducted a bridge deck condition assessment. They used thermography and ground-penetrating radar technology to detect the defects on a concrete bridge in Canada. An acoustic inspection technique was applied to compare the results from these methods. A detailed defects location map was generated with a combination of these methods. For the thermography on a moving platform, as shown in Figure 2.10, T. Omar et al. [169] mounted the thermal camera on a vehicle to scan a bridge deck and identify the corrosion status for the bridge at daytime and night time, respectively. In addition, they classified the condition of the bridge deck into three categories according to the distribution of temperatures. They first used the thermal camera to scan along the bridge and pre-processed the thermal image sequences to enhance the temperature contrast. Following by that, the images were registered and stitched together to produce a temperature map for the bridge. As shown in the figure, a new map will be generated after using machine learning based algorithms to classify the regions on the bridge through the temperature distribution. The bridge was divided into the categories of conditions after a threshold statistical study and the results were compared with an acoustic inspection technique.

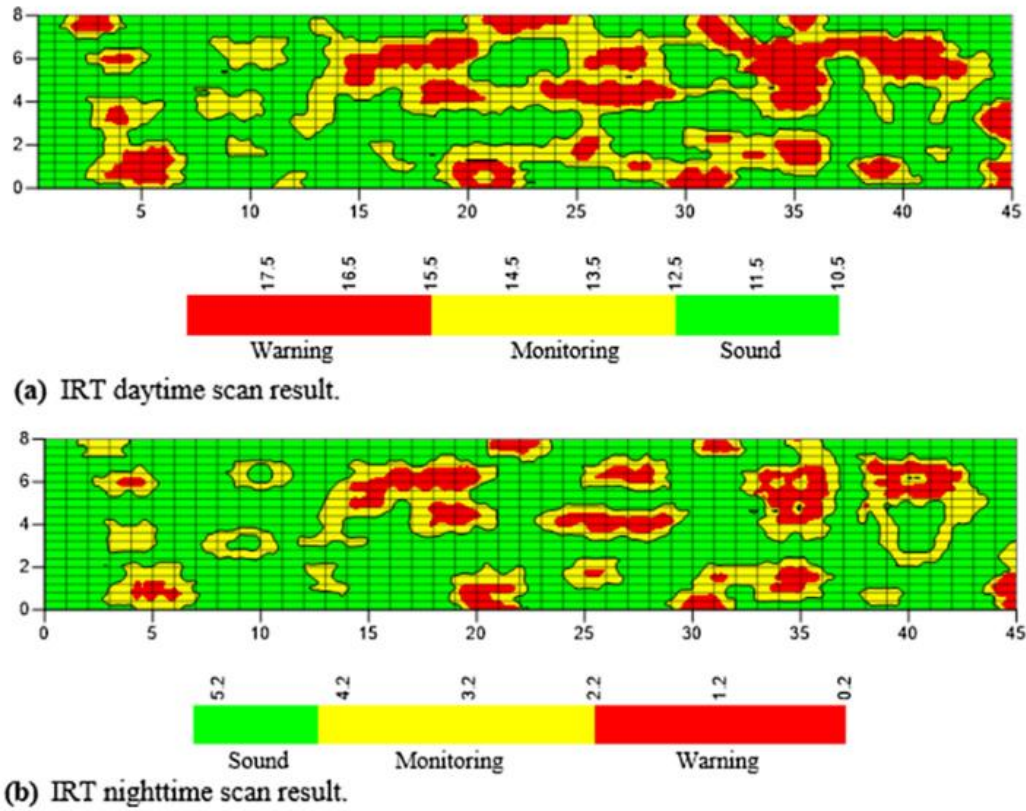


Figure 2.10 (a) Daytime thermal imaging result. (b) night-time thermal imaging result [169]

To reach a wider monitoring area, they mounted the thermal camera on an UAV to scan another bridge[126]. Two bridge decks were scanned with the UAV assisted thermal imaging, and the thermal image sequences were post-processed with the same procedure. The regions of the bridges were divided into “warning”, “monitoring”, and “sound” region according to the temperature contrast. An analysis for the determination of the threshold of each region was also conducted. They verified the scanning results with another potential half-cell test. Despite the convenience and low cost, some limitations such as UAV battery, UAV vibration and the ideal fight time need to be solved in future studies.

Due to the large area, pavements also need an efficient and cost-effective SHM method to inspect the delamination, cracks, flaws and other regional imperfections[170, 171]. Similar to the buildings and bridges, the thermal camera identifies the defects on pavements by temperature contrasts. A. Moropoulou et al. [172] used thermal imaging to inspect the defects on the pavements in an airport. The thermal camera was set with 15 frames/second sampling rate. Pavements were cleaned and dried before the scan to enhance the temperature contrast, and a control system was designed for the inspection path. The delaminated areas were identified after the scanning, but Moropoulou pointed out that the ground moisture, surface texture and solar radiation may affect the scanning result. He also did another

scanning and verified the result with a penetrating radar experiment[173]. J. Dumoulin et al.[174] conducted laboratory-scale pulsed thermography and principal component thermography on some asphalt pavement samples. Two 500 W halogen lamps were used to provide the external heat for the active thermography. Different shapes of cracks were inspected, and a numerical analysis verified the result. This method can provide a significant temperature contrast, but it leaves a limitation for on-site monitoring with the lack of a heat source covering a large area.

This section reviewed thermal imaging applications for large on-site structures, such as buildings, bridges and pavements. These applications are summarised in Table 2.3. Thermography was mainly used to identify the surface cracks, voids, delamination and corruptions on the structures. Thermal imaging presented a good inspection result with the advantage of the low-cost, large monitoring area, efficient monitoring and post-processing. However, previous studies revealed that in-situ SHM by thermography would be affected by a variety of ambient conditions such as the solar radiations, monitoring time and wind loads, and the monitoring results based on a single frame of temperature map are affected by these factors. Therefore, the reliability and accuracy of thermography for in-situ structures need to be improved. The transient events resulting from the ambient weather variations can be used to enhance the monitoring result.

Table 2.3. Applications of thermography on large on-site structures

Application	Thermography method	Thermal camera	Monitored objects	Reference
Historical buildings	Passive	Unstated	Crack and defects	[160]
	Passive	NEC TH926	Whole building	[161]
	Passive	FLIR T620bx	Whole building	[162]
	Passive	Avio TVS 2000 Mk II series)	exterior wall	[157]
	Passive	FLIR T360	exterior wall	[158]
	Active	Thermo Tracer TH 7800	exterior wall	[165]
Bridges	Active	aIRview infrared system	marble, sandstones and bricks	[166]
	Passive	BST focal plane array IR sensor	Bridge condition	[175]

	Passive	FLIR T420	Bridge condition	[176]
	Passive	FLIR SC5600, T650 and T420	Bridge subsurface damage	[167]
	Passive	FLIR P6	Bridge defects	[168]
	Passive	FLIR T650sc	Bridge delaminations	[169]
	Passive	FLIR Vue Pro	Bridge delaminations	[126]
Pavements	Passive	FLIR A615	Concrete pavement	[170]
		AGEMA		
	Active	Thermovision Scanner 900LW	Pavement	[171]
	Passive	Avio Tvs 2000Mk II LW,	Airport pavements delamination	[172]
	Passive	Avio Tvs 2000 Mk II LW	Airport pavements deterioration	[173]
	Active	FLIR S65	Asphalt pavement samples	[174]

2.5 Environmental effects on thermal imaging of on-site structures

Due to the uncertain monitoring conditions, on-site thermal imaging can be affected by different ambient factors such as solar loadings, wind speeds and ambient temperatures[177, 178]. Identifying the effects of these factors and studying the ideal monitoring conditions for thermography is important for thermal imaging to get a reliable result. M.R. Clark et al.[179] conducted several thermography surveys on some bridges. They found out the delamination areas of the bridge decks with long term monitoring, and the average temperature difference between the delaminated areas and the non-delaminated areas was around 0.2-0.3°C. They also pointed out that the temperature monitoring by thermal imaging is limited by the climate conditions, where the temperature difference between the non-damaged region and the damaged region was small when the ambient temperature is low, and the solar heating is weak. To solve this problem, a favourable time window for thermal imaging monitoring needed to be determined before the inspection. A. Watase et al. [180] and Matsumoto et al. [181]investigated the favourable monitor time window for the bridge deck in a day. As shown in Figure 2.11, they conducted some experimental works to identify the influences of environmental weather conditions at the varied time of a day to inspect the voids and delamination on the bridge. They also investigated the relationship between the

temperature profiles of the concrete material on the bridges and the ambient weather information to predict a suitable monitoring time on the bridge. They used the concrete test plates with varied thicknesses and mount the temperature probes on the plates to record the data.

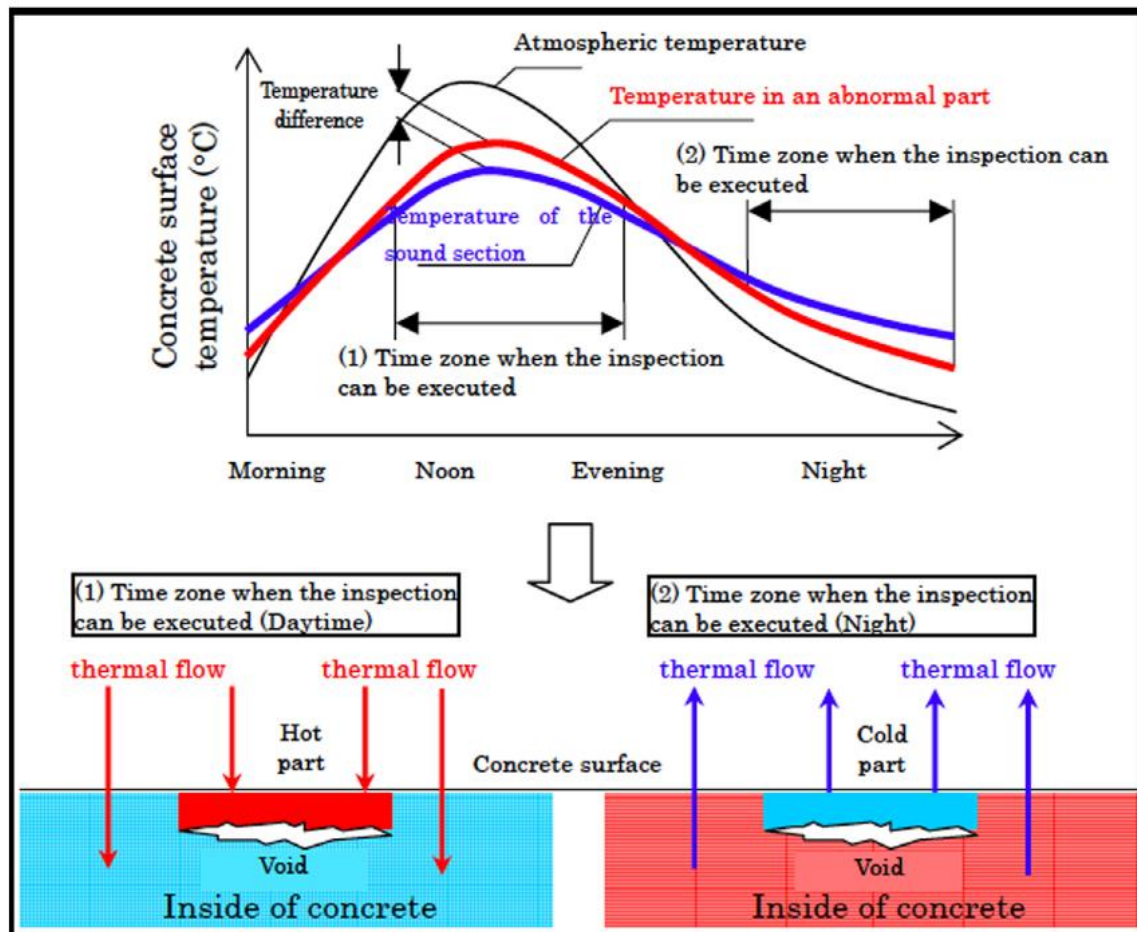


Figure 2.11 Temperature profile and heat flow of a concrete structure with delamination [181]

Thermography was deployed to generate a regression model to determine the relationship between the temperature gradients of concrete material and the environmental information. G. Washer et al.[182] studied the effects of solar radiation loadings and winds on the inspection of subsurface features in the concrete. They aimed to find out an optimum environmental condition to do the inspections on the concrete materials. They embedded the same size of test specimen ($300 \times 300 \times 13$ mm) at a depth of 1, 2, 3, and 5 inches from the surface of the concrete and recorded the temperature evolutions of each area with varying wind speeds and solar loads. As shown in Figure 2.12, as a conclusion, their results showed that the temperature contrast of each region on the surface of the concrete has a relation with the solar loading power and the ambient temperature but does not have a linear relation with the wind speed.

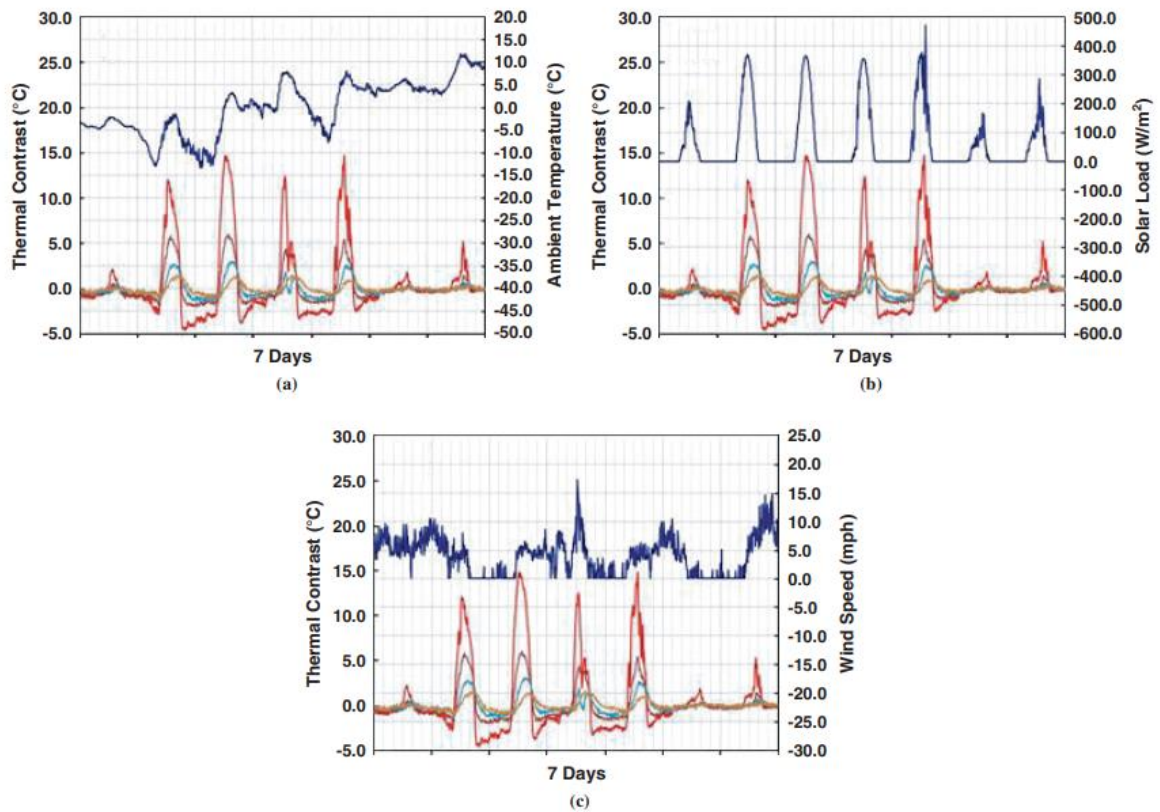


Figure 2.12 Concrete block temperature profiles with the (a) ambient temperature. (b) solar intensity. (c) wind speed. [179]

As shown in Table 2.4, this section reviewed some environmental factors that affect the thermography results on outside structures. In summary, most of the previous research focused on finding out the ideal monitoring for a single frame of thermal scanning, where the scanning result depends on a variety of ambient conditions and monitoring time, and the result can still be affected by the threshold of the thermal image, which can result in an inaccurate monitoring result. Therefore, on-site thermal imaging requires a long-term thermography method that can evaluate the structural health condition during the transient event and inspect the comparison of temperature changing rates, not the comparison of temperature in a time spot.

Table 2.4. summary of influence factors in the thermography for outside structures

Influence factors	Thermal imaging method	Thermal camera	Reference number
Monitoring time, solar loading	Passive	FLIR S65	[178]

Ambient temperature, solar loading	Passive	FLIR i7 and the FLIR ThermaCAM SC640	[177]
Solar loading	Passive	Agema Thermovision 900 Camera	[179]
Monitoring time	Passive	ThermaCAM SC64	[180]
Solar loading, wind speed	Passive	Research grade thermal camera	[182]

2.6 Infrared thermal imaging theory

2.6.1 Fundamental concepts

Thermal cameras measure the temperatures by receiving the infrared wave emitted by the surface of the objects. Every object that is above absolute 0 degrees will emit infrared waves into surroundings, and the relation with the temperature of the objects and the power of emitted infrared energy is named as Stefan-Boltzmann's law as the following equation [183]:

$$\frac{Q}{A} = \varepsilon \sigma T^4 \quad (2.1)$$

Where Q represents the power of surface emitted energy with the unit of Watt, A is the emission surface area in m², T means the absolute temperature of objects in Kelvin degree, σ is the constant of Stefan-Boltzmann with the value of $5.676 \times 10^{-8} \text{ W m}^2 \text{ K}^4$ and the ε represents the emissivity of a specified emitting surface with a specific wavelength and absolute temperature T. Moreover, the observed peak wavelength in an emission phenomenon is related to the absolute temperature of the objects $\lambda_{\max} T = 2897.7 \text{ umK}$, where λ_{\max} is the maximum wavelength of the infrared ray. As shown in Figure 2.13[184], the radiometry spectrum is divided into the ultraviolet(0.01-0.4 μm) visible waves (0.4-0.7 μm) and infrared waves(0.7-1000 μm), according to the wavelength of the waves [185, 186]. Thermal camera mainly detects the waves within the infrared spectrum. During thermal imaging, the detected temperature depends on the emissivity ε of monitored objects[187].

An ideal object which can absorb all electromagnetic waves is named the “black body”, the emissivity of the black body is defined as 1, and the emissivity of other objects is defined as the ratio of the radiation energy emitted by the surface of the object to the radiation energy emitted by a black body under a given temperature and the same condition. Therefore, the emissivity of an object is between 0 and 1.

Emissivity is equal to 1 minus reflectivity. When an object has a low emissivity (i.e., high reflectivity), it is difficult to use the thermal camera to measure the exact temperature of the object since the objects act like a “mirror” and reflect the radiations from other objects. To get an accurate monitoring result, the inspected surface is recommended to have high emissivity ($\epsilon > 0.9$). Yue et al. [127] measured the infrared spectrum of the HDPE material using the Fourier-transform infrared spectroscopy, and the result is shown in Figure 2.14. It can be found that the emissivity of the HDPE material is more than 0.9 in the long-wavelength spectrum (wavelength 8-15 μm , temperature -80 - 89°C), which indicates that the HDPE is suitable to be monitored with the thermal imaging technique.

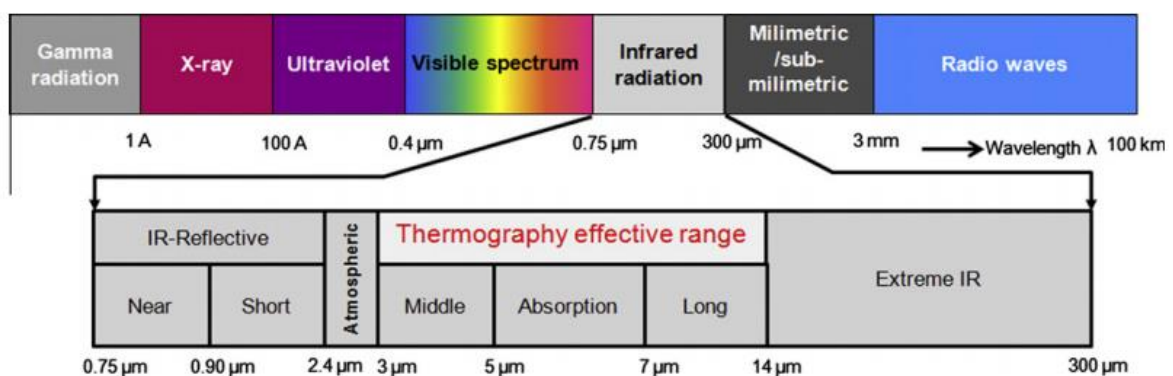


Figure 2.13 Wavelength of radiometry spectrum[184]

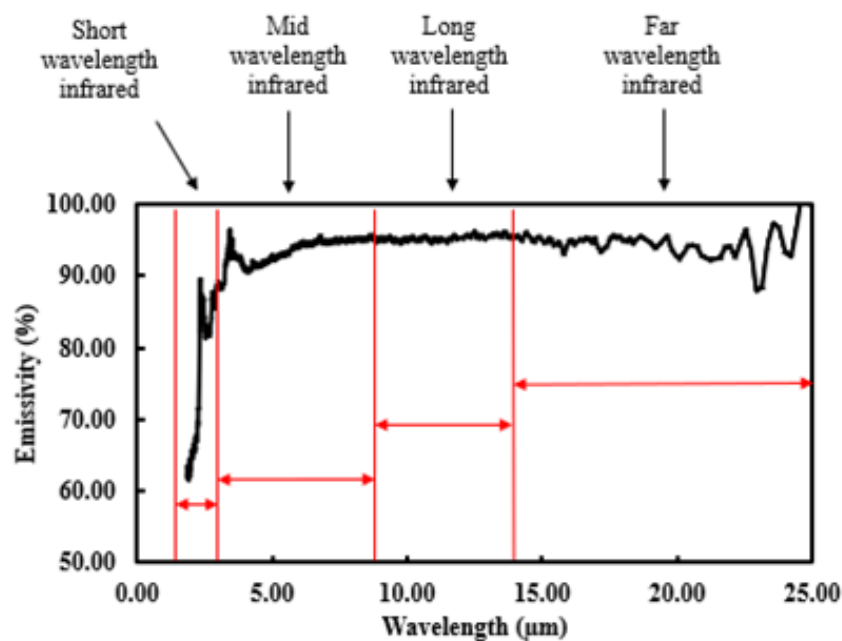


Figure 2.14 Emissivity spectrum of the HDPE geomembrane material [127]

Thermal imaging is used to highlight the defects or anomalies in the internal part of a structure through the temperature contrast, resulting from the uneven heat flow when there is a discontinuity in the structures. The heat energy always flows from a high-temperature object to a low-temperature object through the heat transfers, which are conduction, convection, and radiation. The temperature response of objects during the heat transfer process is determined by the density ρ (kg/m³) and the specific heat C_p (J/kg K). In the thermal conduction process, the thermal conductivity (W/m °C) is a thermal property to indicate the heat transfer rate for a material. The amount of heat flux will increase with thermal conductivity for the same amount of a temperature gradient. It is reported that in general, $K_{\text{solids}} > K_{\text{liquids}} > K_{\text{gas}}$. Thermal diffusivity is a term governed by thermal conductivity, density and specific heat. It can be obtained through the equation[188]:

$$\alpha = \frac{k}{\rho C_p} \quad (2.2)$$

Where α is the thermal diffusivity and a larger α can make the material reach the thermal equilibrium faster than less diffusive materials. Effusivity is another important term that describes the ability of the material to exchange heat with its surroundings. And it is calculated through the equation [189]:

$$e = \sqrt{k\rho C_p} \quad (2.3)$$

2.6.2 Heat transfer of geomembrane under the solar radiation loading

Pelte et al. reported that the heat transfer balance of a unit area of a geomembrane exposed under the solar radiation could be expressed as below[190]:

$$\alpha G = h(T_{GM}(t) - T_a) + \phi(x = 0, t) + \mu_{GM} C_p \frac{dT_{GM}(t)}{dt} \quad (2.4)$$

Where α is the solar radiation absorption coefficient which is around 0.7 for HDPE geomembrane[190]; G is the solar energy power per unit area on the surface of the geomembrane; h is the overall heat exchange coefficient between the geomembrane with ambient; T_{GM} is the temperature of the geomembrane; T_a is the ambient temperature, ϕ is the heat flux in the soil per unit area; x is the depth of the under surface soil; μ_{GM} is the mass per unit area of the geomembrane; and C_p is the specific heat of the soil. In this equation, the left-hand side of the equation αG represents the absorbed solar energy by geomembrane per unit area; the first term on the right-hand side of the equation $h(T_{GM}(t) - T_a)$ represents

the energy exchanged with the ambient above the up surface of the geomembrane per unit area (including convection and radiation); the second term on the right-hand side of the equation $\phi(x = 0, t)$ represents the conduction heat flux in the soil per unit area; the third term on the right-hand side of the equation $\mu_{GM}C_p \frac{dT_{GM}(t)}{dt}$ represents the increase of the internal energy per unit area. The equation reveals that the solar energy absorbed by the geomembrane flows to the ambient through convection and radiation; to the under-surface soil through conduction and stays in the body of the geomembrane to increase the internal energy and increase the temperature of the geomembrane.

For the heat transfer (conduction) of subsurface soil, the temperature distribution can be calculated by the following second equation of thermal diffusion [191]:

$$\frac{1}{a} \frac{dT(x, t)}{dt} = \frac{d^2T(x, t)}{dx^2} \quad (2.5)$$

Where at the interface between the soil and the subsurface of geomembrane, given that $T(0, t) = T_{GM}(t)$, the expression of thermal diffusion can be obtained from the following equation:

$$a = \frac{\lambda}{\rho C_p} \quad (2.6)$$

Where a is the thermal diffusivity of the soil, λ is the thermal conductivity of the soil, ρ is the density of the soil, and C_p is the specific heat of the soil. Assuming that there is a perfect contact between the soil and the geomembrane, and the initial temperature of the soil is uniformly distributed as T_i . Therefore, the geomembrane temperature $T_{GM}(t)$ can be expressed as below:

$$T_{GM}(t) = T(X = 0, t) = T_a + \frac{1}{h} \left[\alpha G + 3 \frac{\lambda[(T_i - T_a) - \alpha G/h]}{\delta(t) + 3\lambda/h} \right] \quad (2.7)$$

And $\delta(t)$ can be found in the following equation:

$$\frac{Q}{A} = \varepsilon \sigma T^4 + \frac{\lambda}{h} [\delta(t) + 3\lambda/h] = \delta(t) \left[\delta(t) + \frac{6\lambda}{h} \right] \frac{d\delta}{dt} \quad (2.8)$$

When the geomembrane is horizontally placed, $h=h_h$ and the h_h can be obtained through the following equation:

$$h_h = \frac{p}{T_{GM} - T_a} \quad (2.9)$$

Where p is the absorbed power per unit area by the geomembrane. The relation between the applied solar energy and the absorbed solar energy is:

$$\alpha = \frac{p}{G} \quad (2.10)$$

When the geomembrane is vertically placed, $h=h_v$ and the h_v is equal to:

$$h_v \cong \frac{p}{T_{GM} - T_a} \quad (2.11)$$

Therefore, if the power of solar radiation and the material properties of the HDPE geomembrane is known, the temperature profiles of the HDPE geomembrane can be predicted through the equations.

2.6.3 Theories of thermal imaging monitoring on structures

Thermal imaging detects the subsurface defects or structural differences by the temperature contrast on the surface of the objects. The external heat energy spread into a deeper part of the structure through thermal conduction [192-195]. In the thermography, which requires an external heat input, the temperature evolution on the surface of the object is determined by the equation[196]:

$$T(t) = \frac{Q}{e\sqrt{\pi t}} \quad (2.12)$$

Where Q is the external input energy per unit area, T(t) is the temperature over time t of on the surface of the material, e is the thermal diffusivity and t is the time. When there is a subsurface defect or structural difference, the one-dimensional temperature solution can be expressed as[197]:

$$T(t) = \frac{Q}{e\sqrt{\pi t}} \left[1 + 2 \sum_{n=1}^{\infty} R^n \exp\left(\frac{-n^2 L^2}{\alpha t}\right) \right] \quad (2.13)$$

Where α is the thermal diffusivity, L is the characteristic length of the depth of the defects or length of structural difference, and R is the thermal wave reflection coefficient of the interface. In this equation, R plays as a benchmark to evaluate the efficiency of the heat transfer at the interface, and it can be calculated with the equation[198]:

$$R = \frac{e_1 - e_2}{e_1 + e_2} \quad (2.14)$$

where e_1 is the thermal diffusivity of media 1 and e_2 is the thermal diffusivity of media 2. This equation reveals that when there is another material under the detected objects, there will be a medium between the two materials. The efficiency of heat transfer at the interface depends on the mismatch of thermal effusivity at the interface. In addition, because of the lateral thermal diffusion, the lateral heat dissipation also affects the heat transfer efficiency, and the L may be affected by the 3-D heat transfer. Therefore, different interfaces between the materials will result in various R . This can make the $T(t)$ different at varied interfaces or damaged regions.

Some researchers considered other suitable methods to process the temperature curves from thermal imaging experiments, and these methods were used to determine the profile of defects quantitatively. Previous research found that the depth of the defects at the subsurface of a structure relates to the specific characteristic time (SCT) [199], which is defined as the peak time in the first or second derivation of the temperature decay curves during the transient temperature decay events. Some methods are developed based on a contrast between the thermal image frames with a reference thermal image frame at the SCT. Ringermacher et al. used the average temperature of the measured surface as a reference temperature to determine the defect depth[199]. M. Pilla et al. used the initial frames to start the transient temperature decay events as a reference frame[200]. The peak contrast time (PCT) [201, 202] method was used by identifying the peak time of the max value of the temperature contrast between the damaged region and the undamaged region. An undamaged area was first selected as a reference, and the temperature contrast is proportional to the square of the defect depth. The relation can be expressed as:

$$\Delta T = 2At^{(-\frac{1}{2})} \sum_{n=1}^{\infty} R^n e^{(-\frac{n^2 w}{t})} \quad (2.15)$$

Where ΔT is the temperature contrast, and the w expressed as $w = L^2/\alpha$, and A can be expressed as $A = Q/e\sqrt{\pi}$.

Similar to the PCT method, the peak slope time (PST) method[203-205] estimates the defect depth by the second-order derivation of the temperature decay curves. The expression is shown as:

$$\Delta T = 2At^{(-\frac{5}{2})} \sum R^n e^{(-\frac{n^2 w}{t})} \left[\left(\frac{n^2 w}{t} \right)^2 - \frac{3n^2 w}{t} + \frac{4}{3} \right] \quad (2.16)$$

PST method picks the peak time on the first derivation of the thermal contrast equation as the SCT, and it was found that the PST was also proportional to the square of the defect depth.

The logarithmic peak second derivative (LPSD) [206] method finds the SCT in the LPSD of the transient temperature decay curves. The expression is shown as:

$$\frac{d^2(\ln T)}{d(\ln t)^2} = \frac{t}{T} \frac{dT}{dt} - \frac{t^2}{T^2} \frac{d^2T}{dt^2} \quad (2.17)$$

Where

$$T' = -\frac{1}{2}At^{(-\frac{3}{2})} + 2At^{(-\frac{3}{2})} \sum R^n e^{(-\frac{n^2w}{t})} (\frac{n^2w}{t} - \frac{1}{2}) \quad (2.18)$$

And

$$T'' = \frac{3}{4}At^{(-\frac{5}{2})} + 2At^{(-\frac{5}{2})} \sum R^n e^{(-\frac{n^2w}{t})} \left[(\frac{n^2w}{t})^2 - \frac{3n^2w}{t} + \frac{3}{4} \right] \quad (2.19)$$

Z. Zeng et al. used this method to estimate the defect depth. They pointed out that the LPSD curves were obtained directly from the calculation and did not need a reference. Still, the SCTs in the LPSD curves may be affected by the 3D heat diffusion effects, affecting the inspection results by an inaccurate peak time. Z. Zeng et al. also developed an absolute peak slope time (APST) method, which can be expressed as:

$$f' = 2A \sum R^n e^{(-\frac{n^2w}{t})} \frac{n^2w}{t^2} \quad (2.20)$$

Where the SCT of the method is located at the first peak of the curves. Z. Zeng used these methods to estimate the defect depth when the defects were in touch with different materials. The results showed that PST, LPSD and APST could accurately estimate the defect depth at different interfaces, but the PCT method can affect the defect depth.

Based on the above equations, the temperature evolution of the geomembrane that contacts the subsurface soil can be predicted with the provided power of input solar energy and the ambient temperature. In addition, different features under the HDPE geomembrane and the defects in the HDPE geomembrane can be detected after the procession of the thermal image sequences.

2.7 Clustering-based image segmentation method

2.7.1 Algorithms for thermal imaging

After getting the thermal images from the camera, quantitative image analysis is required to obtain the information of the temperature evolutions for each pixel. The aim of the post procession for the thermal image is to enhance the quality of the image, enable the quantitative analysis, and capture the hotspot and extract the details of the defects. Histogram equalization and contrast stretching algorithms are utilized to increase the contrast among pixels. Image segmentation such as morphological segmentation [207] and two-level segmentation, and image thresholds such as global threshold and fuzzy threshold [208] can help find the hot spot on the specimen efficiently. And the signal processing method such as thermographic signal reconstruction and principal component analysis can also help detect the deeper defects with higher thermal contrast.

The image segmentation aims to subdivide an image into several constituents. According to Jadin, M. et al. [209], thermal image analysis can be divided into three main procedures. As shown in Figure 2.15, the region of interest related to the image segmentation is found at first. After that, the temperature information in each sub-segment can be extracted by algorithms to make them distinguished and classified into different categories. After the classification of the thermal information, a decision-making process is applied to determine whether the detected part-owns defections. The accuracy of the last step depends on whether the region of interest (hot spot) is correct and whether the information is suitably allocated. Hence, the first step is the fatal part of the whole post-processing procedure. The imprecise location of this region affects the following two steps. It is reported that the spectrum of the obtained image could be transferred into a greyscale [207], and the hot spot area could be distinguished by high grey value pixels. To obtain the region of interest (ROI) efficiently and accurately, a high-resolution image is a premise, this normally depends on the distance between the camera and the observed specimen and the resolution of the camera. N.T. Moja & A.J. Willis [210] evaluated several post-processing techniques and stated that histogram equalisation would work out a better isotherms contrast, but generalised eigenvalue decomposition result in a poor result due to the high classification error. Also, they pointed out that the neural network classifiers performed better than the statistical classifiers.

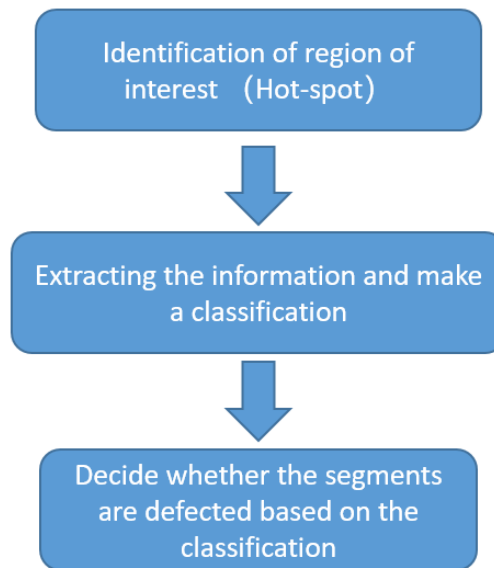


Figure 2.15 General procedures of analysing the thermography

The image threshold method is also a useful tool to analyse thermography, it helps the segmentation and classification of the image. However, the normal image threshold would over segment the image due to that the thermal image is over-centralized intensity distributed and the contrast intensity is low. Also, the complex background and low SNR would challenge outdoor monitoring and increase the difficulty of extracting hot regions from the surrounding area.

Lin et al. [211] proposed the image registration method based on the image matching adjustment algorithm and object oriented division for assessing an electrical device. And R. Ishino [212] applied the method where he utilized high order local auto-correlation features to compare the thermal pattern of a device. Also, the artificial neural network is a powerful tool to analyse dynamic thermography, it would enhance the efficiency of recognition and classification for the images. M. Shafi'I & N. Hamzah [213] created an image segmentation model and aimed to automatically classify the defects into four species: low, intermediate, medium and high. In this study, the RGB colour thermal image is processed through MATLAB where the pixel region tool was created. Then hundreds of samples were put into a three-layer Artificial Neural Network for training. Testing samples validated the model.

2.5.2 Clustering-based image segmentation methods

Given that the temperature contrast of a single frame thermal image is not sufficient to identify defects or structural differences. An image segmentation method needs to be

integrated with thermal imaging to recognize different features. The main aim of using image segmentation in the SHM is to assign the pixels in the image into different groups based on the similarity between regions and classify the monitored region into the damaged region and undamaged region. Clustering-based image segmentation method is used to find out the structural difference with a set of data and separate the data into an n-dimensional feature space based on the similarity in pixel groups.

Unsupervised machine learning clustering-based algorithms, such as the K-mean clustering method, density-based spatial clustering (DBSCAN) method, gaussian mixture model (GMM) method and spectral clustering method, have been widely used image segmentation processes. K-mean clustering [214] is an unsupervised distance-based partitioned clustering method. It has been widely used in statistical analysis with good efficiency[215-217]. The goal of the K-means clustering is to characterize the similarity of data and organize the data into the predefined number of K clusters[218]. The data is characterized based on the feature vector with the pixel values in the image, and the process can be expressed as :

$$d(x_r, c_i) = \left(\sum_{u=1}^U |x_{ru} - c_{iu}| \right)^{0.5} \quad (2.21)$$

where the algorithm defines an initial mean vector c_i for each group, and each data x_r is classified into a group to make a smaller squared error between the empirical mean of the group and the point data. Then, the vectors set is updated, and the iteration will continue until the assignment of the points converges. K-means clustering needs to identify the number of clusters k before the classification. This method is useful when the number of data groups is known before clustering, but the noise pixels in the image would affect the result of clustering. V. Ramos and F. Muge used the K-means clustering method to segment a colour map and identified different infrastructures based on the colour contrast. They used the k-means clustering method in the genetic algorithm [220] to find an optimal partition solution. SS. Savkara et al. [219] used the K-means clustering method to detect the blood cells from the microscopic thin blood images. The proposed method was tested on 60 Giemsa-stained thin blood slides images, and they stated the segmentation could achieve a 98.89% accuracy. Omar et al. [126] used the K-mean method to segment a temperature map of a bridge deck and classified the bridge into different corrosion conditions according to the temperature values.

Density-based spatial clustering (DBSCAN) algorithm[220, 221] is one kind of density-based clustering method. It clusters the data based on a threshold for a neighbourhood search

radius ϵ and a minimum number of neighbourhood points N_{min} is required to find out a core point[222, 223]. Clusters will be created after the core points are defined, and the neighbourhood points will be checked in the created clusters[222]. The process will be repeated until no points can be added to clusters. DBSCAN algorithm is good at processing nonlinear data, and it does not need to identify the number of clusters before the procession. But it cannot process large density data, and the number of clusters cannot be controlled[224]. As shown in Figure 2.16, J. Shen [225] developed a two-step DBSCAN method to cluster the superpixels in the image. They segmented the image through the colour similarity and geometric restrictions at the first step, and then each cluster was merged into a superpixel with a distance calculation defined by the colour and spatial features at the second step.



Figure 2.16 Illustration of superpixel segmentation. The left two images are the images after the proposed clustering stage, right two images are the final results after the merging stage[225]

This method can segment images with a speed of 50 frames per second. KM. Kumar et al.[226] improved the DBSCAN method by using a graph-based index structure method which enhanced the efficiency of the neighbourhood points search process. DBSCAN method performed well when processing the unevenly distributed data or the noisy data, but the parameters N_{min} and ϵ needed to be tested to get a reasonable clustering result.

In GMM clustering[227, 228], the dataset can be regarded as a multivariate distribution consisting of multivariate Gaussian distribution components. Each of the components is determined by the covariance and the mean[229]. The GMM model has been used as a

probabilistic method to obtain a fuzzy classification of the data. The segmentation process was conducted by comparing the probabilities of data when they are fitted in each component[230]. Similar to K-means clustering. The number of components in the GMM model needs to be determined before the classification. F. Riaz et al. pointed out the objects in medical imaging can be modelled as data that follows Gaussian mixture distributions. They use the GMM method to segment the images from dermoscopy, magnetic resonance imaging (MRI), and chromoendoscopy. Z.Ji et al. [231] used a robust generative asymmetric GMM method to segment the magnetic resonance image. They developed an asymmetric distribution model and fit the shape of the data and produced a 3D view of a brain magnetic resonance image. The result showed that their model was flexible to fit the data shapes in varied images and can eliminate the influence of noisy data sets.

The comparison of each clustering method is summarised in Table 2.5. In this study, three kinds of image segmentation methods are investigated to classify the map of HDPE geomembranes, and the classified maps processed images are compared to evaluate the classification quality.

Table 2.5. Summarise of image segmentation methods

Image segmentation method	Parameters	Comparison	Reference
K-mean clustering	Number of data groups k	even cluster size, a small number of clusters. Useful when group number is known, noise data affect segmentation quality	[126, 215-219, 232]
DBSCAN clustering	Data radius, minimum neighbourhood points	Useful in uneven cluster size, non-flat data geometry, useful in noise data set.	[220-226]
GMM clustering	Number of elements	Flat data geometry, general cluster purpose	[227-231]

2.8 Conclusions

This chapter reviewed the roles of HDPE geomembranes in the sewage water treatment plant and the potential exerted effects by the scums. This chapter also reviewed some of the most popular non-contact remote sensing SHM methods, such as the 3-D DIC method, the UAC sensing method, and the mobile sensing method. They are widely adopted in the field of inspection on varied structures such as buildings, bridges, pavements, and floating geomembrane covers. Despite their advantages on wide coverage monitoring tasks, these technologies cannot identify the internal defects or feature differences. Thermography is reviewed as a powerful remote sensing technology to monitor the defects and structural differences. However, based on the current state-of-art of the on-site thermography on large structures, there is a potential to detect the structural difference of large-area structures using the thermography assisted by the applied heating energy. There is hardly any discussion on this application from the literature review. To be more detailed, the research gaps are summarised as:

- Traditionally, in passive thermography, the thermal camera is simply used to monitor the test piece and from the thermal image, a temperature map is constructed. Active thermography involves heating the surface of the object rapidly using an external heat source and observing how the temperature decays with time. The structural difference in the material is detected by variations in the temperature decay rate. Although thermography is a relatively mature technology, it is only limited to inspect a small area or a small specimen where the local temperature is altered. There is a lack of surveys about the large area thermography with the wide coverage heating methods.
- Thermography methods are mainly used to evaluate structural flaws such as debonding and corruptions. There is a lack of discussions of using thermography to distinguish different states of objects such as gas, liquid and solid. A thermal imaging technique that detects structural differences needs to be developed to see through an opaque material and detect the profiles of the substances by comparing the thermal responses.
- Current Infrared thermal imaging on large structures is based on a temperature scan, which depends on analysing a single thermal image frame. This is inaccurate since the temperature contrast varied in each frame of the thermal image. It is difficult for on-site thermography monitoring to find an ideal monitoring time window for the thermography. In addition, on-site thermography lacks an ideal external heat source to enlarge the temperature contrast on

the large structures. It is hard to monitor the development of structural differences with a single frame of the thermal image. Therefore, the works in this study will enhance the thermography monitoring results by evaluating temperature change rates during transient heat transfer events.

- Previous research stated the ambient factors could affect the monitoring results from thermal imaging, but there is a lack of study to correlate the ambient weather information, such as solar radiation and ambient temperature, with the temperature evolutions of the geomembrane in the long term. The transient temperature change events resulting from the variation of solar radiation and ambient temperature can be used to find out the structural differences (damages or different materials) for the large-scale structures.

Therefore, in the next several chapters, a series of studies are carried out to overcome these challenges for thermography on large-area structures.

CHAPTER THREE

3 Methodology & equipment

3.1 Introduction

In order to address the research gaps in Chapter 2, novel quasi-active thermography will be introduced in this chapter. The experimental and computational methodology will be illustrated, and the developed quasi-active thermography will be applied to monitor the structural difference of the geomembrane structures. This chapter will first introduce the experimental setup of the thermal monitoring system for the quasi-active thermography. The emissivity spectrum of the HDPE geomembrane material was measured, and the details of the equipment in the thermography experiment are presented. For the computational works, the details of the finite element model, including the fundamental heat transfer theories, the setup of boundary conditions, and the preliminary verification of finite element models, are illustrated. Following that, to enhance the quality of the thermography, several methods, including Newton's cooling law method, LPSD method, and the frame subtraction method, are introduced to process the recorded thermal image sequences. To distinguish different features under the geomembrane covers, several clustering-based image segmentation methods are introduced to classify the geomembrane areas into different groups. These methods are adopted in the following chapters to address the monitoring challenges for the large-scale floating HDPE geomembrane covers.

3.2 Experiment Set up of the thermal monitoring system for the quasi-active thermography

To ensure the viability of using the IR thermography to monitor the HDPE geomembrane material, the emissivity spectrum of the HDPE geomembrane was at first tested using Fourier-transform infrared (FTIR) spectroscopy in the laboratory. Several pieces of HDPE geomembrane samples in WTP were tested. Figure 3.1 shows the resultant emissivity spectrum of the HDPE geomembrane material. The FTIR result shows that the test sample has a high emissivity (above 95%) within the long-wavelength infrared bandwidth (9–14 μm), confirming that the HDPE geomembrane is suitable long-wavelength infrared thermography inspection.

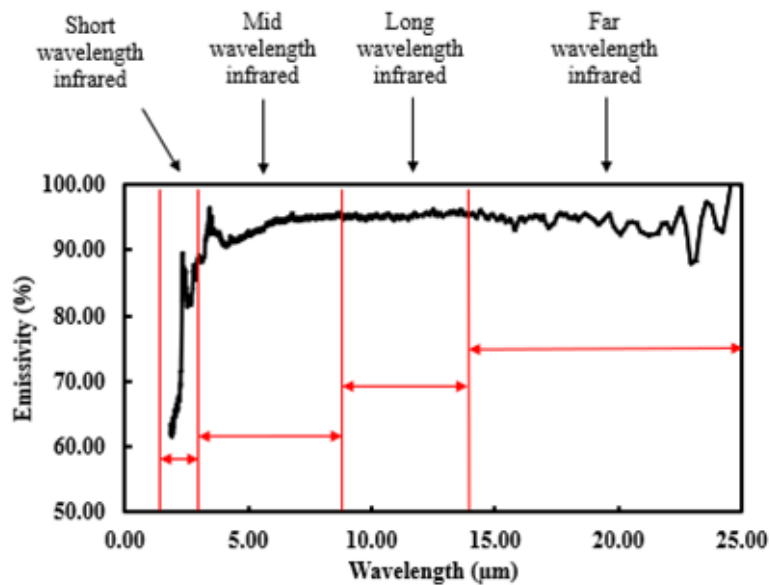


Figure 3.1 Emissivity spectrum of the HDPE membrane from Fourier-transform infrared (FTIR) spectroscopy.

Given that the HDPE geomembrane has been proved with high emissivity and is suitable for thermal imaging test [127], a lab-scale IR thermography experiment set up was designed at the rooftop of a building in Monash University, Melbourne, Victoria, Australia. As shown in Figure 3.2, a thermal camera was fixed on a frame to constantly monitor a sheet of the HDPE geomembrane, which is the same material as floating covers at anaerobic lagoons at the WTP. Four edges of the HDPE geomembrane were clamped around the perimeters of the test rig. In the following IR thermography of the next several chapters, the underside of the HDPE geomembrane will contact different substrates, such as water, solids, or air, to simulate the condition of the floating covers at the sewage treatment plants. The HDPE geomembrane will also be modified with defects, and these defects will hide in the non-air interfaces.



Figure 3.2 Illustration of the IR thermography experiment set up

Figure 3.3 shows the equipment that was used in the experiment, and technical specifications are demonstrated in Table 3.1, A high-resolution IR thermal camera, FLIR A615 manufactured by FLIR Systems, Inc. USA [233] was deployed to monitor the temperature evolution of the geomembrane. It has been verified that the temperature measured by the thermal camera has a $\pm 0.1^{\circ}\text{C}$ error, which is within the range of thermal sensitivity of the thermal camera[127]. An Apogee SP-110 pyranometer [234] manufactured by Apogee Instruments, Inc. USA, was used to record the local solar intensity. In the meantime, A thermal probe of Fluke 287 multi-meter [235] manufactured by Fluke Corporation, USA, was used to record the ambient air temperature. The pyranometer and the thermal probe played together as a real-time weather monitoring system to record the weather information, where the thermal camera recorded the temperature response of the geomembrane under the change of weather. For the long-term experiments, which last more than 24 hours, sampling rates of the above three instruments were set as 10min/ read. While for the short-term experiment which last for no more than 30 mins, the sampling rate of all instruments were set as 3Hz. The whole set up was exposed outside during the experiment. All instruments were set to start recording at the same time to match the time of measured data.

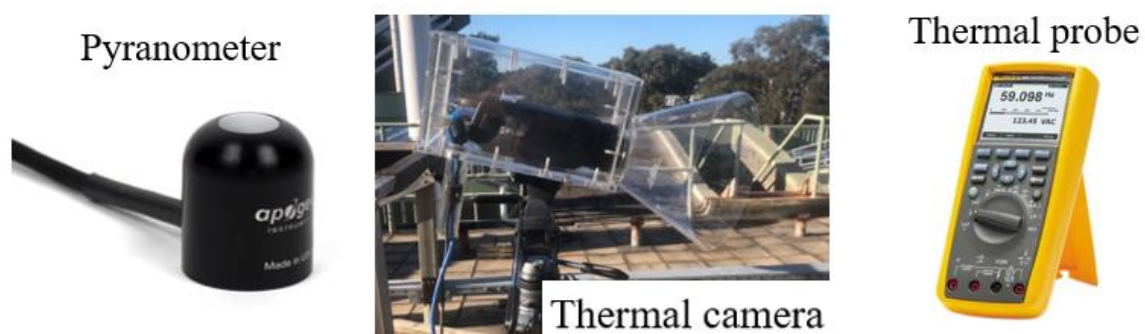


Figure 3.3 Experiment equipment of outdoor thermal imaging monitoring system

Table 3.1 Manufacturer data of experiment instruments

FLIR A615 IR camera	Specification
IR resolution	640×480 pixels
Field of view (FOV)	25°×19°
Sampling frequency	3-50Hz
Minimum focus distance	0.25 m
Accuracy	$\pm 2^{\circ}\text{C}$
Sampling rate	10min/read

Noise equivalent temperature difference (NETD)	< 0.05°C @ +30°C (+86°F) / 50 mK
Detector type	Focal plane array (uncooled microbolometer)
Fluke 287 multi-meter thermal probe	Specification
Operating temperature	-20 °C-55°C
Mass	871g
temperature resolution	0.1°C
Accuracy	± 1%
Sampling rate	10min/read
Apogee SP-110 pyranometer	Specification
Sensitivity	0.2mV/Wm ⁻²
Output range	0-400mV
FOV	180°
Mass	90g
Sampling rate	10min/read

3.3 Finite element analysis set up and preliminary computational analysis

A finite element (FE) model is constructed and shown to reliably predict the experimentally observed thermal transients and cooling constants. This FE model is set up to simulate a progressive scum accumulation with time, employing a specified scum-berg geometry and a stepwise change in thermal properties. The results indicate a detectable change in the cooling constant at different locations on the cover, thereby providing a quantitative basis for characterizing the scum accumulation beneath the cover. The practical application and limitations of these results are briefly discussed in Chapter 6.

HDPE geomembrane is typically deployed out in the open environment where the underside usually rests on the liquid wastes or scum. The cross-sectional boundary conditions for the heat transfer process between the HDPE geomembrane and the environment in the FEA is illustrated in Figure 3.4. Solar energy is applied to the geomembrane as external heat flux, and the surface of the geomembrane also radiates energy to the surroundings. In the experimental work, the test rig was placed on the concrete floor. The interfaces between the scum and the underside of the geomembrane are considered as in perfect thermal contact.

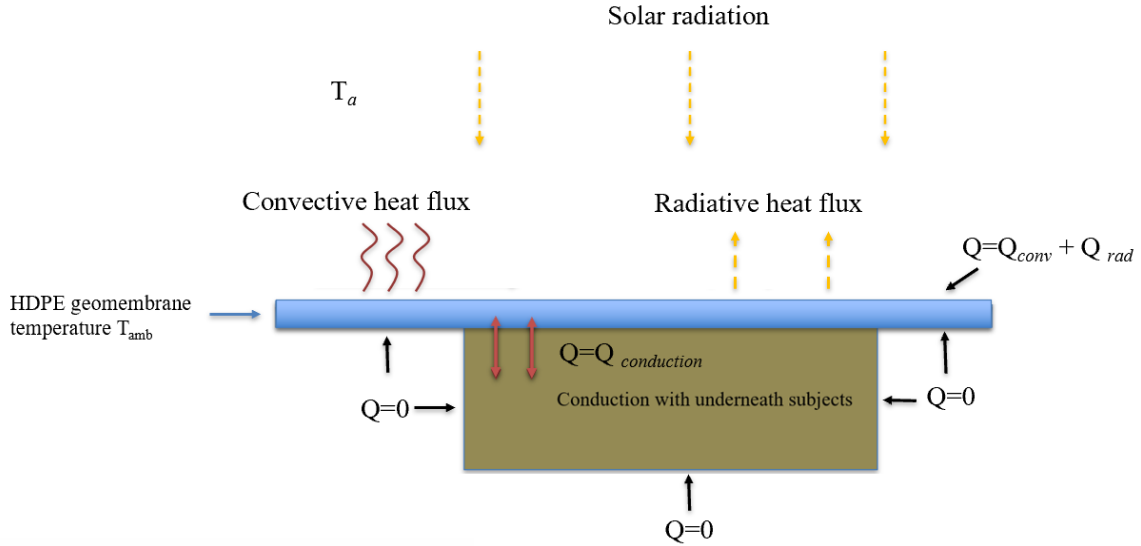


Figure 3.4 Cross-sectional boundary conditions for heat transfer in the FEA

Abaqus computes the heat transfer process between the objects and the ambient environment through a radiative heat transfer and convective heat transfer. And according to the heat convection rate equation, the Abaqus uses the below equation to calculate the convective heat transfer: [190]:

$$Q_{conv} = h[T(t) - T_a] \quad (3.1)$$

Where Q_{conv} the exchanged energy due to the convection, $T(t)$ is the temperature of the objects, T_a is the ambient temperature, and h is the heat transfer coefficient between the object and the ambient, when the geomembrane is put horizontally and exchange heat with the air, the h is set as $13 \text{ W/m}^2\text{K}^{-1}$ [190]. And the Q_{conv} in equation (3.1) is equal to $\rho c L \frac{dT}{dt}$, where ρ is the density, c is the heat capacity, and L is the characteristic thickness of the membrane. The equation (3.1) can be expressed as:

$$\rho c L \frac{dT}{dt} = h[T(t) - T_a] \quad (3.2)$$

After the integration, the equation becomes:

$$T(t) = T_a + [T(t) - T_a]e^{-b_{con}t} \quad (3.3)$$

Where the b_{con} is the convective cooling constant and equals to $\frac{h}{\rho c L}$ that indicates the rates of temperature change.

The computation of the radiative heat transfer process in the Abaqus is expressed as:

$$Q_{rad} = \epsilon \sigma [T(t)^4 - T_a^4] \quad (3.4)$$

where the ϵ is the emissivity of the surface of the objects, and σ is the Stefan-Boltzmann constant. The cooling constant for radiative cooling is expressed as:

$$b_{rad} = \frac{\epsilon \sigma (T(t) + T_a)(T(t)^4 - T_a^4)}{\rho C L} \quad (3.5)$$

As shown in Equation (3.5), the radiative cooling constant varies with the temperature of the objects and the ambient temperature. According to the above equations, the temperature change of the geomembrane can be predicted for a given combination of the power of input heat flux (solar energy) and ambient temperature.

Equations (3.1) to (3.5) show that the heat transfer process of the object can be affected by both convection and radiation. Table 3.2 shows the details of the FE model. The FEA conducted in this dissertation will assume convective heat transfer and radiative heat transfer when investigating the effects of the state of scum formation on the thermal transient on the membrane surface.

The contribution of each to the membrane structure in question is firstly investigated with two preliminary short term FEA studies. A 2mm thick×0.5m wide×1m long membrane with the material properties of the HDPE geomembrane was exposed to a constant 283K ambient temperature, and the initial temperature of the membrane was set at 290K, and the membrane is allowed to cool from 290K to 283K. The emissivity of the HDPE geomembrane material at room temperature is approximately 0.9 [127].

The results shown in Figure 3.5 shows that the simulation using a combination of radiative and convective cooling shows the fastest temperature decay rate. The temperature decay rate is the slowest with radiative cooling. In a separate set of simulations, the same membrane was exposed under the external heat flux to simulate exposing the membrane to solar radiation at 600 W/m². This heat source is applied to the surface of the membrane for 500s and then stopped abruptly. The results shown in Figure 3.6 show that when only radiative heat transfer exists, the membrane will be heated to a higher peak temperature.

In contrast, in the convective heat transfer, the membrane attained a lower peak temperature. In the case where both convective and radiative heat transfer is present, the membrane temperature reached is the lowest among the three simulations. Therefore, it can be concluded that both convective and radiative heat transfer will affect the transient temperature evolution of the membrane structure, and in the following FEA, both convective heat transfer and radiative heat transfer will be considered when simulating the transit process of the scums.

Table 3.2 Details of FE model

Model data	Specification
Membrane size	2mm*0.5m*1mm
Soil substrates size	0.3m x 0.3m x 0.3m
Model type	3-D deformable solid
Element type	DCC3D8: An 8-node convection/diffusion brick (heat transfer element)
Element shape	Hex
Element size	1mm

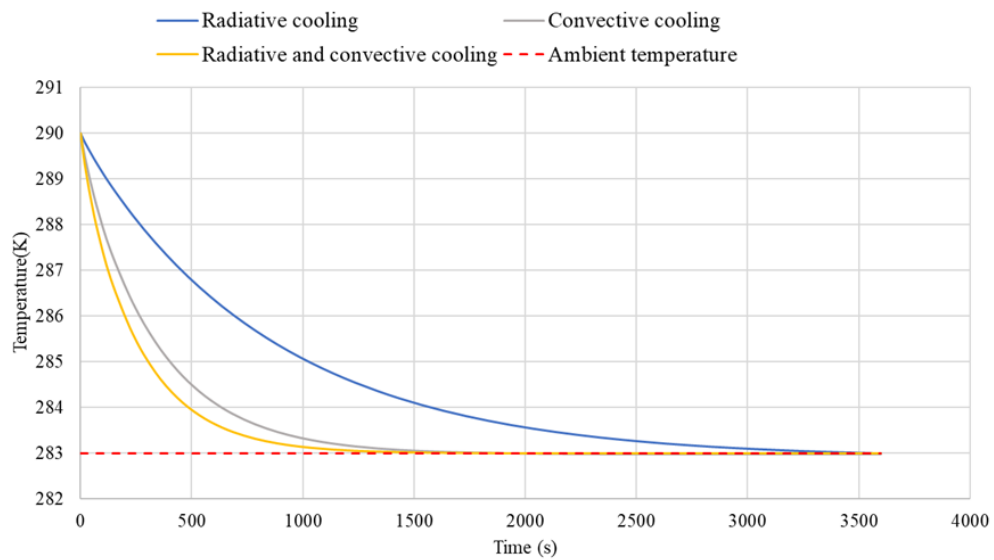


Figure 3.5 Illustration of FEA results (no external heat flux, ambient temperature is constant)

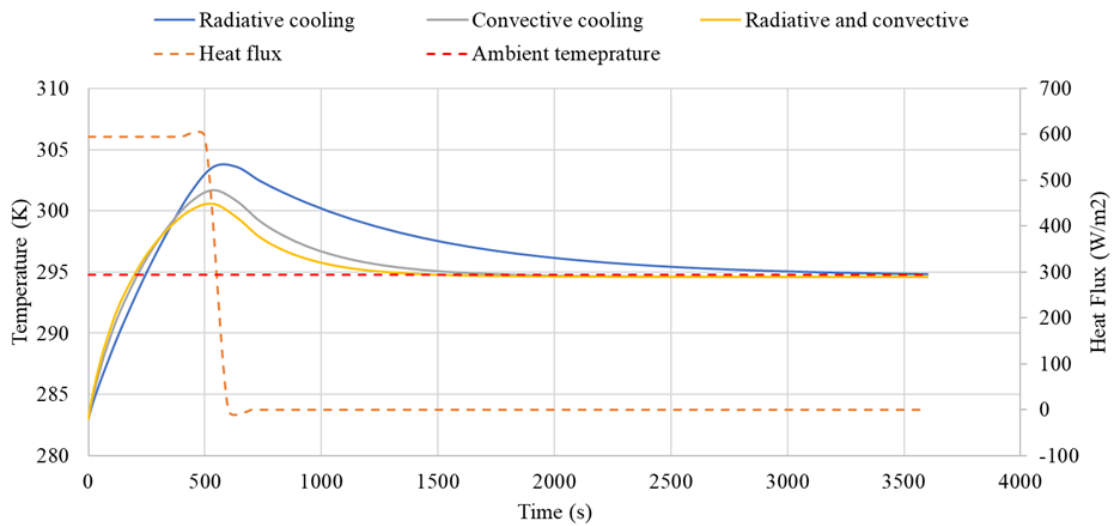


Figure 3.6 Illustration of FEA results (external heat flux was applied for 500s and then stopped, ambient temperature is constant)

3.4 Analysis of thermal image sequences

Data analysis for pulsed thermography generally relies on tracking the surface temperature difference between a potentially defective location and a reference location that is presumed to be defect-free [206, 236, 237]. This temperature contrast curve typically shows a maximum at a particular time instant, known as the peak contrast time (PCT), approximately proportional to the square of the defect depth beneath the surface. The first derivative of the thermal contrast also shows a peak, instant known as the peak slope time (PST), that also correlates approximately with the square of defect depth. In addition to these approaches, Shepard et al. [206] proposed a reference-free approach that relies solely on the temperature evolution at a given point. Their approach evaluates the 2nd derivative of temperature in the logarithmic domain, employing a logarithmic scale for both temperature and time. The peak time for this logarithmic second derivation also correlates approximately with defect depth, and because this peak occurs earlier than PCT and PST, the effects of blurring (due to lateral heat diffusion) are reduced, thereby resulting in clearer delineations of defective regions. Another processing method commonly applied is principal component thermography [238], which uses a singular value decomposition of the thermal response to accentuate defect thermal contrast.

This dissertation proposes an alternative approach based on tracking the cooling kinetics during a decrease in solar intensity due to cloud cover, following a period of sustained heating. For a membrane on air (or biogas), the cooling kinetics is controlled by Newton's law of cooling, as summarised below in Section 3.4.1.1. While this cooling law does not strictly apply for a membrane in contact with water or soil (simulating liquid sewage or scum, respectively), it is still possible to extract a cooling constant by fitting the data to an assumed

exponential decay curve. The expectation is that subsurface defects may lead to detectable spatial variations in this cooling constant. For completeness, the data processing algorithms for the LPSD and frame subtraction are also briefly recalled below.

3.4.1.1 Newton's cooling law method

Heat transfer from a hot membrane in contact with air occurs by convection, q_{conv} and radiation, q_{rad} , i.e.

$$q = q_{conv} + q_{rad} \quad (3.6)$$

Where q denotes the combined heat flux, and the subscripts identify the two contributions. According to Newton's law of cooling [188, 239],

$$q_{conv} = h_c [T(t) - T_a(t)] \quad (3.7)$$

where T, T_a denote respectively the membrane temperature and ambient temperature at a time instant t , and h_c denotes the convective heat transfer coefficient.

Radiative heat transfer satisfies Equation 3.1. Allowing for a radiative heat flux from the surroundings, the net radiative heat flux at the surface of a membrane can be written as follows [188, 239]

$$q_{rad} = h_r \varepsilon \sigma (T^4 - T_a^4) \quad (3.8)$$

where T, T_a must now be interpreted as absolute temperatures (in accordance with Equation 3.1), and Kirchoff's law, equating absorptivity α with emissivity ε has been invoked. For the range of temperatures encountered in the present context, the difference $T - T_a$ is relatively small compared with the absolute ambient temperature T_a , so that Equation (3.8) can be rewritten in the form

$$q_{rad} = h_r [T(t) - T_a(t)] \quad (3.9)$$

$$h_r \approx 4\varepsilon\sigma T_a^3 \quad (3.10)$$

Accordingly, Equation (3.6) can now be rewritten as

$$q = h [T(t) - T_a(t)] \quad (3.11)$$

$$h = h_c + h_r \quad (3.12)$$

The next step in characterising the cooling kinetics is to estimate the Biot number

$$Bi = \frac{hL_c}{k} \quad (3.13)$$

where k denotes the thermal conductivity, and L_c denotes an appropriate characteristic length, which in the present case can be assumed to be the membrane thickness (rather than the more common use of the half-thickness, consistent with the assumption of zero heat flux from the underside of the membrane). Employing $h = 13 \text{ Wm}^{-2}\text{K}^{-1}$ as a representative value for the total heat transfer coefficient for a horizontal membrane, $k = 0.44 \text{ Wm}^{-1}\text{K}^{-1}$ for the conductivity of HDPE [240], and $L_c = 2\text{mm}$ leads to $Bi \approx 0.06$. As this value is less than 0.1, the temperature gradient across the membrane thickness can be ignored [188, 239]. Assuming for simplicity that the ambient temperature T_a can be regarded as being constant, or only slowly time varying, Equation (3.2) can be integrated to obtain

$$T(t) = T_a + (T_i - T_a)e^{-bt} \quad (3.14)$$

$$\tau = b^{-1} = \frac{\rho CL}{h} \quad (3.15)$$

where T_i denotes the initial temperature, and b the cooling constant. Using the parameter values given above leads to the following estimate for the time constant (the reciprocal of the cooling constant b), $\tau \approx 270\text{s}$.

Although Equation (3.14) has been derived by assuming that the ambient temperature remains constant, τ nevertheless provides a useful characteristic time, e.g., for setting a time interval for assessing the thermal contrast, or for discarding transient events that occur on a time scale much shorter than τ .

For a membrane in thermal contact with a substrate such as water or soil, there is a significant heat transfer by conduction to the substrate (as there would also be for liquid sewage or scum. Accordingly, the above estimate for the Biot number is not applicable, and Equations (3.2, 3.14) are also not strictly applicable. Nevertheless, temperature decay profiles $T_{(i,j)}$ recorded for each pixel (i, j) in the region of interest can be curve-fitted to Newton's cooling law, Equation (3.14), to obtain a corresponding cooling constant, $b_{(i,j)}$ for each pixel location, in the expectation that spatial variations in this fitted constant may serve to identify regions with subsurface defects.

3.4.1.2 Logarithmic peak second-order derivative (LPSD) method

The LPSD of the temperature $T(x, y, t)$ is given by

$$J(x, y, t) = \frac{d^2(\ln T)}{d(\ln t)^2} = \frac{t}{T} \frac{dT}{dt} - \frac{t^2}{T^2} \frac{d^2T}{dt^2} + \frac{t^2}{T} \left(\frac{dT}{dt} \right)^2 \quad (3.16)$$

For the case of pulsed thermography, Shepard et al. [206] have shown that J reaches a maximum value J_{max} at a characteristic time that correlates with the square of defect depth, but occurs earlier than PCT or PST, thereby reducing the extent of blurring due to lateral heat diffusion, which leads to a clearer delineation of defective regions. In their implementation, the experimental temperature data is fitted by a low order polynomial in the logarithmic domain, which serves as a low-pass filter that preserves the essential thermal response while also providing an analytical representation for J .

In outdoors thermal imaging, the ambient temperature is not constant. Also, the external heat flux (solar radiation) is expected to fluctuate during the cloud covers events. Therefore, the characteristic time cannot be used to correlate with the thickness of the depth in the outdoors thermal imaging. In the present work, the LPSD method was modified by using the values of J_{max} to estimate the profiles of substrates and the defects. The Savitsky-Golay algorithm is employed, with a window size of 11, for data smoothing and calculating the derivatives on the right-hand side of Equation (3.15). At a 3 Hz sampling rate, this represents an approximate 4 s window, which is considered short enough to avoid biasing the derivative calculation. The resulting value of J_{max} is plotted, and the resulting map is assessed as a basis for identifying subsurface defects.

3.4.1.3 Frame subtraction method

In this method, an image is obtained by subtracting the temperature field at a time instant t_n from that at an earlier time t_{n-1} in the cooling sequence, and the absolute values of temperature changes over the whole event are summed up to produce an image $I(x, y)$, i.e.

$$I(x, y) = \sum_{n=1}^N |T(x, y, t_{n-1}) - T(x, y, t_n)| \quad (3.17)$$

Where

$$t_n = t_0 + n \times \Delta t \quad (3.18)$$

and t_0 denotes the chosen start point for the transient event, whereas t_N denotes the chosen endpoint of the transient event.

It is noted that if the temperature T is a strictly monotonically decreasing function of time, Equation (3.17) reduces to

$$I(x, y) = T(x, y, t_0) - T(x, y, t_N) \quad (3.19)$$

i.e., the resulting image would only depend on the start and endpoints and not on the choice of time interval Δt . However, there are short time-scale fluctuations in solar radiation in the present context that can result in short timescale increases in temperature during the course of what is overall a cooling transient. These short time-scale fluctuations are captured when using a time interval $\Delta t = 10$ s, and it was found that by using the absolute value of the temperature difference between successive time instants, as indicated in Equation (3.17), one obtains an enhanced contrast between defective versus intact regions, relative to what would be obtained from Equation (3.19).

3.5 Image procession methodology

A single frame of the unprocessed thermal image has difficulties defining the anomaly region or defining different interfaces under the geomembranes. The thermal image scale is subjectively determined based on the visual interpretation, which will result in the misinterpretation of the structural health condition. In addition, WTP needs an inspection technique to help determine the distribution of different objects under the cover. As the temperature of the geomembranes will change according to the environment during a day, the temperature contrast on the surface of the geomembranes will become large during warmer periods, and it will become small in cool periods[127]. A contour plot of the temperature distribution is not sufficient to classify different regions and calculate the corresponding areas. Therefore, an image process procedure is applied, as shown in Figure 3.7. Recorded thermal images are at first imported into MATLAB, and the collected temperature information contained in the thermal image will be transferred into a map of the cooling constant with the algorithm based on Newton's cooling law.

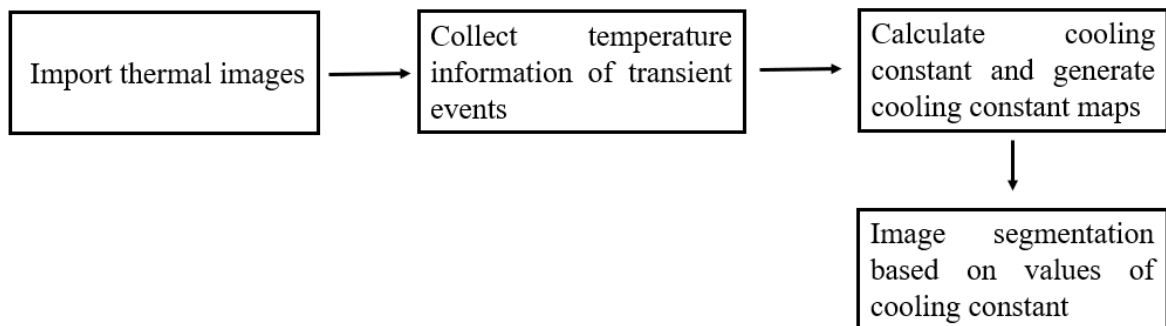


Figure 3.7 Flow chart of image procession

Similar to the thermal image, subjective selection of the threshold of the cooling constant map will also lead to a limitation in identifying regions on the cover. Here the image segmentation technique performs as a thresholding classification tool to arrange the data into categories. Several unsupervised clustering-based machine learning image segmentation algorithms are used with the aim of classifying the surface of HDPE geomembranes into different regions based on temperature changing rates in the cooling constant map. Data clustering has been used to divide a large number of data points into different groups such that data points in the same group are similar to those in other groups and have been widely used in image segmentation[224, 241]. The segmentation method can be divided into supervised classification and unsupervised classification[126], where the supervised classification needs a training procedure to get the desired result, while in the unsupervised classification, the algorithm requires the data to find its structure itself, and the result is unknown. In this thesis, the K-mean clustering algorithm, the density based spatial clustering algorithm and the Gaussian mixture model (GMM) clustering algorithm are used to perform the image segmentation on the cooling map to define the scum region, biogas region and sewage water region on the cover.

K-mean clustering[214] is an unsupervised distance-based partitioned clustering method, and it has been widely used in statistical analysis with good efficiency. The goal of the K-means clustering is to characterize the similarity of data and organize the data into the predefined number of K clusters[218]. The data is characterized based on the feature vector with the pixel values in the image, and the process can be expressed as:

$$d(x_r, c_i) = \left(\sum_{u=1}^U |x_{ru} - c_{iu}| \right)^{0.5} \quad (3.20)$$

where the algorithm defines an initial mean vector c_i for each group, and each data x_r is assigned to a group to minimize the squared error between the point data and the empirical mean of the group. Then, A new set of vectors is updated, and the iteration continues until the assignment of the points converge. K-means clustering is useful when the number of clusters k is known, but the noise pixels in the image would affect the result of clustering.

Density-based spatial clustering (DBSCAN) algorithm[220] is one kind of density-based clustering method. It clusters the data based on a threshold for a neighborhood search radius ε and a minimum number of neighborhood points N_{min} required to find out a core point. Clusters will be created after the core points are defined and the points will be checked in the created clusters[222]. The process will be repeated until no points can be added to

clusters. DBSCAN algorithm is good at processing nonlinear data, and it does not need to identify the number of clusters before the procession. But it cannot process large density data, and the number of clusters cannot be controlled[224].

In GMM clustering, the dataset can be regarded as a multivariate distribution consisting of multivariate Gaussian distribution components. Each of the components is determined by the covariance and the mean[229]. The GMM model has been used as a probabilistic method to obtain a fuzzy classification of the data. The segmentation process was conducted by comparing the probabilities of data when they are fitted in each component[230]. Like K-means clustering, the number of components in the GMM model needs to be determined before the classification.

CHAPTER FOUR

4 Development of Quasi-active Thermal Imaging to Identify Features under the Geomembrane Covers Using Ambient Solar Energy

Long-term quasi-active thermography was first developed in this chapter. A study was introduced using a quasi-active thermal imaging method that used ambient solar radiation to determine the extent of the solid matter under the geomembranes. This method was devised by using infrared thermography and a pyranometer to constantly monitor the transient temperature response of the HDPE geomembranes using the time-varying ambient solar radiation. Newton's cooling law was implemented to define the resultant cooling constants. The results of laboratory-scale tests demonstrated the capability of the quasi-active thermography to identify the presence and the extent of solid matter under the cover.

Transient temperature cooling events on the geomembranes were also used to evaluate the rate of change of temperature. K-means clustering, density-based spatial clustering and Gaussian mixture model-based image segmentation techniques were used to classify each interface under the cover. The proposed method was verified in laboratory experiments with different interfaces.

This chapter demonstrated, experimentally, the importance of measuring the surface temperature of the cover and solar intensity profiles to obtain the cooling process when during variations in solar intensity during normal sunrise, sunset, daily transitioning from the morning–afternoon–evening. The timescale associated with these events were different, and the results show that these daily transient temperature cycles of the geomembranes can be used to detect the extent of the accumulation of solid matter underneath the geomembranes.

4.1 Introduction

As reported in Chapter 1, currently, there is no method to effectively “see-through” the opaque covers to define the spread of the scum underneath the cover. The distribution of scums, biogas and water under the opaque covers cannot be estimated as well. The physical walk on the cover and visual inspection of the cover are the main methods deployed to determine the distribution and extent of semi-solid to solid scum and scumburbs. The inspection process is labor intensive, time-consuming and involves some inherent risks which we aim to eliminate or reduce.

Therefore, the development, accumulation, and potential movement of solid scumbers will adversely affect the structural integrity of the floating covers at the primary treatment lagoon and, thus, there would be a benefit in being able to monitor the transition of scum from a semi-solid to a solid-state, and the presence and distribution of scumbers.

This chapter aims to adapt a more quantitative, automated, effective, and safe technique to accurately determine the presence of scum and scumbers under the floating covers without the need for a worker/inspector to make contact with the cover physically. This chapter also aims to develop a continuous structural health monitoring technique to identify areas of scums, biogas, and sewage water under the cover. With the developed monitoring technique, WTP can improve the collection process of biogas, ensure the structural integrity of the cover, efficiently eliminate scums, and maximize the expected service life of the floating cover.

4.2 Development of Long Periods Quasi-Active Thermal Imaging to Monitor the Accumulation of Scums under the Geomembrane Covers

4.2.1 Introduction

As the raw sewage is untreated before entering the lagoon system, some content such as fats, oils, floating solids, buoyed sludge, or other fibrous materials in the raw sewage may separate from the liquid sewage and float to the surface of the lagoon [3]. These elements can form into a solid mass called “scum”. The scum in the anaerobic lagoon is a mixture of floating solids, undigested sludge and trapped gases formed during anaerobic digestion. This scum can become buoyant and accumulate under the cover and develop into a large solid body, creating an iceberg-like effect, which is also called “scumberg” effect because some are above the water's surface (under the cover) while some stays below the surface. The scum can move under the surface and even attach itself to the underside of the floating covers. Scum can move and grow over time with varying volume and hardness. The development of scum will exert the following influences on the cover:

- Scumbers block the pathway of biogas and produce “whaleback” regions on the surface of the cover, affecting the movement and collection of biogases by the covers. Whaleback regions will generate regional strain and stress on the HDPE geomembranes material.
- The existence of scumbers causes a vertical displacement of the membrane surface. When the wind blows over the cover, the cover will then be exposed to an increased lateral drag force, which can affect the structural integrity of the cover.

- If the scum has developed a hard crust, this may scratch the under-surface of the cover, if the scum moves horizontally and has not yet attached itself to the cover, and potentially result in the development of highly localized non-through cracks which have the potential to become a through-crack.
- Scumbers can deform the covers in a vertical direction and have an impact on its structural integrity, which might then be made even worse when the accumulated scum move under the cover, as any horizontal movement will also exert a lateral drag on the covers if the scum has attached itself to the underside of the cover material.

Due to the size of the lagoon and the hazardous environment, a remote sensing capability is preferred. A method of quasi-active thermography is proposed to determine the existence and the extent of the scum under a geomembrane cover with the aid of ambient solar radiation. The newly proposed method is examined under laboratory conditions using an outdoor test facility at Monash University. While the laboratory test specimen scale is small compared to the actual cover, the study reported in the chapter yielded important and useful information for the adaptation of this novel thermographic technique to determine the extent of scum accumulation under the large HDPE floating cover at the WTP. In the experiment reported in this chapter, the actual HDPE cover material is used. The solid scum is simulated using solid matter (i.e., clayey soil) as this was reported to have similar thermal properties to the solid scum at WTP. The HDPE cover was laid over the simulated scum (i.e., a block of clayey soil). The details of the materials in this thesis are shown in the Table 4.1 below.

Table 4.1 Summary of material properties in the experiment

Material	Density (kg/m ³)	Thermal conductivity (W/m*K)	Specific heat (J/kg*K)	Thermal diffusivity (mm ² /s)
HDPE geomembrane	940 [240]	0.44[240]	1900[240]	0.246
Air (at 20 °C)	1.2754	0.138	1000	19
Water (at 20 °C)	997	0.6	4184	0.144
Soil	1350 [242]	0.47 [243]	1900 [244]	0.183
Scum	913 [245]	0.5 [246]	1400 [247]	0.391

The outdoor test facility allowed for investigations into the appropriateness of the different timescales associated with the varying solar radiation for determining the presence and the extent of simulated solid scum under the cover material. It was found that the thermal transients during daybreak and nightfall can be used to determine the existence and accumulation of the clayey soil block under the HDPE geomembranes.

Part of the content of this section appears as, Ma, Y., Wong, L., Vien, B. S., Kuen, T., Kodikara, J., & Chiu, W. K. (2020). Quasi-Active Thermal Imaging of Large Floating Covers Using Ambient Solar Energy. *Remote Sensing*, 12(20), 3455.

4.2.2 Quasi-Active thermographic method

4.2.2.1 Preliminary concept of quasi-active thermography

Infrared thermography is a well-developed non-contact inspection technique that has been successfully implemented in the field of structural health monitoring, especially for concrete buildings, bridges, rail infrastructure and aircraft structures. These infrared thermal cameras can be located more than 20 m away from the object to be inspected or monitored. Thermography measures the temperature distribution of an object by detecting the infrared energy emitted over an area. It uses differences in temperature to identify the flaws (i.e., cracks, stress concentration area and substance or damage beneath the surface) in the object. In addition, thermal imaging has recently been widely applied in evaluating the structural health condition of composite structures [4–6] and polymers [7–11].

The challenges posed by the sheer size of the cover makes conventional thermography impractical, and the flammable biogas generated in the sewage under the covers precludes the use of any powered equipment in the vicinity of the floating cover. In addition, safe work practices dictate any equipment used near the covers is to be intrinsically safe, and no heat or ignition source is to be within a horizontal or vertical distance of 20 m of the anaerobic lagoons. For active thermography, traditional heating methods such as halogen lamps, hot air guns or ultrasonics are both unsuitable and impracticable as they cannot heat such a large region uniformly and simultaneously. Similarly, conventional passive thermography is not applicable since the defects or variation in the covers themselves do not cause or result in localized heating or cooling. Moreover, identifying solid matter under the cover is not the same as identifying defects within the cover material—both are useful to know, but they are very different things that require quite different intervention actions at WTP. Therefore, a more practical thermography method is needed that uses a naturally occurring heat stimulus

that impinges on the surface of the cover to assess the structural integrity of these large membrane-like floating covers. As a variation to passive thermography, the naturally occurring heat stimulus (i.e., solar radiation) is measured, and the associated timescale is acquired and utilized in the analyses of the results. In the proposed experimental inspection method, it was found that the transient geomembrane temperature variations due to daily solar intensity cycles will facilitate the detection of solid matter in contact with the underside of the cover material. In the daytime, solar radiation from the sun's emissions continuously heats the membrane, and this is similar to the heat up process in classic active thermography. Then in the afternoon, as the solar intensity at the surface of the cover decreases with the setting of the sun, the membrane cools down by convection heat transfer, and a transient temperature decay event begins on the membrane. This process lasts for the whole night until the solar intensity increases again from zero at sunrise, and the transient cooling event ends at this point. The proposed method uses naturally occurring heat from the environment, and no heating or cooling system is deployed during the experiment. In addition, the heat power and the way of heating are not controlled, and the heat period is much longer than traditional active thermography. The input heat will not be withdrawn during the monitoring (solar radiation still exists when the radiation power is reduced during the cooling). Given that this thermal imaging method does not monitor the self-heating objects and used external heat as a stimulus, this proposed thermal imaging method is termed quasi-active thermography.

In this chapter, long-duration thermal imaging experiments were conducted at an outdoor test facility at Monash University. The aim was to determine the measurement parameters to detect the existence and the accumulation of solid matter under the cover material that replicates the scum at WTP. A clayey soil was used in experiments, as this was easier, cleaner and safer to manipulate in an experimental set-up. The main aim of these laboratory-scale tests was to establish the appropriate measurement principles and the associated analyses settings required to quantify the extent of the solid matter covered by the geomembranes. The clayey soils are known to have similar thermal conductivity [24,25], specific heat capacity [26,27] and density [28,29] with the scum, and the scum is difficult to obtain without lifting a section of the cover. The transient events generated by the time-varying solar radiation were captured by the pyranometer, which was used to record the solar intensity and define the start points and the end points of these transients. The HDPE geomembranes that were laid over the clayey soil were exposed to the sun for several days.

The temperature profiles of the geomembranes recorded by the thermal camera were analyzed in conjunction with the solar radiation data.

4.2.2.2 Newton's cooling law for quasi-active thermography

In this chapter, Newton's law of cooling is used to identify where the underside of the HDPE geomembrane material is in contact with the clayey soil as simulated solid scum. This is intended to be analogous to the situation at WTP where the sections of the floating covers in contact with the scum are expected to have a different temperature change rate to the geomembranes in contact with liquid sewage or biogas. Given the temperature gradients between the scum regions and regions not in contact with the scum are constantly responding to the changing solar intensity, it will be difficult to use a single frame of a thermal image to identify the regions of the cover in contact with the scum by just using the temperature contrast. Therefore, the proposed quasi-active thermography uses the different thermal transients acquired to identify the regions of HDPE geomembranes sample that is in contact with clayey soil. The pyranometer provides important information to facilitate the determination and acquisition of appropriate transients over a defined time period during which a sizeable transient can be used to direct the acquisition of useful data to determine the existence and quantify the size of clayey soil under the cover. These thermal transients will be analyzed using the temperature data contained in the acquired thermal image sequences. The transient curves are smoothed and fitted in Newton's law of cooling, and the resultant values of cooling constants k are plotted in a map. Then, parts of the geomembrane in contact with sub-surface objects will appear in strong contrast to the parts without sub-surface objects.

4.2.3 Proof of concept (quasi-active thermography)

4.2.3.1 Experiment setup

A 2 mm thick sheet of HDPE geomembrane (provided by Melbourne Water Corporation) was cut into a size of 1.1 m by 0.8 m and fitted to the frame of a test container, as shown in Figure 4.1. The membrane specimen is the same material used to cover the first part of the anaerobic lagoons at WTP. The emissivity spectrum of the HDPE geomembrane was tested using Fourier-transform infrared (FTIR) spectroscopy in the laboratory. Several pieces of HDPE geomembrane samples in WTP were tested.

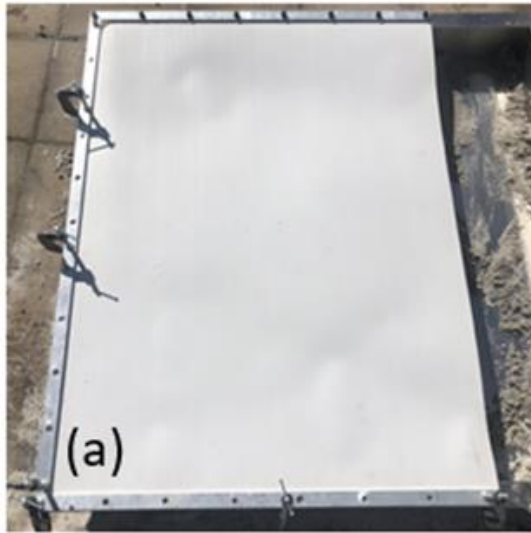


Figure 4.1 A high-density polyethylene (HDPE) geomembrane specimen was clamped on the aluminium container

A solid block of clayey soil with an area of 0.15 m by 0.15 m was compacted in 0.1 m deep rectangular aluminum containers (1.1 m by 1.1 m), as shown in Figure 4.2, and was used to simulate the scum at WTP. The prepared HDPE sheet was then clamped onto the aluminum container (see Figure 4.1) with the underside of the center portion of the HDPE geomembrane resting on the top surface of the clayey soil. The entire set-up was then moved to an open, outdoor area on a cloudless day. A long-wavelength infrared thermal camera, FLIR A615 (manufactured by FLIR Systems, Inc. Wilsonville, Oregon, U.S), with a resolution of 640 by 480 [31] was set up to record the surface temperature of the cover. The temperature measured by the thermal camera was verified by a thermal couple in the laboratory, and the difference is within $\pm 0.01^{\circ}\text{C}$, which is within the temperature sensitivity of the thermal camera. The solar intensity at the test site was measured using an Apogee SP-110 pyranometer (manufactured by Apogee Instruments, Inc. Logan, U.S) [32]. Figures 4.3 (a) and (b) show the long-wavelength infrared thermal camera FLIR A615 and the Apogee SP-110 pyranometer, respectively. The schematic diagram of the experimental setup is shown in Figure 4.4. The start and end points of transient events are shown in 24-hour format. The experiment was conducted in winter, in which the reliability of the quasi-active thermography can be verified with a low level of solar radiation (stimulus). The experiment ran overnight, starting from 13:01:13 on the first day until 14:14:33 on the second day. Both thermal camera and pyranometer were collecting the data at a sampling rate of 3 Hz.

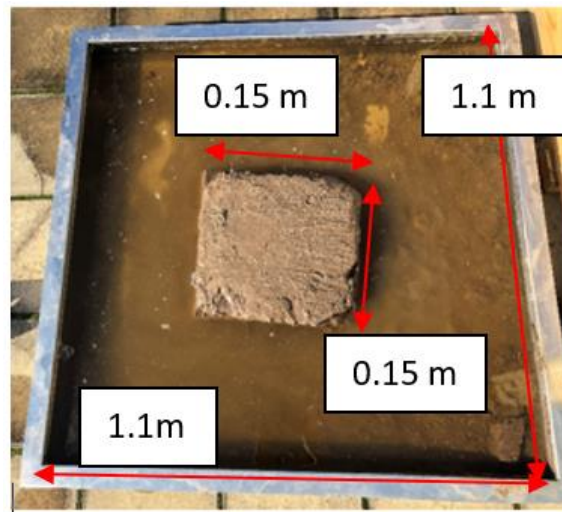


Figure 4.2 A clayey soil block in a 0.1 m deep rectangular aluminium container was used to simulate the scum at WTP.



(a)



(b)

Figure 4.3 (a) FLIR A615 thermal camera and (b) Apogee SP-110 pyranometer.

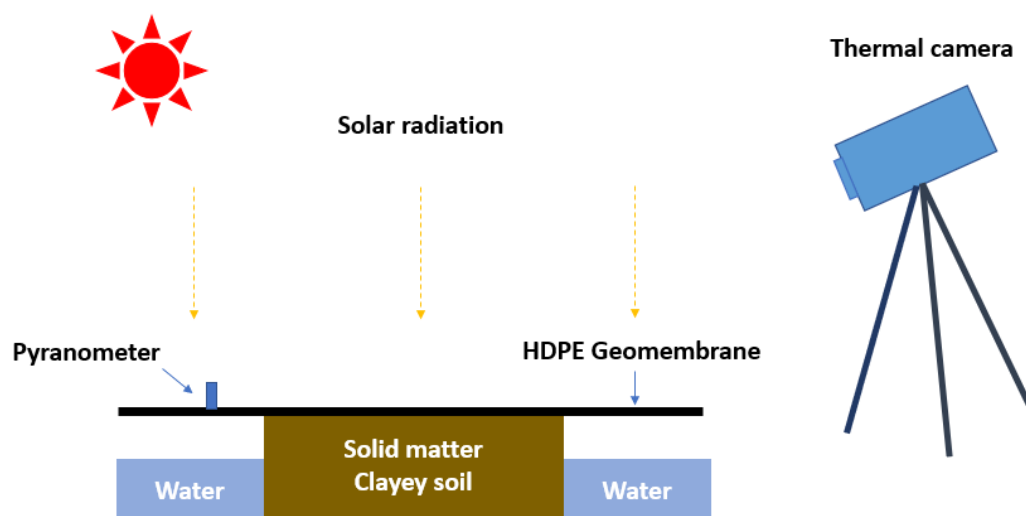


Figure 4.4 Schematic drawing of the experimental set-up.

4.2.3.2 Cooling constant estimation using Newton's law of cooling

One transient cooling event is expected to commence during the experiment in the afternoon. Since the location of the under-surface soil is known, two points on the HDPE geomembrane were chosen for comparison, one was selected at the point where the geomembrane is in contact with the block of clayey soil, and another point was selected at a point away from where the simulated scum under the geomembrane. The temperature information at both points was extracted from all the obtained thermal images (during the experiment) and plotted in Figure 4.5. Different points in the same region will have slightly different temperatures, but this will not affect the cooling process. The solar intensity data obtained from the pyranometer is also shown in this figure. The reduction in the solar intensity shown in the figure is recorded as the afternoon progresses. As hypothesized, the thermal response at the regions of the HDPE that is in contact with the soil and those in contact with the air are not markedly different.

Since the solar intensity is not constant and the pyranometer has a $\pm 1\%$ accuracy, there are some noises in the measured data. During the night, the measured solar intensity should be zero without the sunlight input. Therefore, the solar intensity after sunset was regarded as 0.

It is noted that on the first day, the temperature of the HDPE region that is not in contact with the clayey soil started to decrease at 13:01:13, see Figure 4.5. Similar results were also measured on the second day (after 14:04:33). These points mark the starting point of the commencement of the transient cooling event.

For the points on HDPE in contact with the block of soil, due to the thermal conduction between the soil and the geomembrane, the thermal response is markedly different from the point on the HDPE that is not in contact with the soil. The thermal transient at the point on the HDPE in contact with the soil commenced at 14:46:13. It appeared at 15:37:53 on the second day. The transient events of both points ended at 08:21:13 on the morning of the second day when the solar intensity increased, and the geomembrane became warmer.

It can be seen in Figure 4.5 that the rates of temperature decay at the two selected points are quite different (black point on the HDPE that is in contact with the block of soil and green point on the HDPE that is not in contact with the soil). Figure 4.5 shows that the temperature at the measured point away from the soil (green line) responded rapidly with the reduction in solar intensity, whereas the thermal transient differs markedly at the measured point

directly above where the compacted block of soil. This phenomenon can be due to two reasons:

The soil has a higher heat capacity than air ($C_{p,air}$ is $1.005 [33] \text{ J}\cdot\text{g}^{-1}\cdot^{\circ}\text{C}^{-1}$ and $C_{p,soil}$ is $2.25 \text{ J}\cdot\text{g}^{-1}\cdot^{\circ}\text{C}^{-1} [34]$). A block of soil can store more heat than air and the temperature of the soil is more stable in cooling, resulting in a slower cooling rate at the soil-cover interface region. The HDPE cover can absorb the heat radiated by the block of soil and air, and a portion of the absorbed heat can be re-emitted back to the soil and the air. The cover material acts like a reflective layer that partially reflects the heat to the soil and air (absorb from soil and air and re-emitted back to soil and air). The thermal wave reflection coefficient [18] of the air interface and soil interface is different, leading to the efficiency of heat exchange difference between the air/geomembrane medium and the soil/geomembrane medium.

These are the principles of interest for this experiment, which can be used to identify and evaluate the extent of the scum underneath the cover (i.e., at the lagoons at the WTP).

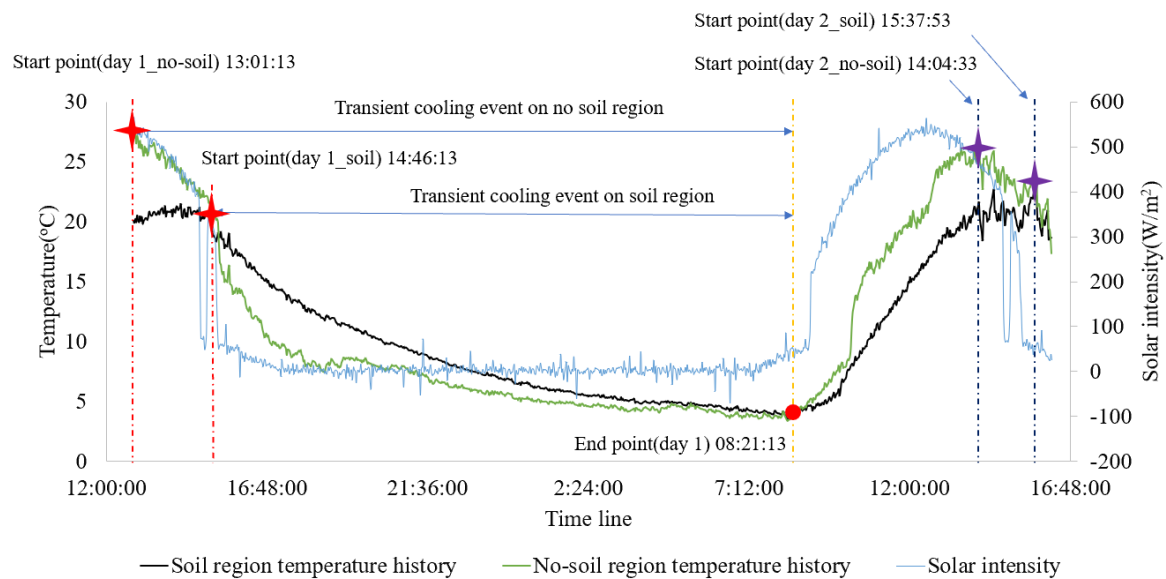


Figure 4.5 Temperature profile of geomembrane and solar intensity history.

Newton's law of cooling is used to define the rate of cooling during the thermal transient. The temperature histories during the transient cooling events for both selected points were fitted with Newton's cooling law using the curving fitting tool in MATLAB. It is noted here in the experiment, the ambient temperature T_a varied with time. While in the curve fitting, the value of T_a was set as the final temperature of the transient event (4.3°C) and kept as a constant value over the whole event. This is because the cooling constant is proportional to

the temperature difference between the ambient conditions and the geomembrane. Varied ambient temperature will make the cooling constant change over time, and the cooling constant will not be consistent in the curve fitting if the ambient temperature changes. Therefore, the curve fitting with Newton's cooling law assumed that the geomembrane is cooling at a constant ambient temperature, and the resultant efficient cooling constant k can be consistent over the whole event. Given that the temperature of the geomembrane changes quite slowly at the end of the event, it was assumed that the geomembrane achieves ambient temperature at this point, and the ambient temperature was set as the value at this point.

Figure 4.6 shows the fitted plots for the point away from the block of soil and at the location of the soil, respectively. Table 4.2 shows the properties of curve fit (R-squared and root mean square error) and estimated cooling constant, k . The result shows that the cooling constant of the no-soil region $k_{\text{no-soil}}$ is 0.00925, and the cooling constant of the soil region k_{soil} is 0.00484. The lower value of the cooling constant of the cover in the region over the soil suggests that the temperature of the geomembrane at this region will decrease slower than that at the region not in contact with the soil. This is due to the conductive heat exchange between the HDPE sheet and the soil. The goodness of curve fitting, in the region over the soil gave an R-squared value of 0.9748, which means 97.48% of the temperature data comply with the model of Newton's cooling law. Furthermore, the RMSE for the region not in contact with the soil region is 0.8675. The R-squared and the RMSE for the soil region also presented a reasonable goodness of curve fitting. Both indexes indicate that the cooling of the HDPE cover in the experiment agrees with Newton's law of cooling.

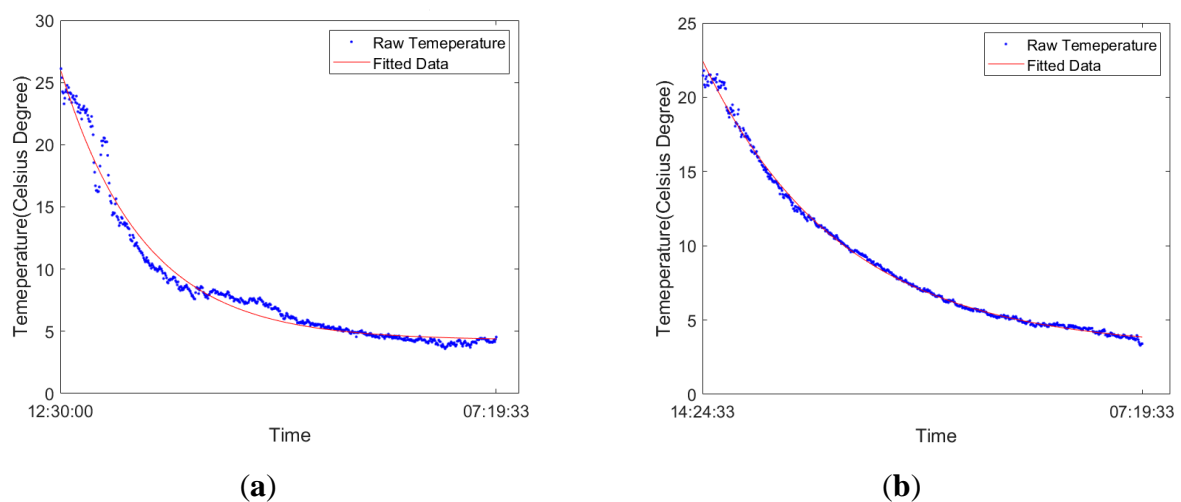


Figure 4.6 (a) curve fitting of the temperature decay curve of the no-soil region on the geomembrane and (b) curve fitting of the temperature decay curve of the soil region on the geomembrane.

Table 4.2 Details of transient event for each region on the membrane.

Region	Highest temperature(°C)	Lowest temperature(°C)	Fitted Cooling constant, k	R-squared	RMSE
No-soil region	26.1	4.3	0.00925	0.9748	0.8675
Soil region	22.5	4.3	0.00484	0.9973	0.2608

To demonstrate the advantage of this proposed technique, the cooling constant over the entire HDPE sheet is calculated using one transient cooling event. For comparison purposes, the optical image taken of the HDPE material with soil underneath is plotted together with the thermal image at one instant and the resultant cooling constant mapping in Figure 4.7 (a–c), respectively. Figure 4.7 (a) was taken using an optical camera and shows the location of the hidden soil (underneath the cover). Figure 4.7 (b) shows the raw thermal image taken at an instant (single frame) by the thermal camera during the transient event, a thermal contrast can be seen on the thermal image, however, the difference in temperature between the soil region and no-soil region is small (approximately 4 °C at this instant). As shown in Figure 4.5, the temperature contrast between the regions with and without the soil changes with the time in a day. The thermal contrast also depends heavily on which frame was chosen for analysis. Moreover, the condition of the cover (i.e., dirt, fold line and view angle) can also affect the accuracy of the temperature measurement.

Figure 4.7 (c) shows a map (640×480 resolution) of cooling constants calculated using Newton’s law of cooling. The cooling constant at the region over the soil was determined to be within 0.005 and 0.007 (with a higher value around the soil edges). For better identification of the soil, a colour threshold was set to show only the range between 0.005 and 0.007, and the rest was red for Figure 4.7 (c). The reason to set up this filter is to show the profile of under-cover soil and to eliminate the influence of noisy data. The profile of the soil under the cover can then easily be identified and outline as shown in Figure 4.7 (c), and the cooling constant gradient region of the soil is a result of the rough surface of soil and the uneven contact between itself and the cover. The results show a good agreement between the geometry of the actual block of soil with that estimated from the thermal images. This experiment shows that the night period provides enough time for the quasi-active thermography to determine the presence of the soil under the membrane and to facilitate the

estimation of the extent of the soil under the membrane. Thus, the proposed quasi-active thermography method is shown to be able to identify the presence and extent of the under-surface soil.

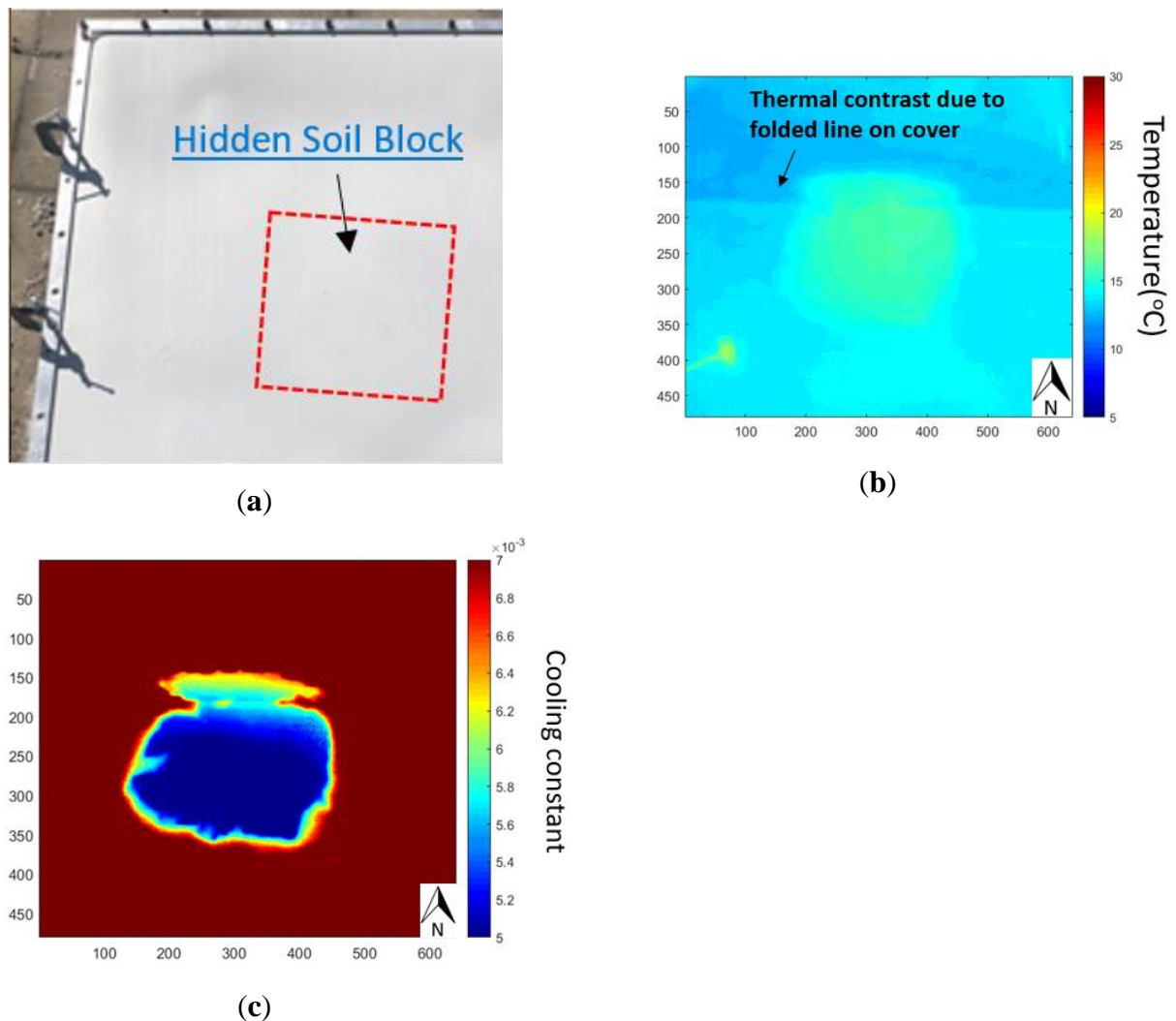


Figure 4.7 Comparison of profiles of soil under HDPE geomembrane: (a) optical photography. (b) raw thermal image was taken during the experiment. (c) map of cooling constant derived from Newton's cooling law.

4.2.3.3 Verification of the consistency of the quasi-active thermography

In traditional active thermography inspections, the length of heat up and cool down periods can be controlled, and the input power of heat can also be adjusted. However, in long timescale quasi-active thermography, the length of transient events is determined by the solar intensity. In addition, each transient event is non-repeatable since the daily time from the sunset to the sunrise is different and temperature profiles will also vary from day to day and from season to season. This can lead to a difference in the cooling period of the cover

during each transient cycle. The results presented in this section is used to verify the measurement consistency of the quasi-active thermography test. A continuous two-day experiment was conducted, and the maps of cooling constants in two transient cooling events were compared to test the consistency of the results. An irregular shape of soil was placed under the HDPE sheet. The same experimental set-up (see Figure 4.4) was used, and the temperature profile of the top surface of the cover and the solar intensity history were monitored using FLIR A615 thermal camera and pyranometer, respectively. Figure 4.8 shows the solar intensity profile over two days with temperature history at two selected points on the cover (red line: Point at the soil region and green line: Point away from soil region). Two transient cooling events are also labelled in Figure 4.8, and the important information of each event are listed in Table 4.3. Again, Newton's law of cooling is used to fit into the transient cooling events for both events at both points, and the results are plotted in Figure 4.9 (a–d). The estimated cooling constants with R-squared and RMSE of these four curves are reported in Table 4.4.

It can be observed from Table 4.4 that the cooling constants on each region on the second day were higher than those on the first day. This is due to the fact that the length of transient events on day two was shorter than on day one, and the initial temperatures of the geomembrane on day two is higher than on day one. This indicates a faster cooling process on day two, resulting in a higher value of cooling constant for the geomembrane. In addition, the cooling constant for the region of the material over the soil is smaller than that for a no-soil region, and this agrees with the result in Section 4.2.3.2. These measurements differences could be due to (1) differences in environment condition (solar intensity, wind speed and ambient air temperature) in each day which affected the heat transfer coefficients, (2) difference in initial temperatures of the cover in each transient cooling event and (3) different condition of contact between the soil and the HDPE material. However, the contrasts of cooling constants between the soil region and the no-soil region are still significant enough to identify the extent of the under-cover soil. Therefore, it can be concluded that the cooling constant in each transient event is different due to the non-repeatable surrounding conditions. Hence, the values of the cooling constant should be normalized in each experiment.

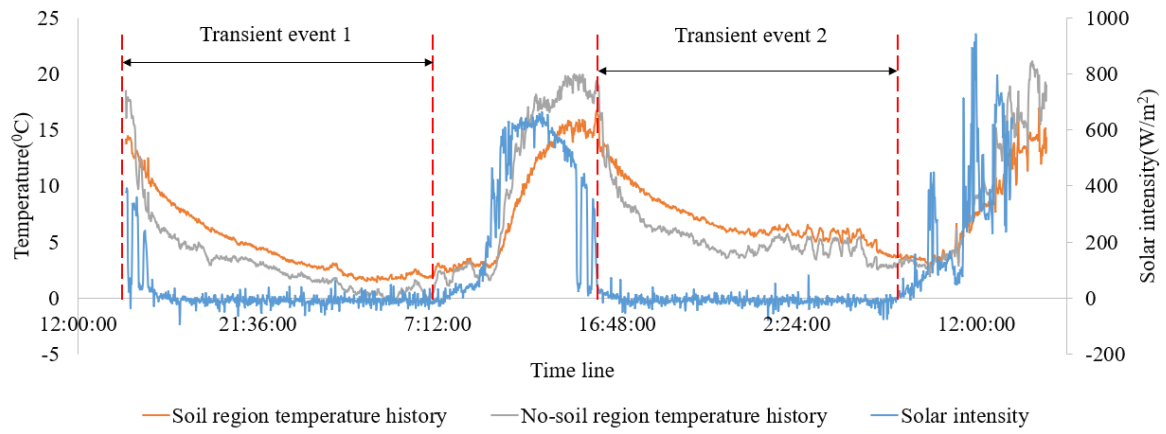
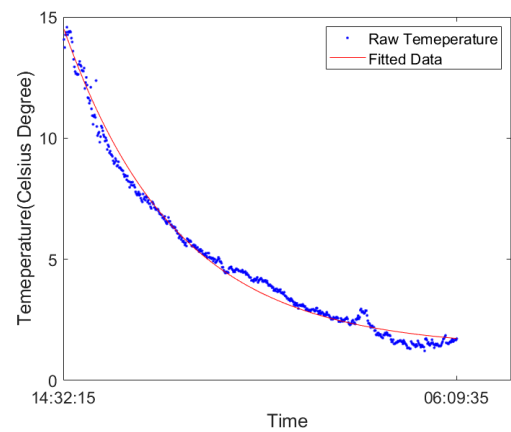
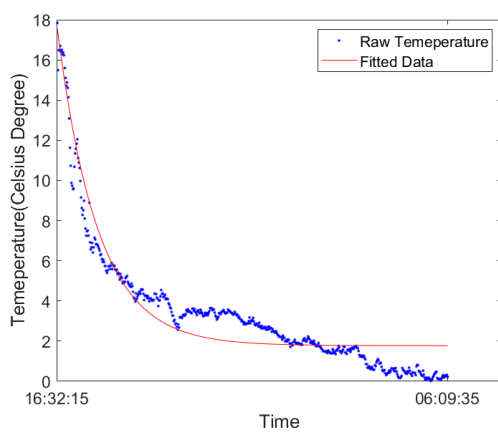


Table 4.3 Curve fitting details of example pixels in each day.

Region		Transient events start points	Transient events end points	Initial geomembrane temperatures (°C)	Final Geomembrane temperatures (°C)
No-soil region	Day 1	16:32:15	07:07:55	17.84	0.31
	Day 2	16:14:35	06:30:17	19.29	3.57
Soil region	Day 1	16:32:15	07:07:55	13.72	1.60
	Day 2	16:14:15	06:30:17	16.41	2.81



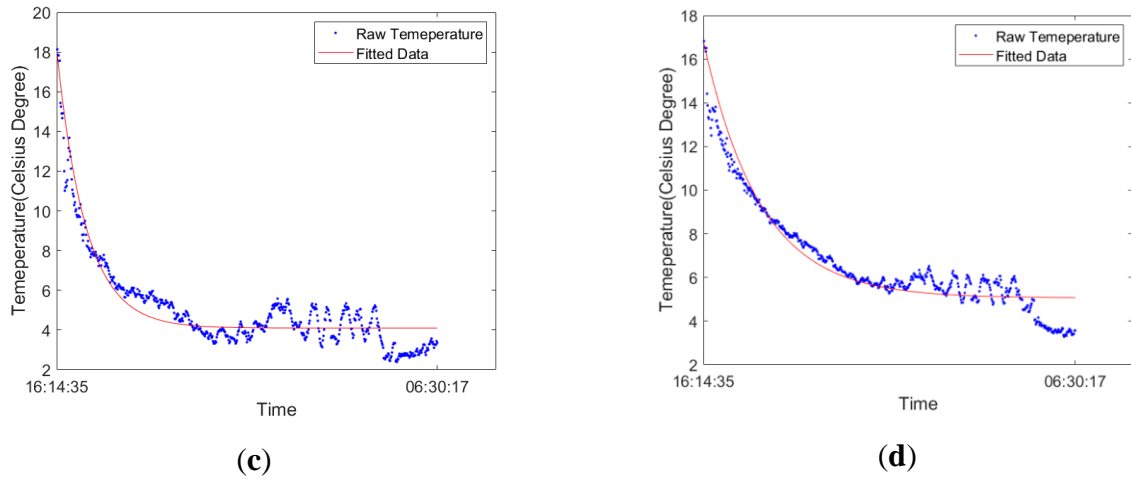


Figure 4.9 Curve fittings of pixels over two days. (a) pixel example on the no-soil region on day 1. (b) pixel example on the soil region in day 1. (c) pixel example on the no-soil region on day 2. (d) pixel example on the soil region on day 2.

Table 4.4 Curve fitting details of example pixels in each day.

Day	Region	Fitted	R-squared	RMSE
		Cooling constants		
1	No-Soil region	0.01813	0.9004	0.9871
1	Soil region	0.00763	0.9888	0.3534
2	No-soil region	0.02163	0.8851	0.8283
2	Soil region	0.01081	0.9104	0.7507

The maps of cooling constants of the membrane over two days were plotted and are shown in Figure 4.10. The resolution of the image in this experiment is 480 by 420 pixels (i.e., 201,600 pixels). To validate the measurement consistency, a normalization study was conducted to make the threshold of defining the with-soil region the same in two days experiment. The histograms of values of cooling constant are shown in Figure 4.11 and it can be observed that the values approximate the normal distribution. The cooling constant plot shown in Figure 4.11 is scaled with respect to the peak value shown in Figure 4.11. The cooling constants maps in Figure 4.10 were divided by the background spans (0.01262 on day one, 0.01512 on day two), and the normalized maps are plotted in Figure 4.12. The upper limit of the threshold is set as 1 given that the cooling constant at the region over the soil region is always lower than the background. It can be observed that the normalized cooling

constant of the soil region is roughly lower than 0.65. A statistical study of the threshold to determine soil region in the cooling constant map was conducted with a 0.05 step change in the up limits of the normalized cooling constant. Table 4.5 shows the comparison of the area of soil region in two days experiment. 2.94% mean difference indicates that the quasi-active thermography in two days experiment has a good measurement consistency. This indicates that although cooling constant values change in different transient events, the k_{soil} and $k_{\text{no-soil}}$ will change proportionally, and the results are consistent after normalization. For comparison, the mean soil region areas from the statistical analysis were extracted in MATLAB code, and the contrast in Figure 4.13 shows the difference of measurement. Nevertheless, in each measurement, the proportional contrast in cooling constant between the cover with and no-soil beneath the cover material can still be differentiated easily and can be used to define and outline the soil profile in contact with the cover. This experiment again provides evidence of the consistency of quasi-active thermography measurements with different ambient temperature profiles and lengths of transient events.

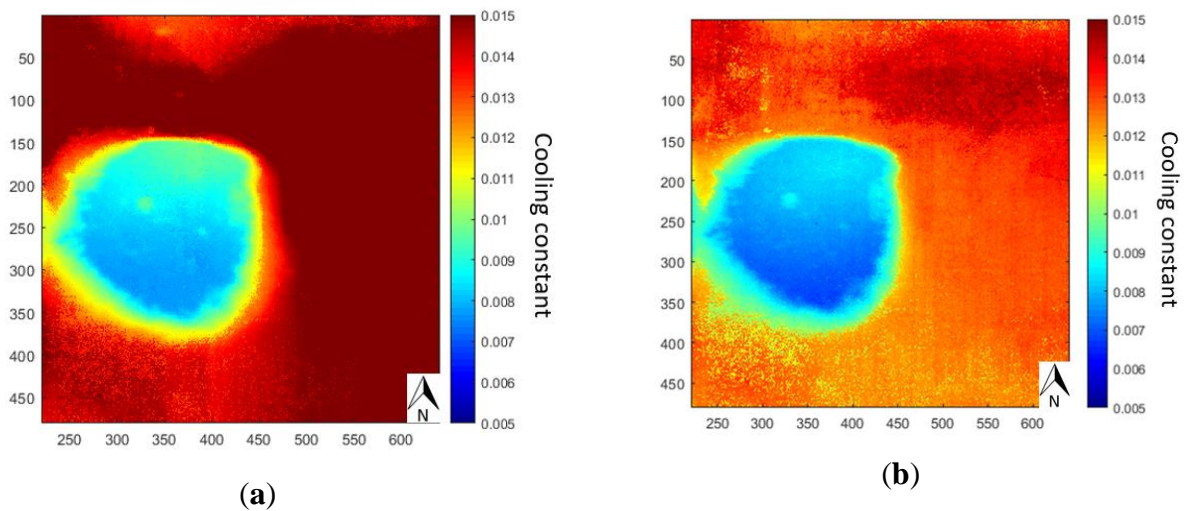


Figure 4.10 Processed cooling constant maps over two days. (a) cooling constant map on day 1. (b) cooling constant map on day 2.

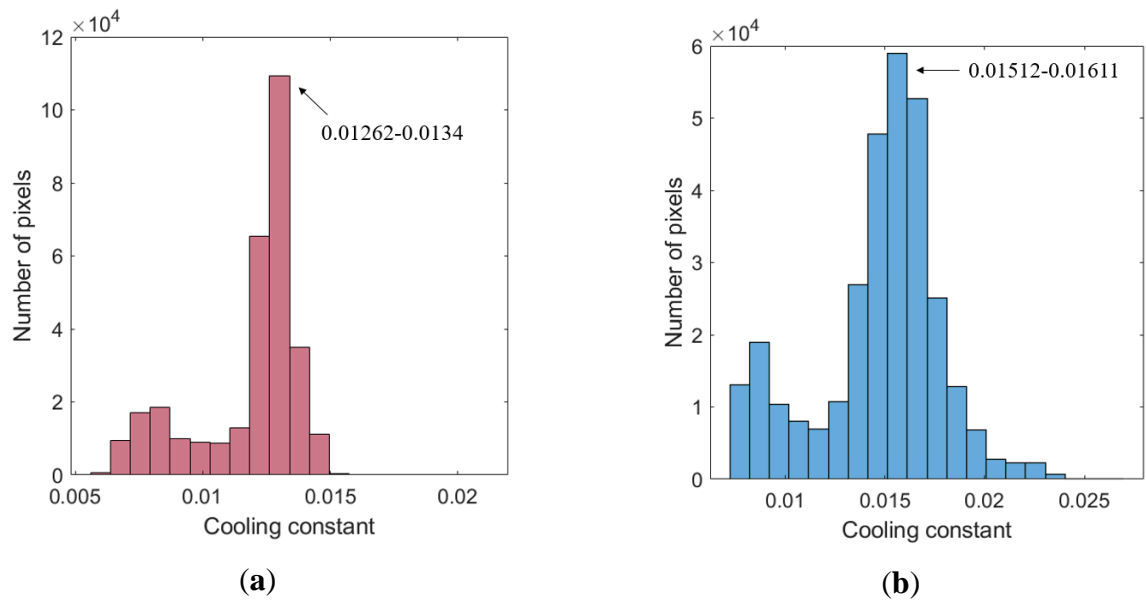


Figure 4.11 Cooling constant distribution in cooling constant maps of the two days experiment. (a) day 1. (b) day 2.

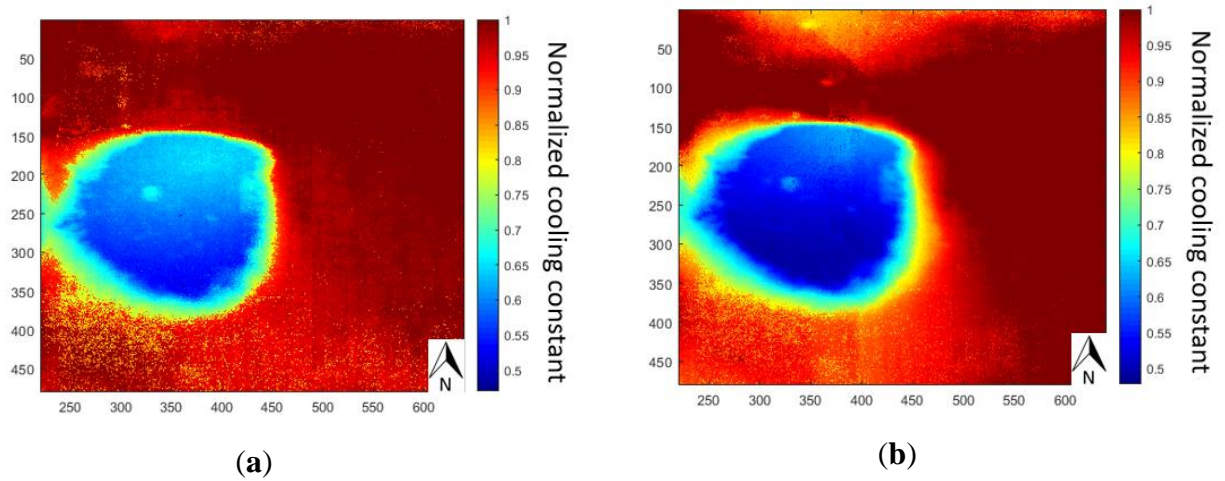


Figure 4.12 Normalized cooling constant maps of two days experiment. (a) cooling constant map on day 1. (b) cooling constant map on day 2.

Table 4.5 A statistical study of the effects of cooling constant map threshold on the detected soil region.

Threshold	Geomembrane condition (%)					
	Soil region			No-soil region		
	Day 1	Day 2	Difference	Day 1	Day 2	Difference
0–0.75	27.13	29.09	1.96	72.87	70.91	1.96
0–0.7	24.03	25.14	1.11	75.97	74.86	1.11
0–0.65	20.97	20.71	0.26	79.03	79.29	0.26
0–0.6	17.17	11.99	5.18	82.83	88.01	5.18

0–0.55	11.21	5.00	6.21	88.79	95.00	6.21
Mean	20.10	18.39	2.94	79.90	81.61	2.94
Standard deviation	5.54	8.78	2.33	5.54	8.78	2.33

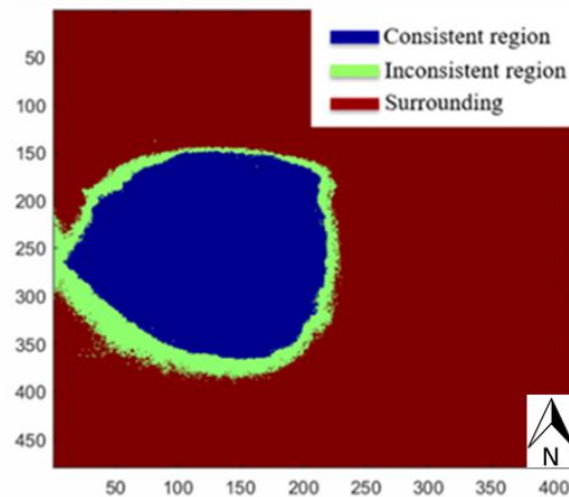


Figure 4.13 Soil profile measurement difference in two days monitoring.

4.2.4 Monitoring of accumulation of soil build-up under the geomembrane

In Section 4.2.2.3, the quasi-active thermography monitoring has successfully demonstrated its reliability, repeatability, and capability to identify and locate the soil underneath the cover material. In this section, quasi-active thermography monitoring is further examined to monitor the development (growth) of soil experimentally to simulate the expansion of the area of scum under the HDPE covers on the anaerobic lagoons. To accomplish the aim, the same experimental setup, as described in Chapter 3, is used. A multiple-day quasi-active thermography experiment was conducted with more compacted soil added to the aluminium container each day (i.e., to simulate the growth in the extent of the scum at WTP).

On the first day of the experiment, a soil block (approximately 10 kg) was compacted in a corner in an aluminium container. The prepared HDPE sheet was then covered over the aluminium container. Both the infrared thermal camera and pyranometer were set up to collect data at 3 Hz starting at 12:00:00. The second day at noon, the HDPE cover was first removed, and an additional 20 kg of soil was then compacted around the existing soil to simulate the buildup of scum. The recordings were resumed after replacing the HDPE cover. The same simulated growth of the soil was repeated on the third day of the experiment by

adding approximately 40 kg of garden soil. The overall recording of data ended at 9:30 AM on the fourth day.

The temperature history at a selected point (away from the soil region) on the membrane and the local solar intensity history are plotted in Figure 4.14. The solar intensity history shows more fluctuation in signal in the first two days during the daytime, this is indicating that these days were relatively cloudy. Whilst the solar intensity on the third day changed smoothly, showing that this day was a relatively clear day with little cloud cover. Throughout the entire experiment, three transient cooling events were identified, and the period of each event is defined in Figure 4.14 and listed in Table 4.6. Each of the transient cooling events was again analyzed using Newton's law of cooling. Since the scale of the cooling constant is different each day, the scales of the cooling constant were normalized again from 0 to 1. The optical photos of the condition underneath the cover and their corresponding zoomed normalized maps of cooling constants for each day are shown in Figure 4.15 (a) and (b), respectively.

Figure 4.15(b) shows that the soil underneath the membrane can be identified and outlined using the cooling constant mapping obtained from the cover. In addition, the areas of the soil underneath the membrane were noted to have grown larger every day, which agrees with its geometrical profile as shown in Figure 4.15 (a). Although the HDPE cover was disturbed every day, the outcomes are still very promising for monitoring the development of the scum beneath the covers at WTP.

The newly proposed technique—quasi-active thermography has thus far shown its capability to identify, outline and monitor the growth of solid matter (i.e., a clayey soil) underneath the HDPE geomembrane material. The technique can potentially be extended to a field trial in the near future to determine the location and extent of semisolid and solid scum under the large floating covers at the WTP. The quasi-active thermography has been verified, examined and showed its potential application in this chapter. Further research can also be done by using the same proposed technique to evaluate the structural integrity of the large floating cover.

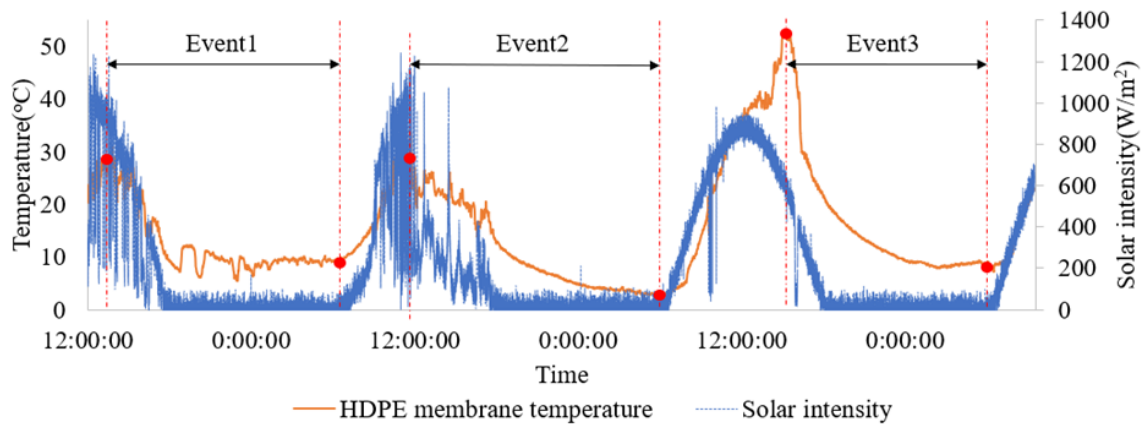
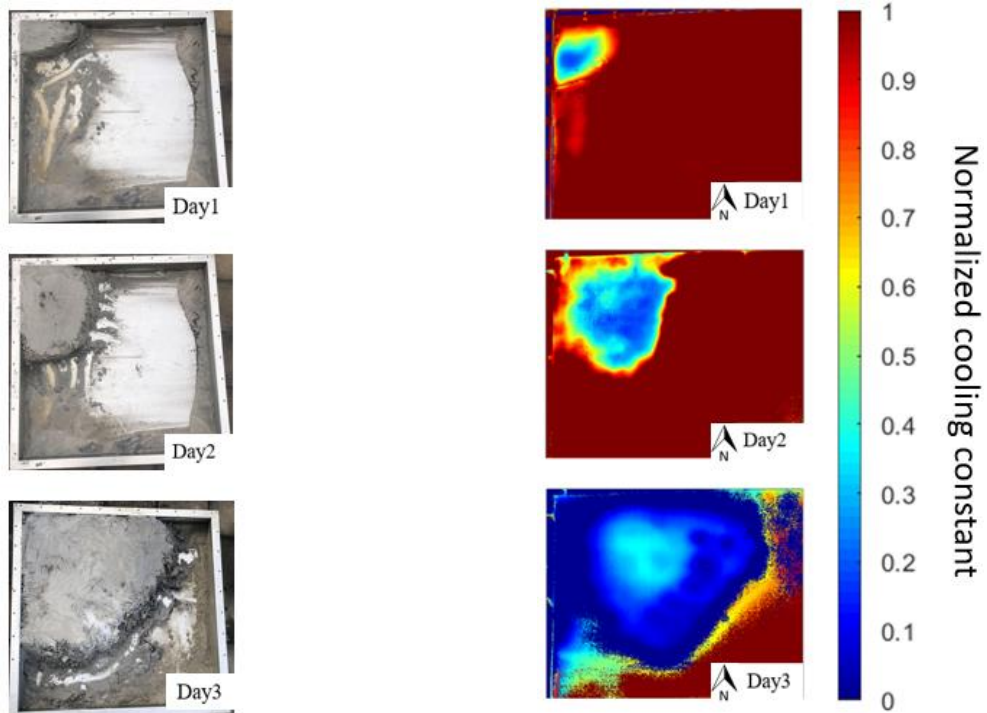


Figure 4.14 HDPE geomembrane temperature profile and solar intensity history in three-day quasi-active thermography experiment

Table 4.6 Details of daily transient events.

	Transient events start points	Transient events end points	Initial geomembrane temperatures (°C)	Final Geomembrane temperatures (°C)
Day 1	13:31:05	6:48:00	17.84	9.07
Day 2	11:59:33	6:30:17	19.29	2.97
Day 3	15:43:00	6:14:24	13.72	7.23



(a)

(b)

Figure 4.15 Comparison of photography and processed thermal images. (a) soil composite profiles from photography. (b) zoomed soil composite profiles from processed thermal images.

4.3 Clustering-based Thermal Imaging Monitoring on Large Floating Covers using Ambient Weather Information

4.3.1 Introduction

The uncertainties of the substrate under the cover affect the structural integrity of the covers in many ways. In this section, some clustering-based image segmentation methods were introduced to distinguish different substrates under the geomembranes.

4.3.2 Thermal imaging method

4.3.2.1 Thermography monitoring on large structures

The quasi-active thermography experiment set up developed in Section 4.2 was adopted in the studies in this section. Given that there is a transient cycle for the ambient temperature and solar intensity, the temperature of the outside structures may rise from the morning with the absorption of the heat from the ambient and the solar radiation. In the evening, the temperature of the structure will fall with the emission of heat into the environment, and the withdraw of the heat from the solar radiation. Therefore, the temperature contrast between the anomaly region and surroundings may depend on the occasion of the inspection, and the temperature thresholds were decided empirically. This will lead to the inaccuracy and unreliability of the inspection. In the quasi-active thermography analysis, the temperature changing rate of the geomembrane was obtained by fitting the cooling curve of the geomembrane, and the anomaly region was identified by a different temperature cooling rate. This method is more accurate and reliable than a single shot of thermal imaging, but it requires the thermal camera to run over a whole day to get a condition map.

4.3.2.2 Newton's cooling law for comparison of cooling rate

When biogas or water contact with the subsurface of the geomembrane, heat is exchanged between the interfaces by the thermal convection, while the heat is exchanged by conduction when the geomembrane is in contact with the solids. The theoretical background of the heat transfer between interfaces were illustrated in Equations (2.13-2.15). if there is a mismatch of materials, the temperature of the surface of the material will be changed by the varied R , and the anomaly region can be registered in the thermal image by the temperature contrast.

Therefore, because of the efficiency of the heat transfer between different interfaces, the mismatch of the material at the interface and ways (conduction, convection) of heat transfer both affect the temperature changing rate on corresponding regions of the cover. Hence, in this chapter, given that biogas, sewage water and scums under the HDPE geomembrane provide different interfaces, different regions under floating covers can be identified by comparing the transient temperature changing rates, and the contrast of temperature changing rate from the thermal imaging can be used to classify different objects under the cover.

Given that temperatures of HDPE geomembrane floating covers and ambient temperature vary according to solar radiation power in a day, Newton's cooling law is used to identify scums, biogas, and sewage water under the cover comparing the k in a day. This method is more accurate than simply using the distribution of temperature as a guide to distinguish objects under the cover since it analyses the temperature response of geomembrane based on long-term transient temperature changes and does not focus on a single frame of the randomly selected thermal image. A map of the cooling constant will be generated to demonstrate the temperature changing rate over long-term transients. The corresponding regions with different objects under the cover can be registered by the cooling constant contrast.

4.3.3 Thermal imaging monitoring on the HDPE geomembrane

4.3.3.1 Investigation of the suitable thermal imaging monitoring period with ambient weather information

To validate the reliability of the technique, the experiment was carried out in the winter when the solar intensity and ambient temperature were low, with which the daily temperature variation of the geomembrane was small. As shown in Figure 4.16, the experiment started at 13:01:13 on the first day and ended at 14:14:33 on the third day. The temperature probe and the pyranometer continuously recorded the ambient weather information with the thermal camera monitored the daily temperature profile of the HDPE geomembrane. Given that the position and the area of the subsurface soil block were known, the temperature profiles of randomly selected points on the soil region and no-soil region are shown in Figure 16. Although temperature profiles of different points on the same region were slightly varied, transient temperature profiles of these points were assumed as similar because of similar thermal diffusions at the same interface. It can be observed that the temperature of the HDPE geomembrane changed with the ambient weather over the whole experiment. Temperatures

on both regions of the geomembrane started to cool off at 14:31:15 with the decreased solar intensity and ambient temperature. The temperature of the geomembrane kept going down in the afternoon and night until 07:07:55 in the morning on the second day, where the solar intensity increased from 0 with the ambient temperature also increased. Both the solar intensity and the ambient temperature increased in the morning, and the temperature of the geomembrane increased as well. A similar weather variation and transient geomembrane temperature cycle happened on the second day. While in the morning on the third day, the weather is cloudy (solar intensity fluctuated), but the overall solar intensity and the ambient temperature still increased, which led to an overall increased temperature profile of the geomembrane. Figure 4.16 reveals that: (1) the temperature of the geomembrane will respond according to the daily weather information such as solar intensity and ambient temperature, and the transient thermal response of the HDPE geomembrane will repeat every day despite that there is a variation of the values of temperature. (2) The temperature contrast between the soil region and the no-soil region varied at different times in a day, verifying that a single frame of the thermal image is not enough to find out the anomaly region for an outside structure. A randomly selected monitoring time can lead to an incorrect result. On the other hand, the temperature changing rate during the whole transient event is helpful to identify different interfaces under the geomembrane.

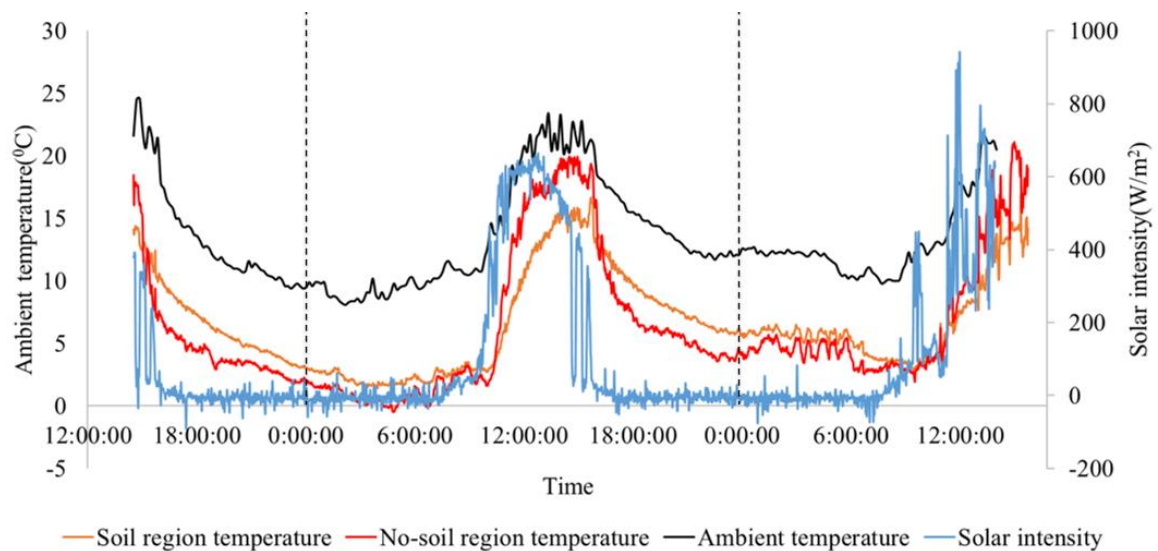


Figure 4.16 Recorded experiment data (solar intensity, ambient temperature and temperature profiles of a randomly selected point on soil region and a randomly selected point on the no-soil region on the geomembrane)

As mentioned above, a desirable monitoring period needs to be identified in a day to ensure the reliability of the thermal imaging monitoring and to assist in distinguishing different regions under the cover. The acquired thermal image sequences were collected from the

thermal camera. Given that the sampling rate of the thermal camera was set as 10s / frame, cooling constants were calculated every 10s. 10 sample points were randomly selected on the membrane (5 on the soil region and 5 on the no-soil region), and the absolute values of cooling constants k for these points over the whole experiment were calculated. To correlate the cooling constant k of the geomembrane with the weather information, the profile of the ambient temperature profile was plotted in Figure 4.17 (a) and the solar intensity was plotted in Figure 4.17(b). These two figures reveal those cooling constants of regions on the geomembrane were large during the daytime (period 1=13:01:13-14:11:15 in day 1, period 2= 07:07:55-17:11:15 in day 2, period 3 = 07:41:15-14:01:15 in day 3), where the solar intensity was not equal to 0. While after the sunset, where the solar intensity was equal to 0, the cooling constants of points on all regions were approximately equal to 0. This is because of the lack of heat stimulus during the night. Although the temperature of the geomembrane still cooling during the night (see Figure 4.16), the monitoring during the night is not helpful with the tiny difference of cooling constants between the soil region and the no-soil region. It is noted that ambient temperature will change according to the solar intensity as the environment received the heat from the sunlight, and the ambient temperature will be used to calculate the cooling constants. 4 regions were highlighted in Figure 4.17.

Cooling constants on soil regions and no-soil regions were averaged, and the mean values are shown in Figure 4.17. Several findings are summarised below:

- Cooling constants on both soil region and no-soil region were large during the daytime, and they increased significantly in the morning with the increase of the solar intensity. While cooling constants decreased at noon as the solar intensity remained stable at this time. After that, values of cooling constants increased again with the increased solar intensity changing rate.
- The contrast of cooling constants between the soil region and the no-soil region was around 0 when the solar intensity remained stable, and the contrast became significant when the solar intensity changed abruptly. Therefore, it is reliable to conduct thermal imaging monitoring at the high solar intensity changing rate period, and the contrast of cooling constant at different regions can help distinguish the interfaces at the underside of the geomembrane.

The cooling constant of the soil region remained stable in the daytime, which was the result of the thermal conduction from the underside of the geomembrane to the soil, where the heat

from the sunlight was stored in the soil. While the cooling constant on the no-soil region changed fast with the variation of solar intensity, the heat was stored in the geomembrane since the thermal convection between the underside of the geomembrane and the air was inefficient.

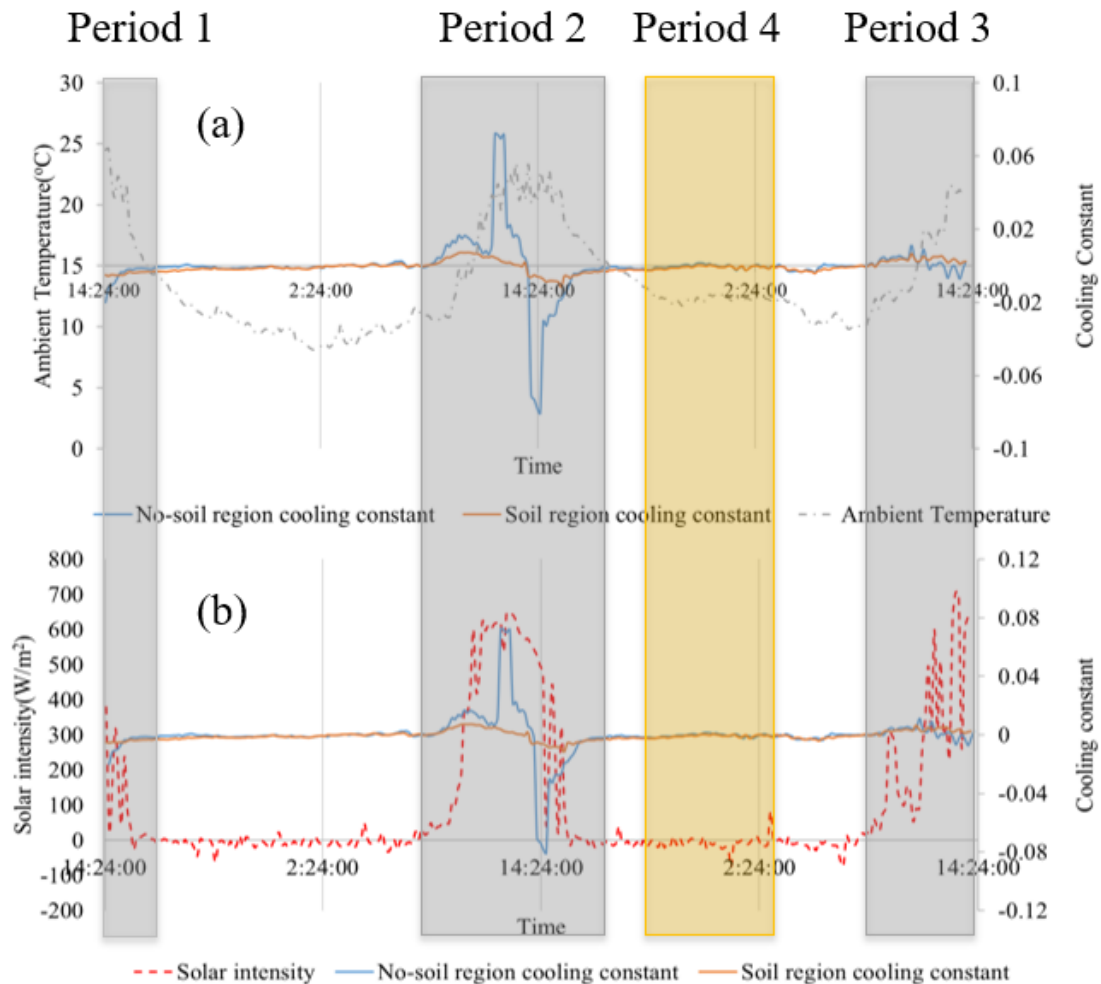


Figure 4.17 Illustration of cooling constants on soil region and no-soil region with solar intensity and ambient temperature change. (a) local ambient temperature history and cooling constant profiles. (b) local solar intensity history and cooling constant profiles

To identify the soil profile under the geomembrane, cooling constants were calculated from the thermal image sequences with Equation (3.3), and values of cooling constants were summed up to enlarge the contrast and uncover the soil regions. As shown in Figure 4.18, several cooling constant maps were generated for highlighted periods in Figure 4.17. Figure 4.18 (a-e) shows the cooling constant maps generated from summations of cooling constant over different periods. Figure 4.18(b-f) shows the cooling constant maps generated from averages of cooling constant over different periods. Figure 4.18 (a and f) were generated from the period 1 (13:01:13-14:11:15) in Figure 4.17; Figure 4.18 (b and g) were generated from the period 2 (07:07:55-17:11:15) in Figure 4.17; Figure 4.18 (c and h) were generated

from the period 3 (07:41:15-14:01:15) in Figure 4.17; Figure 4.18 (d and i) were generated from period 1, 2 and 3 in Figure 4.17 and Figure 4.18 (e and j) were generated from the period 4 (17:21:15-01:21:15) in Figure 4.17. Since cooling constant maps were generated with different thermal image sequences, scales of the maps were set individually for each map. Figure 4.18 (a-e) shows that an overall profile of soil was presented in the cooling constant map for period 1, but a small region of soil is blurred in the figure. In addition, the edge of the soil region is not clear and the contrast between the soil region and the no-soil region is small. Figure 4.18 (b and c) from periods 2 and 3 shows that the contrasts between regions become significant, and the edges of the soil regions are clearer. This is because these figures were calculated from larger amounts of thermal images, and the cooling constant values accumulate over time. In Figure 4.18(d), the profile of the soil region is most obvious with the thermal images from periods 1, 2 and 3 were calculated. However, Figure 4.18 (e) makes it difficult to recognize the soil regions from the background. Due to the small difference between the soil region and no-soil region in the low solar intensity changing rate period. The summation of the cooling constant can result in a blurred map which is not helpful to identify the interface under the geomembrane.

Regarding the averaged cooling constant map in Figure 4.18 (f-j), similar to the maps of summation of cooling constants, longer thermal image sequences will help identify the profile of soil regions, and the result of period 4 also does not help. While the overall profile of soil regions in averaged cooling constant maps is not clear as in maps of summation of cooling constants, this is because the contrast of averaged cooling constant map does not accumulate over time, and the sum of the difference of cooling constant values are larger than the averaged values. Hence, it can be summarized from this experiment that the thermal imaging monitoring under the stimulus of sunlight can identify the interfaces under the geomembrane with the aid of Newton's cooling law, and profiles of objects will be clearer with the increasing length of thermal imaging sequences.

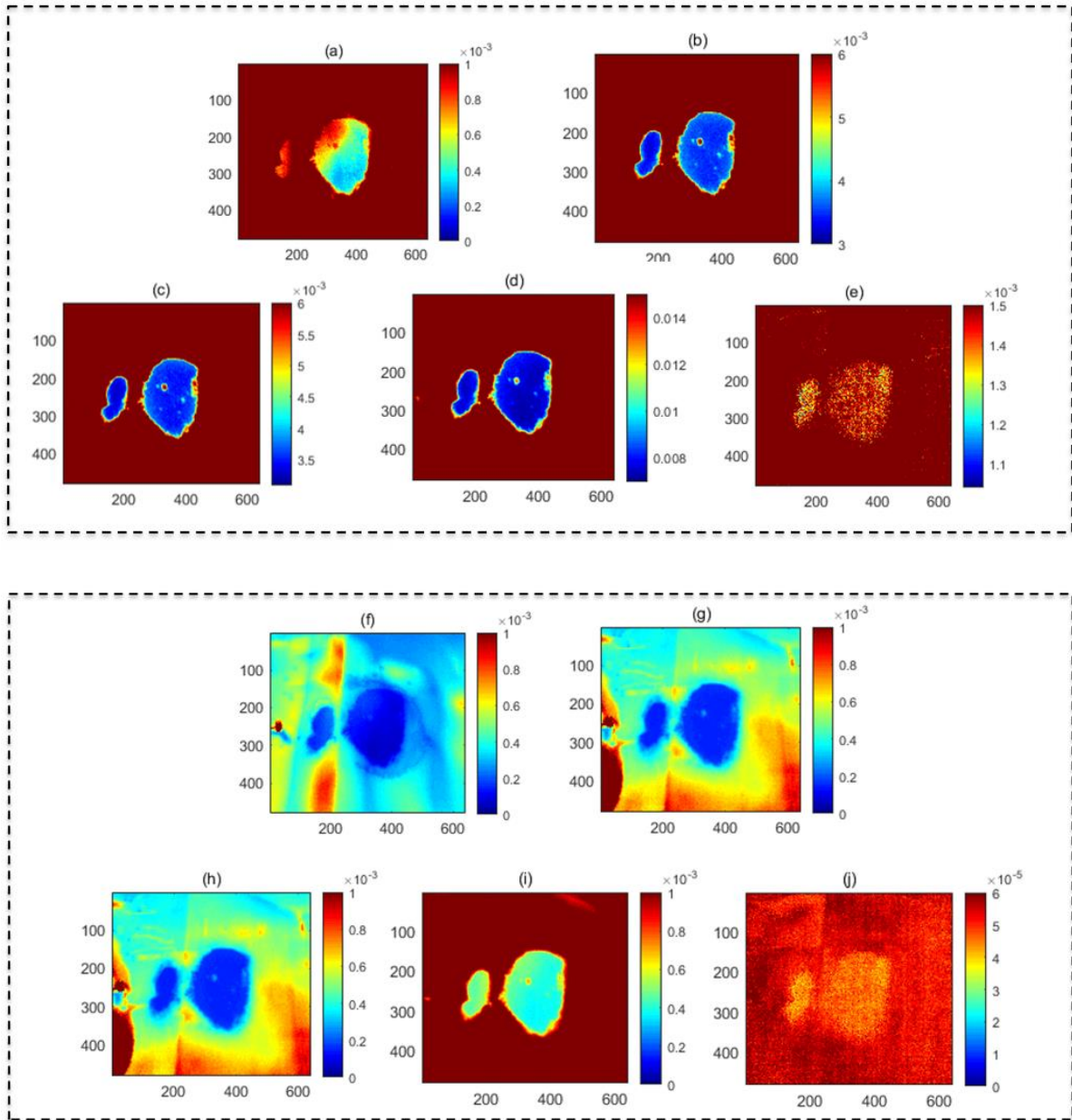


Figure 4.18 Generated cooling constant maps at different periods in the two days experiment. (a-e) the sum of cooling constants from thermal image sequences in Figure 4.17. (f-j) average of cooling constants from thermal image sequences in Figure 4.17. (a and f) period 1. (b and g) period 2. (c and h) period 3 (d and i) period 1, 2 and 3 (e and j) period 4.

Although the long-term thermal imaging monitoring can identify the interfaces under the geomembrane, the quasi-active thermal imaging is proposed to be deployed in the WTP as a large area coverage structural health monitoring technique. The thermal camera needs to be mounted at a quite high altitude to cover a large monitor area, which will lead to difficulty adjusting the focus and the monitoring orientation, resulting in a structural stability problem at the high altitude. In addition, thermal image sequences are too long for daily monitoring, and continuous long-term monitoring is inefficient in the data processing. Therefore, a more efficient monitoring method needs to be developed to shorten the monitoring period.

Thermal imaging monitoring on a UAV can cover a large area of the geomembrane floating cover via remote sensing, but the UAV has a limitation of short flight time due to the limitation of the battery. A commercial UAV with a thermal camera can fly around 40 mins after being fully charged. In this chapter, the developed quasi-active thermal imaging method is tested with the short-term monitoring and cooling constant maps were generated over different lengths of thermal image sequences to investigate the practicality of the UAV aided thermal imaging monitoring. As shown in Figure 4.19, cooling constant maps were generated from different lengths of thermal image sequences in period 3 of Figure 4.17. Figure 4.19 (a) is a cooling constant map that is generated from period 2 (07:07:55-17:11:15) in Figure 4.17. It presents a clear profile of the interfaces under the geomembrane, but the monitoring period is too long for UAV monitoring. Figure 4.19 (b) is generated from the first 60 mins in period 2 of Figure 4.17. 6 sets of cooling constant values are summed up to compare the contrast, where the small soil region is blurred in the map and the contrast between the soil region and no-soil region is not uniform, but the soil region still can be identified. In Figure 4.19 (c), the cooling constant map generated from the first 40 mins monitoring shows the profile of the soil region with a non-significant contrast, but the soil regions still can be identified. For Figure 4.19 (d), which is generated from a 10 mins monitoring (two frames of thermal images), the whole image becomes blurred, and the profile of the soil region cannot be identified. These four figures reveal that a short thermal image sequence (around 40-60 mins with 4-6 thermal images) can still demonstrate a reasonable profile of interfaces under the cover, even though some of the soil regions are blurred, and the cooling constant contrast is not significant. This study provides an insight into using UAV aided thermal imaging to conduct a structural assessment efficiently and accurately on a large area.

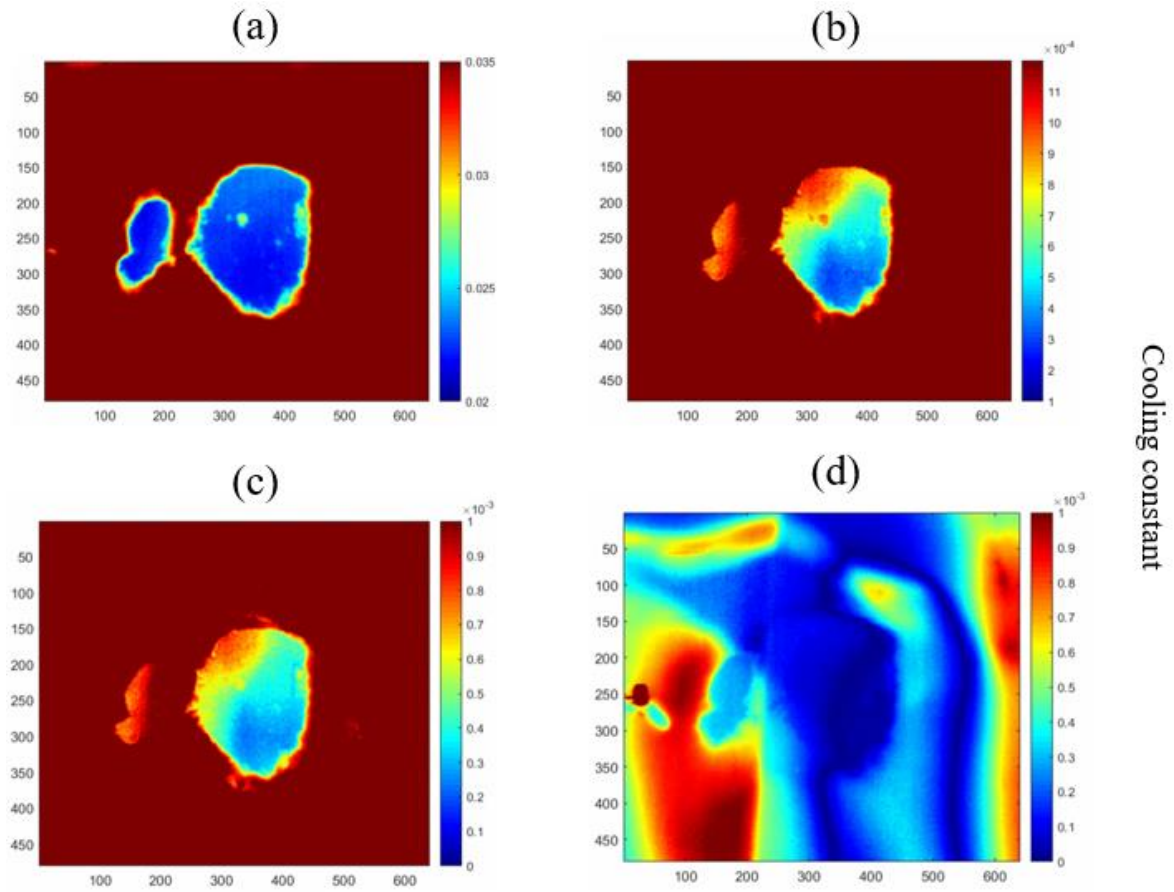


Figure 4.19 Comparison of cooling constant maps generated from different lengths of periods. (a) sum of period 2 thermal image sequences (b) sum of 60 mins thermal image sequences (6 frames) (c) sum of 40 mins thermal image sequences (4 frames) (d) single frame of cooling constant maps in 40 min

4.3.3.2 Classification of different interfaces under the HDPE geomembrane

Based on the above findings with the developed thermal imaging technique, an experiment was set up to identify three interfaces (air, water and soil) under the geomembrane, which simulates the interfaces (biogas, sewage water and scums) under the floating covers at the WTP. As shown in Figure 4.20, the three statuses of objects were filled in the test rig, where the water was isolated at the bottom by a barrier, the soil block was built at the top left corner of the test rig, and the rest of the space in the test rig was naturally filled with air. It is noted that some parts of the view of the thermal camera were projected to the ground, and these parts are not the area of interest. Similar to the previous experiment in Section 3.2, the whole set-up was exposed under sunlight during the daytime and the monitoring last for 40 mins. A thermal image sequence that included 4 frames of thermal images was analysed with Equation (3.3).



Figure 4.20 Test rig filled with soil, air and water at different regions under the HDPE geomembrane cover

As mentioned in Chapter 2, thermal imaging can provide an efficient and large area coverage structural assessment, but the cooling constant contrast among regions is insignificant. When several interfaces exist at the undersurface of the geomembrane at the same time, it is difficult to distinguish interfaces based on the contrast in a contoured cooling constant map. Therefore, several unsupervised clustering-based machine learning image segmentation algorithms, such as K-means clustering, DBSCAN clustering and GMM clustering, were deployed to segment the cooling constant map into several parts based on the values of the cooling constant. The details of these image segmentation methods were illustrated in Chapter 3. As shown in Figure 4.21, the cooling constant map was plotted after the calculation with Newton's cooling law. Due to the uneven ground surface, only part of the geomembrane contacted the water. In this figure, the areas of each region are demonstrated on the map. In addition, the air region can be distinguished from another two regions with a large contrast. However, the soil region and the water region cannot be distinguished due to the small difference in the cooling constant, and the presences of each region in the map depend on the threshold of the cooling map. K-means clustering method was at first deployed for analysis, and the results are shown in Figure 4.22. Since the number of clusters needs to be determined in this method, the number of clusters k was set as 3, 4 and 5. Figure 4.22 shows $k=3$, where the air region is distinguished from another two regions, but the water region and the air region are classified as the same region. Figure 4.22 (c) shows $k=4$, where all three regions are recognized, and the fourth region is the surrounding region. When

$k=5$, Figure 4.22(d) shows a similar result with $k=4$, while contours around each region are divided into more layers, this is because the lateral thermal conduction results in a varied cooling constant at the edge of each region. Compared to the cooling constant map in Figure 4.22(a), figures with $k=4$ and 5 present agreed with profiles of each region. As in the experiment, there are three interfaces under the geomembrane, and there is a surrounding environment, the data in the cooling constant map was determined to be categorized into 4 groups ($k=4$). Figure 4.23 (a) shows the profiles of each region and Figure 4.23(b) shows the data distribution ranges for each cluster. It can be found that the water region has the lowest values of cooling constant, and the soil region has a higher cooling constant than the soil region. The air region has the highest values of cooling constant and takes the largest region in the image, and the surrounding region locates at the edge of each region and some surrounding parts in the image. As a result, this algorithm successfully predicted different interfaces under the HDPE geomembrane.

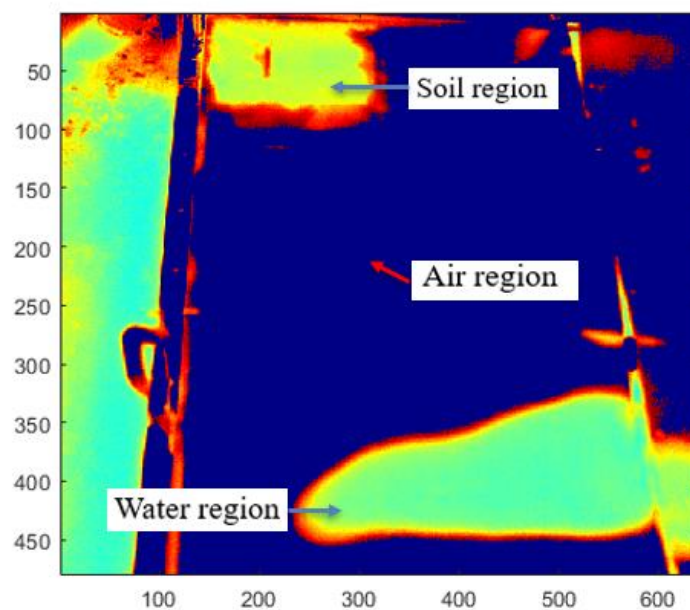


Figure 4.21 Cooling constant maps with three regions (soil region, water region and air region) on the HDPE geomembrane

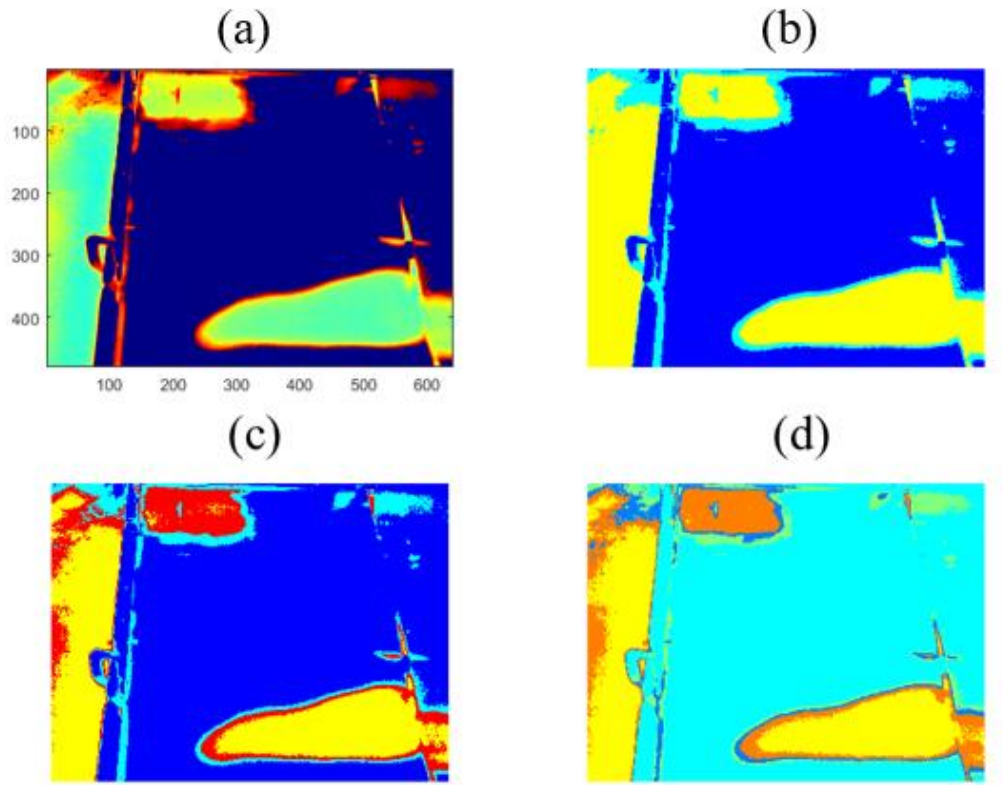


Figure 4.22 Comparison of results from K-means clustering method with different k values (a) Cooling constant map (b) $k=3$ (c) $k=4$ (d) $k=5$

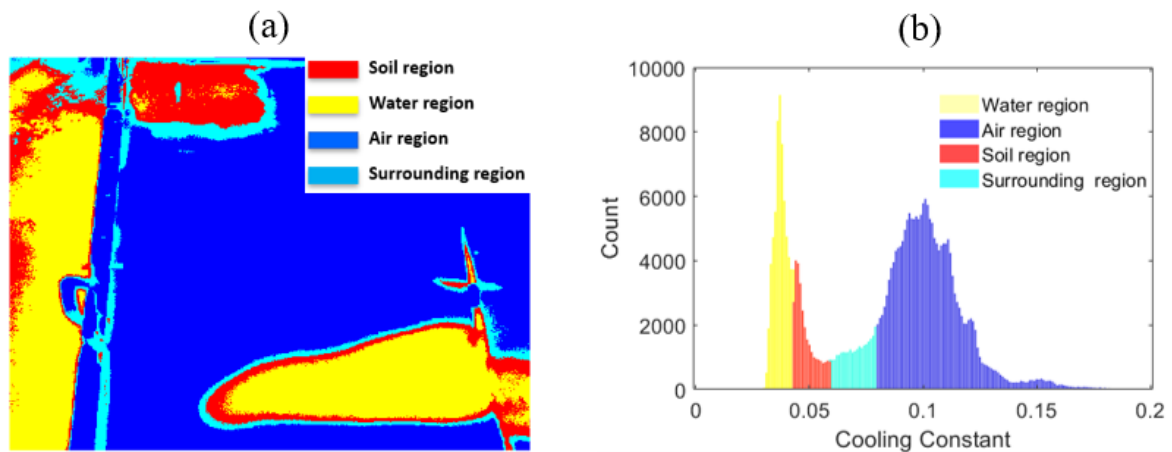


Figure 4.23 (a) classification of regions with K-means clustering method ($k=4$) (b) data distribution of each cluster

The result of the DBSCAN clustering method is shown in Figure 4.24. Figure 4.24(b) shows the processed image with $\epsilon=0.000055$ and $N_{min}=600$. The soil region, the water region and the air region can be distinguished in the image. As the DBSCAN method automatically determines the number of clusters, the image is divided into 3 clusters and the surrounding region is not recognized. Figure 4.24 (c) shows the result when $\epsilon=0.0001$ and $N_{min}=600$.

The data is divided into 3 clusters again, and the air region is distinguished, while the air region and the water region cannot be distinguished. Figure 4.24 (d) shows a similar result with Figure 4.24 (c) with $\epsilon=0.000055$ and $N_{min}=200$. Therefore, the DBSCAN method, in Figure 4.24 (b) shows a reasonable result, and the profiles of each region are shown in Figure 15 (a). Figure 4.25 (b) shows the data distribution for Figure 4.25(a), where the water region data takes the smallest area in the image, and the data mainly distributes at the water region and some of the surrounding regions in Figure 4.25(a). Soil region data distributes at the soil region, the outer layers of the water region and some parts of the surrounding region in Figure 4.25 (a). It is found that some of the soil region data is smaller than water region data, which is because some of the data in the water region in Figure 4.25 (a) was classified as soil region data. Similarly, some of the data in the water region in Figure 4.25(a) is classified as the air region data, resulting in some of the low cooling constant values data is classified as the air region data in Figure 4.25(b). Although some of the points were not classified correctly, the DBSCAN method can overall segment the cooling constant map and present profiles of each region.

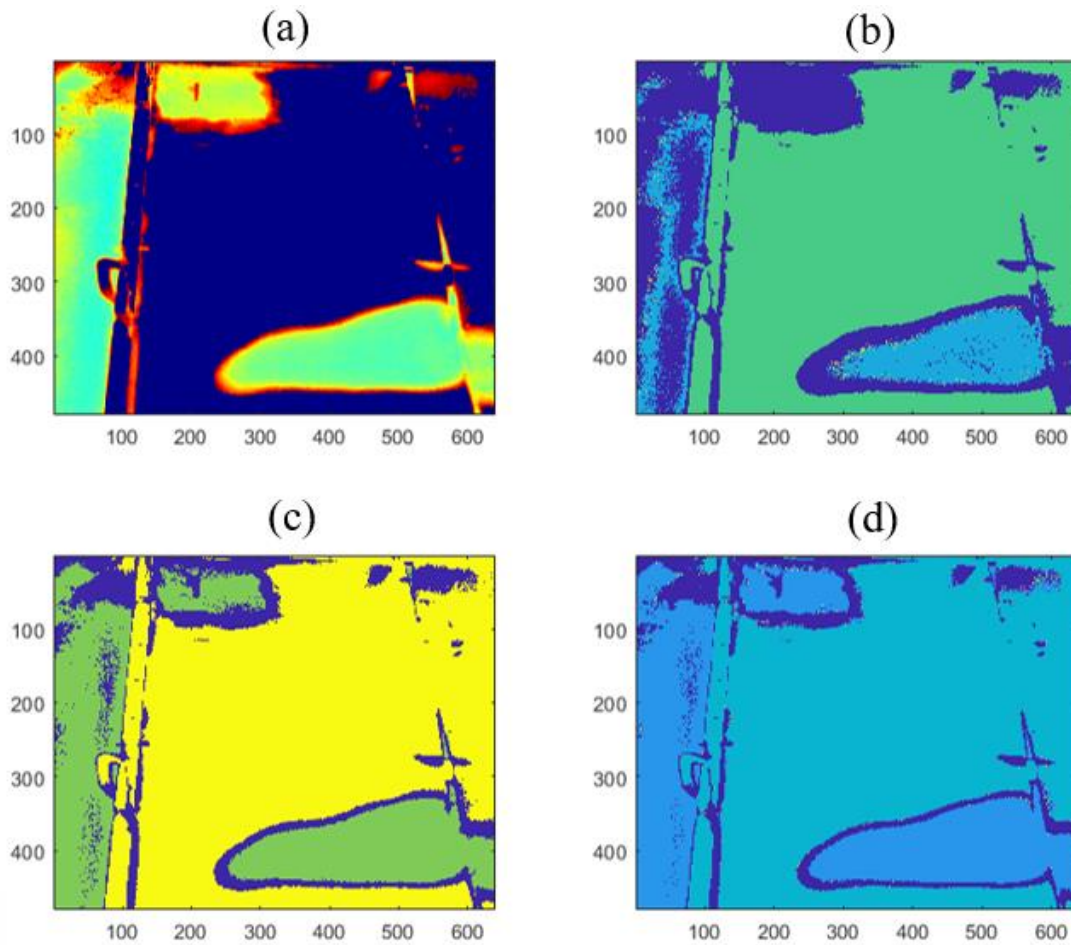


Figure 4.24 Comparison of results from DBSCAN method .(a) cooling constant map (b) $\epsilon=0.000055$, $N_{min} =600$ (c) $\epsilon=0.0001$, $N_{min} =600$ (d) $\epsilon=0.000055$, $N_{min} =200$

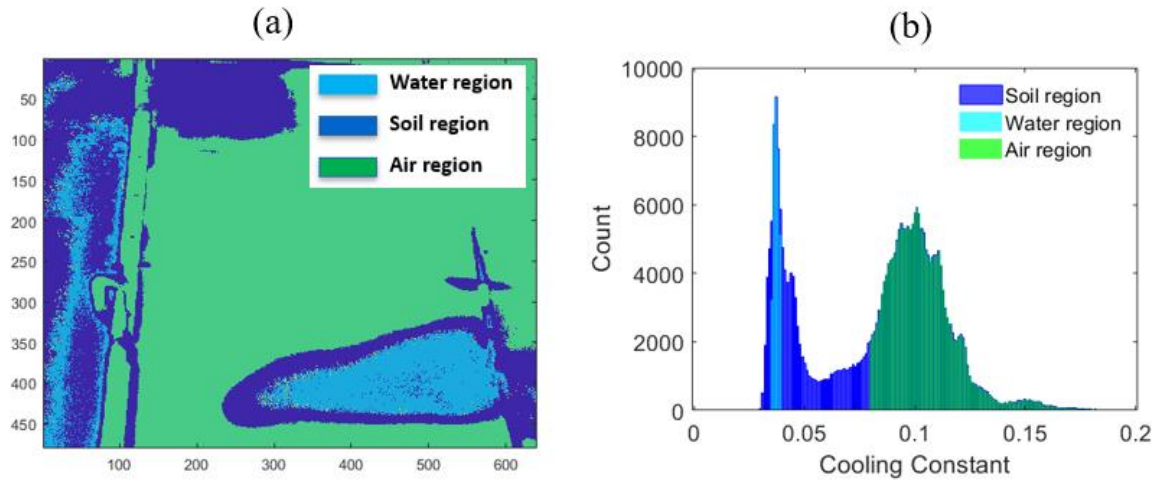


Figure 4.25 (a) Classification of regions with DBSCAN method ($\epsilon=0.000055$, $N_{min}=600$) (b) data distribution of each cluster

The segmentation result with the GMM method is shown in Figure 4.26. Figure 4.26 (b) shows the result with 3 components, and the air region can be distinguished from another two regions (water region and soil region). Soil region and water region are not distinguished since they are classified as the same components, and some of the other areas are classified as the third component. Figure 4.26 (c) shows the result with 4 components, presenting a suitable classification with all three regions classified. Figure 4.26 (d) can also classify all of the three regions, and the edges of the soil region and the water region are further classified into more layers. Similar to the K-means cluster methods, the GMM method with 4 components presents a suitable segmentation result, and the profiles of each region are shown in Figure 4.27 (a). Figure 4.27(b) illustrates the data distribution of each cluster in Figure 4.27(a), where the soil region data takes a larger area than the water region data, which is because the out layer of the water region is classified as the soil region. The result shows that the GMM method can segment the cooling constant map according to the cooling constant values.

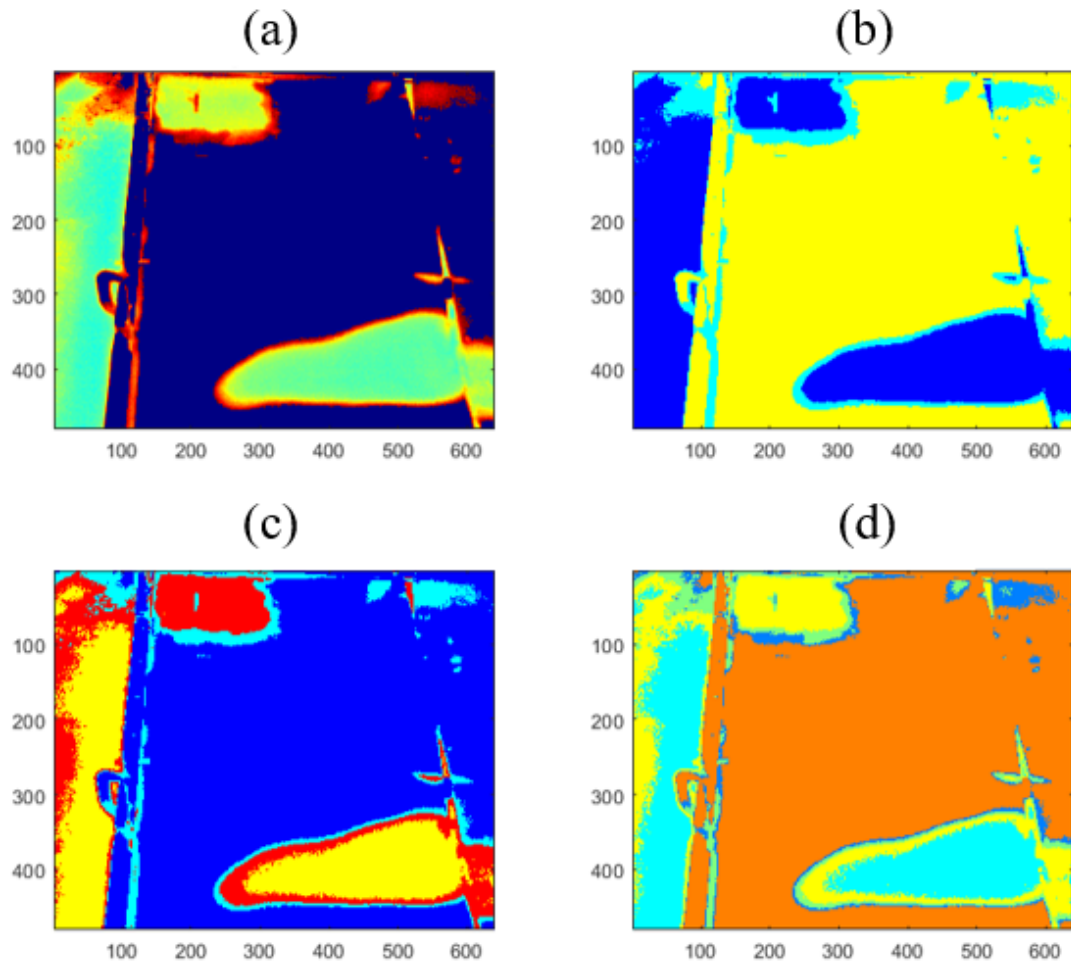


Figure 4.26 Comparison of results from GMM method. (a) cooling constant map (b) components number=3 (c) components number=4 (d) components number=5

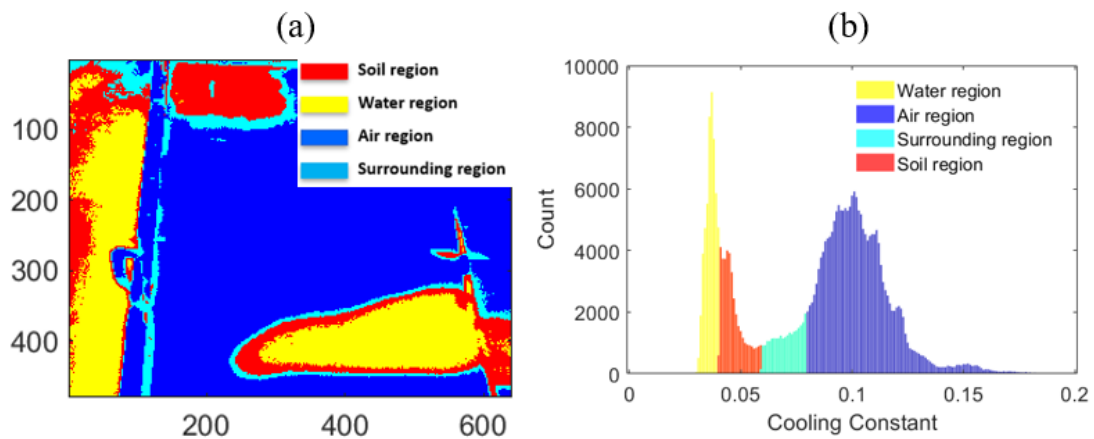


Figure 4.27 (a) Classification of regions with GMM method (components number=4) (b) data distribution of each cluster

The above results suggest that the developed image processing techniques based on quasi-active thermography can be used at the WTP for identifying the profiles of scums regions,

biogas regions, and sewage water regions with the aid of the UAV. It is noted that during the monitoring, the view of the thermal camera should be filled with geomembranes, or the algorithm will register the surrounding background as one kind of interface and potentially lead to confusion. So far, it can be concluded that the clustering based quasi-active thermal imaging technique can be used for the identification of interfaces under the HDPE geomembrane, and the monitoring result can be obtained from a relatively short term of monitoring the stimulus of solar radiation.

4.4 Conclusions

In this chapter, quasi-active thermography has been introduced, validated and examined experimentally to detect the presence and the expansion of soil under HDPE geomembrane material. It was found that thermography with the aid of the ambient temperature and the solar intensity can efficiently classify different regions by comparing the temperature changing rates. In this method, thermal imaging uses ambient weather information to analyse the temperature responses of the HDPE floating covers. The desirable monitoring periods are defined by correlating the solar intensity with the temperature changing rate of the geomembrane. The proposed technique uses naturally occurring transient cooling events resulting from daily solar intensity cycles. These cooling cycles are defined by the pyranometer data acquired. The temperature profiles of the transient cooling event can then be analyzed using Newton's law of cooling. By estimating the cooling constant at every monitored point, a map of cooling constant distributions based on the cooling rate can be constructed, and the results have successfully demonstrated the advantage of the cooling constant mapping to identify, outline and monitor the extent of under-surface soils.

A clustering-based image segmentation assisted quasi-active thermography technique has also been experimentally investigated to predict multiple interfaces under the HDPE geomembrane material. The proposed thermal imaging uses the daily transient temperature response from the naturally applied solar radiation stimulus to predict the profiles of attached objects. The desirable monitoring periods for the quasi-active thermography were identified by calculating the cooling constant at different times in a day. A cooling constant map was first generated based on the obtained thermal images, and the K-mean clustering algorithm, DBSCAN clustering algorithm and the GMM clustering algorithm were applied to classify interfaces based on the values of cooling constant in the map. The key findings of these studies are summarized below. Clustering-based machine learning algorithms partition the areas of each region under the HDPE geomembrane by comparing the temperature changing rates. This technique can be used to predict the distributions of scums, sewage water and

biogas under the cover without contact measurements, and hence it can assist in the decision-making process for scum removal and the maintenance of the effective operation of floating covers.

In Chapter 7, the conclusions from this work will be further used for field trials to practically monitor the growth in the extent of the scum under the floating covers in WTP with the ambient solar energy.

CHAPTER FIVE

5 Detection of the defects in geomembranes with different interfaces using the quasi-active thermography

This chapter presents an exploratory investigation on the use of a short term quasi-active thermography technique to detect the presence of artificially induced penetrating and part-penetrating defects on a HDPE geomembrane specimen. The proposed thermography inspection method utilised ambient sunlight as the input thermal energy and cloud shading as the trigger for thermal transients. Outdoor laboratory-scale experiments were conducted to study the proposed inspection technique. An infrared thermal camera and a pyranometer were used to record the thermal responses of the HDPE material as a result of solar intensity variation. The viability of using periodic cloud cover transients to drive this inspection technique is reported. In addition, an image processing algorithm was formulated based on the frame subtraction method to enhance the identification of the defects.

This chapter also illustrates a study where the temperature profile was analysed using three different algorithms for thermal transient analysis, viz. Newton's law of cooling, a LPSD method and a frame subtraction method. The outcomes from each of the algorithms were examined and compared. The results show that, with appropriate selection of the thermal transient analysis algorithm, quasi-active thermography inspection can be used to distinguish different substrates and to determine the presence of non-surface penetrating defects.

5.1 Introduction

As reported in the introduction, hardened scum may scratch the underside of the geomembrane and generate part-penetrating defects. This chapter introduces a quasi-active thermography technique to detect the presence of penetrating and part-penetrating defects on the HDPE cover material. The results reported were obtained from a series of experiments conducted on a rooftop that is fully exposed to the prevailing weather conditions. The proposed technique utilized variations in the ambient solar radiation to detect and identify these defects.

This chapter aims to report on the development of a non-contact thermal imaging SHM method to detect concealed defects that are in contact with air (simulating biogas), water (simulating liquid sewage) and simulated scum (i.e., garden soil). Two quasi-active thermal

imaging inspection experiments were conducted to inspect synthetic defects in a geomembrane with different substrates. The experiments were conducted in an open space using sunlight intensity fluctuation from short periods of cloud shading. The results presented are obtained using three different image analysis methods. Experimental results reveal that the proposed inspection method can locate subsurface defects in a HDPE geomembrane with different substrates. This approach provides a new quasi-active thermal imaging method to evaluate the structural integrity of large-scale floating structures as the basis for SHM.

5.2 Development of Short Periods of Quasi-active Thermography to Detect the Defects in Geomembranes

5.2.1 Introduction

The application of conventional active thermography on structures as large as the floating covers at WTP would require a large amount of thermal energy and time to ensure the uniform flow of the heat flux into the structure and is therefore considered impracticable for use in the real world of the WTP. In a particular type of active thermography, a pulsed thermal wave is applied on the top surface of a specimen. When the radiation source is turned off, the heat flows into the component penetrating thermal conduction, and the top surface temperature will decrease. When the thermal wave reaches defects such as delamination, the air gap which has a larger thermal resistance will interrupt the propagation of the energy. As a result, thermal energy will be retained in this region, and the surface above this region will register a higher temperature than the surrounding area [236]. This section investigates whether cloud-cover will provide transients in timescales that will facilitate detecting the defects on the cover material. The shadings from the cloud will temporarily block the solar radiation and generate a thermal transient on the surface of the geo-membrane material.

A series of geo-membrane test specimens were used. It will be supported in a test rig on an exposed roof top. A pyranometer will be used to record the change in solar irradiance during cloud-cover events. A series of temperature and irradiance transients will be acquired. The test membrane will have a series of surface penetrating and part-surface penetrating defects on it. Given that the floating cover can be in direct contact with the raw sewage and can be separated from the raw sewage by the presence of the biogas, the test membrane will be tested in the following arrangement:

- a. Suspended on water (to simulate the cover in contact with the raw sewage)
- b. Supported on the test rig where part of the cover will be in contact with water, leaving an air gap between the surface of the water and the membrane (to simulate the presence of biogas).

5.2.2 Identification of transient event due to cloud movement

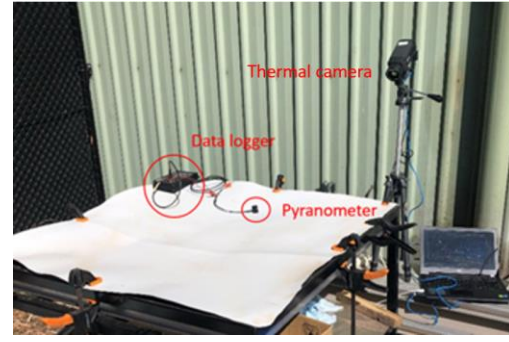
The prepared geo-membrane ($1\text{ m} \times 1\text{ m} \times 2\text{ mm}$ thickness) was clamped onto an aluminium test rig, as shown in Figure 5.1(a). An Apogee SP-110 pyranometer[248] was installed on the tested HDPE geo-membrane to monitor the radiation energy exerted on the surface of the specimen. An A615 FLIR infrared thermal camera [233] which contains an uncooled Vanadium Oxide detector array of size 640×480 , was placed beside the geomembrane to record the temperature of the surface of the geomembrane. These measurement equipment were allowed to monitor the radiation information continuously, the transient events due to cloud shading can be monitored and then correlated with the information obtained from infrared imaging over an extended period. The infrared imaging during these transient events will be studied in detail.

A preliminary test was conducted as a baseline study by leaving the experimental set up outdoor for 1 hour (see Figure 5.1 (b)). Both solar intensity and thermal imaging were recorded at 3 Hz over the test period. Figure 5.2 shows the solar intensity history measured by pyranometer and temperature profile measured at a point from the thermal images over 1 hour. The experiment was conducted on a cloudy day the pyranometer data showed that the sun was not covered by the cloud three times over the test period (see Figure 5.2).

During each transient event (with and without cloud cover), the temperature transients on the membrane are evident. The first event, which happened between 12:12:30 and 12:23:20 of the experiment, is labelled in the figure. The transient event started at 12:12:30 when the pyranometer detected the cloud-cover event. Temperature transient on the membrane is evident a few seconds into the cloud-cover event. Then the sun reappeared from the cloud at 12:23:20, according to the pyranometer data. A corresponding thermal transient was recorded several seconds into this event. It is found in Figure 5.2 that a cloud cover event can result in up to 5°C of temperature change on the membrane.



(a)



(b)

Figure 5.1 Experiment set up (a) high-density polyethylene (HDPE) geomembrane was clamped on the test rig. (b) illustration of the data acquisition phase

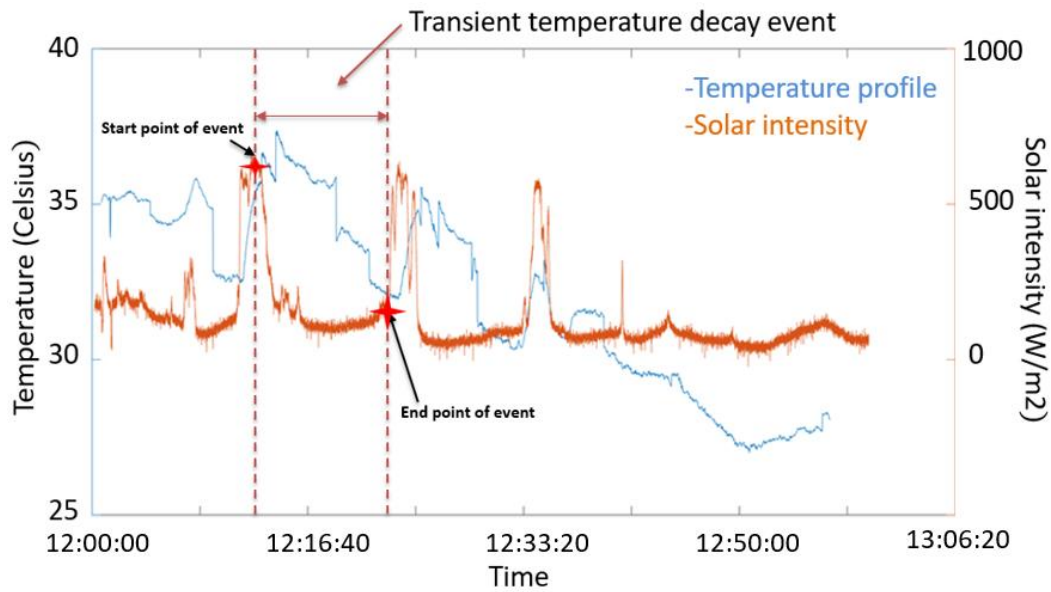


Figure 5.2 Temperature profile on HDPE membrane and local solar intensity history

5.2.3 Procession of thermal image

It is proposed that the thermal transients brought about by the cloud-cover events be used to determine the presence of defects on the membrane material. The quality of the raw thermal images in quasi-active thermography will be affected by noise. The defects are difficult to find in the original image as defects are only based on a single captured frame in one event. The inspection technique will rely on identifying the transient events and collating the corresponding thermal transient events to enhance the ability to identify the penetrating and part-surface penetrating defects on the floating cover. In this section, two different frame subtraction algorithms in Chapter 3 were tested (see Equation (3.17) and Equation (3.19)). These algorithms will be applied to the thermal transients acquired from multiple transient events to reduce the effects of noise.

This work aims to experimentally investigate the application of quasi-active thermography under laboratory conditions on an exposed roof top. The work will be presented in two sections, (1) Detection of part-surface penetrating defect on the membrane and (2) detection of surface penetrating defect using quasi-active thermography.

5.2.4 Detection of part-penetrating damages on air

In this part of the work, the ability to detect the presence of part-penetrating subsurface defects on the geo-membrane material in contact with air will be assessed. The purpose of this section is to investigate the capability of quasi-thermography for distinguishing the subsurface part-penetrating defects.

As shown in Figure 5.3, a series of defects were created on the subsurface of a $0.5\text{ m} \times 1\text{ m} \times 2\text{ mm}$ membrane using laser cutting equipment. The dimensions of these defects are shown in Table 5.1. The experiment setup is shown in Figure 5.4. A pyranometer and thermal camera were put alongside the membrane. The membrane was exposed to solar radiation for 32 minutes. The experiment was carried out on a cloudy day. As shown in Figure 5.5, there were 2 cloud cover events over the membrane that gave rise to two thermal transients on the membrane. The start point and endpoint of each event were highlighted in the figure. Event 1 and event 2 are demonstrated in detail, respectively, and the detailed temperature and solar intensity data are shown in Figure 5.6 and Figure 5.7. The temperature decay events start at the local maximum point of the solar intensity and end at the local minimum point of solar intensity. Temperature evolution between these two points was utilised to find the defects. Thermal images taken in these 2 events were processed with the two equations developed in Section 5.2.3, and the processed images are shown in Figure 5.8. The results are shown in Figure 5.8 (a) show that all the defects were detected with the given transients using Equation 3.17. Defects 5-8 are not quite clear and can be attributed to the smaller defect depths. In addition, the profile of length and width of the defects can also be distinguished in the image. Figure 5.8 (b) shows the image with processed data using Equation 3.19. All defects were detected, while defects numbers 5-8 are not as clear as Figure 5.8 (a). The images obtained using Equation 3.17 is superior to those with Equation 3.19. It is also evident that Equation 3.19 is good for noise reduction and clearly shows the profile of defects. While Equation 3.17 performs better in identifying the position of defects. The experiment shows that temperature transient events during the short period of cloud cover are sufficient for thermography to capture the part-penetrating defects on HDPE geo-membrane.

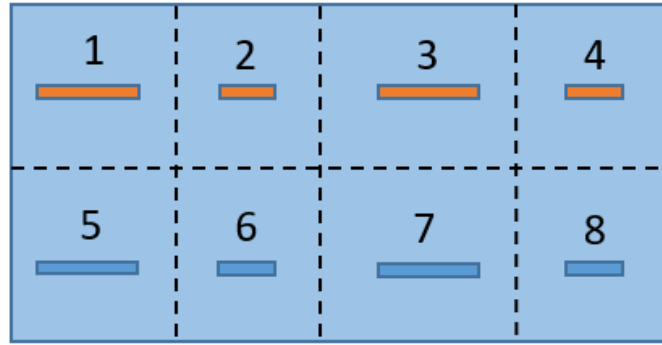


Figure 5.3 Distribution of part-penetrating defects on HDPE geo-membrane

Table 5.1 Profiles of part-penetrating defects on the geomembrane

Defects number	Defect length (cm)	Defect width (cm)	Defect thickness (mm)
1	10	1	1
2	5	1	1
3	10	0.5	1
4	5	0.5	1
5	10	1	0.5
6	5	1	0.5
7	10	0.5	0.5
8	5	0.5	0.5

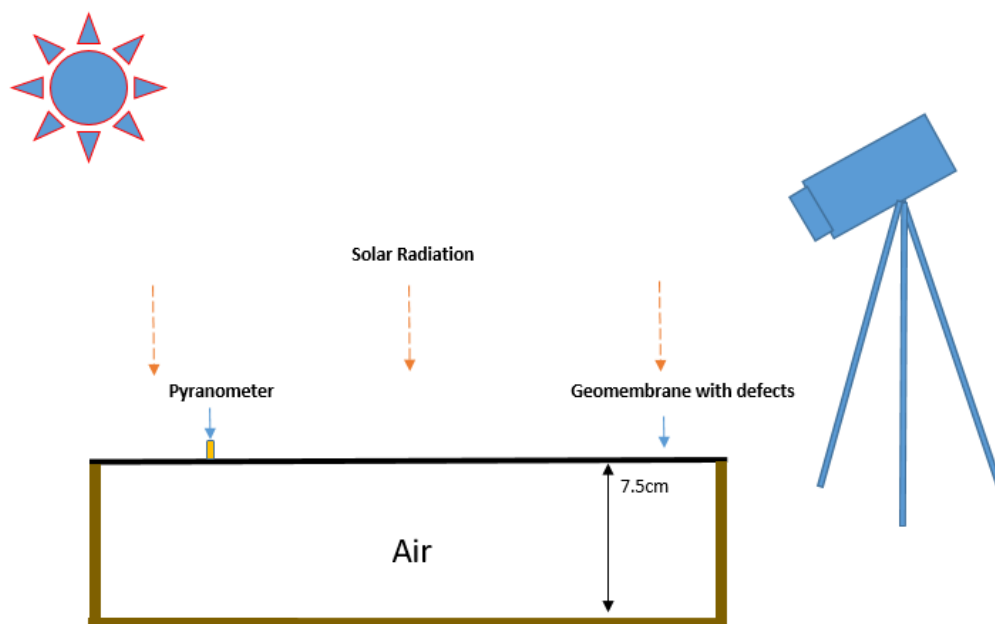


Figure 5.4 Experiment set up of detecting part-penetrating defects on air

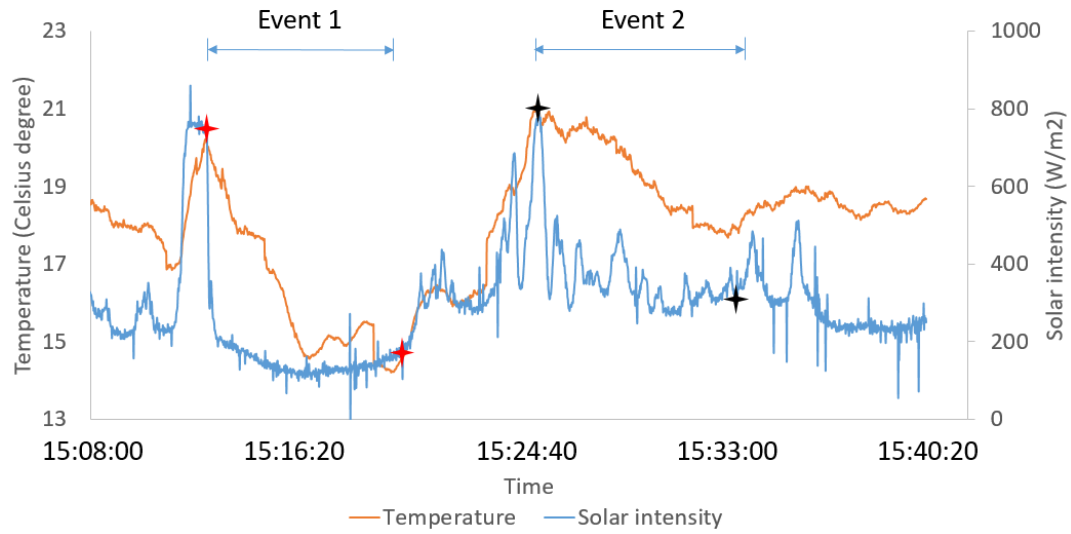


Figure 5.5 Geomembrane temperature profile and local solar intensity history. 2 transient events are highlighted

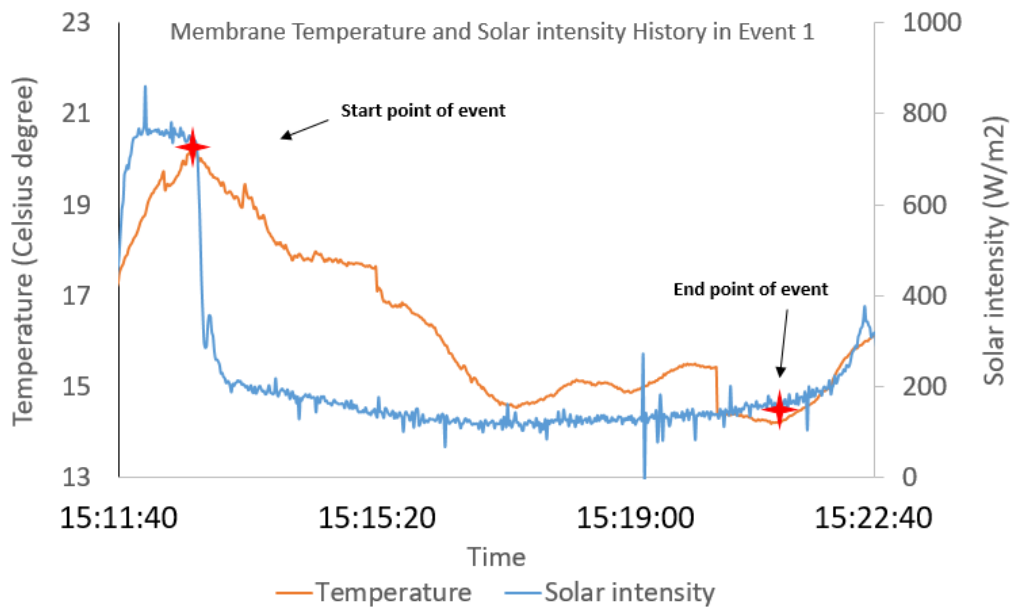


Figure 5.6 Temperature evolution and solar intensity history on the membrane in event 1 in Figure 5.5

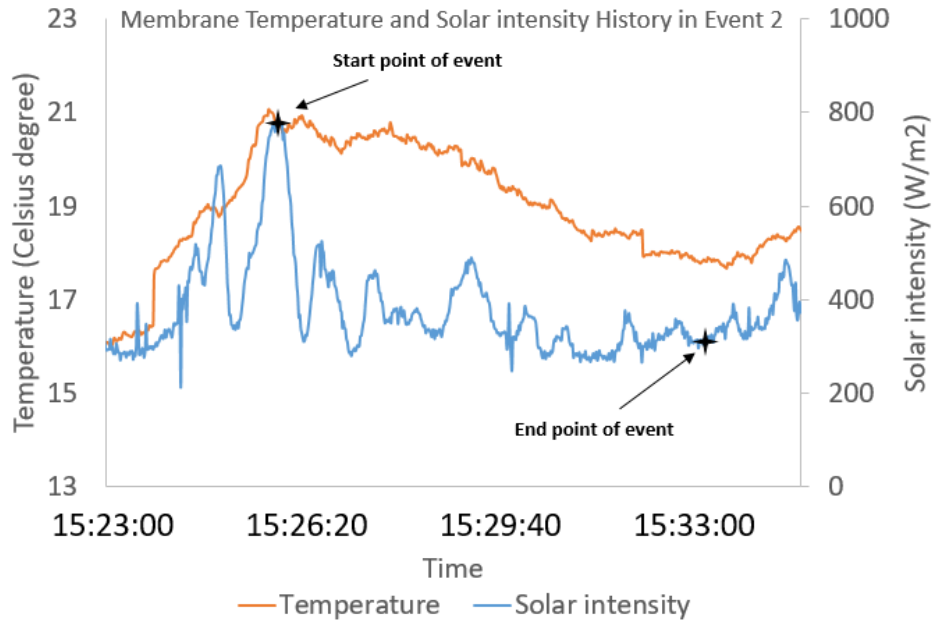


Figure 5.7 Temperature evolution and solar intensity history on the membrane in event 2

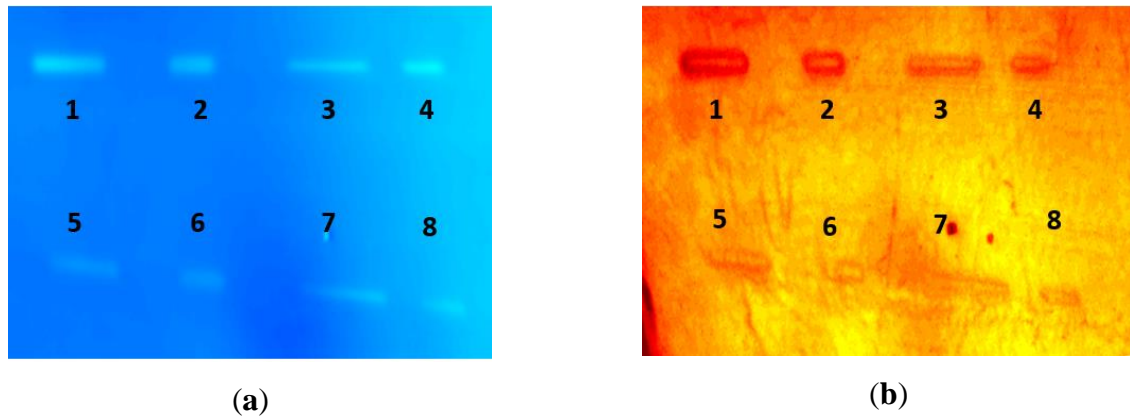


Figure 5.8 (a) Processed thermal image sequence with Equation (3.17). (b) Processed thermal image sequence with Equation (3.19)

5.2.5 Detection of part-penetrating damages with different interfaces

In the sewage water treatment plants, it is reported that geo-membrane floats on the water ponds and generated gas will produce gas bubbles and lift the cover in some regions. Defects will not only appear on the air bubble region but also appear on the water region. Therefore, this section will identify the defects in the air and the water by quasi-active thermography. Figure 5.9 shows the test setup. Part of the membrane specimen floats on the water to simulate the sewage water region at the treatment plant. The remaining portion has an air gap to simulate the air bubbles in the floating cover at the treatment plant. Defects number 1, 2, 5 and 6 in Table 5.1 were located at the air region, and defects numbers 3, 4, 7 and 8 were located at the water region. The experiment set-up was put outside for 1 hour. Multiple

cloud shading events happened. Figure 5.10 shows the temperature and solar intensity history in 1 hour, and the solar intensity fluctuates several times, 6 most significant events were selected and highlighted in the dark region. The solar intensity in these regions decreases abruptly, resulting in transients on the membrane material.

Figure 5.11 (a) shows that the edge between the air region and water region is obvious. This is because of the geomembrane-water medium. Heat is exchanged by thermal convection, where the heat exchange rate will vary with different interfaces and are determined by the thermal properties of the materials across the interface[197]. Therefore, the temperature is varied between the geomembrane-air medium and the geomembrane-water medium. The left part is the air region where defects 1, 2, 5, 6 exists. The higher thermal resistance of air compared with water affected the thermal transients on the specimen resting on water, this will result in a local temperature increase and a warmer colour in the thermal image associated with the part of the membrane resting on the water surface. The right part is the water region, the heat stored in the membrane in this region will flow towards the water, which has higher specific heat and results in cooler temperature. Defects 3, 4, 7, 8 are located in this region. Using the raw unprocessed thermal data, only defect numbers 1 and 2 with the largest defect depth and width of defect can be identified, and the defects in the water region are not found. Temperature data stored in thermal images in the 6 events were then calculated by Equation 3.17 and Equation 3.19, respectively. Figure 5.11 (b) shows the result from Equation 3.17, all defects were found, and the profile of defects in the air region are clearer. Defects in the water region can be found, but due to some heats are absorbed by water, the profile is not as clear as that in the air region. In addition, the profile of defects 5-8, which have 0.5mm defect thickness, is not as clear as the profile of defects 1-4 with 1 mm defect thickness. Figure 5.11(c) shows the result from Equation 3.19. It was found that defects in the air region are not as clearly defined as Figure 5.11 (b), and the defects in the water region cannot be distinguished. Defects 5 and 6 are also not clearly defined compared with those obtained using Equation 3.17. This can also be attributed to the small defect thickness.

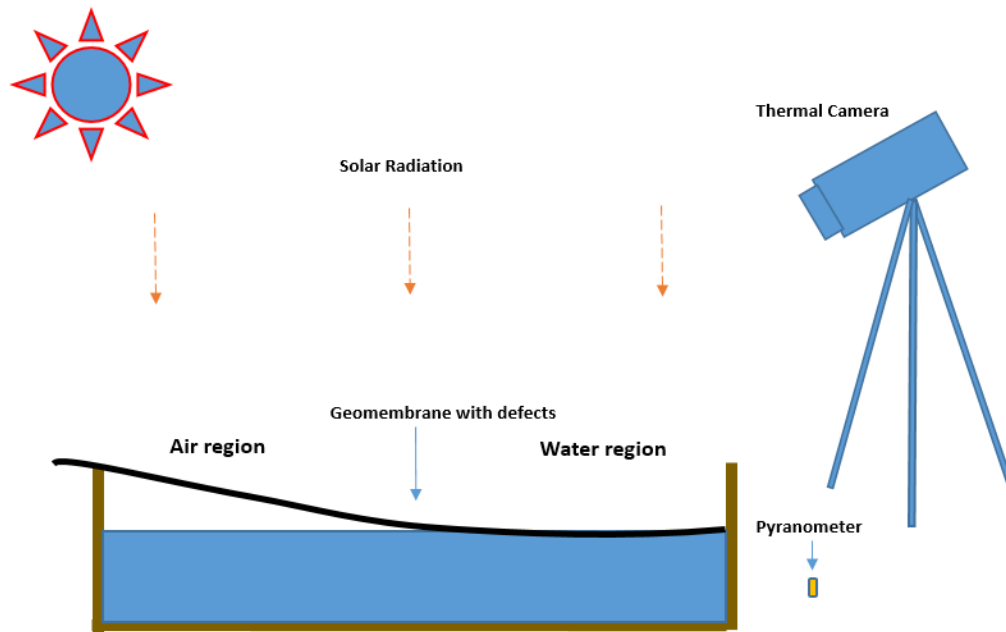


Figure 5.9 Experiment set up of detecting part-penetrating defects on air and water

Hence, the results indicate that thermography with the aid of naturally happened transient events is adequate to capture the defects of HDPE materials that contact air or water despite that defects that sit on water are harder to find than those that sit on air. The edge between the air region and water region can be found through a temperature gradient. In addition, Equation 3.17 performs better in finding the part-penetrating defects both on air and on water, while the profile of deeper defects will be more difficult to be detected.

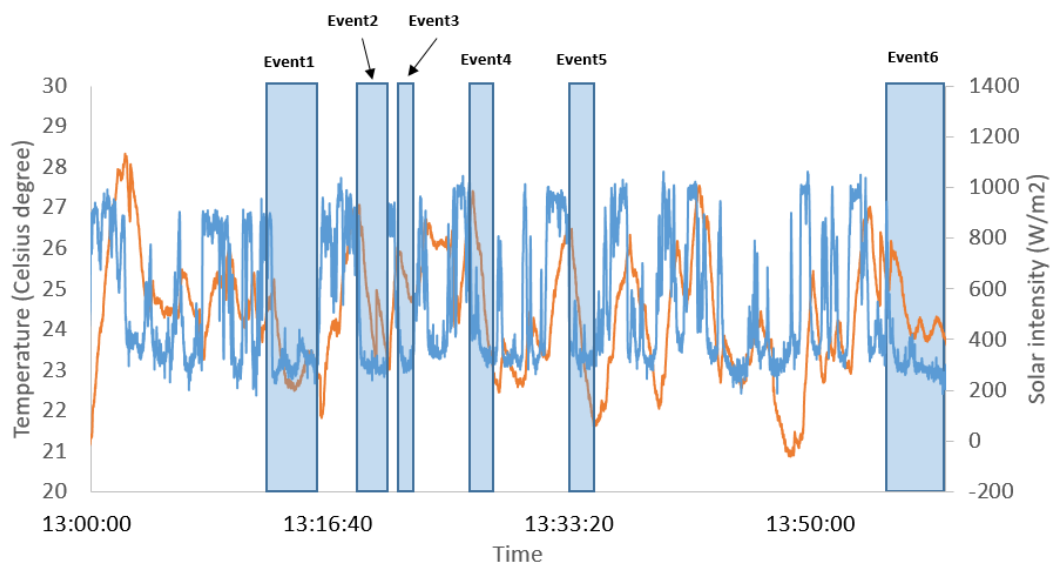


Figure 5.10 Geomembrane temperature profile and local solar intensity history. 6 transient events are highlighted

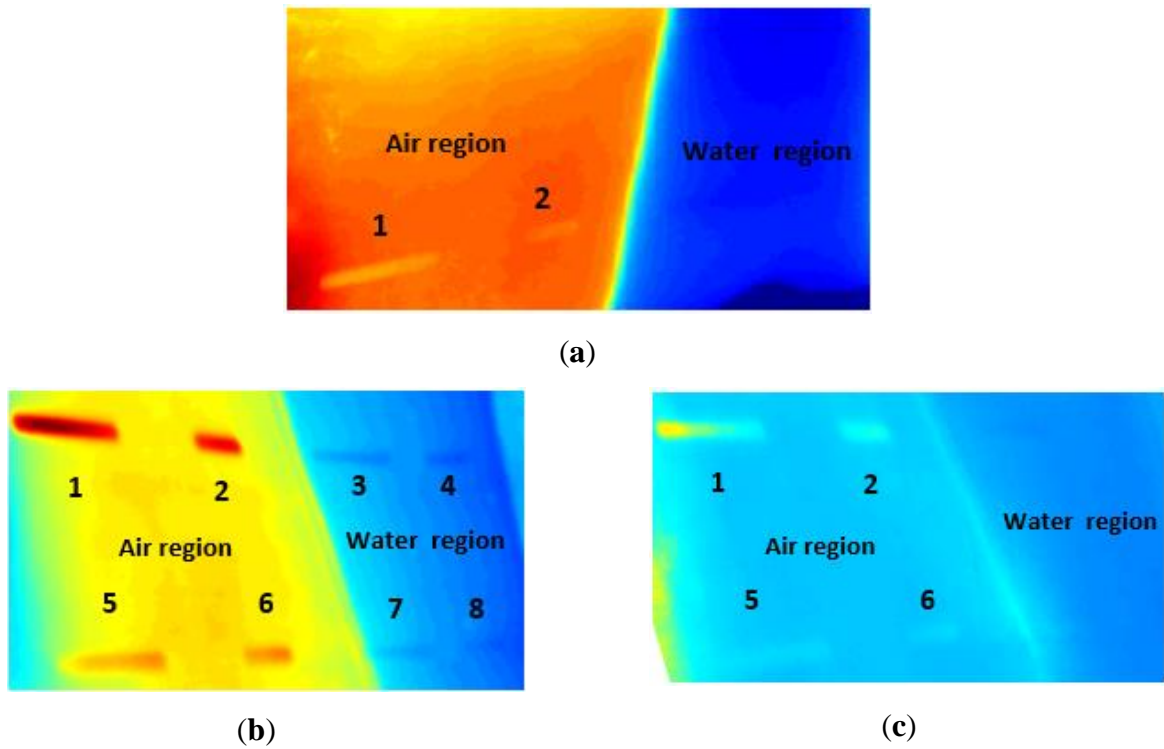


Figure 5.11 (a) Raw infrared thermal image (b) processed thermal image sequence with Equation 3.17 (c) processed thermal image sequence with Equation 3.19

5.2.6 Detection of surface penetrating defects

Surface penetrating damages happen when there a crack is formed on the material surface. Inspecting the cover material for these surface penetrating defects on geomembrane is helpful to maintain the structural integrity of the whole cover. Five different lengths of surface penetrating defects were artificially created on a $0.5\text{m} \times 0.5\text{m} \times 2\text{mm}$ HDPE membrane, as shown in Figure 5.12. The lengths of each defect are shown in Table 5.2. This membrane was supported on an aluminium test rig, the membrane was exposed to the outdoor environment 10 minutes. During this time, 3 cloud-cover events were recorded. Figure 5.13 shows the membrane temperature evolution and solar intensity evolution. Each event is defined by the local maximum and minimum value of solar intensity, as shown in the figure. The data in event 1 is shown in detail in Figure 5.14. It is found that membrane temperature will decrease by up to 4 degrees within 80 seconds during a cloud cover event. Membrane temperature evolutions in the recorded three events were analysed using Equation 3.17 and Equation 3.19. Figure 5.15 shows the outcomes for first and second algorithms, respectively, giving rise to indices from Equation 3.17 and from Equation 3.19. The region with the penetrating defect shows a thermal contrast with the surrounding area. In addition, both algorithms can identify the profile of different defects, and the surrounding

temperature noise is reduced. The results show that the cloud cover events give rise to sufficient thermal transients for detecting these surface penetrating defects.

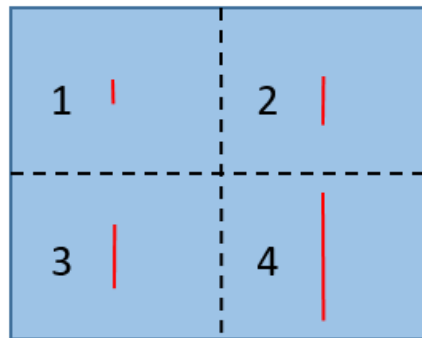


Figure 5.12 Geomembrane with 4 different lengths of cut-through defects

Table 5.2 Length of defects on the geomembrane

Defects number	Defect length (cm)
1	3
2	5
3	7
4	10

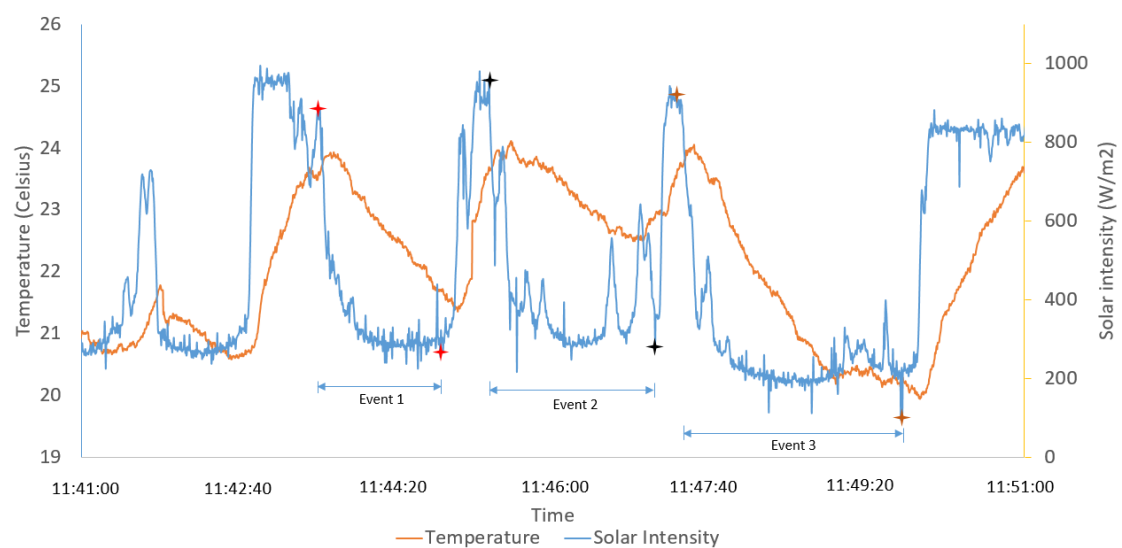


Figure 5.13 Temperature profile of the geomembrane and the local solar intensity history

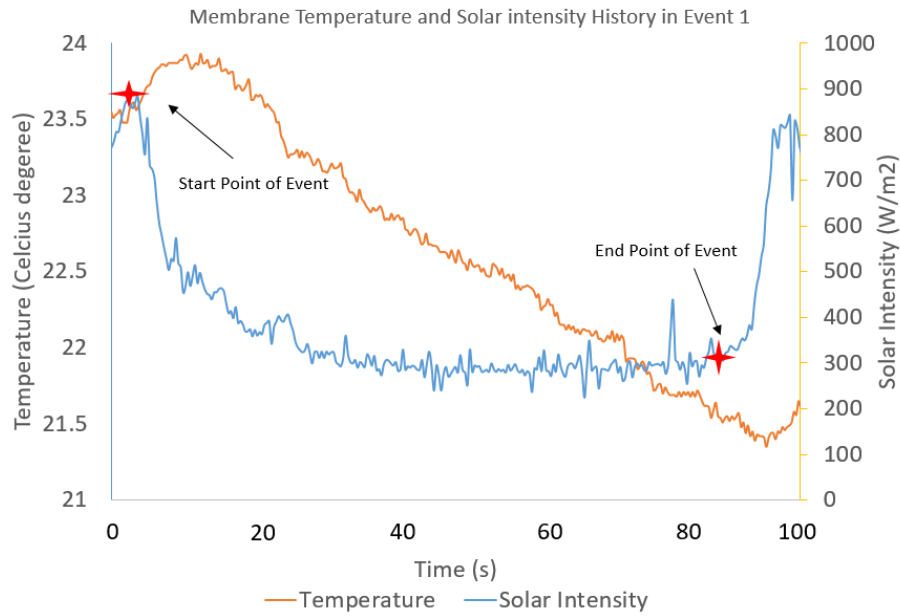


Figure 5.14 Temperature profile of the geomembrane and the local solar intensity history in event 1 in Figure 5.13

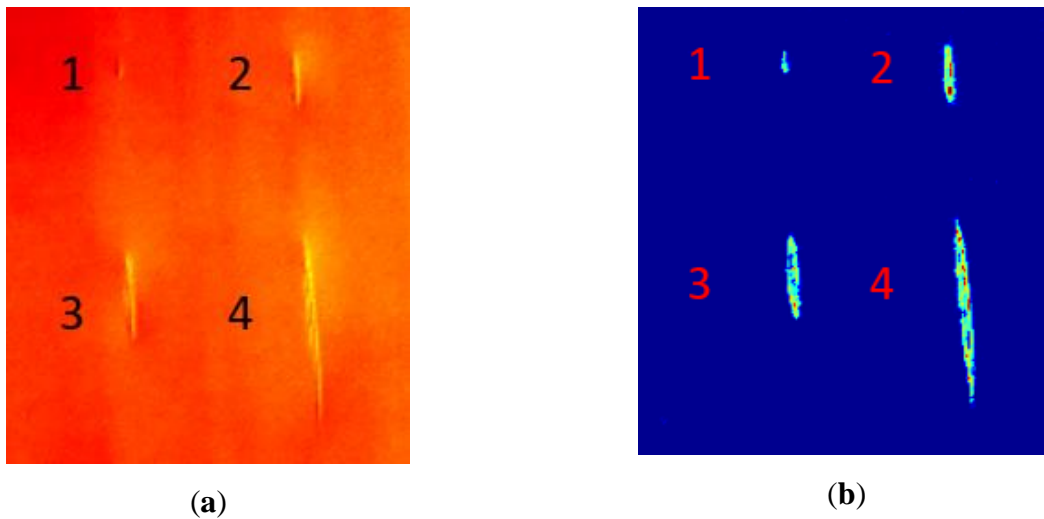


Figure 5.15 (a) Processed thermal image sequence with Equation 3.17 (b) Processed thermal image sequence with Equation 3.19

5.3 Detection of Defects in Geomembranes on Different features

5.3.1 Introduction

As mentioned in Section 5.2, since the defects exist under the cover, inspecting defects on the cover (e.g., cracks) is a challenge. This challenge is compounded if these defects are initiated at the sewage side (i.e., underside of the geomembrane), and do not break through to the top surface, i.e., the defects are non-through. To further complicate the inspection problem, the underside of the membrane may be in contact with different media, viz. liquid

sewage, scum (consolidated solid matter), and biogas. This study aims to use the quasi-active thermography inspection method to identify non-surface penetrating defects in the geomembrane when the geomembrane is in contact with various substrates.

Subsurface defects are most likely to be in contact with scumbers and liquid sewage. These non-air substrates increase the difficulties in detecting the presence of membrane defects. It is also difficult to apply a stimulus and monitor the vibrational response using contact inspection techniques due to the large size of a membrane (more than 8 hectares[30]). Therefore, this section focuses on a novel detection strategy based on a non-contact thermal method that works with naturally occurring ambient variations to inspect floating covers. This inspection technique has the potential to be an integral part of a structural health monitoring regime for this large asset, providing early warning of damage to enable more efficient asset management and maintenance of the cover.

5.3.1.1 Experiment set up

A transient event occurs when cloud shading reduces sunlight intensity on the membrane. The temperature of the membrane decreases due to a decline of input heat. Suppose a defect alters the heat-transfer characteristics of the membrane. In that case, this will result in a local variation in the temperature distribution on the membrane surface, hence its IR emission. When the sun reappears from the cloud another transient event occurs in response to an increase in the local solar intensity. These temperature transients are similar to those induced in pulse thermography [249, 250], but using a naturally occurring stimulus. Accordingly, our approach can be aptly described as quasi-active thermography.

The transient events caused by the cloud shadings can happen many times in a day, with the temperature gradients in the membrane depending on the duration of cloud shading and the density of the clouds. In our experiments, the local solar radiation intensity and the temperature of the membrane are recorded by a pyranometer and a thermal camera, respectively, as shown in Figure 5.16. The measured temperature-decay curves at each location are employed to derive a cooling constant, and a resulting map of this cooling constant provides the basis for finding defects or the boundaries between different substrates.

Figure 5.16 illustrates the integrated data acquisition setup for quasi-active thermography. Two membranes were sourced from WTP (same as the actual membrane) and fixed in turn on a 110 cm (L) × 110 cm (W) × 10 cm (D) aluminium test rig with screws. An IR thermal camera FLIR A615 [233] and a pyranometer Apogee SP-110 [234] were set up 0.5 m horizontally away from the test rig to measure the surface temperature profile of the

membrane and the local solar intensity, respectively. To validate the infrared thermal imaging accuracy, the measured temperature from the thermal camera was at first compared with a FLUKE 287 multimeter contacting thermal probe. A commercial software package was employed to control the thermal camera for recording the temperature evolution of the membrane. The Apogee SP-110 pyranometer was placed on the same level beside the thermal camera (set up 1 m above floor level). The pyranometer was connected to a data logger and the solar intensity was acquired in real-time and time-stamped using commercial data acquisition software. To ensure a synchronous profile for the data, the sampling rate of the pyranometer was set to be the same as the frame rate of the thermal camera (3 Hz). The outdoor laboratory-scaled experiment was set up on the rooftop of a building at Monash University, where the test set-up is not susceptible to any shading from nearby structures or buildings.

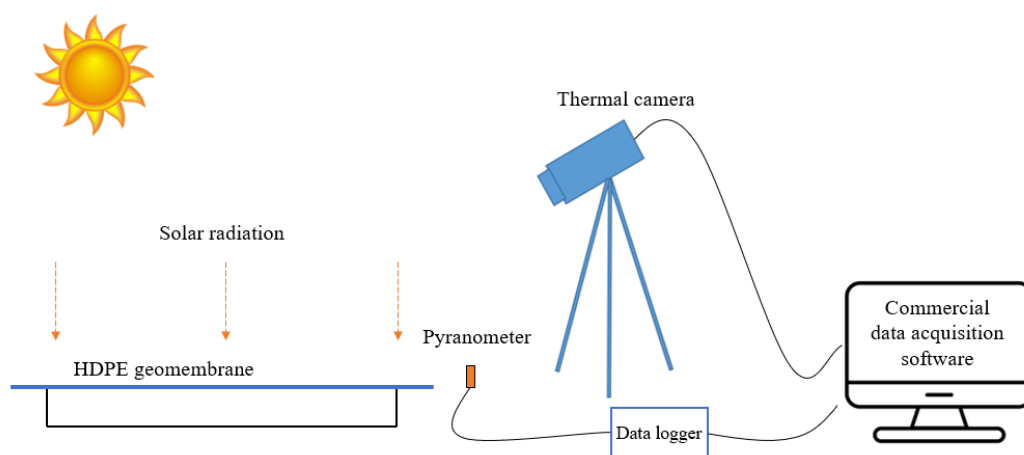


Figure 5.16 Illustration of data acquisition phase in the quasi-active thermography experiment

5.3.1.2 Defects in the HDPE geomembrane with substrates

The aim of this study is to assess the ability of quasi-active thermography to detect underside non-surface-penetrating defects lying over various substrates. In the present experimental work, garden soil was used to simulate scum because its relevant properties (i.e. density, thermal conductivity and specific heat) are similar to those of solid scum, as summarised in Table 4.1, where the thermal diffusivities of each material can be calculated through the given density, thermal conductivity and specific heat [242, 245, 246, 251-253]. Therefore, the membrane in this experiment was placed in contact with soil, water and air to mimic, respectively, contact with scum, sewage and biogas in the treatment plant.

Figures 5.17(a) and 5.17(b) show schematic drawings of the cross-sectional view of the two membranes and the test rig with different substrate configurations. In Figure 5.17(a), a part of the membrane was brought into contact with water with the rest suspended in the air. This simulates biogas pockets under the floating covers at the WTP. In Figure 5.17(b), one part of the membrane is in contact with a soil block, which simulates a region of scum, and the other part is suspended in the air.

Defects of different sizes were manufactured into the underside surface of two separate membranes by laser cutting. Figures 5.18(a) and 5.18(b) show a plan view (top) of the distribution of synthetic defects on the underside of two different membranes, where the geometry of each defect is detailed in Tables 5.3 and 5.4, respectively. As shown in Figure 5.18(a), on the first membrane, defects 1-4 were in contact with water and defects 5-8 were in contact with air. In Figure 5.18(b), defects 1-6 were in contact with soil and defects 7-12 were in contact with air. Figure 5.19 further illustrates the profiles of defects with a cross-sectional view. The two membranes were fixed on the aluminium test rig and left exposed to solar radiation during the daytime for several hours, while transient events resulting from cloud shading were recorded using the IR thermal camera and pyranometer set-up.

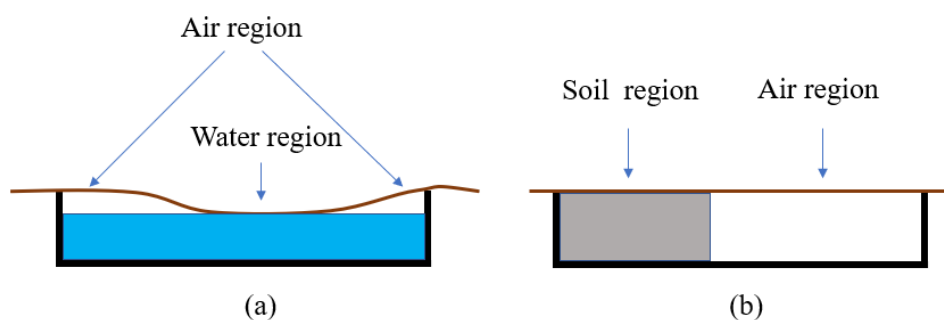


Figure 5.17 Side profiles of the test rig. (a) HDPE geomembrane on air and water. (b) HDPE geomembrane on air and soil

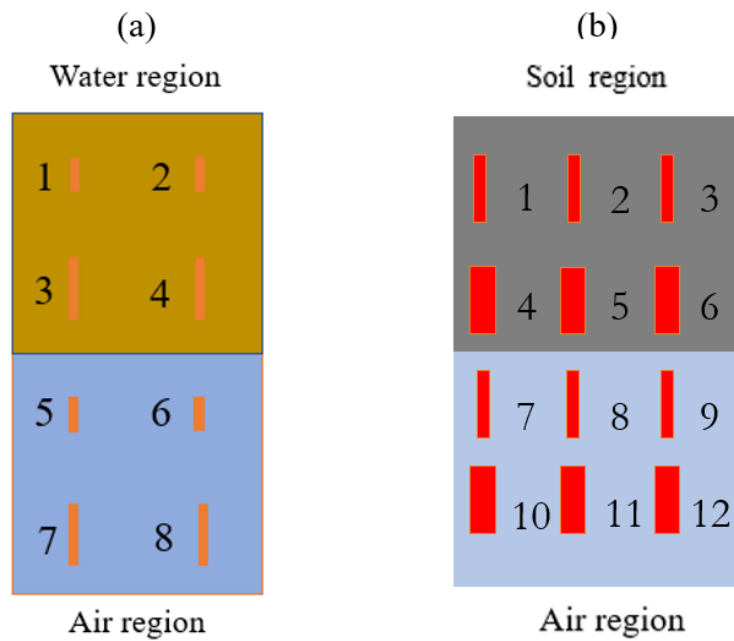


Figure 5.18 Distribution of defects on the HDPE geomembrane. (a) defects in contact with soil and air. (b) defects in contact with water and air

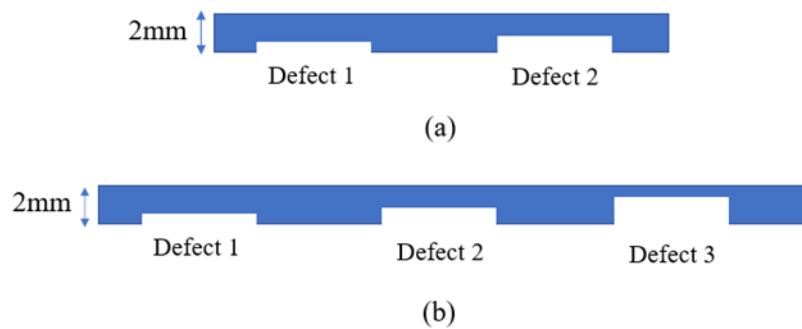


Figure 5.19 Cross-sectional review of two HDPE geomembranes. (a) profiles of defect 1 and defect 5 on the first geomembrane. (b) profiles of defects 1, 2 and 3 on the second geomembrane

Table 5.3 Details of defects of the geomembrane in Figure 5.18 (a)

Defects number	Defects length(cm)	Defect width (cm)	Defect thickness(mm)	Locations of defects
1	5	0.5	0.5	Water region
2	5	0.5	1	
3	10	0.5	0.5	
4	10	0.5	1	

5	5	1	0.5	Air region
6	5	1	1	
7	10	1	0.5	
8	10	1	1	

Table 5.4 Details of defects of geomembrane in Figure 5.18(b)

Defects number	Defects length(cm)	Defects width(cm)	Defects thickness(mm)	Locations of defects
1			0.5	
2		1	1	
3			1.5	Soil region
4			0.5	
5		2	1	
6	10		1.5	
7			0.5	
8		1	1	Air region
9			1.5	
10			0.5	
11		2	1	
12			1.5	

5.3.2 Results and discussion

Two experimental cases were considered as previously described, viz.,

- Case 1: a geomembrane with water and air substrate (Figure 5.18(a)), and,
- Case 2: a geomembrane with soil and air substrate (Figure 5.18(b)).

For both cases, thermal image sequences were acquired at a frame rate of 3 Hz, but to reduce the computational burden of analysis, sequences were down sampled to an effective rate of 0.1 Hz prior to processing.

5.3.2.1 Case 1: Inspection of defects on water and air substrates

The first inspection for Case 1 comprised an observation lasting 20 minutes, starting at 13:15:00, as shown in Figure 5.20. Three cloud shadings events were observed within this

time. Not all the cloud shading events were taken into consideration because some did not cause a significant temperature transient. For example, Figure 5.20 shows a small solar intensity fluctuation within a short time (less than 10 seconds) 1 minute after the start of the experiment, inducing only a subtle change in temperature ($\sim 0.1^\circ\text{C}$) in the membrane. The solar radiation during cloud cover events comprises a series of local maxima (i.e., local heating during the overall cooling event). Such events were therefore excluded from the analysis. In the thermography of a 2 mm thick HDPE membrane, a more significant temperature reduction is required for detection. Therefore, a pragmatic criterion for selecting a useful event for analysis is that the solar intensity should be reduced by more than 400 W/m^2 and cloud shading should last more than 1 minute.

Figure 5.20 shows a desirable cloud shading event starting at around 13:18:08 and ending at 13:19:30 (a duration of 82 s), during which the local solar intensity reduced, resulting in the temperature of the membrane falling from 25.2°C to 22.4°C . The temperature decay curves for all pixels from the highlighted event between the dashed lines in Figure 5.20 were analysed using the three analysis methods described in Chapter 3.

The results are shown in Figure 5.21. They are evaluated based on: (1) the ability to distinguish between the substrates; and (2) the ability to identify subsurface defects. The raw thermal image, shown in Figure 5.21(a), was taken at the midpoint of the transient event. In this image, the water region can be distinguished due to its significantly lower temperature, the defects are visible, but their profiles are not clear.

Figure 5.21(b) shows a map of the cooling constant obtained by the approach described in Newton's cooling law method, based on a calculation encompassing the whole cooling period. The membrane and water regions are more distinct in this result, and the defects in the region with an air substrate produce easily discernible signatures. Defects number 6 and 8 (as identified in Figure 18(a)) exhibit more contrast than defects 5 and 7, which correlates with them being nearer the surface. In the membrane-water region, defects 2 and 4 (cf. Figure 5.18(b)) produce a somewhat weaker contrast that is barely discernible, whereas Defects 1 and 3 are barely visible but visible nonetheless, the former less so because it is partially obscured by a vertical strip artefact, which is consistent with the small size of those defects. Thus, it can be concluded that Newton's cooling law method provides a more effective approach for damage detection compared with the visual inspection of a single image frame.

Figure 5.21(c) illustrates a map of the peak value of the logarithmic second derivative, as presented in Chapter 3. It successfully shows the boundaries between the water and air

regions, and there is sufficient contrast to detect defects 5-8 in the air region, whereas defects in the water region are barely visible. The result from the frame subtraction method is plotted in Figure 5.21(d). Similar to Figure 5.21(c), the boundary between the water region and the air region can be identified via contrast. Defects number 5-8 in the air region can be identified in Figure 5.21(d), and there is also a faint indication of defects 2 and 4 in the water region.

This comparison of the merits and limitations of the three methods is summarised in Table 5.5.

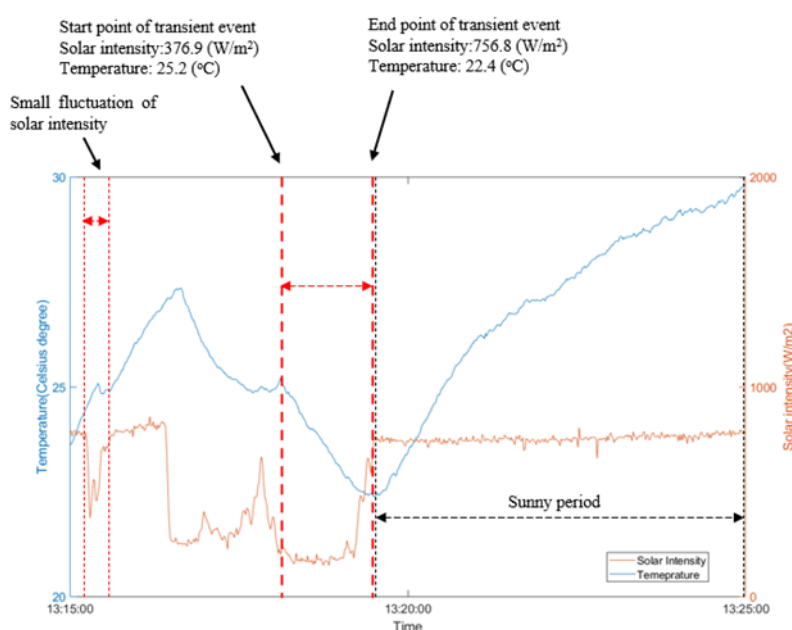


Figure 5.20 Temperature profile from a pixel on no-water region in the thermal image sequences and solar intensity history

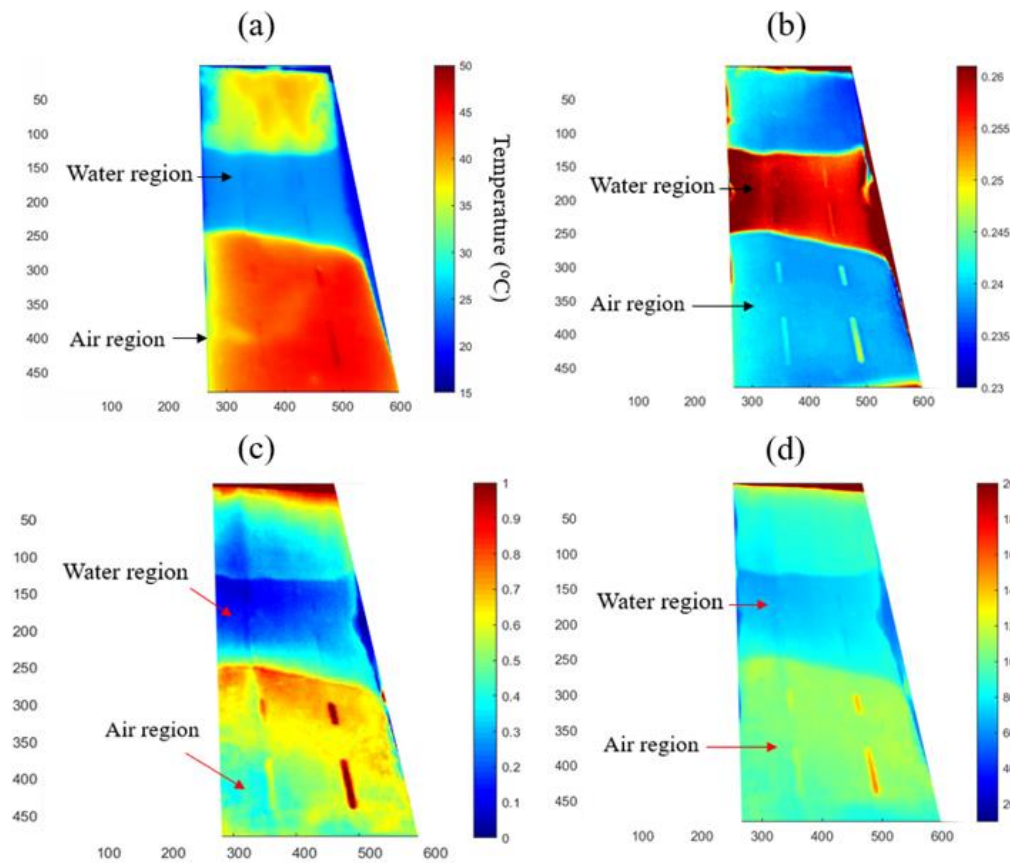


Figure 5.21 Results of analysis of thermal image sequences with different methods: (a) a single frame of the raw thermal image, (b) cooling constant map based on Newton's cooling law analysis, (c) LPSD method, and (d) frame subtraction method.

Table 5.5 Summary of merits and demerits of each method in Case 1

	Air region and water region identification	Defects identification on air region	Defects identification on water region	Image quality
Raw thermal image	Yes	Barely visible	Barely visible	Clear
Newton's cooling law method	Yes	Yes	Yes	Clear
LPSD method	Yes	Yes	Barely visible	Clear

Frame subtraction method	Yes	Yes	Barely visible	Clear
-----------------------------	-----	-----	-------------------	-------

5.3.2.2 Case 2: Inspection of defects on soil and air substrates

For the second case study, the water was drained from the previous set up and garden soil was compacted in the aluminium test rig before being covered by the membrane, ensuring good thermal contact between the membrane and soil. The test set-up was left outdoor overnight to ensure thermal equilibrium.

The quasi-active thermal inspection commenced at 12:00:00 during a period of high solar intensity, as shown in Figure 5.22. A cloud shading event occurred from 12:10:00 to 12:27:45. Local solar intensity decreased from 1100 W/m^2 to 271.6 W/m^2 (a change of 828 W/m^2). This event resulted in a temperature reduction of $12.4 \text{ }^\circ\text{C}$, which was enough for the thermal transient analysis. A short fluctuation in solar intensity was also noted at 12:18:00 during the transient event, but it lasted less than 30 s and did not lead to a significant change in the temperature response of the membrane. Therefore, this fluctuation can be ignored for the purposes of transient thermal analysis.

The three methods described in Chapter3 were applied, and the results are presented in Figure 5.23. Figure 5.23(a) shows a single frame of the raw thermal image, which was taken at the mid-point of the transient events (12:20:00) with the colour bar showing the temperature range. The single frame raw thermal image presented in Figure 5.23(a) shows high thermal contrast between the soil region and the air region, defects in the soil region are visible but defects in the air region are not visible.

Figure 5.23(b) shows a map of the cooling constant obtained from Newton's cooling law method. The boundary between the soil and air regions can again be clearly identified on the map. However, the defects in the air region are not visible, and there is only a faint indication of defects 4-6 in the soil region.

Figure 5.23(c) shows a map of the peak value of the logarithmic second derivative of the membrane temperature. This map shows a contrast between the soil region and the air region, but the subsurface defects could not be detected except for faint indications of defects 5 and 6 in the soil substrate.

The results from the frame subtraction method are shown in Figure 5.23(d). This method was implemented with the first frame (corresponding to t_0) taken at the start of the transient

event, the final frame at the end of the transient event at approximately 12:27:00, and with a time step of $\Delta t = 10$ s. Most of the subsurface defects can be identified (specifically defects 2,3,5,6 in the soil region and defects 8,9,11,12 in the air region), and the colour contrast can be considered to provide an indication of the defect depth, in view of the observation that the strength of contrast increases with decreasing membrane thickness. However, the contrast between substrates is reduced due to the altered threshold that has been employed in this image display, so as to highlight the defects.

These results demonstrate the advantages of analysing the entire thermal transient profile rather than a single image frame for detecting subsurface defects, even in the presence of different substrates. The merits and limitations of the three transient analysis methods are summarised in Table 5.6, which can be compared with Table 5.5 for Case 1. It appears that a combination of the three analysis methods can best achieve the objectives of identifying the different substrates, as well as detecting subsurface defects when in contact with different substrates. For example, maps of the cooling constant from Newton's cooling law method and of the LPSD can most clearly distinguish the substrates beneath the membrane, whereas the map from the frame subtraction method can most clearly detect subsurface defects when in contact with either soil, water or air region. However, a further systematic study of the process parameters is required to optimise the implementation of these techniques in practical applications.

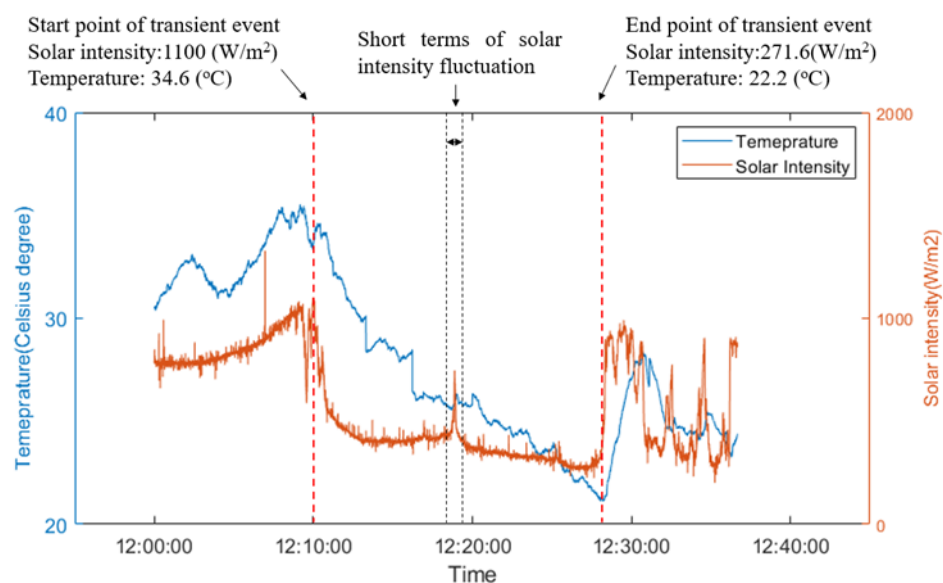


Figure 5.22 Temperature profile from a pixel on the air region in thermal image sequences and solar intensity history

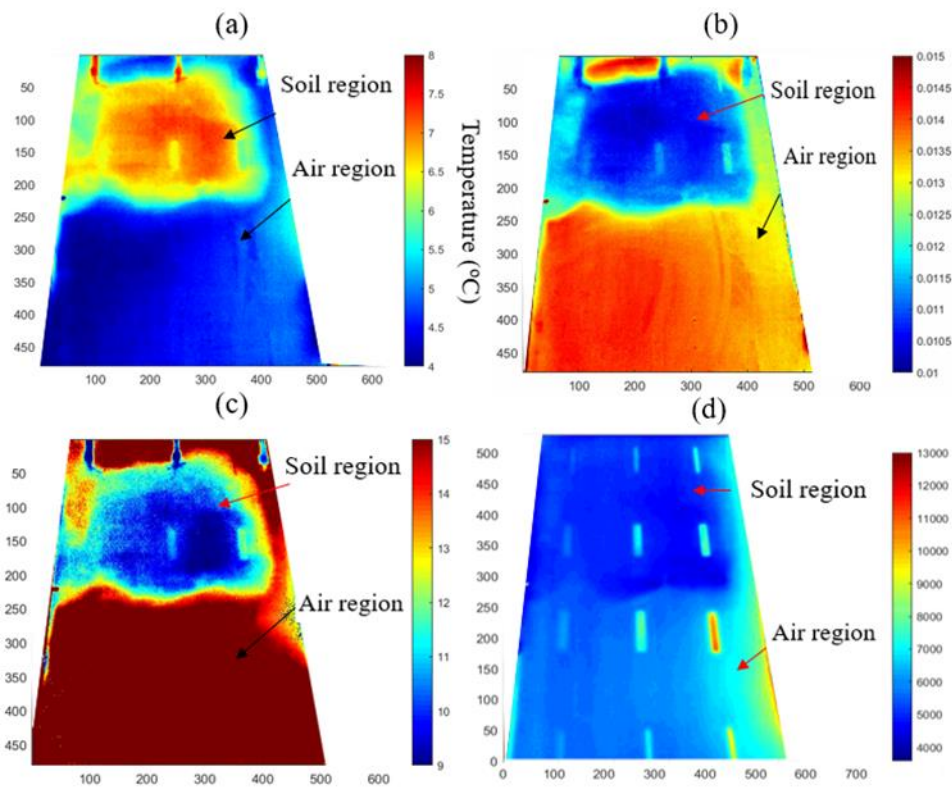


Figure 5.23 Results of analysis of thermal image sequences. (a) a single frame of the raw thermal image. (b) cooling constant map of Newton's cooling law analysis. (c) result of the LPSD method. (d) result of the frame subtraction method

Table 5.6 Summary of merits and demerits of each method in Case 2

	Air region and soil region identification	Defects identification on air region	Defects identification on soil region	Image quality
Raw thermal image	Yes	No	4-6 are visible	Clear
Newton's cooling law method	Yes	No	4-6 are visible	Clear

LPSD method	Yes	No	5-6 are visible	Clear
Frame subtraction method	Yes	Yes	Yes	Not Clear

5.3.2.3 Investigation and Monitoring period and frame rate

Throughout the experiment conducted in Section 5.3.2.2, it is noticed that the outcome from Newton's cooling law analysis depends heavily on the time taken for analysis (period of the transient event) and frame rate for processing. The thermal images were acquired at 3 Hz, but to save computational power for post-processing, only the thermal images with 10 seconds intervals were chosen for analysis in Case 1 (135 seconds) and Case 2 (20 minutes), respectively. To further investigate the effect of frame processing rate, the same results obtained in Case 2 is used.

Thermal images with 5 minutes interval over the entire 20 minutes thermal cooling transient were first tried with four frames for processing. The resultant cooling constant map is presented in Figure 5.24 (a). Figure 5.24 (a) shows the soil region becomes larger when compared to Figure 5.23 (c), and the soil region and air region still can be distinguished through the contrast, while all of the subsurface defects are hard to be detected or identified through the contrast.

The post-processing was then conducted using all the thermal images (3 Hz) within the transient event, and the processed data was presented in Figure 5.24 (b). With a high frame rate for processing, all subsurface defects were identified, and the depth of the defects can also be distinguished by the contrast. However, the soil region and air region can no longer distinguish as there is no clear boundary to distinguish these two regions.

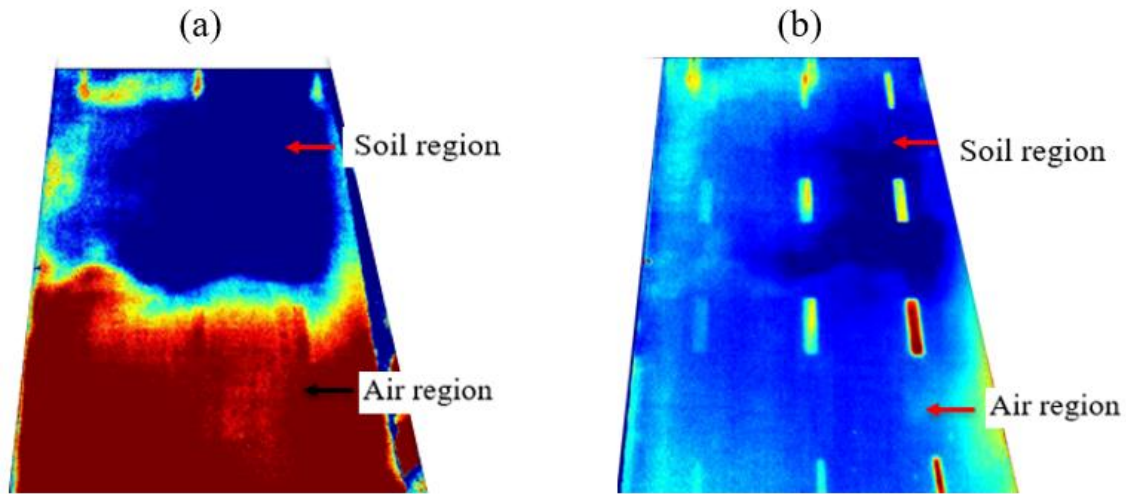


Figure 5.24 Cooling constant maps from Newton's cooling law (a) monitoring period 20mins, frame rate 5mins/frame, (b) monitoring period 5 mins, frame rate 3 frame/second

It can be found that in Figure 5.24 (b), defects with different depths have different values of cooling constant. This indicates that there is a relation between the defect depth and the cooling constant. Therefore, cooling constant values on the geomembrane surface with different defect depths were selected, and a standard deviation error bar with 2σ is plotted in Figure 5.25. It can be observed that:

- Cooling constant values of geomembrane increases with the increase of defect depth.
- Geomembrane over the air region has overall larger cooling constants than that of the geomembrane over the soil region.

Therefore, it can be concluded that the ability to detect these non-surface penetrating defects with different substrate conditions using quasi-active thermography is determined by the monitoring period and the post-processing frame rate. A lower frame rate is useful for distinguishing different mediums of substrates, whereas the higher frame rate is helpful in the tasks of identifying subsurface defects. Hence, one can select an optimum frame rate for post-processing the data acquired using quasi-active thermography according to the inspection aims.

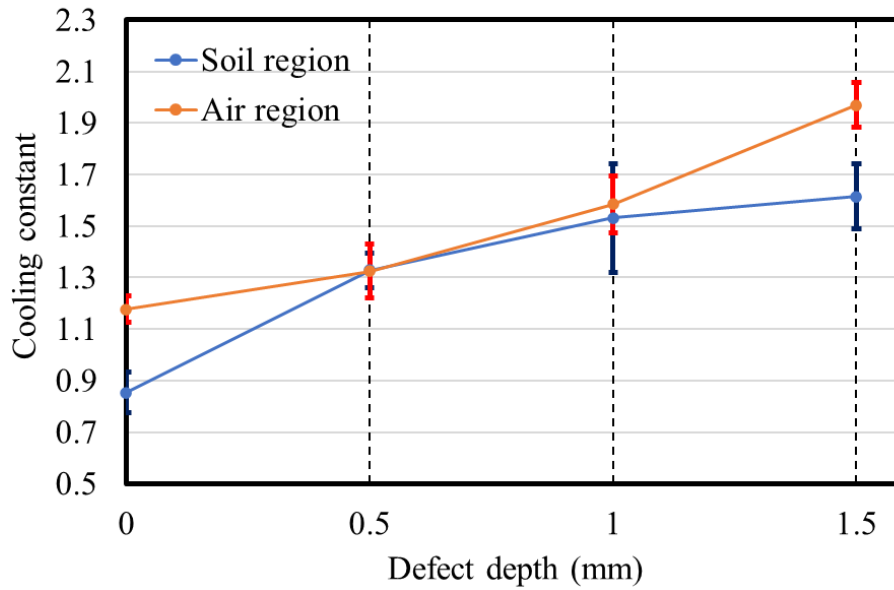


Figure 5.25 Error bars with 2σ for cooling constants of defects on the air region and the soil region

5.3.3 Conclusions

This chapter presents new concepts and algorithms for quasi-active thermography inspection of an HDPE membrane in contact with various substrates. This quasi-active approach relies on naturally occurring variations in solar intensity due to cloud cover events to generate temperature transients suitable for thermographic analysis. A laboratory-scale experimental evaluation of this approach was undertaken. The experimental results verified that cloud shadings that result in reduced solar intensity could lead to identifiable temperature decay transients. It is determined that only transients resulting from solar intensity reductions of more than 400 W/m^2 lasting for more than 1 minute should be employed for analysis. Three transient thermal image processing methods were investigated based on (i) a map of the cooling constant obtained by curve-fitting the temperature decay curve to an assumed exponential decay, in accordance with Newton's law of cooling; (ii) a map of the peak value of the LPSD of temperature; (iii) a frame subtraction method that employs the absolute value of the temperature differences between successive frames at a prescribed time interval. The results were compared with those from a single-frame thermal image to assess their relative capability to identify various substrates and defect subsurface defects on different substrates. The key findings of this study are summarised as:

- Compared to the map of temperature obtained from a single frame of the raw thermal image, the analysis based on the transient cooling process of membranes can better determine the presence of subsurface defects. The surface temperature of the

membrane can be used to distinguish the substrate medium (soil, water and air) and subsurface defects in the membrane.

- The three different thermal transient analysis methods have their own merits and limitations so that a combination of the three appears to be most suitable.
- The modified LPSD and Newton's cooling law methods show reasonable performance in distinguishing different substrates under the membrane cover, but the defect profiles are comparatively hard to identify on different substrates.
- The frame subtraction method with a predefined time interval provides the best indication of subsurface defects, especially in the presence of soil and air substrates, and the contrast values also correlate with the depth of the defects, thereby suggesting that a quantitative evaluation of defect severity may be possible.

While these results are very promising, a detailed computational modelling, is still required to optimise the selection of parameters for the various approaches. A bigger area of thermal imaging monitoring from a greater distance is also demonstrated in Chapter 7.

CHAPTER SIX

6 Assessing the state of scum-berg transition process under the floating covers using thermal means

The structural integrity of the geomembrane covers may be affected by the development of scum that accumulates on the underside of the covers and can even deform the cover, and the states of the scum transit from fluffy to hard over time. A non-contact thermography method was reported in Chapters 4 and 5, to identify the features and defects under the cover using ambient solar radiation profiles. It is known that the scum is formed initially from liquid matter. The work presented in this chapter investigated the potential of the thermography technique to identify the various stages of the transition of scum from a soft liquid state to the ultimate development of solid scum. Given that this development is hard to replicate experimentally, the ability to monitor such development was investigated with a series of finite element analyses (FEA). In these FEA, the input conditions for the model include local weather information such as ambient temperature and solar intensity. Transient thermal analyses were conducted to identify the various stages of development of the scum beneath the membrane cover. The FEA model was first validated with laboratory test results. It is subsequently used to profile the development of the scum as it transitions from a soft liquid state to a hard-solid state.

6.1 Introduction

Given that scums under the cover accumulate and transits gradually, and the liquid scums are known to transform into solid and accumulate under the cover. An accumulation of scum on the underside of the cover can reduce the volume of the anaerobic region under the cover available to treat all of the incoming raw sewage and can even impact the amount of biogas generated by the microorganisms as well as the ability to harvest what biogas is produced. In addition, scum exists in a continuum between its fluffy state to its solid-state. The solid scum can result in a more significant deformation on the cover structure. One of the challenges in managing this cover is the ability to determine the state of the scum that is accumulated beneath.

The distribution and state of the scum under the covers need to be determined to assist planners and operators in making better decisions relating to the management and maintenance of the anaerobic lagoons. Current practice at the WTP to establish the extent

and state of the scum under the cover involves a person walking on the cover. The state of scum is qualitatively (i.e., subjectively) assessed as “Hard”, “Medium”, “Soft”, and “Fluffy”. This form of assessment is inefficient and exposes the workers to potential risks[25]. This chapter aims to determine if the thermal transient technique developed by Yue et al. [37, 127] can be used to establish a quantitative methodology to classify the state of the scum formation.

This chapter reports an investigation into the effects of the state of scum formed under the membrane material on the thermal transient on the floating cover during two naturally occurring thermal events. This study aims to build up a localised quick determination tool to identify the rate of temperature change of the HDPE geomembrane covers and to determine the state of scum formation. As shown in Figure 6.1, in work presented, the finite element model of a geomembrane/sewage is first validated using a set of experimental results. The local weather information includes solar intensity and ambient temperature recorded experimentally by pyranometers and thermal couples, respectively. These acquired data will be used as input into the finite element analysis software to solve the resultant temperature change of the HDPE geomembrane, where the underside of the HDPE geomembrane is in contact with the varied state of scum. The thermal transients of the HDPE geomembrane due to the naturally changing solar radiation is calculated. Newton’s cooling law is used to calculate the cooling constant associated with the different states of scum.

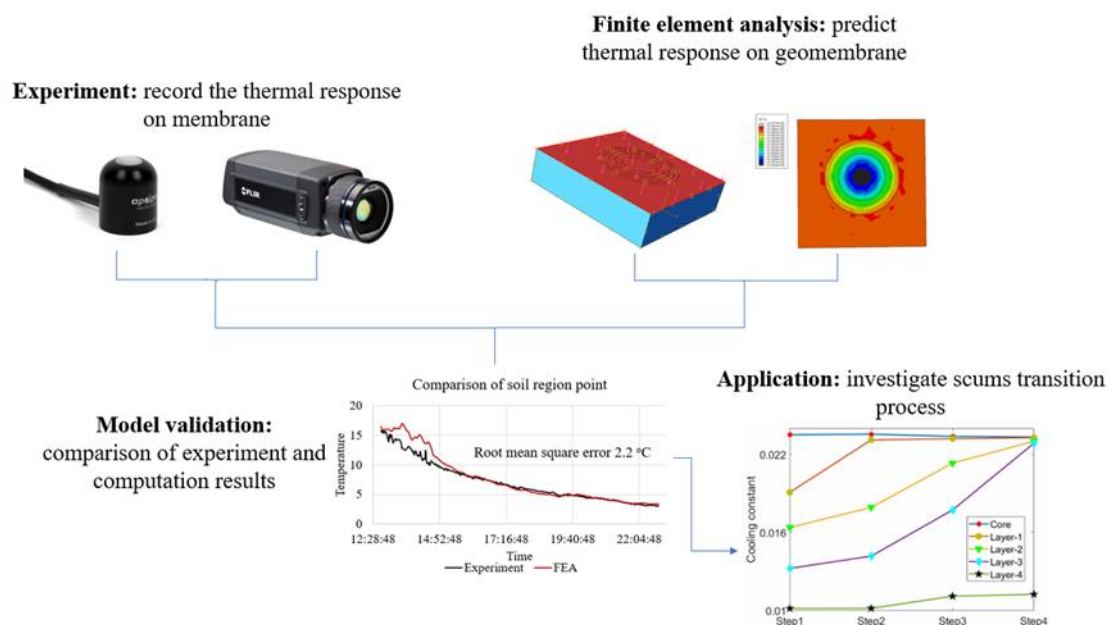


Figure 6.1 Illustration of the procedure of using ambient solar intensity and temperature to estimate the temperature profile of HDPE geomembrane

6.2 Methodology

6.2.1 Experiment set up

A laboratory-scale experiment was set up at an open space on an exposed roof-top to simulate the anaerobic lagoons at the WTP. Figure 6.2 shows a 1m × 0.5m HDPE geomembrane specimen installed on an aluminium apparatus. The edges of the HDPE geomembrane were clamped on the perimeters of the apparatus by aluminium frames. To simulate the accumulation of scumberg under the cover, some region of the tray was filled with clayey soil. The membrane was installed over the tray where there are regions in contact with the clayey soil and regions suspended over the air (termed as “no-soil” region).

An Apogee SP-110 pyranometer [234] and Fluke 287 multi-meter were deployed to record the local weather data. Both of them were put alongside the test apparatus for the entire one-day experiment. The experiment set up was put on the rooftop of a building and exposed to solar radiation over 24 hours.



Figure 6.2 HDPE geomembrane specimen on test apparatus

A FLIR A615 thermal camera [233] was set up alongside the HDPE geomembrane to measure the surface temperature (see Figure 6.3). It was deployed with the pyranometer and temperature probe to monitor the temperature profile of the geomembrane at the same time. Temperature profiles are calculated by the finite element models and will be verified by the recordings from the thermal camera.

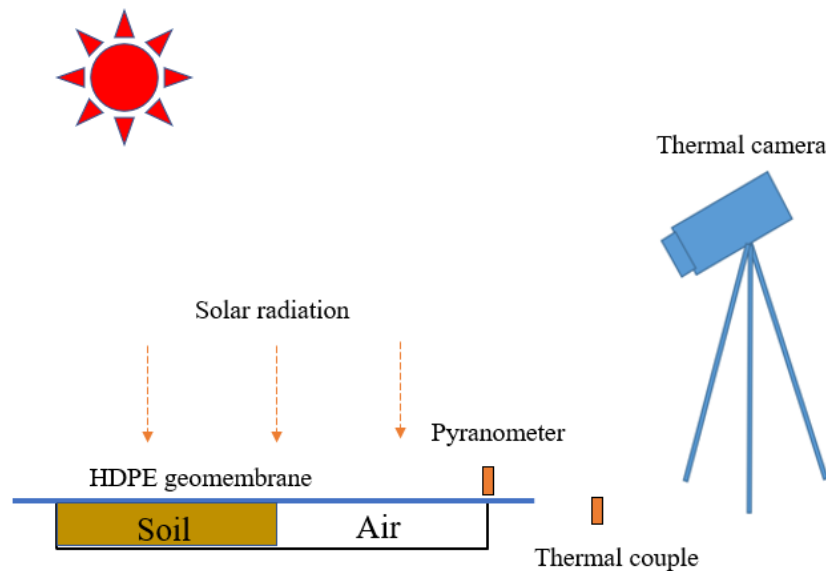


Figure 6.3 Illustration of the experiment set-up

As shown in Figure 6.4, the experiment started at 6 AM on the first day and ended at 6 AM on the morning of the second day. A pyranometer was set up to measure the solar intensity with a sampling rate of 3 Hz, and the temperature probe was set to measure the ambient temperature once every 10 mins. It can be observed that the solar intensity increased from 0 W/m² at 6 AM till to ~650 W/m² at around 12 noon and decreased thereafter, due to extensive cloud cover. After the sunset, the solar intensity remains at 0 W/m² until the sun rises in the morning on the second day. The recorded solar radiation is used as input into the FE model to predict HDPE geomembrane during the day. The temperature change on the geomembrane during the experiment was recorded with a thermal camera.

Temperature profiles of a point on the surface of the geomembrane that is in contact with the garden soil and a point on the surface of the geomembrane at the “no-soil” region are shown in Figure 6.5. This figure shows that the thermal response of the membrane is dependent on the material that it is in contact with on its underside. The aim is to determine if these thermal responses can be used to quantify the state of the formation of scum-berg under the membrane. This will be investigated using a series of FEA where the analyses approach is first validated against the membrane temperature measured during the 24-hour period.

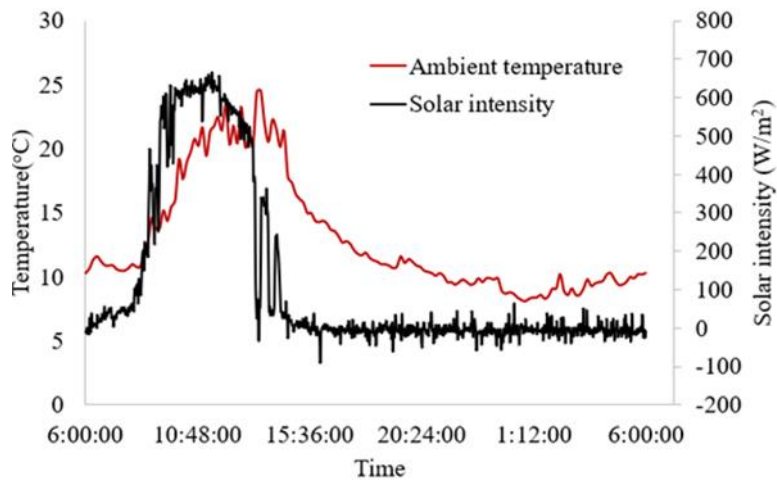


Figure 6.4 Recorded solar intensity and ambient temperature profile

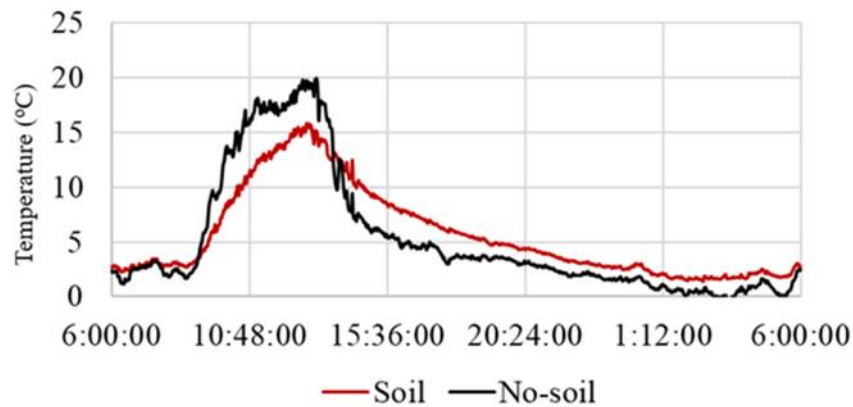


Figure 6.5 Temperature profiles of soil region and no-soil region points on the HDPE geomembrane

6.2.2 Finite element model

In this study, Abaqus Computer-Aided Engineering (CAE) is deployed to analyse the temperature change of the HDPE geomembrane using the measured solar intensity as an input condition and ambient temperature as the predefined varied fields. As shown in the Figure 6.6, The 0.5m×1m 3-D membrane model was applied to the HDPE geomembrane instance with the mesh size of 1mm. Given that the temperature change of the HDPE geomembrane under the cycle of solar radiation and ambient temperature is the point of interest, the thermal expansion effect of the HDPE geomembrane is temporarily not taken into consideration.

In the validation process with the thermal camera, given that the scum exists under the cover and hard to be obtained, clayey soil was deployed in the experiment to simulate the scums

at the water treatment. Therefore, in the FE model, soil properties were also applied to the subsurface solid model to compare the FE analysis result with the experiment results. The emissivity of the HDPE geomembrane at the WTP had been measured in previous works [127]. The time-dependent thermal FE analysis is conducted over 24 hours with a time step of 100s.

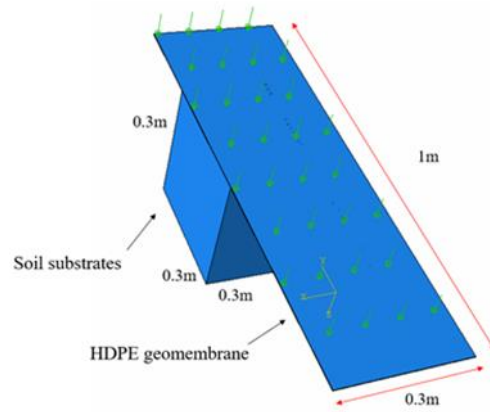


Figure 6.6 Finite element model (FEM) of geomembrane contacts with soil

6.2.3 Newton's cooling law and temperature validation

Newton's cooling law [188] is used to compare the predicted temperatures from the FE analysis with the measurement of thermal imaging measurements. During the cooling process, Newton's law of cooling reveals that the cooling rate of the objects is proportional to the temperature difference between the ambient and the object. The relation is expressed as:

$$\frac{dT_{GM}}{dt} = -k(T_{GM} - T_{amb}) \quad (6.1)$$

After integration and the identification of the initial condition, the equation becomes:

$$T_{GM} = T_a + (T_i - T_{amb})e^{-bt} \quad (6.2)$$

where b is the cooling constant which implies the rate of the temperature reduction during cooling. In the heat transfer process, where the term k indicates how fast the temperature of the object decays to the surrounding temperature. Since the ambient temperature varies with time, the geomembrane temperature difference between the FE analysis and experiment measurements may also vary with time. In addition, when the geomembrane is in touch with the soil at the subsurface, the temperature at the soil region will decay slower than the no-soil region. The cooling constant can be used to define the extent of the soil attached to the geomembrane.

6.3 Results and discussions

Figure 6.7 shows the resultant temperature distribution of the HDPE geomembrane during the heating process using FEA. The initial temperatures on the surface of the membrane were set at 3°C to correspond to experimental data. The temperatures of both regions increased with the increased power of solar radiation. The maximum temperature was attained at around 11:30:00 am, the HDPE geomembrane cooled in the afternoon with the reduction in solar radiation and ambient temperature. The thermal contrast highlights the soil region from the no-soil region.

Given that the heat flux was evenly applied on the surface of the HDPE geomembrane, the nodal temperature on each region was the same. Figure 6.8 shows the temperature profiles of nodes at the soil region and the no-soil region. When the solar intensity is equal to zero during the night, the temperatures of the geomembrane decreased slowly because of the heat exchange with the ambient.

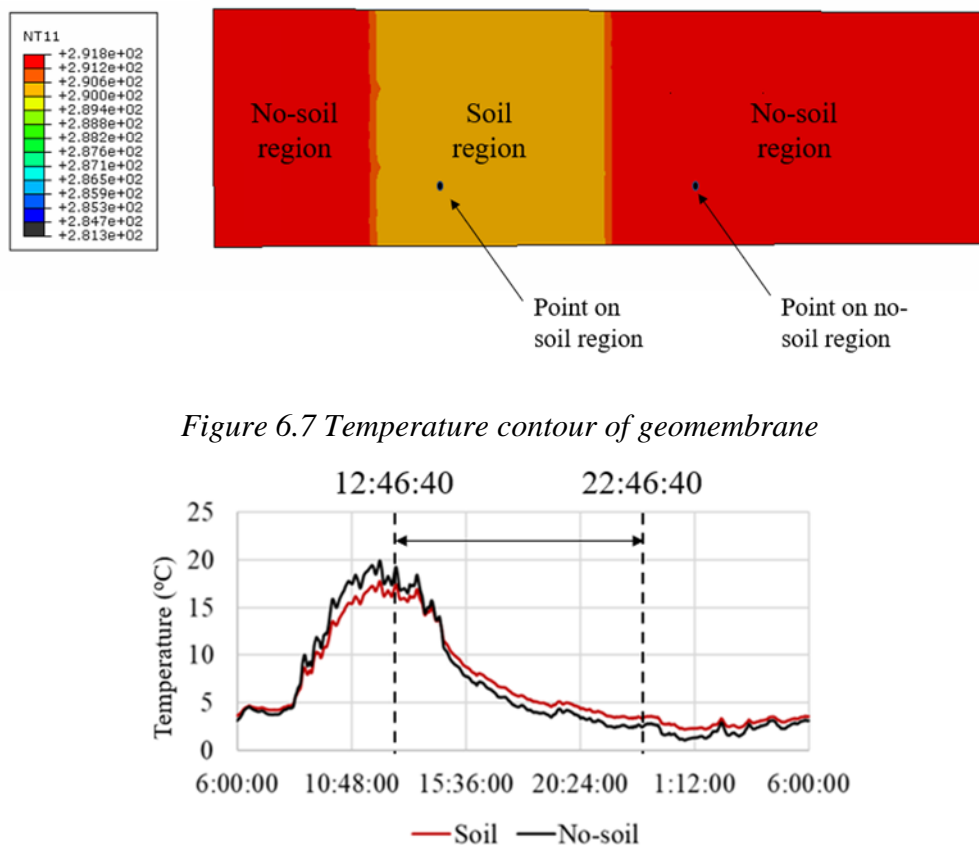


Figure 6.7 Temperature contour of geomembrane

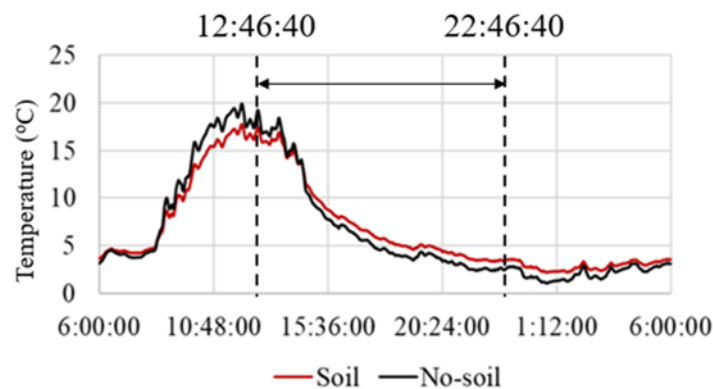


Figure 6.8 Predicted temperature profile of HDPE geomembrane from FE analysis

The FEA results from 12:46:40 to 22:46:40 in Figure 6.8 were compared with the experimental measurements. Figure 6.9 shows the comparison between the FEA and experimental thermal response of the cover over the soil region and the no-soil region. The root mean square error of temperature between the measurement and simulation for no-soil region points is 2.2 °C, and the average temperature difference for the soil region is 8.7°C. The discrepancy in the results for the soil region is attributed to the thermal properties of the soil used in the model. However, the temperature difference between the no-soil region point and soil region point can still be identified.

In addition, the cooling constants were calculated from FEA data and with the experimental data. Table 6.1 shows the good agreement with the calculated cooling constants obtained from the measurements and the simulations. Therefore, the difference in the cooling constant calculated at the soil region and no-soil region will be further used to identify different states of scums in the next section.

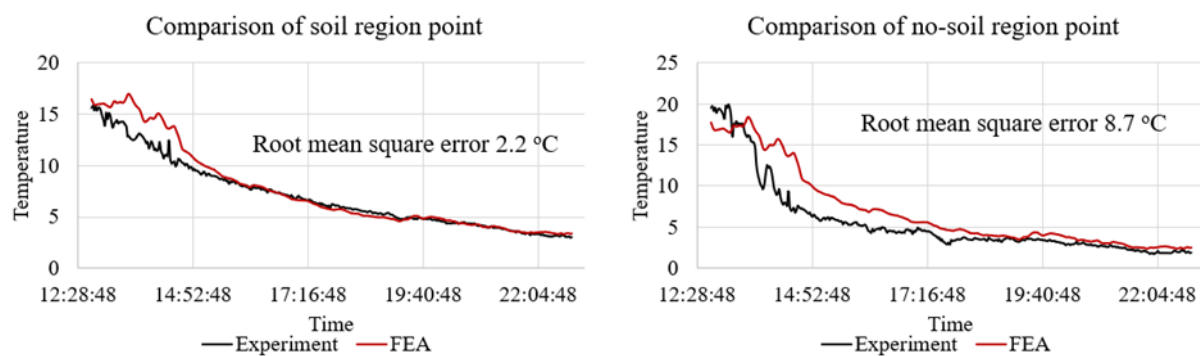


Figure 6.9 Comparison of FE results and experiment measurements

Table 6.1 Illustration of cooling constants

	Experiment		FEA	
	Soil region	No-soil region	Soil region	No-soil region
Cooling constant	0.0077	0.0162	0.0067	0.0123
R-squared	0.99	0.95	0.97	0.95

6.4 Monitoring scum transition

The part of the chapter aims to investigate the thermal response of the membrane due to the changing state of the scum as it transits from its fluffy state to a solid-state. Figure 6.10 shows the simulated geometry of the scum substrates. This 3-D substrates model comprises of 2 parts;(1) the base part of the lagoon model simulating liquid sewage, (2) the parts

simulating the developing scumberg (denoted as core and layer1-layer4). The geomembrane is simulated as a $2\text{m} \times 2\text{m} \times 2\text{mm}$ layer on the top of the lagoon model.

To simulate the transition process of the scums, the various parts of the lagoon model (core and layer1 – layer 4) were assigned with different thermal properties as the states of the scums will gradually transform from fluffy scums to hard scums. It was reported that the bulk density of the scums would increase with the water content [247, 254], and thermal properties of scums such as specific heat and thermal conductivity are lower than those of water. The thermal properties of different states of scums are normalized from hard scum to sewage, and the interpolated thermal properties were shown in Figure 6.11. During the scums transition process, thermal properties of the corresponding region are altered with values in each analyses step to simulate the transition of the state of scumberg from its fluffy to solid-state. The thermal properties in different stages during the transition are defined in 5 states: hard scum, semi-solid scum1, semi-solid scum2, semi-solid scum3 and liquid raw sewage. Given that scums gradually harden over time, the initial state of the model is defined as sewage, and the model will be assigned with interpolated thermal properties of scum to simulate its transition to hard scum. The transitional thermal properties of each layer will be changed in the steps shown in Table 6.2. The transitions are simulated as a 4-step process where the properties of layer1 to layer4 will transit from liquid sewage to hard scum.

The simulation uses input from a pyranometer, and ambient temperature measured for 24 hours (from 6 AM and ended at 6 AM the next day). These measured inputs are set to repeat for 12 days (see Figure 6.12) to simulate exposing the geomembrane over 12 days. At each state of scumberg formation, the model is subject to a 3-cycle day-night-day exposure. On the 4-th day, the state of the scumberg will change as in Table 6.2 and be subject to another 3-cycle exposure. The process is terminated on the 12th day. These exposures allow for the collection of transient temperature cycles each day during the scumberg transition process. The cooling constants of each step during these transitions are calculated.

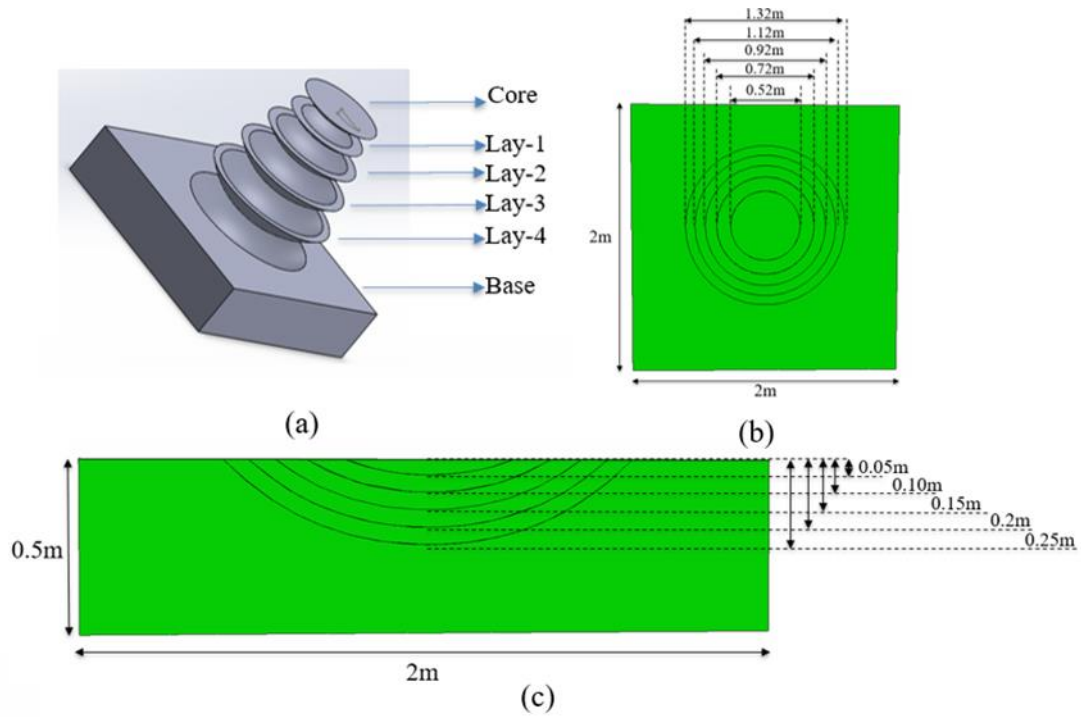


Figure 6.10 Illustration of geometry details of the substrates model. (a) Exploded view of the assembly. (b) Top view of the assembly. (c) Cross-sectional view of the assembly

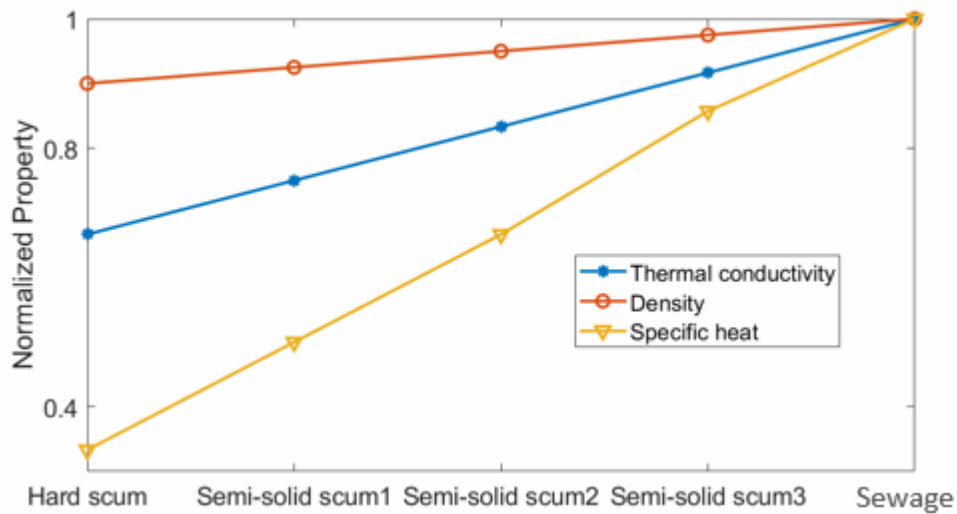


Figure 6.11 Interpolated thermal properties of the base model. Thermal properties change from solid scum to sewage

Table 6.2 Instances state in each analysis step

Region	Step-1	Step-2	Step-3	Step-4
Core	Solid scum	Solid scum	Solids scum	Solid scum

Layer-1	Semi-solid scum 1	Solid scum	Solid scum	Solid scum
Layer-2	Semi-solid scum 2	Semi-solid scum 1	Solid scum	Solid scum
Layer-3	Semi-solid scum 3	Semi-solid scum 2	Semi-solid scum 1	Solid scum
Layer-4	Sewage	Semi-solid scum 3	Semi-solid scum 2	Semi-solid scum 1
Base	Sewage	Sewage	Sewage	Sewage

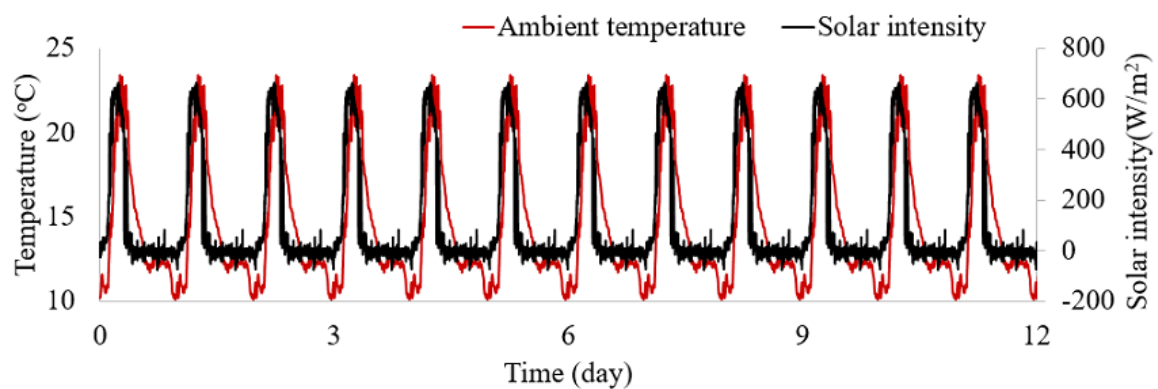


Figure 6.12 Input ambient temperature and solar intensity profiles

Five (5) nodes were selected on the geomembrane regions which contact with the core, layer-1, layer-2, layer-3 and layer-4 of the lagoon model, respectively, and their temperature profiles over 12 days were extracted from computing results and plotted (see Figure 6.13). The initial temperature of the sewage part (base), the scum parts (core to layer-4) and the geomembrane part are set as same at the beginning of the transient heat transfer process. During the 12-day exposure and the corresponding changes in the scumberg, the following are observed:

- From Day 1-3 (step1), Figure 6.13(a), temperature profiles on each region of geomembrane with different substrates, as defined in Table 6.2, show different transient thermal responses. The temperature of the geomembrane region, which contact with the core of the scum increases fastest, and the geomembrane region with layer-4 (liquid sewage) has the lowest temperature change rate.
- From Day 4-6(step2), Figure 6.13(b), the properties of the scum-berg in layer1-layer4 are changed in accordance with Table 6.2. The thermal responses at each region on the

geomembrane are affected by different heat transfer coefficients arising from the change in the state of the scumberg.

- The results from Day 7-9 and Day 10-12 are shown in Figure 6.13(c) and Figure 6.13(d), respectively. During these periods, all layers of the lagoon model have transmitted to a harder state. Both the rate of change of temperature and the maximum temperature values on the geomembrane have increased.

The results in Figure 6.13 shows that the transition of the state of the under-cover scums can be monitored using the thermal transients on the geomembrane when it is in contact with scums.

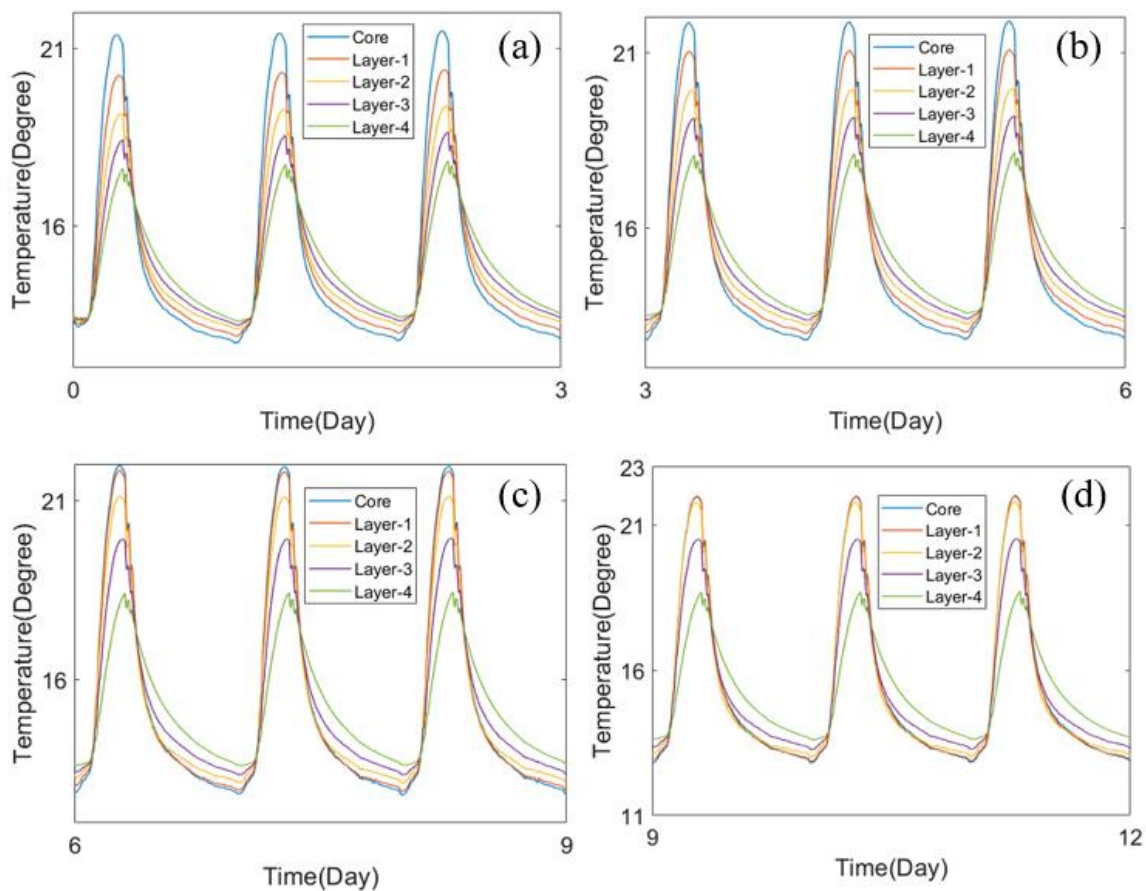


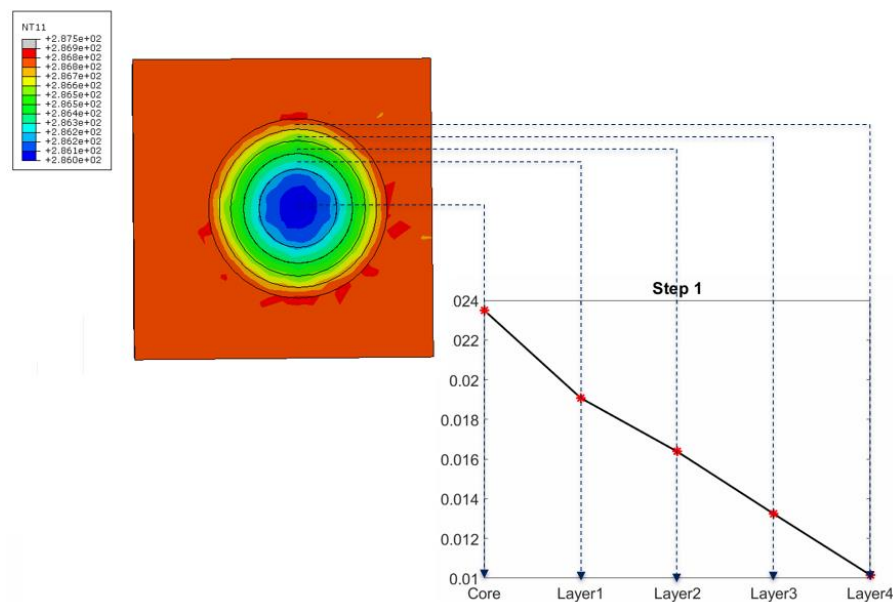
Figure 6.13 Predicted temperature profiles for each region on the geomembrane

The results from the FEA were used to calculate the cooling constants of the geomembrane during the scums transition. At each step (Table 6.2), temperature decay profiles of the nodes on each region on the geomembrane was curve fitted by Newton's cooling law. The temperature contours of the lagoon model in each step are shown in Figure 6.14. The calculated cooling constant at the corresponding regions is plotted on the right of the figure.

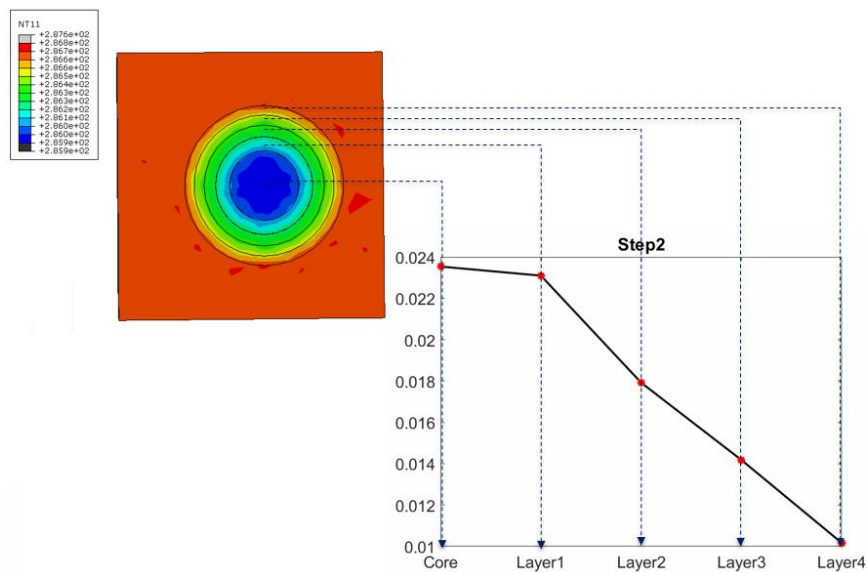
The temperature contour is plotted at the end of the heating cycle in each step. This is when the temperature contrast is most significant in each day in the model.

In Figure 6.14(a), hard scum at the core part of the lagoon is clearly defined. The cooling constants plot shows that the cooling constant of each region on the geomembrane is affected by the scum thermal properties (outer layers of the lagoon model are semi-solid scums at step1).

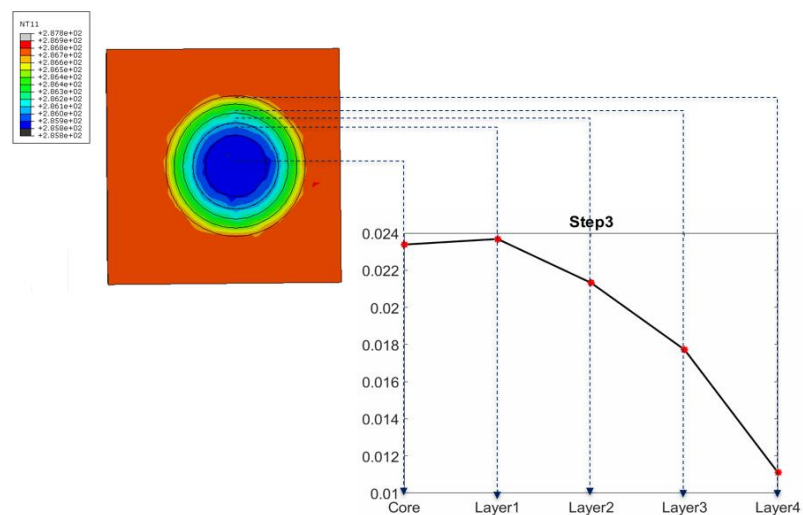
In Figure 6.14(b), hard scums are now expanded to layer-1 of the model, and all other layers are assumed to have become harder than that in step-1. This can also be observed through the temperature contrast. The cooling constant of layer-2 is now approaching that of the core region. However, it is smaller than that of the core region as a result of the lateral thermal conduction with layer-3. In Figures 6.14(c) and 6.14(d), the temperature contour and the cooling constants further highlighted the development of the scumbers. The cooling constants of each region on the geomembrane in each step are summarised in Figure 6.15. These results highlight the potential of using thermal transients to determine the state of the scumberg in contact with the underside of the membrane and the use of the cooling constants to quantify the state of the scumberg that are accumulating on the underside of the membrane. This wide-area analyses technique can potentially reduce the reliance on personnel to walk on the cover to do a manual qualitative inspection.



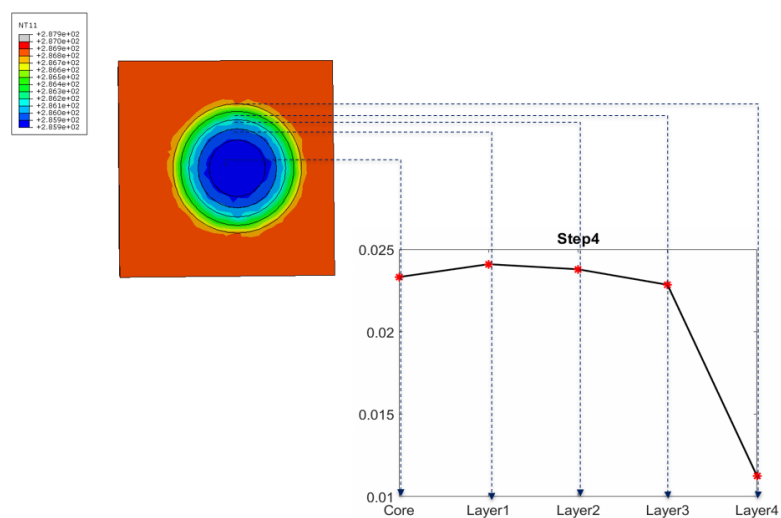
(a)



(b)



(c)



(d)

Figure 6.14 Illustration of cooling constants distributions over each step with the temperature contours. (a-d) step 1, step 2, step 3, and step 4 respectively

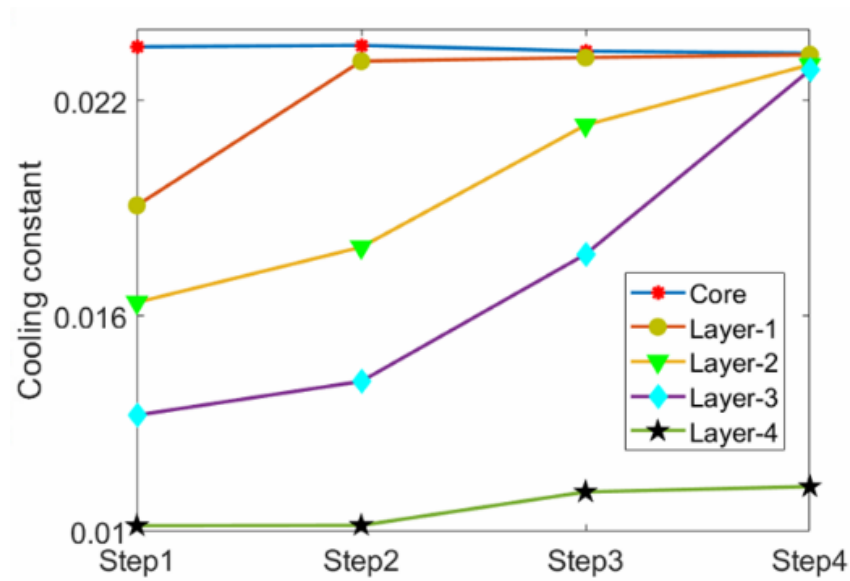


Figure 6.15 Illustration of cooling constant changes for each region on the geomembrane over different steps

6.5 Conclusion

This chapter introduced a proactive computational study to analyse the temperature evolutions of the geomembrane and the scums transition process. The developed technique used environment weather information, such as ambient temperature and solar intensity, to predict the temperature changes of scums during the transition process. In this chapter, the measured weather data from a lab-scale experiment and input of the measured data was imported into the finite element model for computing. The reliability of the temperature prediction method was verified by thermal imaging measurement. This chapter also demonstrated an investigation of the temperature change of the geomembrane cover when it is in touch with the scums during the scums transition process. When the scum transit to a solid-state, the change of thermal properties of scums will influence the temperature profiles of the corresponding regions on the geomembrane. The results show that when the scums transform from a soft state to a semi-solid state and a solid-state, the thermal response of the scum varies, and this can also be identified through monitoring the temperature profiles of the regions on the geomembrane. Therefore, the developed temperature prediction technique can assist in monitoring the temperature change of the geomembrane in the long term efficiently, economically, and safely. Thermal effects resulting from the transition of scums on the HDPE geomembrane cover can also be estimated.

CHAPTER SEVEN

7 Structural health monitoring on large scale geomembranes floating covers using thermography

The monitoring of scums and different features under the geomembrane has been reported in Chapter 4, and the detection of defects has been reported in Chapter 5. In this chapter, the previously developed thermography technique was applied to an on-site monitoring investigation on large-scale floating covers located at the WTP of Melbourne water corporation. Two regions on the floating covers were monitored with long-term thermography. Ambient weather information was recorded to help analyse the transient temperature change events on the surface of the geomembranes. A thermal camera was located nearby the monitored regions and monitored the temperature evolutions of the geomembranes. The acquired thermal image sequences were analysed using the LPSD method and K-mean image segmentation technique. A segmented cover map was generated to identify distributions of different substances. This on-site thermal imaging field aims to demonstrate the developed remote sensing thermography on the floating geomembrane covers at WTP.

7.1 Introduction

As reported in the above chapters, scums will appear as liquid matters initially and transform into a solid-state over time. In addition, the volumes of scums also increase with continual sewage inflow. As shown in Figure 7.1, Scums can spread over a large area. It will float and come into contact with the floating cover. As a result, the existence and the development of the scums under the covers can exert multiple influences on the HDPE geomembrane floating covers, such as:

- The floating cover is designed with features to act as pipelines to extract the biogas generated. When the scums accumulate under the covers, they can block these pathways and reduce the efficiency of the biogas collection.
- When scums solidify and accumulate into a large body, they lift the geomembranes and distort the covers. When the wind blows over these elevated regions, it will produce a lateral drag force and subject to cover material to elevated strain levels.
- The subsurface scums can degrade the geomembrane material over time, thereby significantly reducing the expected service life of the HDPE geomembranes [255-257].



Figure 7.1 Scums at the WTP, they exist under the HDPE floating covers and float on the sewage

This chapter aims to conduct on-site inspections on the floating covers at the water treatment plant using the developed thermography strategy [4, 5]. Therefore, it is important to be able to identify the distribution of material accumulated under the covers as part of the maintenance of and management of the floating cover. The ability of the quasi-active thermography to identify the profiles of substrates such as biogas, scums, and sewages is to be verified in the field trials. And the reliability and suitability of the technique are to be verified in a series of field trials for future applications.

7.2 On-site quasi-thermography methodology

A novel quasi-active thermography technique was developed by Yue et al.[37] to monitor the scums under the covers. They correlated the ambient weather information, including the ambient solar intensity and environmental temperature, with the thermal responses of the material to study the transient temperature decays events of the HDPE geomembranes in a day (from sunrise to sunset). Since the HDPE geomembrane covers are deployed in the open environment, the temperatures of covers changed according to the ambient weather condition, such as daily transient ambient temperature cycles and solar radiation cycles [258]. Quasi-active thermography experiments were conducted for several days. The clayey soil was a replacement and conducted long-term inspections to obtain the thermal image sequences during the temperature variations of the HDPE geomembranes. The lab-scale experiments conducted by Yue et al. verified that the quasi-active thermography could be used to monitor the accumulation of scums under the HDPE geomembrane covers[37]. In this chapter, the developed quasi-active thermography method is to be applied to an on-site thermography inspection on the large floating covers.

7.2.1 Regions for the thermography inspection

Given that HDPE floating covers cover a large area, a thermal camera was mounted on a platform and monitor a selected region of the cover during each trial. As shown in Figure 7.2, the DEM of the HDPE floating covers reported by Leslie et al. [25] shows the elevation of the floating cover above the water level. It was reported by the WTP that the Western section of the covers is in contact with sewage and the elevated part indicates the existence of biogas pockets under the covers. While the Eastern section of the covers is in contact with a variety of states of the scums, and a higher elevated region indicates that the scumberg is lifting the cover. Scums are reported to transform from a soft state to a solid state over time, and their thermal properties also change during the transition [7, 8].

Previous cover-walk surveys were done, and the hardness of the scums was assessed qualitatively. The DEM of the cover suggested the accumulation of scums. The challenge is to identify the state of the scum (i.e., from soft states to its solid-state). In this study, an area of 45m × 165m was selected to be inspected. The detailed structure profiles of the monitored region are shown in Figure 7.3, where “B” indicates the locations of ballasts on the covers, and the “F” means the locations of flotations the presence of the water ponds on the covers (appear in green colour). According to the previous cover walk evaluations, the region selected for trial 1 comprises medium solid scums under the covers. The region selected for trial 2 region has biogas, sewage, and fluffy scums under the covers. The thermal camera was mounted at the edge of the floating covers and to monitor these two regions.

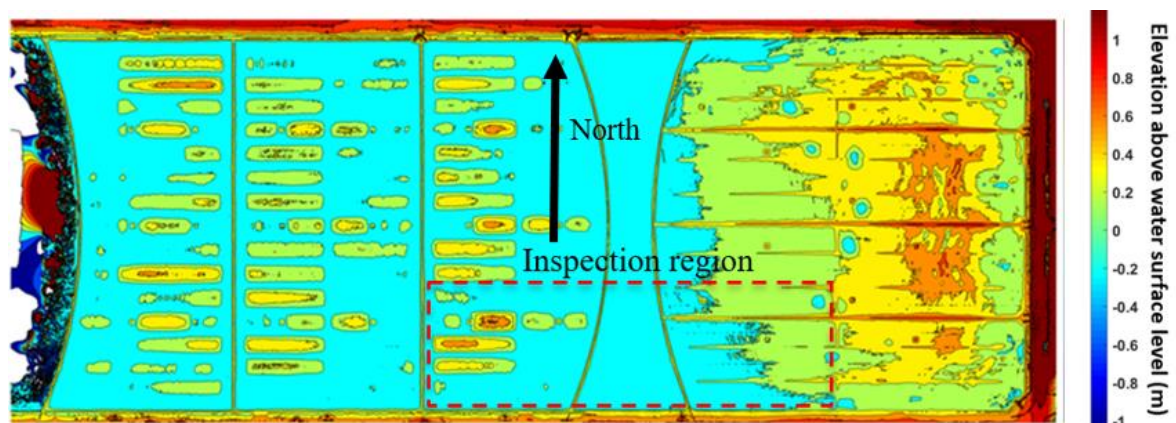


Figure 7.2 Digital elevation model with Unmanned aerial vehicle scan by Leslie et al. [25]



Figure 7.3 Illustration of structures on the monitored region of the floating covers

7.2.2 Experiment set up

Figure 7.4 (a) shows that a FLIR A615 thermal camera [233] was mounted on a tripod, which was put on a platform and fixed by multiple tie-downs. The tripod was adjusted to direct the thermal camera monitor towards the inspected region. The monitor angle of the thermal camera was set as 85 degrees, and the position of the thermal camera was set at 3.1m from the covers level vertically and 2.25m from the edge of the covers horizontally. An Apogee sp-110 pyranometer [234] was put alongside the thermal camera to monitor the local solar intensity profile. In addition, a Fluke 287 multi-meter [235] was used to record the ambient environment temperature. All of the sensors were connected to a laptop in a weatherproof box, and the commercial software was used to control the instruments during the experiment. The sampling rates of all sensors were set as 10mins/read. In addition, all of the sensors were deployed with weatherproof protection to eliminate the risk of wind and rain. The experiments were conducted on sunny and dry days to avoid the influence of moistures, affecting the emissivity of the HDPE geomembranes.



Figure 7.4 Illustration of the thermography set up at the floating covers.

7.3 Result and discussion

7.3.1 Trial 1

As shown in Figure 7.5, the first inspection was conducted in the trial one region. The first inspection covered an area of 45m×67m. The thermal camera was put alongside the floating covers, and two sites were monitored in trial 1. Previous cover-walk surveys reported that these two sites have medium solid scums under the covers. Figure 7.6 shows the recorded experimental data of site one inspection, including the ambient solar intensity and the ambient temperature at 2 points on the cover. These two points are selected on the site one region are:

- a. point 1, where biogas is known to accumulate under the cover, and
- b. point 2 has scum exists underneath the cover.

The experiment started at 10:09:29 in the morning and ended at 22:15:29 in the evening (i.e., the experiment last for 12 hours and 6 minutes). It can be observed from this figure that the temperature of the floating covers increases in the morning due to solar radiation. After 12:00:00, the geomembrane temperature decreases and into the night because of the decreased solar intensity. It is noted that the temperature decay profile is different between the flotation region and the scum region.

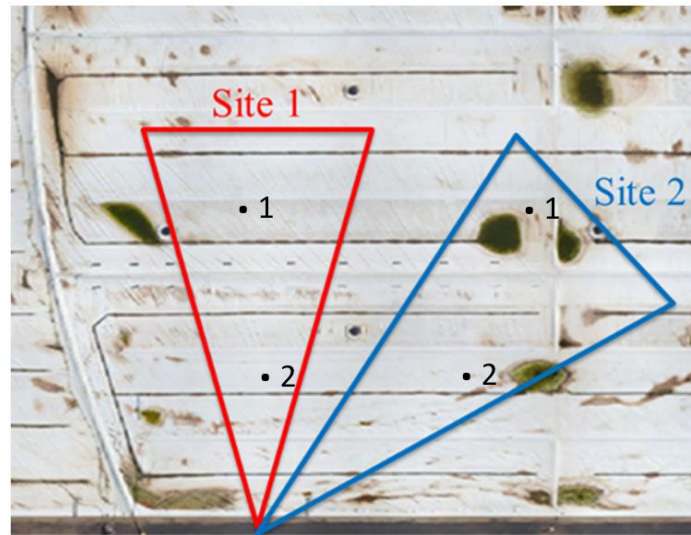


Figure 7.5 Monitored regions of trial 1 in day 1 and day 2

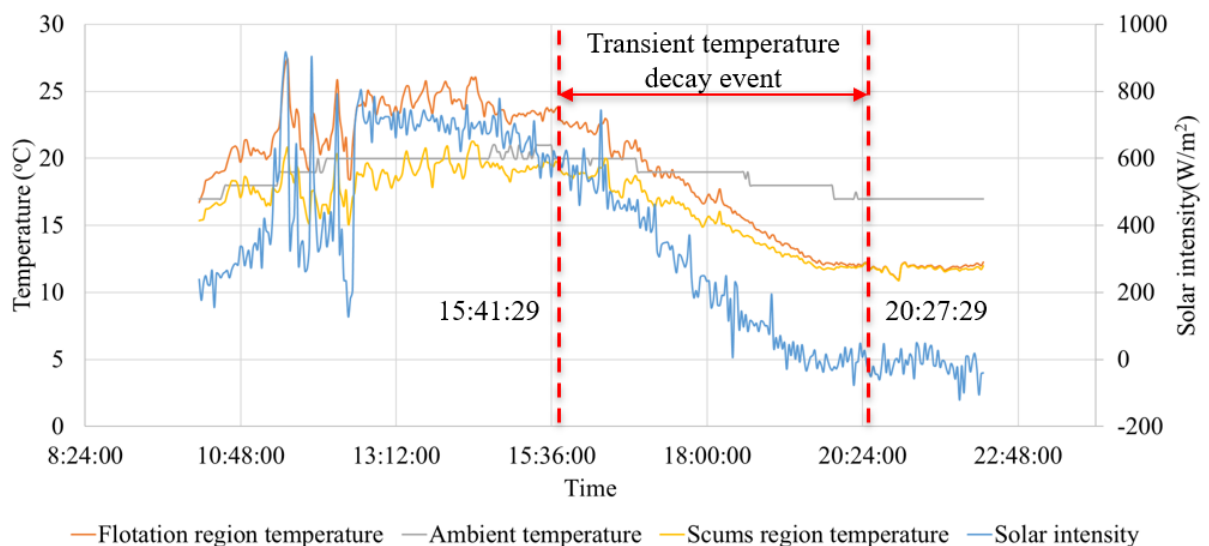


Figure 7.6 Recorded experiment data for site 1 inspection

The thermal image sequences were analysed by the LPSD method. Given that sewage, biogas and scums are unevenly distributed under the covers, and the LPSD map has a continuous value scale, an image segmentation method is further applied to the LPSD map to classify these three kinds of substrates based on the temperature change rates contrasts. The previous cover walks surveys indicated medium solid scums were distributed over the whole area in site 1. Figure 7.7 (a) shows an optical photo of site one and illustrates the structures of this region on the covers, where “F” means flotation lines, which have the low-density floating materials under the covers. These regions are elevated and provide a channel for the biogas to move along the flotation. Hence these regions are expected to have biogas underneath. The “B” means the ballast regions on the covered, they appear as black lines on

the covers, and they are used to provide stability for the floating covers. “W” means the wrinkles on the surface of the floating covers resulting from the accumulations and movements of the subsurface scums. There are small biogas gaps between the underside of geomembranes and scums under these wrinkles. While in the rest of the regions under the covers where the cover surface is flat, the previous cover walks surveys verified that solid scums exist over the whole site. Still, some regions where the scums are not in full contact with the geomembranes and small gaps also exist. In addition, there are some stains on the surface of the covers due to the drying of accumulated water.

Figure 7.7 (b) shows a single frame of the raw thermal image taken at 18:00:00. It can be found that the elevated flotation line region and the flat scums region cannot be distinguished with similar temperature ranges, and the small biogas gaps in the tiny wrinkles cannot be identified through the insignificant temperature contrast. Some prominent wrinkles on the covers are identified due to the reflections of wrinkles from the sunlight and the subsurface biogas. In addition, the stains on the covers present a high temperature due to the low emissivity and reflections from the sunlight.

The results from the LPSD analysis of the thermal image sequences are shown in Figure 7.7(c). This map compares the temperature change rates of the covers during the cooling process. As shown in Figure 7.6, the temperature decay curve from 15:41:29 to 20:27:29 is used in the LPSD analysis. To correlate the information in the LPSD map and optical photo, the profiles of structures are also labelled in Figure 7.7 (c). The following observations made from this figure:

- (1) The cooling rates of the flotation line region and the surrounding scums region shows a significant contrast. This is because the biogas region cools faster than the scums region during the transient temperature decay process.
- (2) The wrinkles and small biogas gaps present a similar cooling rate with the flotation line since all of these regions have biogas underneath.
- (3) since the scums and biogas have different heat transfer efficiencies with the geomembrane materials, the biogas gaps in the wrinkles can be distinguished from the surrounding scums region by contrasting temperature change rates.
- (4) the scums regions have uniform lower temperature change rates compared to the biogas regions. This is because the scums have a higher specific heat, and the rates of

the cooling rates during the transient temperature decay process are lower than that of biogas.

The LPSD map was segmented based on the temperature change rates, and the maps were classified into 3 clusters in Figure 7.7 (d):

- a. The “blue” cluster is associated with the scum regions in Figure 7.7 (c),
- b. The “green” cluster refers to flotation lines, wrinkles, and small biogas gaps in the scum regions. This cluster indicates the areas of covers that are in contact with biogas substrates.
- c. The “red” cluster refers to the stains and some wrinkles which have low emissivity and reflect the solar radiation.

These results show that the thermal imaging study at site one on the floating covers indicates that the quasi-active thermography with the aid of the LPSD method and image segmentation method can identify different substrates under the floating covers and distinguish the structural differences on the covers based on the temperature change rate during the transient temperature decay events.

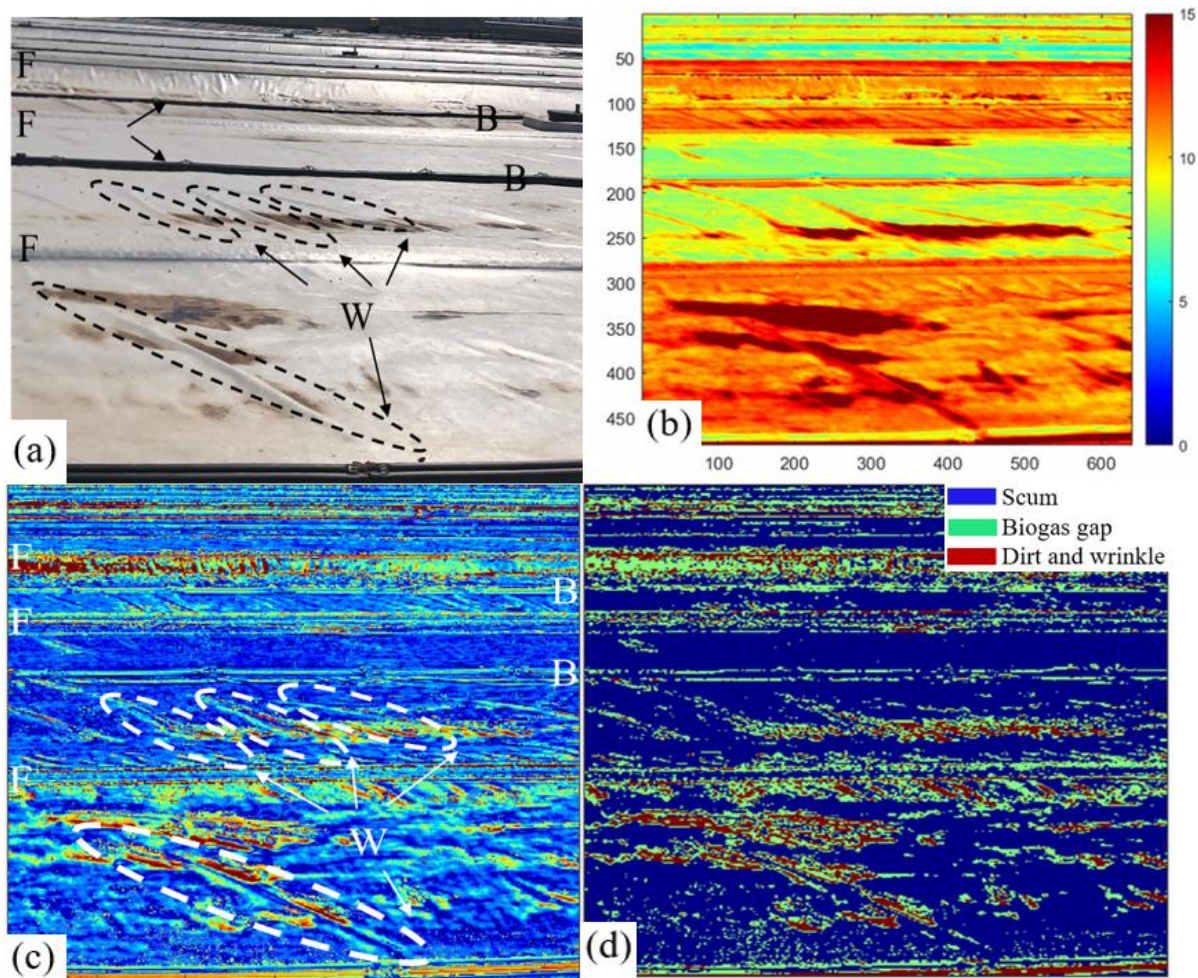


Figure 7.7 (a) optical photo of to illustrate the structures of site 1 (F-flotation line, B-ballast line, W-wrinkle or curvature on the covers). (b) single frame of raw thermal image for site 1. (c) LPSD map for site 1. (d) K-means image segmentation map for site 1.

Figure 7.8 illustrates the recorded experiment data for the site two inspections (see Figure 7.5), where point 1 has biogas underneath and point 2 has scum underneath in Figure 7.5. The experiment started at 17:57:16 in the afternoon on the first day and ended at 12:37:16 on the third day. The experiment lasts for 42 hours and 40 minutes. Similar to the cover temperature profiles from site 1, the cover temperature profiles from site two were affected by the variation of ambient temperature and solar intensity.

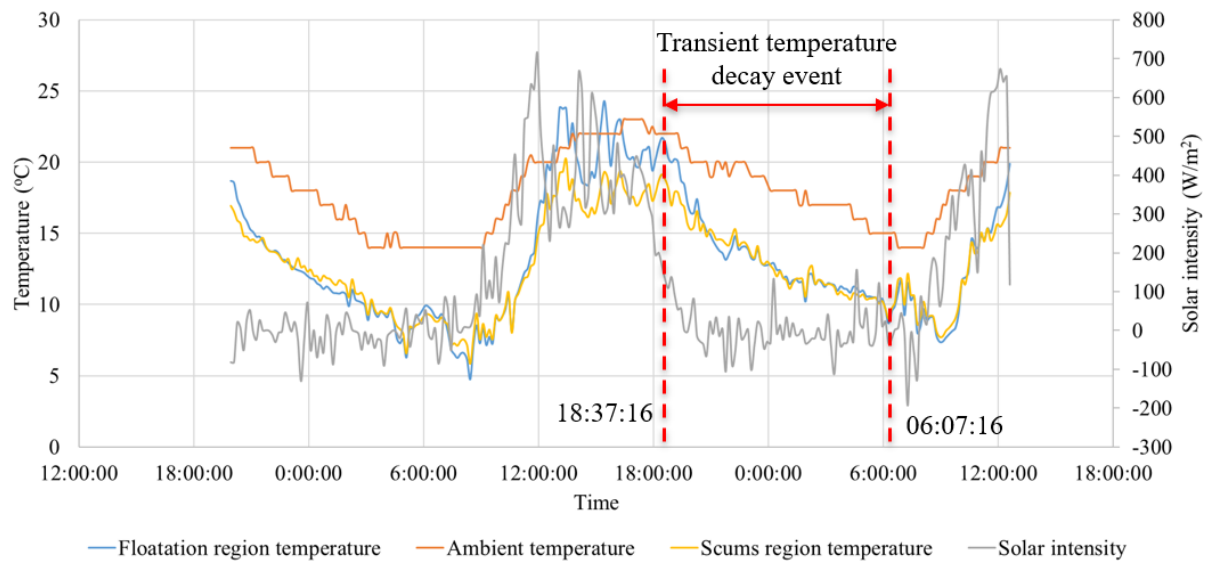


Figure 7.8 Recorded experiment data for site 2 inspection

Figure 7.9 shows the analysis result for the inspection of site 2, where the profiles of flotations, ballasts, and the wrinkles are shown in the optical photo in Figure 7.9 (a). Same as site 1 in Figure 7.7, site 2 have solid scums distributed over the whole site. Biogas exists under the flotation lines, wrinkles and the small biogas pockets, and the surrounding regions under the covers are filled with scums. In Figure 7.9 (b), the temperature contrast between the scum region and the biogas region from a single frame is not significant, while the stains on the floating covers present a high temperature due to the reflection of solar radiation.

As highlighted in Figure 7.8, the temperature decay curves from 18:37:16-06:07:16 were used to conduct an LPSD analysis. The results are shown in Figure 7.9 (c). The flotation line is identified through the high temperature change rate contrast with the surrounding scums region. The small biogas pockets and wrinkles over the scums can also be found through the contrast.

The image segmentation results are in Figure 7.9 (d). This result shows similar consistency to that in Figure 7.7 (d). The scums region, which has a low-temperature change rate, is classified into cluster 1, the regions which have high-temperature change rate with biogas substrates are classified into cluster 2, and the regions which have stains or wrinkles and have high-temperature change rates due to the reflections are classified into cluster 3. Based on the thermal imaging results, the LPSD map and the K-means image segmentation map in this trial show agreed profiles of the structures on the floating covers, and different substrates under the covers can also be identified through the thermal response in the transient temperature decay events.

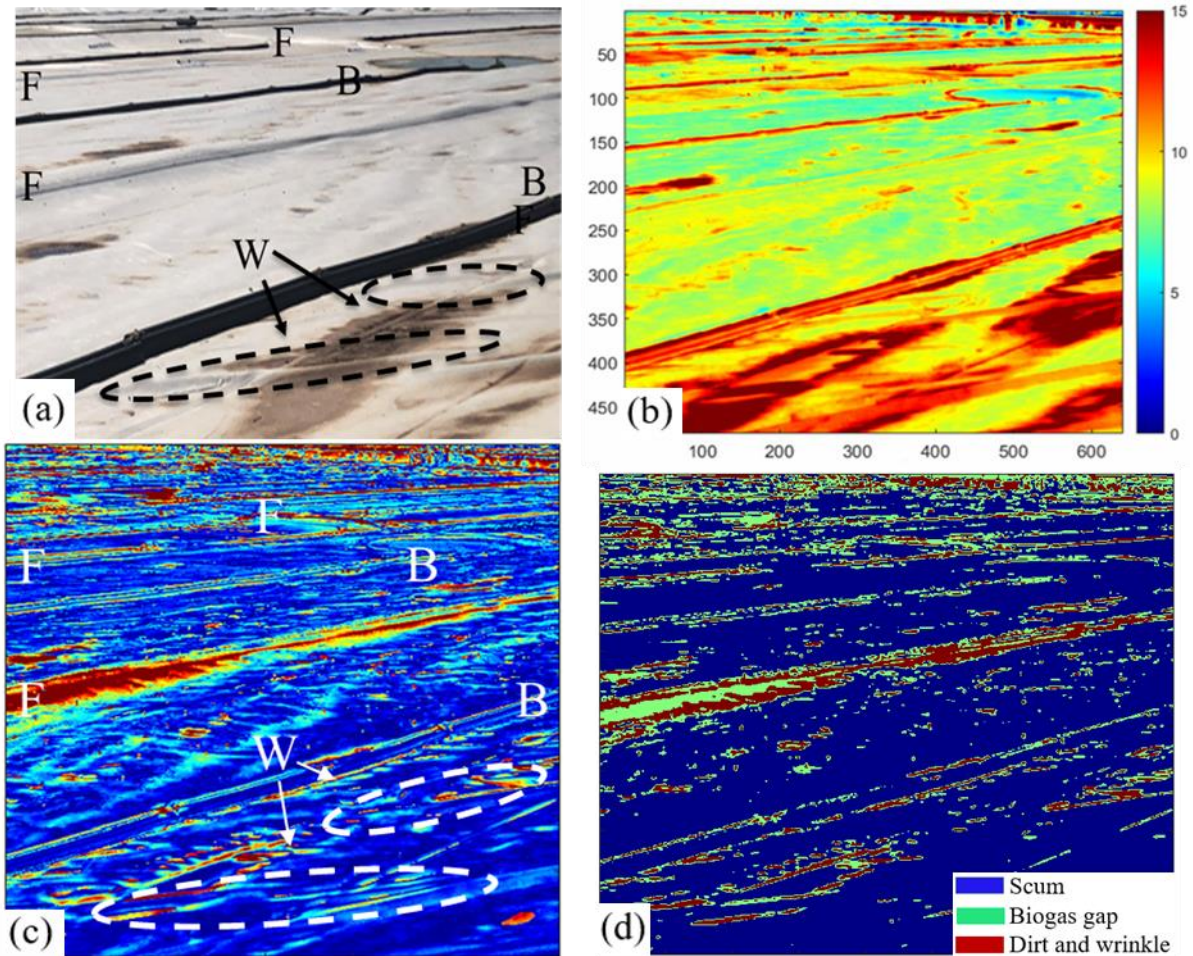


Figure 7.9 (a) optical photo of to illustrate the structures of site 2 (F-flotation line, B-ballast line, W-wrinkle or curvature on the covers). (b) single frame of raw thermal image for site 2. (c) LPSD map for site 2. (d) K-means image segmentation map for site 2.

7.3.2 Trial 2

As shown in Figure 7.10, the third inspection site was selected as the Trial 2 region in Figure 7.3 and covered $43\text{m} \times 27\text{m}$. This region was reported to have biogas pockets, sewage and fluffy scums under the covers. The experimental setup of trial 2 was the same as the setup in Trial 1.

Figure 7.11 illustrates the recorded experiment data, including ambient temperature and solar intensity. The temperature profiles of two sample points of the inspected area in Figure 7.8 are also plotted. It was reported that point 1 has biogas underneath and point 2 has soft sewage underneath. The experiment started at 15:14:37 on the first day and ended at 22:14:37 on the second day.



Figure 7.10 Monitored region in trial 2

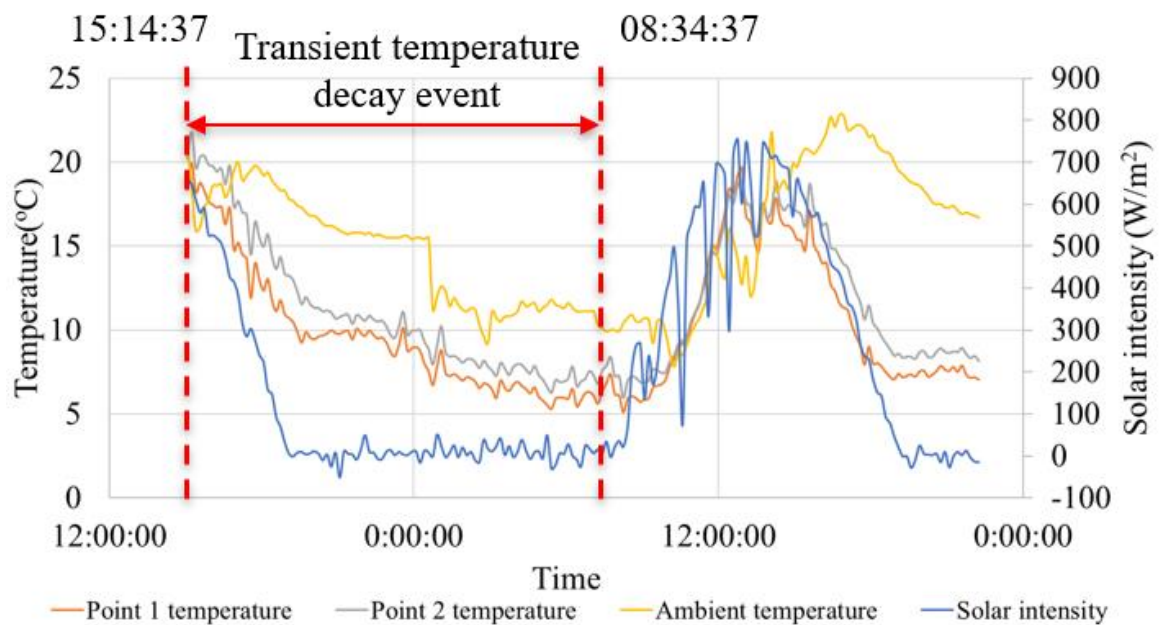


Figure 7.11 Recorded experiment data for site 3

Figure 7.12 shows the structural details and the analysis results for trial 2. In Figure 7.12(a), six segments of HDPE floating covers are highlighted:

- a. Segments 2 have soft sewage underneath, but some biogas gaps exist in the middle area.
- b. Segments 3 and 5 on the left hand of the site are elevated. This is because the generated biogas under the covers results in a gas pocket in these regions.

- c. Segments 4 and 6 are flat and previous surveys reported that sewage and fluffy scums existed under these regions. There are some wrinkles on the surface of Segment 4, and the biogas exists under these wrinkles.

Since the measured temperature will be slightly affected by the monitoring orientation, other covers far away from the thermal camera are not considered in this study. Also, the water accumulated on the ballasts is not considered due to the low emissivity.

Figure 7.12(b) shows the raw thermal image of the monitored area, where the substances cannot be distinguished through the temperature contrast. While the LPSD map in Figure 7.12(c) shows a contrast between the flat sewage region and the elevated biogas region, and the curved biogas region can also be distinguished from the flat sewage region on segment 4. This figure shows that the biogas region has a higher temperature change rate than that of the sewage region, which can be attributed to the fact that the sewage has higher specific heat than the biogas. The subsurface sewage slows the temperature decay rate in the sewage region. However, on these segments, some wrinkles reflect the solar radiation and affect the monitoring result.

The segmented LPSD map is shown in Figure 7.12(d), where the sewage is distributed over Segments 1,2 and 4, the biogas gap is distributed over segments 3, 5, and some regions on segment 6, and the wrinkles which have biogas underneath are distributed over segments 3 and 4. However, the segmentation results are affected by the reflections again, and some biogas regions are misidentified as the wrinkles, such as the biogas pockets of segments 3 and 5. These regions were elevated by the biogas, producing wrinkles as and reflecting the sunlight radiation. Therefore, the monitoring orientation is vital to outside thermal imaging, and the reflection from wrinkles can affects the monitoring result.

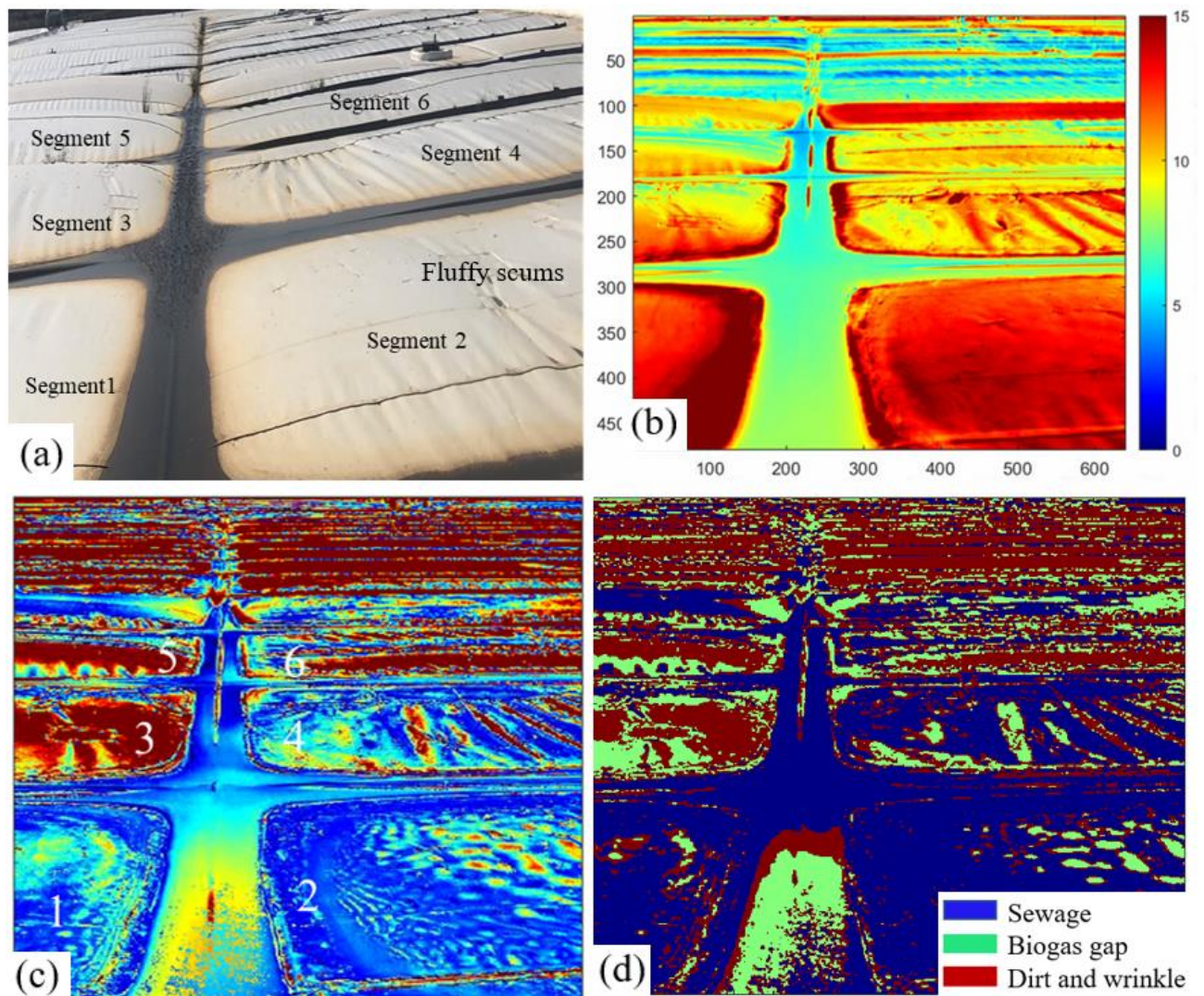


Figure 7.12 (a) optical photo of to illustrate the structures of site 3 (F-flotation line, B-ballast line, W-wrinkle or curvature on the covers). (b) single frame of raw thermal image for site 3. (c) LPSD map for site 3. (d) K-means image segmentation map for site 3.

After trial one and trial 2, it can be concluded that the quasi-active thermography can be used to distinguish different substances under the covers through the comparison of temperature change rates of the covers. The distribution of sewage, biogas and scums can be classified with the segmented LPSD method.

7.4 Conclusion

An on-site thermography inspection field trial was introduced in this Chapter. The main results of this on-site thermography study were summarized as below:

- Biogas channels under the flotation lines could be identified with a higher temperature change rate contrast in the LPSD map.

- The scums under the covers could be identified with the lower temperature change rate in the LPSD map, and some small biogas gaps within the scums region could also be distinguished through the contrast in the LPSD map.
- Biogas pockets regions and sewage regions could be distinguished through the comparison of temperature change rates, but the curvatures could affect the monitoring results with a reflection from the sunlight.
- Image segmentation technique can help classify different substances under the covers through the classification of temperature change rates.

CHAPTER EIGHT

8 Conclusions and future works

This thesis developed a novel wide coverage remote sensing technology to fill in on-site large-area structural health monitoring gaps. The main contribution of this thesis is that the developed quasi-active thermography helped identified the structural differences, such as different substrates under the cover, the accumulation of the solids, and the existence of defects in different interfaces. The investigations in this thesis used the naturally happened thermal response due to the variations of ambient weather, such as the solar intensity variations and the ambient temperature cycles, to enhance the results of the quasi-active thermal imaging. Thermal imaging with different time scales was used to study different kinds of structural differences. Several algorithms and FEA analysis were also used to understand better the heat transfer theories behind the membrane structures' thermal response. In addition, clustering-based machine learning image segmentation algorithms were integrated with the thermal image to help identify different substrates under the opaque membrane structures.

8.1 Conclusions

The main findings and contributions of this thesis are summarised below:

- Quasi-active thermography was at first developed in Chapter 4 to identify the profiles of solid objects under the geomembrane cover. The results have evidenced that the proposed monitoring technique is repeatable and reliable, and the proposed quasi-active thermography inspection was shown to have real potential for the field deployment to monitor the growth of the under-surface objects.
- The developed quasi-active thermography technique was then used to detect the defects in the geomembrane in Chapter 5. Short terms of cloud shades in the experiments were used to stimulate the transient events on the geomembrane. It was found that the penetrating and non-penetrating defects can be detected with multiple thermal imaging analysis methods. In addition, defects on different substrates such as solid and fluid can also be detected. More studies were done to further enhance the reliability and efficiency of the quasi-active thermography.
- Chapter 6 used the computational analysis to simulate the transit process of the scums under the cover. The thermal responses of the geomembrane that were in contact with

different states of scums were also investigated. It is recognised that the results summarized in this chapter are dependent on the assumed geometry and time evolution of substrate material properties, which may not be fully representative of the actual process of scum accumulation at the WTP. However, it seems reasonable to expect that the change in the cooling constant that is predicted by the current modelling assumptions is representative of what would be measured in practice, and therefore that monitoring the cooling constant should constitute a promising approach for quantitative characterization of scum accumulation beneath the floating covers. The result in this chapter provides an insight for the future field trial experiments。

- The trials reported in Chapter 7 show the viability of the developed quasi-active thermography method to identify the distributions of different kinds of substrates existing under the floating covers of the sewage treatment plant. It also highlighted some challenges that will need to be overcome for future applications. A series of on-site thermal imaging inspections were conducted at different parts of the floating covers. A quasi-active thermal imaging strategy was applied to determine the presence of sewage, biogas, and scums under the opaque covers using the covers' daily transient temperature change events. The cooling cycles were defined by the ambient solar energy and temperature evolutions.

In this thesis, the development of the quasi-active thermography technique uses the ambient weather information to conduct robust and efficient structural health monitoring on large-area structures. The unique novelty of this thesis is to use naturally occurring solar intensity and ambient temperature variations to monitor large-scale on-site structures such as geomembranes located over a large area. It enhanced the thermal imaging quality by analysing the long terms and short terms of naturally happened transient temperature changing events of structures. This robust SHM technique can ensure the structural integrity of the floating covers, efficiently eliminate scums and maximize the expected service life of the floating cover. The developed quasi-active thermography technique also has a great potential to extend to other types of large structures under other types of ambient disturbance.

8.2 Future works

This thesis presents an insight into using thermal imaging to conduct the on-site large area SHM on the membrane structures. The research also shows a method to identify objects under the structures using ambient weather information such as solar energy and the ambient temperature variations. The following recommendations for future works are

worth to be considered to fill in further the gaps of monitoring the large structures using thermal imaging:

- The field trial works in this thesis monitored two regions on the floating cover. To monitor a larger area or the whole floating cover, thermal imaging is required to be conducted at a higher altitude, and this can be done when the thermal camera was mounted on the UAV. A UAV assisted thermal imaging can enhance the efficiency of thermal imaging significantly. Some problems of UAV assisted thermal imaging are yet to be solved, such as the limitation of UAV battery, the stability of the platform to provide a stable thermal view, and the algorithms of quasi-active thermography to enhance the contrast when the resolution of the image was reduced at a higher altitude.
- Currently, the quasi-active thermography can distinguish different features under the cover such as scums, sewage and biogas pockets by comparing temperature change rates. In the future, some works can be done further to identify these features through the machine learning algorithms, and this can further enhance the accuracy and reliability of the thermal imaging results.
- As reported in Chapter 1, scumbers is a large body of solid objects, and only a part of them is floating above the sewage surface. Currently, quasi-active thermography can identify the accumulation of the area of the scumbers, and future studies can focus on estimating the volume of the scumbers through the thermal response of the geomembrane.

The scums under the cover transit from a liquid state to a harder and dryer state. In future studies, thermography can be conducted to further distinguish different states of scums by comparing the thermal responses of regions on the geomembrane cover.

9 References

1. Breitenbach, A. and M. Smith. *Overview of geomembrane history in the mining industry*. in *Proceedings 8th International Conference on Geosynthetics*. 2006.
2. Athanassopoulos, C., et al., *Evaluation of geomembrane puncture potential and hydraulic performance in mining applications*. Proc., Tailings and Mine Waste'08, 2009: p. 189-198.
3. Giroud, J. and R. Bonaparte, *Leakage through liners constructed with geomembranes—part I. Geomembrane liners*. Geotextiles and Geomembranes, 1989. **8**(1): p. 27-67.
4. Rowe, R.K. and S. Rimal, *Aging of HDPE geomembrane in three composite landfill liner configurations*. Journal of Geotechnical and Geoenvironmental Engineering, 2008. **134**(7): p. 906-916.
5. Rowe, R., S. Rimal, and H. Sangam, *Ageing of HDPE geomembrane exposed to air, water and leachate at different temperatures*. Geotextiles and Geomembranes, 2009. **27**(2): p. 137-151.
6. Wang, L., et al., *Laboratory test and modelling of gas pressure under geomembrane subjected to the rise of groundwater in plain reservoirs*. Geotextiles and Geomembranes, 2021. **49**(1): p. 81-96.
7. Bhowmik, R., J. Shahu, and M. Datta, *Failure analysis of a geomembrane lined reservoir embankment*. Geotextiles and Geomembranes, 2018. **46**(1): p. 52-65.
8. Lavoie, F.L., et al., *HDPE Geomembranes for Environmental Protection: Two Case Studies*. Sustainability, 2020. **12**(20): p. 8682.
9. Adams, M.W., *Application of HDPE at a sewage treatment plant*. Geotextiles and Geomembranes, 1997. **15**(4-6): p. 269-276.
10. Bucur, E., et al., *Odour pollution assessment through indirect methods based on the monitoring of technological parameters-case study*. 2019.
11. Chen, Z., et al., *Impact of using high-density polyethylene geomembrane layer as landfill intermediate cover on landfill gas extraction*. Waste Management, 2011. **31**(5): p. 1059-1064.
12. Abdelaal, F. and R. Rowe, *Degradation of an HDPE geomembrane without HALS in chlorinated water*. Geosynthetics International, 2019. **26**(4): p. 354-370.
13. Zhang, H., *Study on the Internal Force of Geomembrane of Landfill in Heavy Metal Contaminated Area*. Earth Sciences Research Journal, 2020. **24**(1): p. 111-118.
14. Kavazanjian Jr, E. and A. Gutierrez, *Large scale centrifuge test of a geomembrane-lined landfill subject to waste settlement and seismic loading*. Waste Management, 2017. **68**: p. 252-262.

15. Ng, C.W., et al., *A novel vegetated three-layer landfill cover system using recycled construction wastes without geomembrane*. Canadian Geotechnical Journal, 2019. **56**(12): p. 1863-1875.
16. DeGarie, C., et al., *Floating geomembrane covers for odour control and biogas collection and utilization in municipal lagoons*. Water science and technology, 2000. **42**(10-11): p. 291-298.
17. Ng, H.-B., C.-W. Qi, and X.-M. Tan, *Covered Anaerobic Lagoons with Hdpe Geomembrane: Experiences in Developing Asian Countries*, in *Advances in Environmental Geotechnics*. 2010, Springer. p. 828-833.
18. Sadlier, M. and X. Zhou, *Floating Cover for Leachate Lagoon at Hangzhou*, in *Geosynthetics in Civil and Environmental Engineering*. 2008, Springer. p. 532-535.
19. Abdelaal, F., M. Morsy, and R.K. Rowe, *Long-term performance of a HDPE geomembrane stabilized with HALS in chlorinated water*. Geotextiles and Geomembranes, 2019. **47**(6): p. 815-830.
20. Eithe, A.W. and G.R. Koerner, *Assessment of HDPE geomembrane performance in a municipal waste landfill double liner system after eight years of service*. Geotextiles and Geomembranes, 1997. **15**(4-6): p. 277-287.
21. Jones, D.R.V. and N. Dixon, *Shear strength properties of geomembrane/geotextile interfaces*. Geotextiles and Geomembranes, 1998. **16**(1): p. 45-71.
22. Needham, A., J. Smith, and E. Gallagher, *The service life of polyethylene geomembrane barriers*. Engineering geology, 2006. **85**(1-2): p. 82-90.
23. Koerner, G.R. and R.M. Koerner, *Long-term temperature monitoring of geomembranes at dry and wet landfills*. Geotextiles and geomembranes, 2006. **24**(1): p. 72-77.
24. Abdelaal, F.B. and R.K. Rowe, *Effect of high temperatures on antioxidant depletion from different HDPE geomembranes*. Geotextiles and Geomembranes, 2014. **42**(4): p. 284-301.
25. Wong, L., et al., *Remote Monitoring of Floating Covers Using UAV Photogrammetry*. Remote Sensing, 2020. **12**(7): p. 1118.
26. Chiu, W.K., et al., *Large Structures Monitoring Using Unmanned Aerial Vehicles*. 2017. p. 415-423.
27. Afonin, K., et al. *The Use of Municipal Solid Waste as Secondary Energy Resources on the example of the Housing Complex Novopatrushovo, Tyumen*. in *IOP Conference Series: Materials Science and Engineering*. 2020. IOP Publishing.
28. Yap, C.C., et al., *Comparison of different industrial scale palm oil mill effluent anaerobic systems in degradation of organic contaminants and kinetic performance*. Journal of Cleaner Production, 2020. **262**: p. 121361.

29. Wong, L., et al. *Structural assessment of large membrane structures using an unmanned aerial vehicle*. in *Asia-Pacific Workshop on Structural Health Monitoring 2018*. 2018. NDT.net.
30. Vien, B., et al., *Strain Monitoring Strategy of Deformed Membrane Cover Using Unmanned Aerial Vehicle-Assisted 3D Photogrammetry*. Remote Sensing, 2020. **12**(17): p. 2738.
31. Wong, L., et al., *Structural Assessment of Large Membrane Structures Using an Unmanned Aerial Vehicle Aided Photogrammetry: Determination of Flight Parameters and Trials at the Western Treatment Plant*. Journal of Nondestructive Evaluation, Diagnostics and Prognostics of Engineering Systems, 2019. **2**(4).
32. Kannan, M.S. and N. Lenca, *Field guide to algae and other "scums" in ponds, lakes, streams and rivers*. 2013, Burlington, KY: Northern Kentucky University.
33. Lemmer, H., *The ecology of scum causing actinomycetes in sewage treatment plants*. Water Research, 1986. **20**(4): p. 531-535.
34. Meghari, A.R. and R.K. Omar, *Physicochemical Characterization of Sewage Sludge of Gaza Wastewater Treatment Plant for Agricultural Utilization*. IUG Journal of Natural Studies, 2017.
35. Šebo, J., M. Gróf, and M. Šebová, *A contingent valuation study of a polluted urban lake in Košice, Slovakia: The case of the positive distance effect*. Journal of environmental management, 2019. **243**: p. 331-339.
36. Benjamin Steven Vien, L.W., Thomas Kuen, L. R. Francis Rose and a.W.K. Chiu, *A Machine Learning Approach for Anaerobic Reactor Performance Prediction Using Long Short-Term Memory Recurrent Neural Network*. Materials Research Forum, 2021. **Vol. 18, pp 61-70, 2021**.
37. Yue Ma, L.W., Benjamin Steven Vien, Thomas Kuen, Nik Rajic, L.R. Francis Rose, Jayantha Kodikara, Wing Kong Chiu, *Quasi-Active Thermography for Structural Health Assessment of Large Geomembranes*. Materials Research Proceedings, 2021. **Vol. 18, pp 79-86, 2021**.
38. Wang, G. *Analysis on the Key Points of Architectural Design of Underground Totally Buried Sewage Treatment Plant*. in *IOP Conference Series: Materials Science and Engineering*. 2020. IOP Publishing.
39. Leslie Wong, B.S.V., Yue Ma, Thomas Kuen, Frank Courtney, Jayantha Kodikara, Francis Rose, Wing Kong Chiu, *Development of Scum Geometrical Monitoring Beneath Floating Covers Aided by UAV Photogrammetry*. Materials Research Proceedings, 2021. **Vol. 18, pp 71-78, 2021**.

40. Du, B., et al., *Progress and trends in fault diagnosis for renewable and sustainable energy system based on infrared thermography: A review*. Infrared Physics & Technology, 2020. **109**: p. 103383.
41. Lucchi, E., *Applications of the infrared thermography in the energy audit of buildings: A review*. Renewable and Sustainable Energy Reviews, 2018. **82**: p. 3077-3090.
42. Osornio-Rios, R.A., J.A. Antonino-Daviu, and R. de Jesus Romero-Troncoso, *Recent industrial applications of infrared thermography: A review*. IEEE Transactions on Industrial Informatics, 2018. **15**(2): p. 615-625.
43. Palumbo, D., P. Cavallo, and U. Galietti, *An investigation of the stepped thermography technique for defects evaluation in GFRP materials*. NDT & E International, 2019. **102**: p. 254-263.
44. Sirikham, A., et al., *Estimation of damage thickness in fiber-reinforced composites using pulsed thermography*. IEEE Transactions on Industrial Informatics, 2018. **15**(1): p. 445-453.
45. Moreno, R., et al. *Towards automatic crack detection by deep learning and active thermography*. in *International Work-Conference on Artificial Neural Networks*. 2019. Springer.
46. Schwarz, K., et al., *Hot movements on soil surfaces–Innovative insights into microbial dynamics using passive infrared thermography*. Geoderma, 2021. **385**: p. 114879.
47. CAPRIOTTI, M., S. STERNINI, and F.L. DI SCALEA, *Passive Defect Detection and Imaging in Structures by Cross-correlations of Infrared Thermography Measurements*. Structural Health Monitoring 2017, 2017(shm).
48. Berthe, J. and M. Ragonet, *Passive infrared thermography measurement of transverse cracking evolution in cross-ply laminates*. Strain, 2018. **54**(6): p. e12293.
49. Cheng, C.-C., T.-M. Cheng, and C.-H. Chiang, *Defect detection of concrete structures using both infrared thermography and elastic waves*. Automation in construction, 2008. **18**(1): p. 87-92.
50. Daffara, C., et al., *A Cost-Effective System for Aerial 3D Thermography of Buildings*. Journal of Imaging, 2020. **6**(8): p. 76.
51. Lee, D.-S., et al., *A field study on application of infrared thermography for estimating mean radiant temperatures in large stadiums*. Energy and Buildings, 2019. **202**: p. 109360.
52. Rowe, R.K. and H.P. Sangam, *Durability of HDPE geomembranes*. 2002. p. 77-95.
53. Stark, T.D., T.A. Williamson, and H.T. Eid, *HDPE geomembrane/geotextile interface shear strength*. Journal of Geotechnical Engineering, 1996. **122**(3): p. 197-203.
54. Müller, W.W., *HDPE geomembranes in geotechnics*. 2007: Springer.

55. Hillman, R. and T. Stark, *Shear strength characteristics of PVC geomembrane-geosynthetic interfaces*. Geosynthetics International, 2001. **8**(2): p. 135-162.
56. McWatters, R. and R. Rowe, *Transport of volatile organic compounds through PVC and LLDPE geomembranes from both aqueous and vapour phases*. Geosynthetics International, 2009. **16**(6): p. 468-481.
57. McWatters, R.S. and R.K. Rowe, *Diffusive transport of VOCs through LLDPE and two coextruded geomembranes*. Journal of Geotechnical and Geoenvironmental Engineering, 2010. **136**(9): p. 1167-1177.
58. Scheirs, J., *A guide to polymeric geomembranes: a practical approach*. 2009: John Wiley & Sons.
59. Koerner, G. and R. Koerner, *Long-term temperature monitoring of geomembranes at dry and wet landfills*. Geotextiles and Geomembranes, 2006. **24**(1): p. 72-77.
60. Jafari, N.H., T.D. Stark, and R.K. Rowe, *Service Life of HDPE Geomembranes Subjected to Elevated Temperatures*. Journal of Hazardous, Toxic, and Radioactive Waste, 2014. **18**(1): p. 16-26.
61. Akpinar, M.V. and C.H. Benson, *Effect of temperature on shear strength of two geomembrane-geotextile interfaces*. Geotextiles and geomembranes, 2005. **23**(5): p. 443-453.
62. Hanson, J.L., et al., *Compaction characteristics of municipal solid waste*. Journal of geotechnical and geoenvironmental engineering, 2010. **136**(8): p. 1095-1102.
63. Yeşiller, N., et al., *Thermal analysis of cover systems in municipal solid waste landfills*. Journal of geotechnical and geoenvironmental engineering, 2008. **134**(11): p. 1655-1664.
64. Yeşiller, N., J.L. Hanson, and W.-L. Liu, *Heat generation in municipal solid waste landfills*. Journal of Geotechnical and Geoenvironmental Engineering, 2005. **131**(11): p. 1330-1344.
65. Sengar, R., K. Singh, and S. Singh, *Application of phycoremediation technology in the treatment of sewage water to reduce pollution load*. Indian Journal of Scientific Research, 2011. **2**(4): p. 33.
66. Renou, S., et al., *Landfill leachate treatment: Review and opportunity*. Journal of hazardous materials, 2008. **150**(3): p. 468-493.
67. Kjeldsen, P., et al., *Present and long-term composition of MSW landfill leachate: a review*. Critical reviews in environmental science and technology, 2002. **32**(4): p. 297-336.
68. Wiedinmyer, C., R.J. Yokelson, and B.K. Gullett, *Global emissions of trace gases, particulate matter, and hazardous air pollutants from open burning of domestic waste*. Environmental science & technology, 2014. **48**(16): p. 9523-9530.

69. Loganath, R. and D. Mazumder, *Performance study on organic carbon, total nitrogen, suspended solids removal and biogas production in hybrid UASB reactor treating real slaughterhouse wastewater*. Journal of Environmental Chemical Engineering, 2018. **6**(2): p. 3474-3484.
70. Braber, K., *Anaerobic digestion of municipal solid waste: a modern waste disposal option on the verge of breakthrough*. Biomass and bioenergy, 1995. **9**(1-5): p. 365-376.
71. Zaks, D.P., et al., *Contribution of anaerobic digesters to emissions mitigation and electricity generation under US climate policy*. Environmental science & technology, 2011. **45**(16): p. 6735-6742.
72. Schmidt, T., et al., *Investigating the impact of seasonal temperature variation on biogas production from covered anaerobic lagoons treating slaughterhouse wastewater using lab scale studies*. Journal of Environmental Chemical Engineering, 2019. **7**(3): p. 103077.
73. Dube, P., et al., *Enhancing recovery of ammonia from swine manure anaerobic digester effluent using gas-permeable membrane technology*. Waste management, 2016. **49**: p. 372-377.
74. Lisboa, M.S. and S. Lansing, *Characterizing food waste substrates for co-digestion through biochemical methane potential (BMP) experiments*. Waste management, 2013. **33**(12): p. 2664-2669.
75. Cowley, C. and B.W. Brorsen, *Anaerobic digester production and cost functions*. Ecological Economics, 2018. **152**: p. 347-357.
76. Niles, M.T. and S. Wiltshire, *Tradeoffs in US dairy manure greenhouse gas emissions, productivity, climate, and manure management strategies*. Environmental Research Communications, 2019. **1**(7): p. 075003.
77. Siregar, Y. and E. Romaito. *Study of Comparison between Covered Lagoon Method and Anaerobic Digester for POME Processing in Biogas Renewable Energy: A Review*. in 2020 4rd International Conference on Electrical, Telecommunication and Computer Engineering (ELTICOM). 2020. IEEE.
78. Matthews, M.W., S. Bernard, and L. Robertson, *An algorithm for detecting trophic status (chlorophyll-a), cyanobacterial-dominance, surface scums and floating vegetation in inland and coastal waters*. Remote Sensing of Environment, 2012. **124**: p. 637-652.
79. Morrison, G., et al., *Assessment of the impact of point source pollution from the Keiskammahoek Sewage Treatment Plant on the Keiskamma River-pH, electrical conductivity, oxygen-demanding substance (COD) and nutrients*. Water Sa, 2001. **27**(4): p. 475-480.

80. Pitman, A., *Design considerations for nutrient removal activated sludge plants*. Water Science and Technology, 1991. **23**(4-6): p. 781-790.
81. Van Lier, J.B., et al., *Anaerobic sewage treatment using UASB reactors: engineering and operational aspects*, in *Environmental anaerobic technology: applications and new developments*. 2010, World Scientific. p. 59-89.
82. Halalsheh, M., et al., *Effect of SRT and temperature on biological conversions and the related scum-forming potential*. Water Research, 2005. **39**(12): p. 2475-2482.
83. Pereira, J., J. Celani, and C. Chernicharo, *Control of scum accumulation in a double stage biogas collection (DSBC) UASB reactor treating domestic wastewater*. Water Science and Technology, 2009. **59**(6): p. 1077-1083.
84. de Souza, C.L., *Estudo quantitativo e qualitativo de espuma acumulada em reatores UASB tratando esgotos domésticos*. 2006.
85. Rose, J.L., *Success and challenges for ultrasonic testing in NDT and SHM*. Materials Evaluation, 2010. **68**(5): p. 494-500.
86. Abbas, M. and M. Shafiee, *Structural health monitoring (SHM) and determination of surface defects in large metallic structures using ultrasonic guided waves*. Sensors, 2018. **18**(11): p. 3958.
87. Zhao, Y., et al., *A laser-based fiber Bragg grating ultrasonic sensing system for structural health monitoring*. IEEE Photonics Technology Letters, 2016. **28**(22): p. 2573-2576.
88. Witoś, M., et al., *NDE and SHM of critical parts using magnetic and electromagnetic methods*. Acta Physica Polonica A, 2018. **133**(3): p. 697-700.
89. Wevers, M. and K. Lambrihs, *Applications of acoustic emission for SHM: A review*. Encyclopedia of Structural Health Monitoring, 2009.
90. Strantza, M., et al., *Evaluation of SHM system produced by additive manufacturing via acoustic emission and other NDT methods*. Sensors, 2015. **15**(10): p. 26709-26725.
91. Budiman, J. *Effects of temperature on physical behavior of geomembranes*. in *Proceedings of the Fifth International Conference on Geotextiles, Geomembranes, and Related Products*. International Geosynthetics Society, Easley, SC, USA. 1994.
92. Ghee Koh, C., L. Ming See, and T. Balendra, *Damage detection of buildings: numerical and experimental studies*. Journal of structural engineering, 1995. **121**(8): p. 1155-1160.
93. Wahab, M.A. and G. De Roeck, *Damage detection in bridges using modal curvatures: application to a real damage scenario*. Journal of Sound and vibration, 1999. **226**(2): p. 217-235.

94. Hasni, H., et al., *A new approach for damage detection in asphalt concrete pavements using battery-free wireless sensors with non-constant injection rates*. Measurement, 2017. **110**: p. 217-229.
95. Kuang, K.S.C., et al., *Plastic optical fibre sensors for structural health monitoring: A review of recent progress*. Journal of sensors, 2009. **2009**.
96. Lynch, J.P. and K.J. Loh, *A summary review of wireless sensors and sensor networks for structural health monitoring*. Shock and Vibration Digest, 2006. **38**(2): p. 91-130.
97. Ye, X., T. Jin, and C. Yun, *A review on deep learning-based structural health monitoring of civil infrastructures*. Smart Structures and Systems, 2019. **24**(5): p. 567-585.
98. McCormick, N. and J. Lord, *Digital image correlation*. Materials today, 2010. **13**(12): p. 52-54.
99. Helfrick, M.N., C. Niezrecki, and P. Avitabile. *Curvature methods of damage detection using digital image correlation*. in *Health Monitoring of Structural and Biological Systems 2009*. 2009. International Society for Optics and Photonics.
100. Dworakowski, Z., et al., *Vision-based algorithms for damage detection and localization in structural health monitoring*. Structural Control and Health Monitoring, 2016. **23**(1): p. 35-50.
101. Acikgoz, S., M.J. DeJong, and K. Soga, *Sensing dynamic displacements in masonry rail bridges using 2D digital image correlation*. Structural Control and Health Monitoring, 2018. **25**(8): p. e2187.
102. Feng, M.Q., et al., *Nontarget vision sensor for remote measurement of bridge dynamic response*. Journal of Bridge Engineering, 2015. **20**(12): p. 04015023.
103. Bell, E.S., et al., *Instrumentation, digital image correlation, and modeling to monitor bridge behavior and condition assessment*. 2015, New Hampshire. Dept. of Transportation. Bureau of Materials and Research.
104. Xu, Y., J. Brownjohn, and D. Kong, *A non-contact vision-based system for multipoint displacement monitoring in a cable-stayed footbridge*. Structural Control and Health Monitoring, 2018. **25**(5): p. e2155.
105. Radopoulou, S.C. and I. Brilakis, *Automated detection of multiple pavement defects*. Journal of Computing in Civil Engineering, 2017. **31**(2): p. 04016057.
106. Radopoulou, S.C. and I. Brilakis, *Parking camera calibration for assisting automated road defect detection*. 2016.
107. Oh, B.K., et al., *Vision-based system identification technique for building structures using a motion capture system*. Journal of Sound and Vibration, 2015. **356**: p. 72-85.

108. Zhang, C. and A. Elaksher, *An unmanned aerial vehicle-based imaging system for 3D measurement of unpaved road surface distresses 1*. Computer-Aided Civil and Infrastructure Engineering, 2012. **27**(2): p. 118-129.
109. Roca, D., et al., *Low-cost aerial unit for outdoor inspection of building façades*. Automation in Construction, 2013. **36**: p. 128-135.
110. Pollock, D.G., et al., *Detection of voids in prestressed concrete bridges using thermal imaging and ground-penetrating radar*. Washington State Transportation Center (TRAC), 2008.
111. Vaghefi, K., et al., *Combined imaging technologies for concrete bridge deck condition assessment*. Journal of Performance of Constructed Facilities, 2015. **29**(4): p. 04014102.
112. Abdel-Qader, I., et al., *Segmentation of thermal images for non-destructive evaluation of bridge decks*. Ndt & E International, 2008. **41**(5): p. 395-405.
113. Deane, S., et al., *Application of NDT thermographic imaging of aerospace structures*. Infrared Physics & Technology, 2019. **97**: p. 456-466.
114. Winfree, W.P. and D.M. Heath. *Thermal diffusivity imaging of aerospace materials and structures*. in *Thermosense XX*. 1998. International Society for Optics and Photonics.
115. Johnston, J.P., et al., *High-speed infrared thermal imaging during ballistic impact of triaxially braided composites*. Journal of Composite Materials, 2018. **52**(25): p. 3549-3562.
116. Sun, J., et al., *Thermal imaging measurement and correlation of thermal diffusivity in continuous fiber ceramic composites*. 1997, Argonne National Lab., IL (United States).
117. Garra, P., et al., *Monitoring photopolymerization reactions through thermal imaging: A unique tool for the real-time follow-up of thick samples, 3D printing, and composites*. Journal of Polymer Science Part A: Polymer Chemistry, 2018. **56**(8): p. 889-899.
118. Robinson, J.B., P.R. Shearing, and D.J. Brett, *Thermal imaging of electrochemical power systems: a review*. Journal of Imaging, 2016. **2**(1): p. 2.
119. Hussain, A., H. Pu, and D.-W. Sun, *Innovative nondestructive imaging techniques for ripening and maturity of fruits—a review of recent applications*. Trends in Food Science & Technology, 2018. **72**: p. 144-152.
120. Bulanon, D., T. Burks, and V. Alchanatis, *Study on temporal variation in citrus canopy using thermal imaging for citrus fruit detection*. Biosystems Engineering, 2008. **101**(2): p. 161-171.
121. Mota-Rojas, D., et al., *Infrared thermal imaging associated with pain in laboratory animals*. Experimental Animals, 2020: p. 20-0052.
122. Jones, B.F. and P. Plassmann, *Digital infrared thermal imaging of human skin*. IEEE engineering in medicine and biology magazine, 2002. **21**(6): p. 41-48.

123. Hung, Y., et al., *Review and comparison of shearography and active thermography for nondestructive evaluation*. Materials Science and Engineering: R: Reports, 2009. **64**(5-6): p. 73-112.
124. Maldague, X.P., *Introduction to NDT by active infrared thermography*. Materials Evaluation, 2002. **60**(9): p. 1060-1073.
125. Wiecek, B. *Review on thermal image processing for passive and active thermography*. in *2005 IEEE Engineering in Medicine and Biology 27th Annual Conference*. 2006. IEEE.
126. Omar, T. and M.L. Nehdi, *Remote sensing of concrete bridge decks using unmanned aerial vehicle infrared thermography*. Automation in Construction, 2017. **83**: p. 360-371.
127. Ma, Y., et al., *Quasi-Active Thermal Imaging of Large Floating Covers Using Ambient Solar Energy*. Remote Sensing, 2020. **12**(20): p. 19.
128. Hallermann, N. and G. Morgenthal. *Unmanned aerial vehicles (UAV) for the assessment of existing structures*. in *IABSE Symposium Report*. 2013. International Association for Bridge and Structural Engineering.
129. Lorenc, S.J., B.E. Handlon, and L.E. Bernold, *Development of a robotic bridge maintenance system*. Automation in Construction, 2000. **9**(3): p. 251-258.
130. Oh, J.-K., et al., *Bridge inspection robot system with machine vision*. Automation in Construction, 2009. **18**(7): p. 929-941.
131. Lim, R.S., et al. *Developing a crack inspection robot for bridge maintenance*. in *2011 IEEE International Conference on Robotics and Automation*. 2011. IEEE.
132. Bagavathiappan, S., et al., *Infrared thermography for condition monitoring—A review*. Infrared Physics & Technology, 2013. **60**: p. 35-55.
133. Sanati, H., D. Wood, and Q. Sun, *Condition monitoring of wind turbine blades using active and passive thermography*. Applied Sciences, 2018. **8**(10): p. 2004.
134. Roche, J.-M., et al. *Passive and active thermography for in situ damage monitoring in woven composites during mechanical testing*. in *AIP Conference Proceedings*. 2013. American Institute of Physics.
135. Lahiri, B., et al., *Medical applications of infrared thermography: a review*. Infrared Physics & Technology, 2012. **55**(4): p. 221-235.
136. Sham, J.F., et al., *Imaging and condition diagnosis of underground sewer liners via active and passive infrared thermography: a case study in Singapore*. Tunnelling and Underground Space Technology, 2019. **84**: p. 440-450.
137. Bach, P.M. and J.K. Kodikara, *Reliability of infrared thermography in detecting leaks in buried water reticulation pipes*. IEEE Journal of Selected Topics in Applied Earth Observations and Remote Sensing, 2017. **10**(9): p. 4210-4224.

138. Tarin, M. and R. Rotolante, *NDT in composite materials with flash, transient, and lock-in thermography*. FLIR Technical Series, 2011.
139. Saarimäki, E. and P. Ylinen, *An investigation of non-destructive thermographic inspection exploiting phase transition of water for moisture detection in aircraft structures*. Proceedings of QIRT, Krakow, Poland, 2008: p. 2-5.
140. Ibarra-Castanedo, C. and X. Maldague. *Recent progresses in the inspection of aerospace components by infrared thermography*. in 第十七届世界无损检测会议 (17th World Conference on Nondestructive Testing). 2008. 中国机械工程学会.
141. Maierhofer, C. and M. Röllig. *Active thermography for the characterization of surfaces and interfaces of historic masonry structures*. in *Proceedings of the 7th International Symposium on Non-destructive Testing in Civil Engineering (NDTCE)*, Nantes, France. 2009. Citeseer.
142. Tavukçuoğlu, A., et al., *Use of IR thermography for the assessment of surface-water drainage problems in a historical building, Ağzıkarahan (Aksaray), Turkey*. NDT & E International, 2005. **38**(5): p. 402-410.
143. Martínez, J., R. Lagioia, and S. Edenor. *Experience performing infrared thermography in the maintenance of a distribution utility*. in *19th International Conference on Electricity Distribution*, Vienna. 2007.
144. Sakagami, T. and S. Kubo, *Applications of pulse heating thermography and lock-in thermography to quantitative nondestructive evaluations*. Infrared Physics & Technology, 2002. **43**(3-5): p. 211-218.
145. Titman, D., *Applications of thermography in non-destructive testing of structures*. NDT & e International, 2001. **34**(2): p. 149-154.
146. Favro, L., et al., *Thermal wave imaging for aging aircraft inspection*. Materials Evaluation;(United States), 1993. **51**(12).
147. Varis, J. and R. Lehtiniemi, *A thermal nondestructive evaluation system for detecting vertical cracks in unidirectional carbon fiber composites*. Review of scientific instruments, 1997. **68**(7): p. 2818-2821.
148. Mian, A., et al., *Fatigue damage detection in graphite/epoxy composites using sonic infrared imaging technique*. Composites Science and Technology, 2004. **64**(5): p. 657-666.
149. Swiderski, W. and D. Szabra. *Possibility of defect detection in multi-layered composite materials used for military applications by IR thermography*. in *Proc. of the 5th International Workshop on Advances in Signal Processing for Non-Destructive Evaluation of Materials*, Quebec City, Canada. 2005.
150. Omar, M., et al., *Infrared thermography for inspecting the adhesion integrity of plastic welded joints*. NDT & E International, 2006. **39**(1): p. 1-7.

151. Kafieh, R., T. Lotfi, and R. Amirfattahi, *Automatic detection of defects on polyethylene pipe welding using thermal infrared imaging*. Infrared Physics & Technology, 2011. **54**(4): p. 317-325.
152. Flores-Bolarin, J. and R. Royo-Pastor. *Infrared thermography: A good tool for nondestructive testing of plastic materials*. in *Proceedings of the 5th European Thermal-Sciences Conference, Eindhoven, The Netherlands*. 2008.
153. Dassisti, M., et al., *Thermography-enhanced LCA (Life Cycle Assessment) for manufacturing sustainability assessment. The case study of an HDPE (High Density Polyethylene) net company in Italy*. Energy, 2016. **108**: p. 7-18.
154. Gheysari, D., A. Behjat, and M. Haji-Saeid, *The effect of high-energy electron beam on mechanical and thermal properties of LDPE and HDPE*. European Polymer Journal, 2001. **37**(2): p. 295-302.
155. Bendada, A., F. Erchiqui, and A. Kipping, *Understanding heat transfer mechanisms during the cooling phase of blow molding using infrared thermography*. NDT & E International, 2005. **38**(6): p. 433-441.
156. Vollmer, M. and K.-P. Möllmann, *Infrared thermal imaging: fundamentals, research and applications*. 2017: John Wiley & Sons.
157. Avdelidis, N. and A. Moropoulou, *Emissivity considerations in building thermography*. Energy and Buildings, 2003. **35**(7): p. 663-667.
158. Fokaides, P.A. and S.A. Kalogirou, *Application of infrared thermography for the determination of the overall heat transfer coefficient (U-Value) in building envelopes*. Applied energy, 2011. **88**(12): p. 4358-4365.
159. O'Grady, M., A.A. Lechowska, and A.M. Harte, *Quantification of heat losses through building envelope thermal bridges influenced by wind velocity using the outdoor infrared thermography technique*. Applied energy, 2017. **208**: p. 1038-1052.
160. Grinzato, E., P.G. Bison, and S. Marinetti, *Monitoring of ancient buildings by the thermal method*. Journal of Cultural Heritage, 2002. **3**(1): p. 21-29.
161. Lagüela, S., et al., *Automation of thermographic 3D modelling through image fusion and image matching techniques*. Automation in Construction, 2012. **27**: p. 24-31.
162. Fox, M., et al., *Time-lapse thermography for building defect detection*. Energy and Buildings, 2015. **92**: p. 95-106.
163. Pearson, C.C., *Thermal Imaging of building fabric*. 2011: BSRIA Bracknell, UK.
164. Merchant, J.W., *Remote Sensing of the Environment: An Earth Resource Perspective*. Cartography and Geographic Information Science, 2000. **27**(4): p. 311-311.

165. de Freitas, S.S., V.P. de Freitas, and E. Barreira, *Detection of façade plaster detachments using infrared thermography—A nondestructive technique*. Construction and Building Materials, 2014. **70**: p. 80-87.
166. Cadelano, G., et al., *Monitoring of historical frescoes by timed infrared imaging analysis*. Opto-electronics review, 2015. **23**(1): p. 102-108.
167. Hiasa, S., R. Birgul, and F.N. Catbas, *A data processing methodology for infrared thermography images of concrete bridges*. Computers & Structures, 2017. **190**: p. 205-218.
168. Dabous, S.A., et al., *Concrete bridge deck condition assessment using IR Thermography and Ground Penetrating Radar technologies*. Automation in Construction, 2017. **81**: p. 340-354.
169. Omar, T., M.L. Nehdi, and T. Zayed, *Infrared thermography model for automated detection of delamination in RC bridge decks*. Construction and Building Materials, 2018. **168**: p. 313-327.
170. Janků, M. and J. Stryk. *Application of infrared camera to bituminous concrete pavements: measuring vehicle*. in *IOP Conference Series: Materials Science and Engineering*. 2017. IOP Publishing.
171. Oba, K. and M.N. Partl, *Non-destructive IR-thermography for distress detection in asphalt pavements and bridge deck surfacings*. Road Materials and Pavement Design, 2000. **1**(4): p. 407-418.
172. Moropoulou, A., et al., *An application of thermography for detection of delaminations in airport pavements*. NDT & E International, 2001. **34**(5): p. 329-335.
173. Moropoulou, A., et al., *Infrared thermography and ground penetrating radar for airport pavements assessment*. Nondestructive testing and Evaluation, 2002. **18**(1): p. 37-42.
174. Dumoulin, J., et al., *Active infrared thermography applied to defect detection and characterization on asphalt pavement samples: comparison between experiments and numerical simulations*. Journal of modern optics, 2010. **57**(18): p. 1759-1769.
175. Yehia, S., et al., *Detection of common defects in concrete bridge decks using nondestructive evaluation techniques*. Journal of Bridge Engineering, 2007. **12**(2): p. 215-225.
176. Hiasa, S., et al., *Experimental and numerical studies for suitable infrared thermography implementation on concrete bridge decks*. Measurement, 2018. **121**: p. 144-159.
177. Ahlborn, T.M., et al., *Bridge condition assessment using remote sensors*. 2013.
178. Al Gharawi, M., Y. Adu-Gyamfi, and G. Washer, *A framework for automated time-lapse thermography data processing*. Construction and Building Materials, 2019. **227**: p. 116507.
179. Sokavcic, A., *Application of infrared thermography to the non-destructive testing of concrete structures*. 2010, PhD thesis, Gradjevinski fakultet, Sveucilivste u Zagrebu.

180. Watase, A., et al., *Practical identification of favorable time windows for infrared thermography for concrete bridge evaluation*. Construction and Building Materials, 2015. **101**: p. 1016-1030.
181. Matsumoto, M., K. Mitani, and F.N. Catbas. *Bridge assessment methods using image processing and infrared thermography technology*. in *Proc., 92nd Annual Meeting, Transportation Research Board, Washington, DC*. 2013.
182. Washer, G., et al., *Effects of environmental variables on infrared imaging of subsurface features of concrete bridges*. Transportation research record, 2009. **2108**(1): p. 107-114.
183. Blevin, W. and W. Brown, *A precise measurement of the Stefan-Boltzmann constant*. Metrologia, 1971. **7**(1): p. 15.
184. Abbas, A.K., et al., *Neonatal infrared thermography imaging: analysis of heat flux during different clinical scenarios*. Infrared Physics & Technology, 2012. **55**(6): p. 538-548.
185. Palmer, J.M. and B.G. Grant. *The art of radiometry*. 2009. SPIE.
186. Rogalski, A., *Infrared detectors*. 2010: CRC press.
187. Marinetti, S. and P.G. Cesaratto, *Emissivity estimation for accurate quantitative thermography*. NDT & E International, 2012. **51**: p. 127-134.
188. Bergman, T.L., et al., *Fundamentals of heat and mass transfer*. Eighth edition / Theodore L. Bergman, Department of Mechanical Engineering, University of Kansas, Adrienne S. Lavine, Mechanical and Aerospace Engineering Department, University of California, Los Angeles. ed. 2017: Hoboken, NJ : John Wiley & Sons, Inc.
189. Ribet-Mohamed, I., et al., *Advanced characterization of the radiometric performances of quantum well infrared photodetectors*. Infrared physics & technology, 2005. **47**(1-2): p. 119-131.
190. Pelte, T., P. Pierson, and J.P. Gourc, *Thermal Analysis of Geomembrane Exposed to Solar Radiation*. Geosynthetics International, 1994. **1**(1): p. 21-44.
191. Carslaw, H.S., *Conduction of heat in solids*. 2nd ed. ed, ed. J.C. Jaeger. 1986, Oxford [Oxfordshire] : New York: Oxford Oxfordshire : Clarendon Press
New York : Oxford University Press.
192. Maldague, X., *Nondestructive evaluation of materials by infrared thermography*. 1993, London
New York: London
New York : Springer-Verlag.
193. Krapez, J.-C., F. Lepoutre, and D. Balageas, *Early detection of thermal contrast in pulsed stimulated thermography*. Le Journal de Physique IV, 1994. **4**(C7): p. C7-47-C7-50.

194. Ibarra Castanedo, C., *Quantitative subsurface defect evaluation by pulsed phase thermography: depth retrieval with the phase*. 2005.
195. Ibarra-Castanedo, C. and X.P. Maldague. *Defect depth retrieval from pulsed phase thermographic data on plexiglas and aluminum samples*. in *Thermosense XXVI*. 2004. International Society for Optics and Photonics.
196. Maldague, X. and S. Marinetti, *Pulse phase infrared thermography*. Journal of applied physics, 1996. **79**(5): p. 2694-2698.
197. Almond, D.P., P. Patel, and P. Patel, *Photothermal science and techniques*. Vol. 10. 1996: Springer Science & Business Media.
198. Maldague, X., *Theory and practice of infrared technology for nondestructive testing*. 2001.
199. Ringermacher, H.I., R.J. Archacki Jr, and W.A. Veronesi, *Nondestructive testing: Transient depth thermography*. 1998, Google Patents.
200. Pilla, M., et al. *New absolute contrast for pulsed thermography*. in *Proc. QIRT*. 2002.
201. Vavilov, V., et al., *Dynamic thermal tomography: new NDE technique to reconstruct inner solids structure using multiple IR image processing*, in *Review of progress in quantitative nondestructive evaluation*. 1992, Springer. p. 425-432.
202. Favro, L., et al., *IR thermal wave tomographic studies of structural composites*, in *Review of Progress in Quantitative Nondestructive Evaluation*. 1992, Springer. p. 447-451.
203. Favro, L.D., et al. *Imaging the early time behavior of reflected thermal wave pulses*. in *Thermosense XVII: An International Conference on Thermal Sensing and Imaging Diagnostic Applications*. 1995. International Society for Optics and Photonics.
204. Han, X., et al., *Early-time pulse-echo thermal wave imaging*, in *Review of progress in quantitative nondestructive evaluation*. 1996, Springer. p. 519-524.
205. Han, X., L. Favro, and R. Thomas. *Thermal wave NDI of disbonds and corrosion in aircraft*. in *NASA CONFERENCE PUBLICATION*. 1999. NASA.
206. Shepard, S.M., et al., *Reconstruction and enhancement of active thermographic image sequences*. Optical Engineering, 2003. **42**(5): p. 1337-1342.
207. Chou, Y.-C. and L. Yao. *Automatic diagnostic system of electrical equipment using infrared thermography*. in *2009 international conference of soft computing and pattern recognition*. 2009. IEEE.
208. Lahiri, B., et al., *Quantification of defects in composites and rubber materials using active thermography*. Infrared Physics & Technology, 2012. **55**(2-3): p. 191-199.
209. Jadin, M.S. and S. Taib, *Recent progress in diagnosing the reliability of electrical equipment by using infrared thermography*. Infrared Physics & Technology, 2012. **55**(4): p. 236-245.

210. Moja, N.T. and A.J. Willis. *Classification of thermally condition-monitored components using statistical and neural network techniques*. in *Applications of Digital Image Processing XX*. 1997. International Society for Optics and Photonics.
211. Lin, H., et al. *Image registration based on corner detection and affine transformation*. in *2010 3rd International Congress on Image and Signal Processing*. 2010. IEEE.
212. Ishino, R. *Detection of a faulty power distribution apparatus by using thermal images*. in *2002 IEEE Power Engineering Society Winter Meeting. Conference Proceedings (Cat. No. 02CH37309)*. 2002. IEEE.
213. Shafi'i, M.A. and N. Hamzah. *Internal fault classification using artificial neural network*. in *2010 4th International Power Engineering and Optimization Conference (PEOCO)*. 2010. IEEE.
214. Shan, P., *Image segmentation method based on K-mean algorithm*. EURASIP Journal on Image and Video Processing, 2018. **2018**(1): p. 1-9.
215. Garg, I. and B. Kaur. *Color based segmentation using K-mean clustering and watershed segmentation*. in *2016 3rd International Conference on Computing for Sustainable Global Development (INDIACom)*. 2016. IEEE.
216. Warne, P.P. and S. Ganorkar, *Detection of diseases on cotton leaves using k-mean clustering method*. International Research Journal of Engineering and Technology (IRJET), 2015. **2**(4): p. 425-431.
217. Osman, M., et al. *Colour image segmentation of tuberculosis bacilli in Ziehl-Neelsen-stained tissue images using moving k-mean clustering procedure*. in *2010 Fourth Asia International Conference on Mathematical/Analytical Modelling and Computer Simulation*. 2010. IEEE.
218. Jain, A.K., *Data clustering: 50 years beyond K-means*. Pattern recognition letters, 2010. **31**(8): p. 651-666.
219. Savkare, S., A. Narote, and S. Narote. *Automatic blood cell segmentation using K-Mean clustering from microscopic thin blood images*. in *Proceedings of the Third International Symposium on Computer Vision and the Internet*. 2016.
220. Zhao, Y., G. Karypis, and U. Fayyad, *Hierarchical clustering algorithms for document datasets*. Data mining and knowledge discovery, 2005. **10**(2): p. 141-168.
221. Ester, M., et al. *A density-based algorithm for discovering clusters in large spatial databases with noise*. in *Kdd*. 1996.
222. Duan, L., et al., *A local-density based spatial clustering algorithm with noise*. Information systems, 2007. **32**(7): p. 978-986.

223. Ye, Q., W. Gao, and W. Zeng. *Color image segmentation using density-based clustering*. in *2003 International Conference on Multimedia and Expo. ICME'03. Proceedings (Cat. No. 03TH8698)*. 2003. IEEE.
224. Suyal, H., A. Panwar, and A.S. Negi, *Text Clustering Algorithms: A Review*. International Journal of Computer Applications, 2014. **96**(24).
225. Shen, J., et al., *Real-time superpixel segmentation by DBSCAN clustering algorithm*. IEEE transactions on image processing, 2016. **25**(12): p. 5933-5942.
226. Kumar, K.M. and A.R.M. Reddy, *A fast DBSCAN clustering algorithm by accelerating neighbor searching using Groups method*. Pattern Recognition, 2016. **58**: p. 39-48.
227. Nguyen, T., *Gaussian mixture model based spatial information concept for image segmentation*. 2011.
228. Lee, D.-S., et al., *Automatic image segmentation for concealed object detection using the expectation-maximization algorithm*. Optics express, 2010. **18**(10): p. 10659-10667.
229. Fu, Z. and L. Wang. *Color image segmentation using gaussian mixture model and em algorithm*. in *International Conference on Multimedia and Signal Processing*. 2012. Springer.
230. Yin, S., Y. Zhang, and S. Karim, *Large scale remote sensing image segmentation based on fuzzy region competition and Gaussian mixture model*. IEEE Access, 2018. **6**: p. 26069-26080.
231. Ji, Z., Y. Xia, and Y. Zheng, *Robust generative asymmetric GMM for brain MR image segmentation*. Computer methods and programs in biomedicine, 2017. **151**: p. 123-138.
232. Pham, D. and D. Karaboga, *Intelligent optimisation techniques: genetic algorithms, tabu search, simulated annealing and neural networks*. 2012: Springer Science & Business Media.
233. FLIR, *User's manual FLIR A6xx series*, O. FLIR systems: Wilsonville, United States Editor. 2016.
234. Apogee, *Apogee instruments owner's manual pyranometer models SP-110 and SP-230*, Logan.USA, Editor. 2020.
235. Corporation, F., *Fluke 287/289 true-rms Digital Multimeters Users Manual*. 2007.
236. Sun, J., *Analysis of pulsed thermography methods for defect depth prediction*. J. Heat Transf.-Trans. ASME, 2006. **128**(4): p. 329-338.
237. Zeng, Z., et al., *Depth prediction of non-air interface defect using pulsed thermography*. NDT & E International, 2012. **48**: p. 39-45.
238. Rajic, N., *Principal component thermography for flaw contrast enhancement and flaw depth characterisation in composite structures*. Composite structures, 2002. **58**(4): p. 521-528.

239. Çengel, Y.A., *Heat and mass transfer : fundamentals & applications*. Fifth edition. ed, ed. A.J. Ghajar. 2015: New York, NY : McGraw Hill Education.
240. Thakare, K., H. Vishwakarma, and A. Bhave, *Experimental investigation of possible use of HDPE as thermal storage material in thermal storage type solar cookers*. Journal of Research in Engineering and Technology, 2015. **4**: p. 92-99.
241. Celenk, M., *A color clustering technique for image segmentation*. Computer Vision, Graphics, and image processing, 1990. **52**(2): p. 145-170.
242. Zeri, M., et al., *Tools for communicating agricultural drought over the Brazilian Semiarid using the soil moisture index*. Water, 2018. **10**(10): p. 1421.
243. Nikiforova, T., et al., *Methods and results of experimental researches of thermal conductivity of soils*. Energy Procedia, 2013. **42**(0).
244. Kodešová, R., et al., *Thermal properties of representative soils of the Czech Republic*. Soil and Water Research, 2013. **8**(4): p. 141-150.
245. Balasubramanian, R., et al., *Conversion of bio-solids (scum) from tannery effluent treatment plant into biodiesel*. Energy Sources Part A-recovery Utilization and Environmental Effects, 2018. **40**(8): p. 959-967.
246. Song, H.W., et al., *Thermal conductivity characteristics of dewatered sewage sludge by thermal hydrolysis reaction*. Journal of the Air & Waste Management Association, 2014. **64**(12): p. 1384-1389.
247. Milhé, M., M. Sauceau, and P. Arlabosse, *Modeling of a continuous sewage sludge paddle dryer by coupling Markov chains with penetration theory*. Applied Mathematical Modelling, 2016. **40**(19-20): p. 8201-8216.
248. Bondo, K.J., D.R. Brooks, and R.M. Brigham, *Quantifying relative levels of solar radiation at bat roosts using pyranometers*. Wildlife Society Bulletin, 2017. **41**(2): p. 376-380.
249. Genest, M., et al., *Pulsed thermography for non-destructive evaluation and damage growth monitoring of bonded repairs*. Composite Structures, 2009. **88**(1): p. 112-120.
250. Ibarra-Castanedo, C., et al. *Inspection of aerospace materials by pulsed thermography, lock-in thermography, and vibrothermography: a comparative study*. in *Thermosense XXIX*. 2007. International Society for Optics and Photonics.
251. Wang, K.-S., et al., *The thermal conductivity mechanism of sewage sludge ash lightweight materials*. Cement and concrete research, 2005. **35**(4): p. 803-809.
252. Ding, H.-S. and H. Jiang, *Self-heating co-pyrolysis of excessive activated sludge with waste biomass: Energy balance and sludge reduction*. Bioresource Technology, 2013. **133**: p. 16-22.

- 253. Wang, Y., et al., *Specific heat capacity of soil solids: Influences of clay content, organic matter, and tightly bound water*. Soil Science Society of America Journal, 2019. **83**(4): p. 1062-1066.
- 254. O'Kelly, B.C., *Consolidation properties of a dewatered municipal sewage sludge*. Canadian Geotechnical Journal, 2005. **42**(5): p. 1350-1358.
- 255. Rowe, R. and A. Hoor, *Predicted temperatures and service lives of secondary geomembrane landfill liners*. Geosynthetics International, 2009. **16**(2): p. 71-82.
- 256. Rowe, R., *Long-term performance of contaminant barrier systems*. Geotechnique, 2005. **55**(9): p. 631-678.
- 257. Rowe, R.K. and M.Z. Islam, *Impact of landfill liner time–temperature history on the service life of HDPE geomembranes*. Waste management (Elmsford), 2009. **29**(10): p. 2689-2699.
- 258. Hanson, J.L., N. Yesiller, and G. Swarbrick, *Thermal analysis of GCLs at a municipal solid waste landfill*, in *Waste Containment and Remediation*. 2005. p. 1-15.